

Aleksander Sendrowicz
Seweryn Witold Wierdak
Aleksander Omholt Myhre

In-Situ Characterisation of Fatigue Crack Growth by a Combination of Advanced Techniques

Master's thesis in Mechanical Engineering

Supervisor: Alexei Vinogradov

June 2019

Aleksander Sendrowicz
Seweryn Witold Wierdak
Aleksander Omholt Myhre

In-Situ Characterisation of Fatigue Crack Growth by a Combination of Advanced Techniques

Master's thesis in Mechanical Engineering
Supervisor: Alexei Vinogradov
June 2019

Norwegian University of Science and Technology
Faculty of Engineering
Department of Mechanical and Industrial Engineering



Preface and Acknowledgements

This master thesis marks the end of the five year Master of Science degree in mechanical engineering with specialisation in product development and material science, for the authors; Aleksander Sendrowicz, Aleksander Omholt Myhre, and Seweryn Witold Wierdak.

We would like to thank everyone who contributed to this project.

First of all, we want to thank our supervisor, Professor Alexei Vinogradov, for all the support during the project thesis and master thesis. We are very thankful for the time he offered to help us, and all the inspiring conversations. His guidance was priceless.

We would like to thank our co-supervisor Professor Filippo Berto, Antonio Alvaro from SINTEF, and Tore Andre Kristensen from SINTEF for the help they offered. Without this support it would not be possible to perform the laboratory work.

We would like to thank our "office comrade" Florian Schott for all support and conversations during the master project.

Aleksander Sendrowicz would like to thank his family, especially his father who always did his best to answer any questions, and uncle Jacek who encouraged him to think critically and tinker.

Seweryn Witold Wierdak would like to thank his girlfriend, parents, grandparents and brother for the support, and the patience. He will also thank Aleksander Sendrowicz for all the help during the five years of study.

Aleksander Omholt Myhre would like to thank his family and friends for moral support, especially during the last weeks of writing.

Summary

This work describes fatigue crack growth investigation by several advanced techniques applied concurrently; the infrared thermography, acoustic emission, and rapid video imaging combined with digital image correlation. All these methods have been used simultaneously in a Fatigue Crack Growth (FCG) test to analyse the crack growth. This posed challenges which had to be overcome before valuable results could be produced. These challenges included (i) the experimental setup of all the equipment, (ii) synchronising all devices in the setup, and (iii) choosing the right material and load conditions being the first.

The experiment obtained new and interesting results from each technique. This not only allowed us to analyse the data individually, but also to compare data obtained by the different techniques. Some of the data acquired from the experiments were:

- Crack growth data acquired by both cameras.
- Stress field, and plastic zone size measurements by infrared thermography and high-speed photography aided by digital image correlation.
- Crack closure and effective stress intensity based both on infrared thermography and high-speed photography aided by digital image correlation.
- Energy analysis based on infrared and acoustic emission data.

Additionally the tests gave insight into the processes underlying the stage III of the crack growth, and other useful information. Some of the data comparison between different techniques did show very good agreement, like the crack closure measurements, whereas some other showed slightly different results, e.g. the measurements of the plastic zone size.

The general idea of the experiment was fulfilled, which was to gain better understanding of the mechanisms behind fatigue crack growth.

Sammendrag

Denne oppgaven utforsker sprekkvekstutmatting ved samtidig bruk av flere avanserte metoder; infrarød termografi, akustisk emisjon, og høyhastighetsavbildning kombinert med digital bildekorrelasjon. Alle metodene ble brukt sammen i sprekkvekstutmattingstester, for å analysere sprekkvekstforløpet. Dette skapte utfordringer som måtte løses før verdifulle resultater kunne oppnås. Blant utfordringene kan nevnes; det eksperimentelle oppsettet med alle enheter (i), synkronisering av hele oppsettet (ii), og ikke minst valg av riktig testmateriale og lastforhold (iii).

Eksperimentet førte til interessante funn fra hver av de brukte metodene. Dette tillot ikke bare analyse av data individuelt, men også sammenligning av data anskaffet ved hjelp av de ulike teknikkene. Dette inkluderte blant annet:

- Sprekkvekstdata anskaffet ved hjelp av begge kameraene.
- Målinger av spenningsfeltet, samt størrelse på plastisk sone målt med infrarødt kamera og høyhastighetskamera med tilleggsanalyse i form av digital bildekorrelasjon.
- Målinger av sprekkklukking, samt effektiv spenningsintensitetsfaktor målt med infrarødt kamera og høyhastighetskamera med tilleggsanalyse i form av digital bildekorrelasjon.
- Energianalyse basert på infrarød og akustisk data.

I tillegg gav testene en innsikt i hva som foregår i steg III av sprekkvekstforløpet, samt annen nyttig informasjon. Enkelte data fra de ulike teknikkene hadde god overenstemmelse, eksempelvis målinger av sprekkklukking, mens andre, som målinger av størrelse på plastisk sone hadde noe større numeriske avvik.

Utgangspunktet for eksperimentet ble oppfylt: å øke forståelsen av mekanismene som ligger bak sprekkvekstutmatting.

Table of contents

List of Tables	X
List of Figures	XI
List of Abbreviations	XXII
List of Symbols	XXVI
1 Introduction	1
1.1 General introduction	1
1.2 Research method in brief	1
1.3 Problem statement	2
1.4 Limitations	2
1.5 Structure of the report	3
1.6 Authors' contributions	3
2 Theory and literature review	6
2.1 Linear-Elastic Fracture Mechanics	6
2.1.1 Modelling of stress fields	7
2.2 General fatigue theory	11
2.2.1 Crack initiation	12
2.2.2 Crack propagation	13
2.2.3 Failure	13
2.2.4 Crack closure	13
2.3 Infrared thermography and fatigue analysis	14
2.3.1 Basics of infrared thermography	14
2.3.2 Factors affecting temperature in a fatigue test	17
2.3.3 Infrared thermography and fatigue	20

2.4	High-Speed Photography and Digital Image Correlation	24
2.4.1	Optical methods	24
2.4.2	High-Speed Photography	25
2.4.3	Digital Image Correlation	33
2.4.4	Conclusions arising from theory and literature	40
2.5	Digital Image Processing	41
2.5.1	Discrete Fourier Transform	41
2.5.2	Gaussian low-pass filter	44
2.6	Acoustic Emission	46
2.6.1	Fundamentals of Acoustic Emission	46
2.6.2	Acoustic emission from dislocations	49
2.6.3	Acoustic emission related to cracks	52
2.6.4	Acoustic emission from miscellaneous sources	55
2.6.5	Source localisation using acoustic emission	55
2.6.6	AE Signal Processing	57
3	Methodology, materials and experimental setup	63
3.1	Specimens	63
3.1.1	Material	63
3.1.2	Tensile specimen	63
3.1.3	C(T) specimen	65
3.2	Equipment and software used	69
3.2.1	Infrared thermography	69
3.2.2	High-speed imaging and DIC	70
3.2.3	Acoustic Emission	76
3.3	Triggering of the equipment	77
3.3.1	Hardware	77
3.3.2	Software	79
3.4	Experimental procedures for IRT	81

3.4.1	Noise reduction in infrared pictures	81
3.4.2	Motion compensation	83
3.4.3	Temperature and phase shift analysis	86
3.4.4	Stress calculations and Williams' expansion	90
3.4.5	Plastic zone size	95
3.4.6	Heat dissipation	98
3.5	Experimental procedures for HSI and DIC	99
3.5.1	Crack tip detection without using DIC	99
3.5.2	Determining the FCG parameters in Paris regime	101
3.5.3	Investigating the vignetting effect on DIC results	103
3.5.4	Post-processing the tensile test data using DIC	105
3.5.5	Crack tip detection using DIC	107
3.5.6	Measuring crack opening displacements and the effective SIF using DIC	110
3.5.7	Stress analysis and plastic zone size determination using DIC	113
3.6	Experimental Procedures for Acoustic Emission	115
3.6.1	Hit based procedures	115
3.6.2	Waveform streaming procedures	122
4	Results	126
4.1	Test summary	126
4.1.1	Tensile tests	126
4.1.2	Test 1	126
4.1.3	Test 2	126
4.1.4	Test 3	126
4.1.5	Test 4	127
4.1.6	Test 5	127
4.1.7	Test 6	127
4.2	Infrared Thermography	128

4.2.1	Thermoelastic parameter	128
4.2.2	Filtering evaluation	129
4.2.3	Energy dissipation	132
4.2.4	Stress intensity factor	140
4.2.5	Stress fields	142
4.2.6	Crack growth curves	145
4.2.7	Plastic zone	152
4.2.8	Fourier analysis of test 4	161
4.2.9	Qualitative data for stage III of test 6	164
4.3	High-speed imaging and DIC	169
4.3.1	Influence of vignetting on DIC analysis	169
4.3.2	Comparison of strain from DIC and extensometer	173
4.3.3	Engineering and true stress-strain curves	175
4.3.4	Stress intensity factor and crack closure	180
4.3.5	Strain and stress fields	182
4.3.6	Plastic zone	186
4.3.7	Fatigue crack growth parameters in Paris regime	188
4.3.8	Qualitative observation of crack initiation and propagation	192
4.4	Acoustic Emission	197
4.4.1	Count rate curves	197
4.4.2	Hit-Based parameters	200
4.4.3	Signal Energy	206
4.4.4	Summary of Cumulative Hit Parameters	211
4.4.5	Waveforms	214
4.4.6	Clustering	219
4.5	Comparison of results from different methods	224
4.5.1	DIC and IRT	224

5 Discussion **228**

5.1	Infrared Thermography	228
5.1.1	Thermoelastic constant	228
5.1.2	Data filtering	228
5.1.3	Energy dissipation	229
5.1.4	Stress intensity factor	232
5.1.5	Stress fields	233
5.1.6	Plastic zone	234
5.1.7	Crack growth curves	237
5.1.8	Stage III	238
5.2	High-speed imaging and DIC	239
5.2.1	Influence of vignetting on DIC analysis	239
5.2.2	The tensile tests	240
5.2.3	COD, crack closure and the effective SIF analysis	243
5.2.4	Strain fields, stress fields and plastic zone	247
5.2.5	Fatigue crack growth curves and Paris' law parameters	252
5.2.6	Crack initiation, propagation and transition to stage III	253
5.3	Acoustic Emission	256
5.3.1	Quality of Data	256
5.3.2	Count rate versus FCG curves	264
5.3.3	Signal Peaks in Stage II	268
5.3.4	Clustering	269
5.3.5	Transition From Stage II to Stage III	272
5.4	Comparison of the results	274
5.4.1	DIC and IRT	275
6	Conclusion and further work	277
6.1	Conclusion	277
6.2	Further work	280

List of Tables

3	Chemical composition and mechanical properties of AISI 316L	63
4	Thicknesses of the tensile specimens	64
5	Dimensions of the specimen	66
6	Specimen surface preparation	68
7	Frame rate, image resolution and memory capacity summary (from Photron FASTCAM SA-Z Datasheet)	71
8	Summary of fatigue crack growth parameters and R^2 values, based on Thermoelastic Stress Analysis (TSA) and the theoretical stress intensity	152
9	Summary of fatigue crack growth parameters and R^2 values, based on Williams' stress field fit, and theoretical stress intensity	152
10	Summary of fatigue crack growth parameters and R^2 values, based on Williams' stress field fit, and measured stress intensity	152
11	Parameters found using tensile tests	176
12	True stress and true strain values at UTS	179
13	Summary of fatigue crack growth parameters and R^2 values.	188
14	Summary of Acoustic Emission (AE) count rate parameters and R^2 values, based on mean and peak count rate calculations	197
15	Summary of AE count rate parameters and R^2 values, based on mean and peak count rate calculations	199
16	Summary of AE count rate parameters and R^2 values, based on mean and peak count rate calculations of Test 6	200
17	Cluster consistency determined by silhouette criterion of Test 5	221
18	Cluster consistency determined by silhouette criterion of Test 6	223
19	Types of lightning used in high-speed photography	ii

List of Figures

1	The principal modes of fracture. From left to right: mode I, mode II, mode III.	6
2	The theoretical elastic stress fields	8
3	Stress situation for Westergaards solution.	9
4	An illustration of the fatigue crack growth curve	12
5	Atmospheric attenuation (white areas) with a chart of the gases and water vapour causing most of it. The areas under the curve represent the highest Infrared Radiation (IR) transmission.	15
6	The figure illustrates the reflectance, emittance, and transmittance of an object, and attenuation caused by atmosphere.	15
7	Relative sensitivity for different sensors and wavelengths.	16
8	Instantaneous Field Of View (IFOV) (red squares) relative to object size. .	17
9	Maximum thermal increments in specimens under fatigue loading at different stresses, $R=0$. Three phases are shown for 245 MPa.	21
10	Illustration of the phase in a Compact Tension specimen (C(T)) specimen.	22
11	Example of tracking the reference subset in the deformed image using DIC	34
12	Linear transformation of subset coordinates by applying warp function W .	36
13	Original picture in grayscale to be filtered	44
14	Log-magnitude representation of Discrete Fourier Transform (DFT) of the picture in figure 13	44
16	Typical elements of an AE system.	46
17	Common discrete signal parameters.	48
18	One dimensional source location.	56
19	Narrowband (high time-resolution) vs wideband (high frequency-resolution) STFT.	61
20	Tensile specimen with dimensions	64

21	Points where the thickness of samples was measured	64
22	Standard Compact C(T) Specimen for Fatigue Crack Growth Rate Testing.	66
23	The specimen surface seen with the high-speed camera	68
24	Random pattern used for Digital Image Correlation (DIC)-analysis	68
25	Comparison of the plastic zone obtained using different Region Of Interests (ROIs)	74
26	Comparison of the bitmap showing the area of the plastic deformation obtained using different DIC parameters	75
27	Figure showing the trigger algorithm	79
28	Figure showing the graphical interface for trigger software	81
29	The temperature range in the pictures is 1,05K	83
30	First stage of motion compensation	84
31	The two frames are superimposed with different colormaps, adding to a RGB picture	85
32	Final result, the second frame transformed with respect to the first.	85
33	Temperature measurement in a single picture during one acquisition, and a first order Fourier fit	87
34	Temperature amplitude in a single acquisition, based on Fourier fit, and the algorithm	87
35	Second order discrete Fourier fit, A1 and P1 are the first order amplitude and phase shift respectively, and A2 and P2 are the second order terms. On the bottom left, the temperature amplitude from the developed algorithm is shown, and bottom right is the mean temperature in the region of interest. The green cross is crack tip from TSA, and the black one from fitting Williams' stress field.	89
36	A figure showing the measured response and the prediction of that response by the William's expansion	91
37	A figure showing the von Mises stresses based on a hybrid model combining TSA and the Williams' expansion	92

38	Max values of the stress response perpendicular to the crack plane, measured values, derivatives of those, theoretical stress response, and sampling points	94
39	The temperature response, its derivative, and the theoretical response as well as sampling points, values in crack plane	95
40	The phase map and a binary map of the plastic zone calculated from it . .	97
41	The plastic zone based on Laplacian of temperature amplitude	98
42	Original and converted image for use in crack tip detecting algorithm . . .	99
43	The principle of crack tip detecting algorithm	100
44	Image containing the crack and its bitmap representation. The crack tip is found and indicated by a red cross.	101
45	Comparison of both unfiltered-, and filtered image	104
46	104
47	Procedure of finding strains using DIC	106
48	Determining the vertical position of the crack	108
49	Determining the horizontal position of the crack	109
50	Vertical displacement field for use in determination of the crack position .	109
51	112
52	Determining optimal parameters for Crack Opening Displacement (COD) calculation	112
53	Zone of plastic deformation, elements where the equivalent von Mises stress exceed the $\sigma_{0.2\%}$ are represented with white colour	115
54	Example of histogram used for estimation of hit voltage probability mass function	119
55	Waveform stream decomposition method applied to signal energy.	125
56	The values of K_t from the 25 measurements in MPa^{-1}	128
57	Filter performance from test 6, acquisition 1, frame 1, axis in pixel coordinates, and crack tip from Williams' expansion marked with red circle. The colorbar shows temperature in $^{\circ}\text{C}$ for the original, filtered, and the rest pictures and in $^{\circ}\text{C}/\text{pixel}^2$ for the Laplacian picture.	130

58	Filter performance from test 6, acquisition 130, frame 1, axes in pixel coordinates, and crack tip from Williams' expansion marked with red circle. The colorbar shows temperature in °C for the original, filtered, and the rest pictures and in °C/pixel ² for the Laplacian picture.	130
59	Filter performance from test 6, acquisition 140, frame 1, axes in pixel coordinates, and crack tip from Williams' expansion marked with red circle. The colorbar shows temperature in °C for the original, filtered, and the rest pictures and in °C/pixel ² for the Laplacian picture.	131
60	Filter performance from test 6, acquisition 143, frame 1, axes in pixel coordinates, and crack tip from Williams' expansion marked with red circle. The colorbar shows temperature in °C for the original, filtered, and the rest pictures and in °C/pixel ² for the Laplacian picture.	131
61	Filter performance from test 6, acquisition 143, frame 1, magnified to show the region close to crack tip. Axes in pixel coordinates, and crack tip from Williams' expansion marked with red circle. The colorbar shows temperature in °C for the original, filtered, and the rest pictures and in °C/pixel ² for the Laplacian picture.	132
62	Total heat dissipated in plastic zone. Black line is the average value with error bars, and the red line is the amplitude.	133
63	Total heat dissipated in plastic zone per volume. Black line is the average value with error bars, and the red line is the amplitude.	133
64	Heat dissipated at crack tip per volume. Black line is the average value with error bars, and the red line is the amplitude.	134
65	Temperature measured in the sample and the region of interest for energy calculation.	134
66	Total heat dissipated in plastic zone. Black line is the average value with error bars, and the red line is the amplitude.	135
67	Total heat dissipated in plastic zone per volume. Black line is the average value with error bars, and the red line is the amplitude.	135

68	Heat dissipated at crack tip per volume. Black line is the average value with error bars, and the red line is the amplitude.	136
69	Temperature measured in the sample and the region of interest for energy measurements	136
70	The average temperature in a small region at crack tip, while running and after the test was paused. Additionally, a magnification of the flat part where test stopped, with a linear fit.	137
71	Cooling rate of a small region surrounding the crack tip versus stress intensity range.	138
72	Total heat dissipated in plastic zone. Black line is the average value with error bars, and the red line is the amplitude.	138
73	Total heat dissipated in the plastic zone per volume. Black line is the average value with error bars, and the red line is the amplitude.	139
74	Heat dissipated at crack tip per volume. Black line is the average value with error bars, and the red line is the amplitude.	139
75	Temperature measured in the sample and the region of interest for energy calculations.	140
76	Stress intensity and crack closure	141
77	Stress intensity and crack closure	141
78	Stress intensity and crack closure	142
79	Example of stress amplitude fields; window size is of 620 by 252 pixels . . .	143
80	Maximum stresses measured in the sample, both versus the theoretical stress intensity and the measured stress intensity	144
81	Maximum stresses measured in the sample, both versus the theoretical stress intensity and the measured stress intensity	144
82	Maximum stresses measured in the sample, both versus the theoretical stress intensity and the measured stress intensity	145
83	Crack length versus cycles	146

84	Paris curves based on the theoretical stress intensity factor with the results of linear curve fitting and confidence bands (secant method).	146
85	Paris curves based on polynomial filtering and the theoretical stress intensity factor range, with the results of curve fitting and confidence bands	147
86	Paris curves based on crack tip from Williams' stress field fit and the measured stress intensity	147
87	Crack length versus cycles	148
88	Paris curves based on the theoretical stress intensity factor and the secant method, with the results of linear curve fitting and confidence bands	148
89	Paris curves based on polynomial filtering and theoretical stress intensity factor range, with fit and confidence bands	149
90	Paris curves based on crack tip from Williams' stress field fit and measured stress intensity	149
91	Crack length versus cycles	150
92	Paris curves based on theoretical stress intensity factor and secant method, with the results of the linear curve fit with the corresponding confidence bands	150
93	Paris curves based on polynomial filtering and theoretical stress intensity range, with the results of the linear curve fit with the corresponding confidence bands	151
94	Paris curves based on crack tip estimated from the Williams' stress field fit and the measured stress intensity	151
95	Plastic zone size and area vs stress intensity factor range	153
96	Comparison of radius for the three types of plastic zones.	154
97	Contours of plastic zones for given acquisitions, based on the Laplacian (blue), and phase shift (orange	155
98	Monotonic plastic zone size plotted versus theoretical K_{max}	156
99	Contours of plastic zones for given acquisitions at the stress level of $\sigma_{0.2\%}$.	157
100	Plastic zone based on the Laplacian method	158
101	Monotonic plastic zone size plotted versus theoretical K_{max}	158

102	Contours of the plastic zones for given acquisitions at the stress level of $\sigma_{0.2\%}$	159
103	Based on the Laplacian method	160
104	Monotonic plastic zone size plotted versus theoretical K_{max}	160
105	Contours of plastic zones for given acquisitions at the stress level of $\sigma_{0.2\%}$.	161
106	Samples in stage II. Discrete Fourier analysis of second order, amplitudes A1 and A2 as well as mean temperature are given in °C, and phase shift of first and second order P1 and P1, in radians.	162
107	Discrete Fourier analysis of second order, amplitudes A1 and A2 as well as mean temperature are given in °C, and phase shift of first and second order P1 and P1, in radians. Five last measurements.	163
108	Transition to stage III, temperature in °C	164
109	Stage III, temperature in °C	165
110	The crack jump of the last cycle before failure, temperature in °C	166
111	The temperature distribution during the crack growth in the last cycle, temperature in °C	166
112	The process zone with respect to crack tip, temperature in °C	167
113	The maximum (left y-axis) and mean (right y-axis) temperatures occurring in the field of view during the last cycles before failure	168
114	The FOV, ROI, measuring points, and the lines used in investigation	170
115	Vertical and horizontal displacements at the last image analysed	170
116	Comparison of horizontal displacements from the filtered and the unfiltered images	171
117	Comparison of vertical displacements from the filtered and the unfiltered images	172
118	Comparison of the displacement along selected lines from the last of filtered, and unfiltered images	173
119	Measured strains as function of time	174
120	Engineering stress-strain curves	174

121	Analysis of the stress-strain behaviour in the elastic regime, regression line added	175
122	Strains ε_{xx} and ε_{yy} used to find the Poisson's ratio, data from specimen 3 .	175
123	Engineering stress-strain curves	177
124	Engineering stress-strain curves	178
125	True stress-strain curves	179
126	ΔK_{eff} , and crack closure as a function of the Stress Intensity Factor (SIF), ΔK	180
127	ΔK_{eff} and crack closure as a function of the SIF, ΔK	181
128	Applied load as function of COD	182
129	The strains ε_{xx} , ε_{xy} , and ε_{yy} for different K_{max}	183
130	The strains ε_{xx} , ε_{xy} , and ε_{yy} for different K_{max}	184
131	Elastic stress fields (equivalent von Mises stresses) for different K_{max} . . .	185
132	Plastic zone sizes as function of K_{max}	186
133	Bitmaps showing approximate plastic zone for different K_{max}	187
134	Fatigue crack growth curves obtained using high-speed camera, data from Test 1	189
135	Fatigue crack growth curves obtained using High-Speed Imaging (HSI) and DIC, data from Test 4	190
136	Fatigue crack growth curves obtained using HSI and DIC, data from Test 5	191
137	Precracking of specimen 3	192
138	Precracking of the specimen number 3	193
139	Start of the test 6	195
140	Branching of the fatigue crack, branches marked in red circles, the cycles are counted from the test start	195
141	Uneven specimen surface left by the plastic zone, the cycles are counted from the test start	195
142	Slip bands present on the grains affected by the plastic deformation	196
143	Stage III of FCG	196

144	Crack growth rate and AE count rate versus ΔK from Test 4 using two different count rate procedures	197
145	Crack growth rate and AE count rate versus ΔK from Test 5 from each sensor in Test 5	198
146	Crack growth rate and AE count rate versus ΔK from Test 5 using two different count rate procedures	199
147	Crack growth rate and AE count rate versus ΔK from Test 6 using two different count rate procedures	200
148	Statistical moments of hit waveform Power Spectral Density (PSD) from Test 4	201
149	Information entropy production from Test 4	202
150	Statistical moments of hit waveforms PSD from Test 5	203
151	Comparison of normalised Shannon Entropy from Sensor 1 and Sensor 2 during Test 5	204
152	Comparison of normalised 2nd order Renyi Entropy from Sensor 1 and Sensor 2 during Test 5	204
153	Statistical moments of hit waveform PSD from Test 6	205
154	Information entropy production from Test 6	206
155	Comparison of Root Mean Square (RMS) of streamed waveforms and hit waveforms from Test 4.	207
156	RMS and SIF versus cycles from Test 6	207
157	Comparison of absolute Signal Energy (SE) measurements from Sensor 1 and Sensor 2 during Test 5	208
158	RMS and SIF versus cycles from Test 5	208
159	RMS and SIF versus cycles from Test 5	209
160	RMS of hit waveforms from sensor 1 in Test 6 plotted versus cycles, SIF range	210
161	RMS and SIF versus cycles from Test 6	210
162	Close up of RMS and SIF versus cycles based on full waveform stream . . .	211

163	Normalised cumulative of Hits, Shannon Entropy, Renyi Entropy, RMS and Signal Energy versus number of cycles and ΔK from Test 4	212
164	Normalised cumulative of Hits, Shannon Entropy, and Signal Energy versus number of cycles and ΔK from Test 5	213
165	Normalised cumulative of Hits, Shannon Entropy, and Signal Energy versus number of cycles and ΔK from Test 6	214
166	Waveform evolution during Test 4 from evenly distributed "true" acquisitions	215
167	Waveforms of largest peak and lowest valley of RMS near the end of Test 4	216
168	Waveform evolution during Test 5 from evenly distributed "true" acquisitions	216
169	Waveforms of selected peaks and valleys of RMS in figure 159 of Test 5 . .	217
170	Waveform evolution during Test 6 from evenly distributed "true" acquisitions	218
171	Waveforms of peaks and valleys from RMS of Test 6 in figure 161	219
172	Example waveform of clusters from Test 4	220
173	Normalised cumulative of clusters versus number of cycles and ΔK from Test 4	220
174	Example waveform of clusters from Test 5	221
175	Normalised cumulative of clusters versus number of cycles and ΔK from Test 5	222
176	Example waveform of clusters from Test 6	223
177	2 of 5 waveforms from the anomalous cluster 4 from Test 6	223
178	Normalised cumulative of clusters versus number of cycles and ΔK from Test 5	224
179	Crack length versus cycle count for test 5	225
180	Fracture surface for test 5, beachmark separating the precracking from the actual test	225
181	Plastic zone radius for test 5	226
182	Crack closure for test 5	226
183	Effective stress intensity vs theoretical stress intensity for test 5	227
184	Determination of frame corresponding to the maximum load	244

185	Plots of applied load versus COD showing the influence of assumed crack tip position	244
186	Strains affected by lens distortion, from the left: ε_{xx} , ε_{xy} and ε_{yy}	248
187	Strain and stress fields affected by lens distortion	248
188	Strain and stress fields with lens distortion correction factor of -6×10^{-8}	249
189	high-pass filtered waveform and frequency content of early and late stages of Test 4	257
190	Frequency response of Micro-30F sensor (fig. 190a) and Nano-30 sensor (fig. 190b) during dummy testing performed before Test 6	258
191	Figure showing difficulties of analysis of spectral data.	259
192	Count rate curves with 36dB threshold and 41decibel threshold shows no major differences	260
193	Noisy waveform with strong frequency peak	266
194	Close relationship between cluster 2 from Test 4 and crack length, ΔK	267
195	RMS of hit waveforms of Test 4 and Test 6 towards the end stages of each test	268
196	RMS versus mean frequency of the clusters from each test, showing that kmeans doesn't follow the evident contours	271
197	RMS versus cycles of the clusters from each test showing poor grouping	271
198	Mean frequency versus cycles of the clusters from each test	271
199	RMS and squared SIF versus cycles, Test 4	273
200	Chemical composition and properties of the material used for the test specimens	i
201	Survey of HS imaging technology. Figure includes Photron SA-Z used in this work.	ii

List of Abbreviations

ACPD	Alternating Current Potential Drop. 101, 126
ADC	Analog to Digital Converter. 78
AE	Acoustic Emission. X, XI, XIX, 1, 2, 32, 46–59, 61, 62, 76, 78, 116, 117, 121–124, 127, 197–200, 207, 214, 219, 257, 260, 262–266, 269, 272–274, 277, 278, 282, 283
C(T)	Compact Tension specimen. XI, XII, 1, 2, 18, 22, 27, 29, 37, 56, 65, 66, 76, 90, 93, 111, 112, 169, 255, 281
CAD	Computer Aided Design. 5
CB	Confidence Band. 145, 152, 188, 197, 199, 200
CCD	Charge Coupled Device. 25, 26, 32, 33, 37, 57, 71, 246
CMOS	Complementary Metal Oxide Semiconductor. 25, 26, 28, 33, 70
COD	Crack Opening Displacement. XIII, XVIII, XXI, 73, 107, 110–112, 180, 182, 243–246, 250, 251, 281
CTOD	Crack Tip Opening Displacement. 37, 38
DCPD	Direct Current Potential Drop. 2, 38, 80
DFT	Discrete Fourier Transform. XI, 42–44, 59, 60, 103, 122, 123

- DIC Digital Image Correlation. XII, XVIII, 4, 24, 27, 33–40, 65, 67, 68, 70, 72–75, 96, 103, 105, 107, 108, 110, 111, 113, 127, 169, 173, 174, 176, 182, 188, 190, 191, 224, 226, 232, 233, 239–243, 245, 247, 250, 251, 262, 269, 273, 276–278, 280, 281
- DIP Digital Image Processing. 4, 24, 37
- DTFT Discrete-Time Fourier Transform. 42, 59, 60
- EMI Electromagnetic interference. 76, 260
- FCG Fatigue Crack Growth. II, XVIII, 1, 2, 6, 11, 13, 19, 24, 27, 37, 40, 53, 65, 70–72, 102, 103, 107, 111, 113–116, 121, 124, 126, 169, 180, 188–191, 194, 196, 252, 253, 255, 264, 272, 275, 282
- FE Finite Element. 11
- FFT Fast Fourier Transform. 59, 60
- FOV Field Of View. 16, 40, 67, 70, 71, 74, 96, 101–103, 156, 169, 232, 236, 239, 242, 246, 250, 252, 253, 256, 281
- FPA Focal Plane Array. 16
- fps Frames Per Second. 26, 27, 69, 175
- HDT Hit Definition Time. 76
- HLT Hit Lock-out Time. 77

HSI High-Speed Imaging. XVIII, 2, 24, 26, 28, 39–41, 67, 70, 86, 101, 102, 107, 114, 188, 190, 191, 246, 252, 255, 269, 275, 278
 HSP High-Speed Photography. 24, 26, 27, 40

 ICCD Intensified Charge Coupled Device. 25
 IFOV Instantaneous Field Of View. XI, 16, 17
 IR Infrared Radiation. XI, 10, 14, 15, 39, 41, 68, 86, 92, 96, 101, 121, 140, 197, 199, 237, 262, 264, 275, 277, 280
 IRT Infrared Thermography. 1, 2, 18, 20–23, 28, 39, 40, 67, 69, 81, 102, 113, 128, 152, 226, 250, 269, 273, 275–278, 280

 LED Light-Emitting Diode. 28, 70
 LEFM Linear-Elastic Fracture Mechanics. 6, 140, 155, 226, 236, 278, 279

 MOI Moment Of Interest. 69

 NDT Non-Destructive Testing. 55
 NETD Noise Equivalent Temperature Difference. 15, 16, 69, 81

 PAC Physical Acoustics Corporation. 76, 257
 PDT Peak Definition Time. 76
 PIV Particle Image Velocimetry. 24
 PSB Persistent Slip Band. 12, 13

PSD	Power Spectral Density. XIX, 58, 59, 117, 118, 120–122, 201, 203, 205, 219, 221, 222, 258, 270, 278
RMS	Root Mean Square. XIX, XXI, 48, 117, 120, 206–211, 263, 265, 268, 272, 273
ROI	Region Of Interest. XII, 73, 74, 105, 114, 169, 176, 241
RVI	Rapid Video Imaging. 1, 4, 24, 278
SE	Signal Energy. XIX, 208
SIF	Stress Intensity Factor. XVIII, XIX, 7, 13, 18, 38, 40, 53, 54, 110, 111, 180, 181, 207–211, 263, 266, 272, 273
STFT	Short-Time Fourier Transform. 59, 60, 121, 123, 124, 215, 216, 218, 219, 221, 222, 257, 278, 282
TOA	Time Of Arrival. 55, 56
TSA	Thermoelastic Stress Analysis. X, XII, 18, 89, 92, 98, 145–152, 232, 236, 237
TTL	Transistor-Transistor Logic. 32, 243
ZNCC	Zero-mean Normalised Cross-Correlation. 35
ZNSSD	Zero-mean Normalised Sum of Squared Difference. 35

List of Symbols

Sign	Description	Unit
A_{fi}	Amplitude of the i 'th term in Fourier fit	
B_{λ}	Spectral radiance	W/sr m ³
B	Specimen Thickness	mm
C_1	Longitudinal wave speed	m/s
C_2	Shear wave speed	m/s
C_3	Geometric constant	
C_4	Geometric constant for AE power law	
C_{ρ}	Specific heat capacity	J/kg K
C_{ph}	Circle of confusion	mm
C	Paris law constant	
D_1	Hole diameter	mm
D_{1-2}	Distance between sensor 1 and sensor 2	m
D_{ph}	Effective aperture	mm
D	Distance of dislocation from surface	m
E_{an}	Energy release rate during dislocation annihilation	J
E_{br}	Brake energy released per period	J
E_i	Illuminance	lm/m ²
E_{rad}	Energy radiated per second by a screw dislocation	J/s
E	Elastic modulus	GPa
E	Young's modulus	
G	Shear modulus	MPa
H_R	Renyi's entropy	
H_S	Shannon's entropy	

Sign	Description	Unit
H	Exposure	lms/m ²
K_t	Thermoelastic constant	
K_{IC}	Fracture toughness for mode I loading	MPa√m
K_{max}	Maximum stress intensity factor	MPa√m
K_{min}	Minimum stress intensity factor	MPa√m
K_{op}	Crack opening stress intensity factor	MPa√m
K	Stress intensity factor	MPa√m
L	Specimen height	mm
N_s	Number of samples	
N_{ph}	F-number	
N	Number of cycles	
P_{max}	Maximal applied load	N
P_{min}	Minimum applied load	N
P_{op}	Opening load	N
P	Applied load	N
Q	Source function, energy release	
R^2	Coefficient of determination	
R	Minimum to maximum cyclic stress ratio	
S	Area	m ²
T_1	Time of arrival at sensor 1	s
T_2	Time of arrival at sensor 2	s
T	temperature	K
V_w	Wave velocity	m/s
W_1	Total specimen width	mm
W	Specimen width	mm
\bar{a}	Average crack size	mm
\bar{v}	Average velocity	m/s

Sign	Description	Unit
ΔK_{eff}	Effective stress intensity range	MPa \sqrt{m}
ΔK	Stress intensity factor range	MPa \sqrt{m}
$\dot{\epsilon}$	Strain rate	1/s
Φ_v	Luminous flux	lm
Φ	Airy stress function	
Θ	angle-coordinate in polar coordinates	
α_t	Constant for twin pole reaction	
α	Coefficient of linear thermal expansion	1/K
ϵ_{EM}	Fraction of absorbed radiation	
η	AE counts	
λ	Wavelength	m
ν	Poisson's ratio	
ω_0	angular frequency	rad/s
ϕ_{fi}	Phase shift of the i'th term in Fourier fit	
ρ_d	Dislocation density	1/m ²
ρ_m	volumetric mass density	kg/m ³
ρ_{EM}	Fraction of reflected radiation	
σ_0	Stress level at infinity	MPa
σ_1	Major principal stress	MPa
σ_2	Principal stress	MPa
σ_3	Principal stress	MPa
σ_e	True strain	MPa
σ_t	True stress	MPa
σ_x	Normal stresses in x direction	MPa
σ_y	Normal stresses in y direction	MPa
$\sigma_{0.2\%}$	Offset yield strength	MPa
σ	Stress level	MPa

Sign	Description	Unit
τ_{EM}	Fraction of transmitted radiation	
τ	Shear stresses	MPa
$\varepsilon_{e_{axial}}$	Axial strain	
$\varepsilon_{e_{trans}}$	Transverse strain	
ε_e	Engineering strain	
ε_t	True strain	
ε_{xx}	Green-Lagrangian strain	
ε_{xy}	Green-Lagrangian strain	
ε_{yy}	Green-Lagrangian strain	
a_i	Coefficient in William's expansion	
a_n	Surface displacement	m
a_{fi}	Constant of Fourier fit	
a_{notch}	Notch depth	mm
a	Crack length	mm
b_{fi}	Constant of Fourier fit	
b	Burgers' vector	
c	Speed of light	m/s
d_{1-2}	Distance between sensor 1 and AE source	m
f_r	Frame rate	
f_{ph}	focal length	mm
f	Test frequency	Hz
h	Planck's constant	$\text{m}^2 \text{kg/s}$
k_1	Lens distortion correction factor	
k_B	Boltzmann constant	$\text{m}^2 \text{kg/s}^2 \text{K}$
k	heat conductivity	W/K m
l_c	Crystal size	m
l_d	Dislocation length	m

Sign	Description	Unit
l_s	Length scale	m
m	Paris law exponent	
n_d	number of dislocations	
n	AE count rate power law exponent	
p	Probability mass	
r_l	Radius of dislocation loop	m
r_{pl}	radius of plastic zone	mm
r	r-coordinate in polar coordinates	
s_m	Mean value of first stress invariant	MPa
s	First stress invariant	MPa
t	time	s
u_e	Velocity of event	m/s
u_{ph}	distance to subject	mm
v	Velocity	m/s
x	x-coordinate	
y	y-coordinate	

1 Introduction

1.1 General introduction

Fatigue is the phenomenon of material failure at cyclic loading. The fatigue failure might occur at load levels significantly below the yield stress, and it is a major failure mode of the mechanical parts [1]. Lack of knowledge and procedures related to fatigue lead to incidents with costed many lives. Some of the notable catastrophes caused by fatigue failure were Alexander L. Kielland oil platform capsizing [2] or de Havilland DH-106 Comet 1 passenger jets disasters in 1954 [3]. In the aircraft industry there are regulations (FAR/JAR 25) that require for the design of most structural parts of the aircraft the use of a damage tolerant design approach [4]. Many aircraft manufacturers comply with this philosophy for components by applying slow fatigue crack growth strategies in order to insure that the fatigue cracks can be discovered by inspection prior to failure. The focus in this work is directed at damage tolerant approach and thus the Fatigue Crack Growth (FCG).

Since there is a lack of effective theoretical models for fatigue failure, the specific material FCG tests still have a crucial role in the study of the fatigue [1]. One of the fundamental equations describing the stable crack growth in the damage tolerant approach to fatigue, Paris-Erdogan law [5], is indeed based on fitting experimental data. The most common and dangerous cracks in practical engineering problems are mode I cracks. A popular way of performing FCG tests for this kind of cracks is using a Compact Tension specimen (C(T)). The scope of this work is use of three advanced techniques in order to investigate behaviour of AISI 316L stainless steel subjected to mode I fatigue cracks.

1.2 Research method in brief

Three advanced techniques are to be used to acquire data from a fatigue test: Rapid Video Imaging (RVI), Infrared Thermography (IRT) and Acoustic Emission (AE). The techniques

are supported by other equipment as micro controllers for camera triggering, and Direct Current Potential Drop (DCPD) for real time crack growth monitoring.

1.3 Problem statement

The main goals of this work are to:

- Set up an experiment involving use of AE, High-Speed Imaging (HSI) and IRT techniques simultaneously during a FCG test on a standard C(T) specimen, with the fatigue testing machine.
- Acquire useful data arriving from the different techniques.
- Implement methods for data analysis typical for the different techniques.
- Compare data which are reasonable to compare, potential candidates are crack growth rate, plastic zone size, crack closure, and energy measurements.
- Characterise and describe challenges arriving from such a complex experiment.

1.4 Limitations

Some of the main limitations were related to the experiment setup itself. The availability of the equipment at the same time, and the time to set up the experiment, as well as unexpected equipment failures, limited the amount of performed tests. To solve the challenges in the experiment setup, a trigger system was developed to log the data and trigger all of the equipment at the same time, and even more importantly, at a given point in the load signal.

Other challenges was post-processing of the large amounts of data. Software has been both implemented, improved, and developed to do that, but some of the analyses had to be excluded from this work.

Data from the last experiments were acquired close to the deadline, especially the last test, focused on stage III, gave a lot of new data, and due to lack of time, the data analysis was limited. The post-processing methods were not prepared for these data, as the observed behaviour differed from what was observed in previous tests. The acquisition of stage III was poor in the earlier tests, which resulted in that the software for analysis could not be developed.

1.5 Structure of the report

In section 2, the theory integrated with literature review is presented for each of three advanced techniques separately. The information contained in the section refer to the literature, books and other scientific reading.

Section 3 describes the experimental setup, material and methodology. All the necessary information regarding the experiment are described including sample preparation, standard, experimental procedures, and equipment. Additionally, the most significant codes and algorithms, as well as the trigger design are described and explained.

The results from the experiment are presented in section 4 and discussed in section 5. The report is completed by the conclusions and further work covered in section 6. All the additional materials are included in the Appendix or follow as an attachment to the thesis.

1.6 Authors' contributions

Aleksander Sendrowicz was responsible for the following work:

- Infrared imaging, including equipment setup, and data gathering.
- Design, assembly, programming, and setup of the triggering system described in section 3.3.

- Programming of the experiment.
- Analysis and software development for the infrared pictures, described in section 3.4.
- Software development that was also implemented for other techniques e.g. motion compensation used also for RVI, or crack growth analysis.
- Literature review and theory part of infrared imaging in section 2.3, as well as the results and discussion part concerning data acquired using the technique respectively in sections 4.2 and 5.1.
- Describing the theory of theoretical stress fields in section 2.1.1, and implementing these for comparison with results.

Aleksander Omholt Myhre was responsible for

- Acoustic emission, including equipment setup, and data gathering, results and discussion concerning the resulting data.
- Literature review and theory part of acoustic emission.
- Data analysis of acoustic emission data.

Seweryn Witold Wierdak was responsible for

- Rapid video imaging, including equipment setup, and data gathering.
- Analysis of data acquired from rapid video imaging, including digital image correlation.
- Software development for rapid video imaging.
- Design of tensile test samples and and data analysis following from tensile test.
- Literature review and theory related to RVI, Digital Image Correlation (DIC) and Digital Image Processing (DIP), as well as results and discussion about the obtained

data.

- All Computer Aided Design (CAD) necessary in this work.

The rest of the report was developed by all of the co-authors, including the remaining theory, method, discussion of crack growth parameters and issues, as well as conclusions.

2 Theory and literature review

2.1 Linear-Elastic Fracture Mechanics

Normally when the cyclic stresses applied on the component are small so that the plastic deformation ahead of a crack tip is small compared to an otherwise elastic field, then Linear-Elastic Fracture Mechanics (LEFM) assumptions provide appropriate descriptions for FCG [6]. The theory of LEFM is therefore used in the development of the fatigue crack propagation approach, and selected concepts of LEFM must be explained.

An important consideration in fracture mechanics is the orientation of the crack with respect to the applied load. There are three principal fracture modes: tensile opening mode (mode I), in-plane sliding mode (mode II), and anti-plane shear mode (mode III) [6]. Mode I considers a crack with a tensile load applied normal to crack plane. Mode II refers to shearing of the crack faces in the direction of the crack growth. Mode III is shearing of the crack faces in a direction parallel to crack front. Of these, mode I is the most critical [1]. Figure 1 illustrates the three modes. Cases where the applied load is a combination of two or more modes is referred to as mixed-mode fracture.

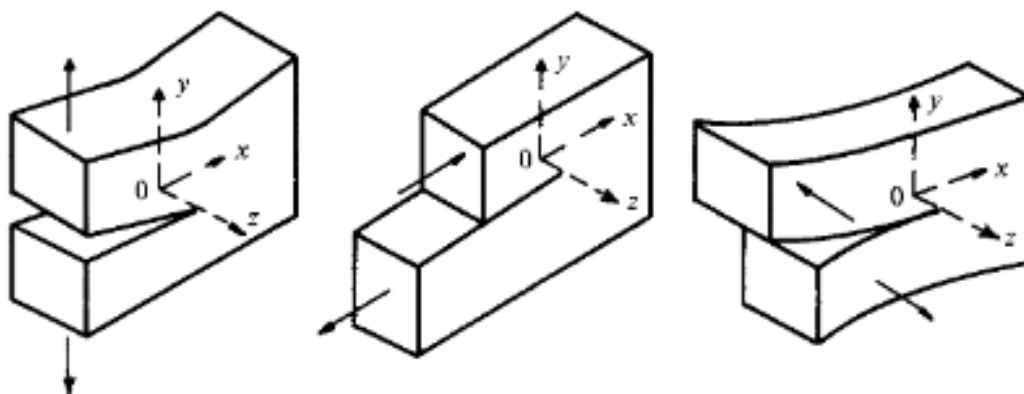


Figure 1: The principal modes of fracture. From left to right: mode I, mode II, mode III. Adopted from S. Suresh. *Fatigue of Materials*. Cambridge University Press, 2 edition, 1998. doi: 10.1017/CBO9780511806575

A crack acts as a local stress raiser. In order to describe the intensity of the stress field ahead of the crack tip, the Stress Intensity Factor (SIF), K , is introduced. The basis for K in the in plane of the material case (mode I and mode II), is an infinite plate of an isotropic solid with a semi-infinite sharp crack. It can be shown [6] that for mode I, the leading terms are:

$$\begin{bmatrix} \sigma_{xx} \\ \sigma_{yy} \\ \sigma_{xy} \end{bmatrix} = \frac{K_I}{\sqrt{2\pi r}} \cos \frac{\theta}{2} \begin{bmatrix} 1 - \sin \frac{\theta}{2} \sin \frac{3\theta}{2} \\ 1 + \sin \frac{\theta}{2} \sin \frac{3\theta}{2} \\ \sin \frac{\theta}{2} \sin \frac{3\theta}{2} \end{bmatrix} \quad (1)$$

Where r and Θ are the polar coordinates, and K_I is the mode I SIF, incorporating the effect of the boundary conditions, crack length and geometry based on the solution of the Airy stress function [6]. In mode I, this results in K_I being defined as:

$$K_I = \lim_{r \rightarrow 0} \left(\sqrt{2\pi r} \sigma_{yy} \Big|_{\theta=0} \right) \quad (2)$$

In other words, K is a measure of the intensity of the stress field near the crack tip, given linear-elastic conditions.

2.1.1 Modelling of stress fields

There are several models describing the stresses near the crack tip. The first one was already described in equation 1. The second model is based on Williams' series [7]. Both of these methods are described and explained in greater detail by Sun and Jin [8]. The stress fields resulting from the models described below are shown in figure 2. Since the models do not account for plasticity, the stresses reach singularity at crack tip.

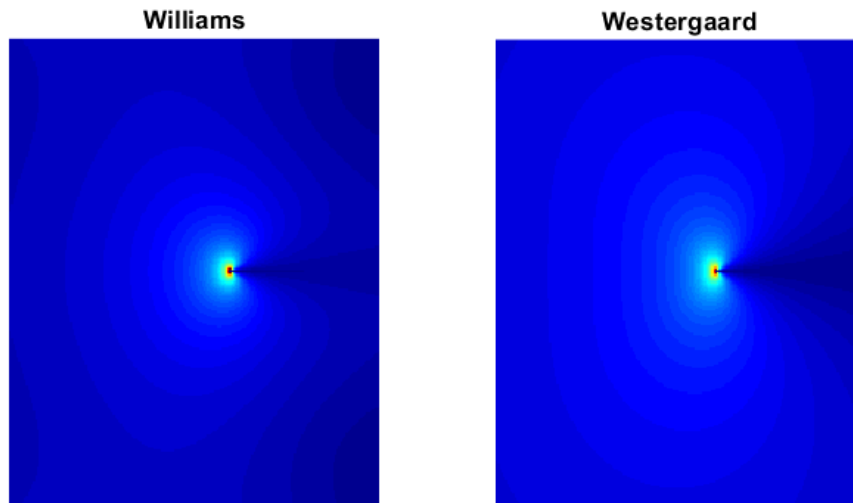


Figure 2: The theoretical elastic stress fields

Westergaards solution

As partially mentioned, the solution is based on an infinite plane with a line crack of length $2a$, and of mode I, subjected to a biaxial stress σ_0 at infinity. The situation is illustrated in figure 3. After some simplifications described in [8], and combining it with the stress intensity factor, the near tip solutions in polar coordinates are given in equation 1, where K is the stress intensity, and r and Θ are the polar coordinates.

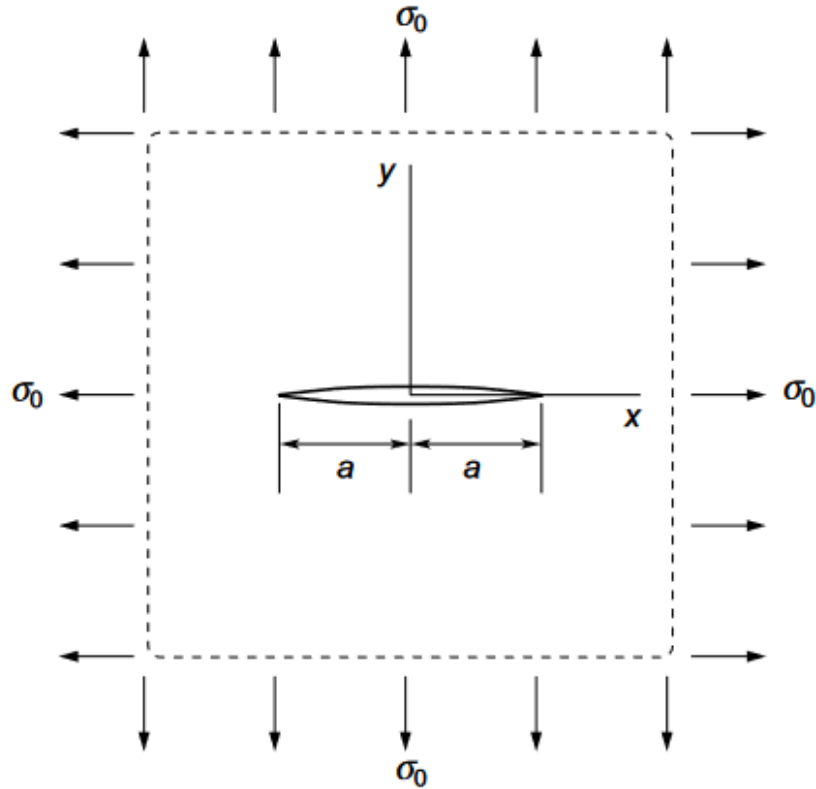


Figure 3: Stress situation for Westergaards solution. Adopted from C.T. Sun and Z.-H. Jin. Chapter 3 - the elastic stress field around a crack tip. In C.T. Sun and Z.-H. Jin, editors, *Fracture Mechanics*, pages 25 – 75. Academic Press, Boston, 2012. ISBN 978-0-12-385001-0. doi: <https://doi.org/10.1016/B978-0-12-385001-0.00003-1>. URL <http://www.sciencedirect.com/science/article/pii/B9780123850010000031>

Equation 1 can be used to approximate the size of the monotonic plastic zone by finding the region in which the von Mises stresses exceed the yield strength of the material. The radius of the plastic zone is often defined as the distance from crack tip to the yield stress in crack plane, and for plane stress condition $\sigma_3 = 0$, the von Mises stresses can be calculated from equation 1, $\sigma_{0.2\%}$ can be inserted, and this will result in r_{pl} shown in equation 3. The equation can also be solved for plane strain, where $\sigma_3 = \nu(\sigma_1 + \sigma_2)$, and this will result in an r_{pl} shown in equation 4. There are other ways of defining the plastic zone or the radius, but the general relation is usually presented as a factor multiplied with $\left(\frac{K}{\sigma}\right)^2$.

$$r_{pl} = \frac{1}{2\pi} \left(\frac{K_{max}}{\sigma_{0.2\%}} \right)^2 \quad (3)$$

$$r_{pl} = \frac{(1-2\nu)^2}{2\pi} \left(\frac{K_{max}}{\sigma_{0.2\%}} \right)^2 \quad (4)$$

Williams' crack tip field

The stresses and displacements can be represented by the Airy stress function Φ which satisfies the biharmonic equation (equation 5) [8]. For a mode I crack the stress field in Cartesian coordinates can be expressed as in equations 6-8.

$$\nabla^2 \nabla^2 \Phi = 0 \quad (5)$$

$$\sigma_x = \sum_{i=1}^{\infty} \frac{i}{2} r^{\frac{i}{2}-1} a_i \left[\left(2 + \frac{i}{2} + (-1)^i \right) \cos \left(\frac{i}{2} - 1 \right) \Theta - \left(\frac{i}{2} - 1 \right) \cos \left(\frac{i}{2} - 3 \right) \Theta \right] \quad (6)$$

$$\sigma_y = \sum_{i=1}^{\infty} \frac{i}{2} r^{\frac{i}{2}-1} a_i \left[\left(2 - \frac{i}{2} - (-1)^i \right) \cos \left(\frac{i}{2} - 1 \right) \Theta + \left(\frac{i}{2} - 1 \right) \cos \left(\frac{i}{2} - 3 \right) \Theta \right] \quad (7)$$

$$\tau = \sum_{i=1}^{\infty} \frac{i}{2} r^{\frac{i}{2}-1} a_i \left[\left(\frac{i}{2} - 1 \right) \sin \left(\frac{i}{2} - 3 \right) \Theta - \left(\frac{i}{2} + (-1)^i \right) \sin \left(\frac{i}{2} - 1 \right) \Theta \right] \quad (8)$$

Where σ_x is the stress in x direction, σ_y is the stress in y direction, τ is the shear stress, a_i are the coefficients of Williams' expansion, r is the radial distance from crack tip, and Θ is the angle between the crack plane and the position. The strength of this approach is that depending on the coefficients, it accounts for additional factors like geometry of the specimen. But to gain a useful stressfield, the coefficients have to be determined. The first order term is related to stress intensity factor, and might be used to calculate the stress intensity from Infrared Radiation (IR) data. The second order term is related to

the T-stress. Xiao and Karihaloo [9] used Finite Element (FE) and hybrid crack element type to find closed form expressions for the first five coefficients, and the values can be calculated from equations given below in equation 9. According to the authors, the model predicts the stress field well, both for small and large $\frac{a}{W}$ values.

$$a_1 = \frac{K}{\sqrt{2\pi}} = \frac{P}{B\sqrt{W}} \left(373.08 \frac{a^5}{W} - 567.33 \frac{a^4}{W} + 321.47 \frac{a^3}{W} - 73.124 \frac{a^2}{W} + 9.8345 \frac{a}{W} + 0.8436 \right) \quad (9a)$$

$$a_2 = \frac{P}{BW} \left(294.23 \frac{a^5}{W} - 520.30 \frac{a^4}{W} + 320.88 \frac{a^3}{W} - 71.481 \frac{a^2}{W} + 2.3668 \frac{a}{W} + 0.9443 \right) \quad (9b)$$

$$a_3 = \frac{P}{BW^{\frac{3}{2}}} \left(-4774.1 \frac{a^6}{W} + 9231.3 \frac{a^5}{W} - 7083 \frac{a^4}{W} + 2799.1 \frac{a^3}{W} - 664.26 \frac{a^2}{W} + 94.265 \frac{a}{W} - 7.6254 \right) \quad (9c)$$

$$a_4 = \frac{P}{BW^2} \left(4013.8 \frac{a^6}{W} - 10191 \frac{a^5}{W} + 10688 \frac{a^4}{W} - 5797.4 \frac{a^3}{W} + 1639.3 \frac{a^2}{W} - 204.27 \frac{a}{W} + 5.4205 \right) \quad (9d)$$

$$a_5 = \frac{P}{BW^{\frac{5}{2}}} \left(-24819 \frac{a^6}{W} + 60484 \frac{a^5}{W} - 58435 \frac{a^4}{W} + 27760 \frac{a^3}{W} - 6422.2 \frac{a^2}{W} + 563.07 \frac{a}{W} + 3.4375 \right) \quad (9e)$$

2.2 General fatigue theory

In the damage tolerant approach to fatigue, the fatigue crack growth phenomenon is usually described employing da/dN - ΔK log-log curves, a sketch is shown in figure 4. The curve is divided into three regions as illustrated. Phrases da/dN - ΔK -curve, and FCG-curve are used interchangeably in this work.

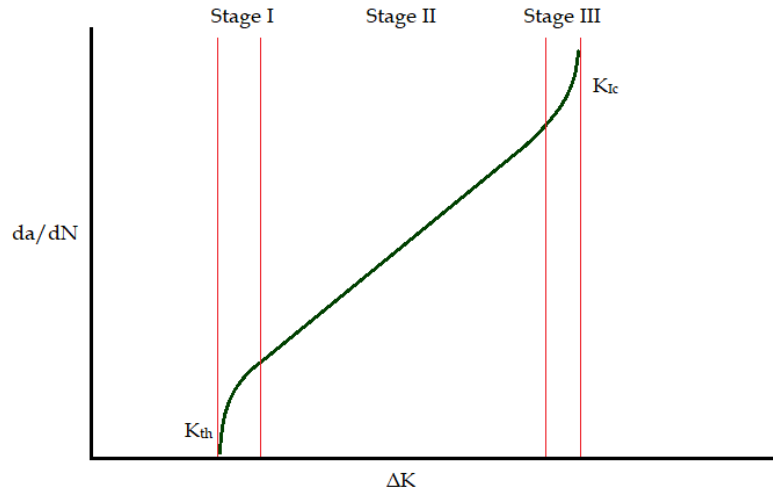


Figure 4: An illustration of the fatigue crack growth curve

2.2.1 Crack initiation

Dislocations are important for initiation of a fatigue crack, as they accumulate at stress intensities at suitable slip planes, and after sufficient amount of loading cycles, usually form Persistent Slip Bands (PSBs). PSBs are both extrusions and intrusions on the surface, where especially the intrusions might work as stress raisers where cracks are initiated [10]. Due to the mechanism, these very early cracks occur at planes of high resolved shear stress. Some materials exhibit a load limit, known as the endurance limit, under which the crack does not propagate. An explanation of such a limit is that under a given load the creation of PSBs is restricted, but the endurance limit is not final, since even though the creation of PSBs is restricted, other mechanisms take over the crack initiation in very and ultra high cycle fatigue [11]. The crack in stage I is sensitive to microstructure of the material. The propagation is of a mixed mode, and the behaviour varies from grain to grain.

2.2.2 Crack propagation

Once the crack has grown larger, it enters stage II, shown in figure 4. In this region the crack growth direction for mode I loading is perpendicular to the maximum tensile stress, although the cracks often follow the PSBs on the microscopic level in the threshold region [10]. Stage II is the largest part of a cracks growth life, and based on experimental data, the crack growth rate in this stage is described by Paris-Erdogan law [5] which is shown in equation 10.

$$\frac{da}{dN} = C\Delta K^m \quad (10)$$

2.2.3 Failure

The final fracture is preceded by stage III. In this stage, the slope of the FCG curve in figure 4 increases. The K_{max} approaches K_{IC} , and when that happens, the final failure occurs. The unstable crack growth is controlled by static modes, and is sensitive to factors like microstructure or loading conditions [6; 12].

2.2.4 Crack closure

According to Elber [13; 14], the fatigue crack subjected only to tensile load (e.g. R=0.1 or R=0.6) may remain partially closed until a load level reaches certain value P_{op} at which the crack fully opens. Such closure effect can be induced by oxides, roughness of fractured surface, or plasticity. Elber postulated that plasticity induced crack closure is caused by the residual tensile plastic wake left behind the crack tip by the monotonic plastic zone that follows it. In addition, the same author assumed that the part of cyclic load below P_{op} does not contribute to crack growth since the crack tip would be stressed only if $P > P_{op}$. For this reason the SIF range $\Delta K = K_{max} - K_{min}$ should be reformulated to effective SIF range $\Delta K_{eff} = K_{max} - K_{op}$ when taking P_{op} in consideration.

2.3 Infrared thermography and fatigue analysis

2.3.1 Basics of infrared thermography

IR is electromagnetic radiation that is often categorised in the wavelength range of 740 nm to 30 cm although these values are not definitive [15]. Every body with an absolute temperature above zero Kelvin emits electromagnetic radiation, and the spectral radiance B_λ with respect to temperature T and the wavelength λ for a perfect black body is given by Planck's law shown in equation 11. h is the Planck's constant, c is the speed of light, and k_B is the Boltzmann constant. A perfect black body is an ideal emitter at every frequency, and the energy is radiated isotropically in all directions.

$$B_\lambda = \frac{2hc^2}{\lambda^5} \frac{1}{e^{\frac{hc}{\lambda k_B T}} - 1} \quad (11)$$

IR is one of three ways heat can be transferred, the two others are convection, and conduction. A body in thermal equilibrium, hit by infrared radiation might reflect, absorb, or transmit the radiation, these properties are quantified by ρ_{EM} , ϵ_{EM} and τ_{EM} respectively, which are fractions that sum up to unity. For an ideal black body in thermal equilibrium, the emissivity (which is equal to absorbance) ϵ_{EM} is equal to 1. The emissivity of a real body is usually dependent on a given wavelength and direction.

To approximate the observed body to a black body, black paint with high emissivity is often applied to the surface. This is to reduce the error like for example a body reflecting a hot background. The paint increases emissivity and reduces the reflectance and transmittance. Additionally the emitted radiation has to pass through the atmosphere and the cameras optics. The atmosphere absorbs some of the waves with a given length, due to different molecules in its composition, this effect is known as the atmospheric attenuation and the absorbed wavelengths and the responsible molecules are shown in figure 5. As mentioned, every body with a temperature above 0 K emits radiation, and so does the atmosphere,

which further affects the measurements. All of these effects are illustrated in figure 6. The optics of the camera also work only for some wavelengths, and all of these factors in addition to the sensors dependence on given wavelengths, as seen in figure 7, make the thermal cameras operate in given spectra. The different sensors do also have different noise levels usually described as the Noise Equivalent Temperature Difference (NETD).

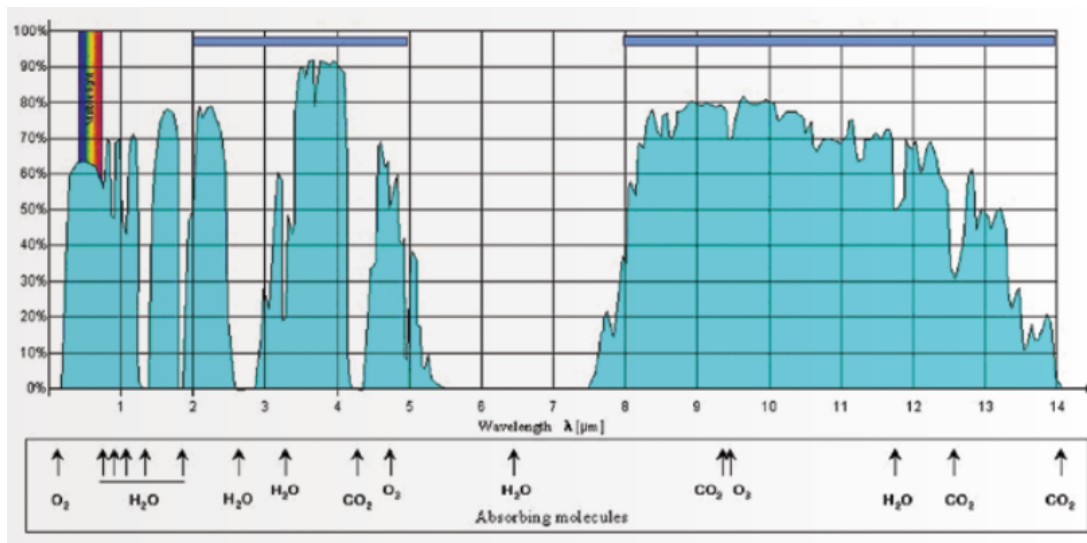


Figure 5: Atmospheric attenuation (white areas) with a chart of the gases and water vapour causing most of it. The areas under the curve represent the highest IR transmission. Adopted from Flir Systems. *The Ultimate Infrared Handbook for R&D Professionals*. Flir Systems, 2012. URL http://www.hoskin.ca/wp-content/uploads/2016/10/flir_thermal_camera_guide_for_research_professionals.pdf

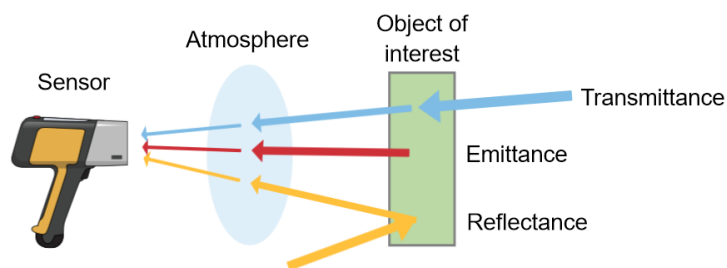


Figure 6: The figure illustrates the reflectance, emittance, and transmittance of an object, and attenuation caused by atmosphere.

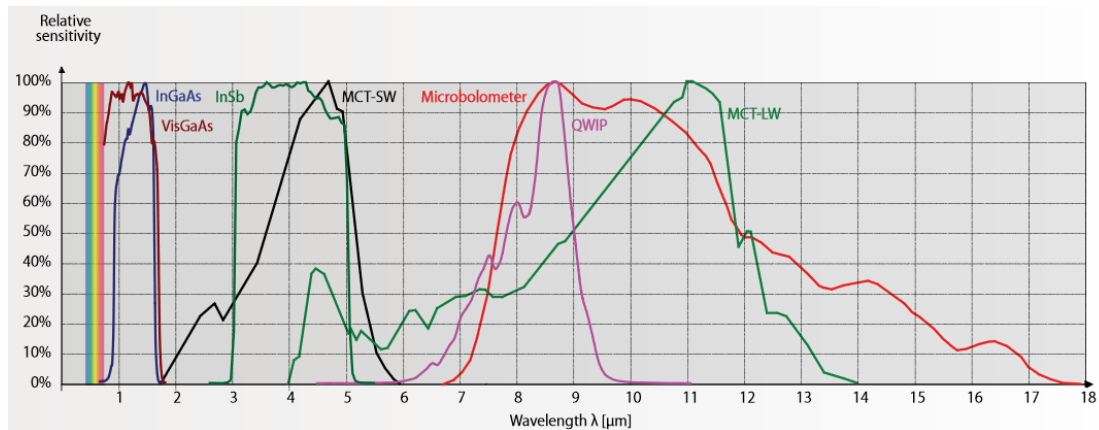


Figure 7: Relative sensitivity for different sensors and wavelengths, adopted from Flir Systems. *The Ultimate Infrared Handbook for R&D Professionals*. Flir Systems, 2012. URL http://www.hoskin.ca/wp-content/uploads/2016/10/flir_thermal_camera_guide_for_research_professionals.pdf

The type of sensor used in the Focal Plane Array (FPA) is critical for good performance. The InSb type of sensor used in this work is a quantum detector, which absorbs photons which elevates the electrons to a higher energy state [16]. The sensor is cooled down to a cryogenic temperature to make it more sensitive and to shorten the response time. Due to this, the NETD is typically 20 mK and the exposure time 1 μ s. Other advantages of this type of sensor is high uniformity of detectors leading to low fixed pattern noise, good image quality, and applicability in high temperatures.

The Field Of View (FOV) is the area observed by the camera at a given distance, and with given optics. This quantity together with resolution determines the spatial resolution or Instantaneous Field Of View (IFOV), which is the area observed by one sensor of the camera. The spatial resolution is important for precise measurements, if an object or region of high temperature is not fully covered by the IFOV, the measurement will not be precise, and will depend on the remaining area covered by the sensor. This issue is illustrated in figure 8 [16, p. 16].

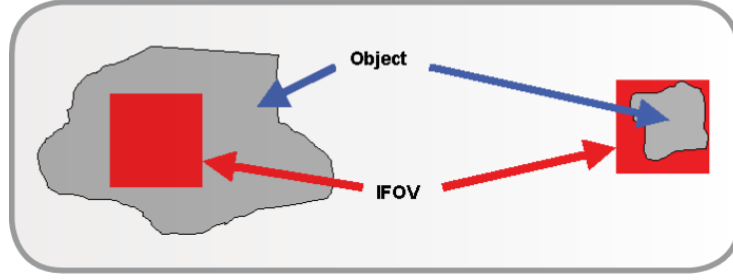


Figure 8: IFOV (red squares) relative to object size. Adopted from Flir Systems. *The Ultimate Infrared Handbook for R&D Professionals*. Flir Systems, 2012. URL http://www.hoskin.ca/wp-content/uploads/2016/10/flir_thermal_camera_guide_for_research_professionals.pdf

2.3.2 Factors affecting temperature in a fatigue test

Thermoelastic effect

An important factor for the temperature variation is the thermoelastic effect [17]. The change in stress state causes a change in the temperature of the material, so for a fatigue test with a frequency high enough to approximate adiabatic conditions, the temperature response due to the thermoelastic effect is expected to be of the same form as the load curve. The relation between change in temperature ΔT is proportional to the change in first stress invariant Δs [18], and is usually on a form given in equation 12 [19]. T is the absolute temperature of the sample and K_t is the thermoelastic coefficient. As Gyekenyesi and Baaklini [19] explained, K_t can be defined as in equation 13. Where α is the coefficient of linear thermal expansion, C_ρ is the specific heat capacity, and ρ_m is the material density.

$$\Delta T = -K_t T \Delta s \quad (12)$$

$$K_t = -\frac{\alpha}{\rho_m C_\rho} \quad (13)$$

The equation above, is a good first order approximation of the thermoelastic parameter. For precise stress measurements however the relation between stress and temperature, is not constant, and it is not even linear [19; 20]. The reason is that the coefficients in equation 13 may significantly vary with temperature and other factors. In addition to temperature, the relation is dependent on the mean load, the dependence on these factors was well described by Wong et al. [20], and plane stress variant of the model is shown in equation 14. This equation can be linearised and simplified with some assumptions to equation 15 for a monotonic loading, which consists of equations 12 and 13 for $s_m = 0$.

$$\rho_m C_\rho \frac{\dot{T}}{T} = - \left[\alpha + \left(\frac{\nu}{E^2} \frac{\partial E}{\partial T} - \frac{1}{E} \frac{\partial \nu}{\partial T} \right) s \right] \dot{s} + \left(\frac{1 + \nu}{E^2} \frac{\partial E}{\partial T} - \frac{1}{E} \frac{\partial \nu}{\partial T} \right) (\sigma_1 \dot{\sigma}_1 + \sigma_2 \dot{\sigma}_2) \quad (14)$$

$$\rho_m C_\rho \frac{\Delta T}{T} = - \left(\alpha - \frac{1}{E^2} \frac{\partial E}{\partial T} s_m \right) \Delta s \quad (15)$$

The phenomenon has different applications, Oliver [21] was the first to use IRT for Thermoelastic Stress Analysis (TSA). The technique was a full-field, non contact stress analysis of a cyclically loaded specimen. It was based on the principle of measuring temperature changes of a solid in its elastic region upon the change in the stress state. The study was one of the first to take advantage of and to show the potential of the technology.

Farahani et al. [22] used the thermoelastic effect to determined the SIF of a C(T) specimen under fatigue loading by mixing it with numerical methods. The results from the TSA were used in the Williams' expansion to calculate the SIF under mode I loading.

Heat dissipation

The work done on a specimen can be as example stored in an elastic field of defects [23], dissipated as heat due to plastic work [23–25], or released as acoustic waves. The heat dissipated can be measured with IRT and it reveals information about the plastic zone, reversed zone, and energy necessary to drive the crack growth.

If the specific heat is assumed to be independent with respect to the internal state of the material and hardening, the source function Q can be determined by using the heat equation, given in equation 16. Since the camera only registers the surface temperature, the equation is averaged across the specimens thickness shown as equation 17, so that only two spatial dimensions describe the energy release. The knowledge about source function further allows to analyse the energy dissipated in the plastic zone, and to analyse the fatigue behaviour based on an energy approach.

$$\rho_m C_\rho \frac{\partial T(x, y, z, t)}{\partial t} = Q + k \left(\frac{\partial^2 T(x, y, z, t)}{\partial x^2} + \frac{\partial^2 T(x, y, z, t)}{\partial y^2} + \frac{\partial^2 T(x, y, z, t)}{\partial z^2} \right) \quad (16)$$

Where T - temperature, Q - source function, k - heat conductivity, ρ_m - material density, C_ρ - specific heat capacity, x, y, z - coordinates, and t - time.

$$Q(x, y, t) = \rho C_\rho \frac{\partial T(x, y, t)}{\partial t} - k \left(\frac{\partial^2 T(x, y, t)}{\partial x^2} + \frac{\partial^2 T(x, y, t)}{\partial y^2} \right) \quad (17)$$

The equation is based on conduction, this assumes no radiation or mass transfer. As Meneghetti and Ricotta [24] explained it, it is a reasonable assumption, as in this case the conduction is orders of magnitude larger than the two other heat transfer mechanisms. However it is possible to include terms into the equation that would account for additional factors like radiation, or convection of the air surrounding the specimen. It is important to note that Q consists of several factors, after an initial period of stabilisation and in stage II of FCG, the time derivative of temperature is mainly affected by the thermoelasticity. This is based in an assumption that the energy dissipation is constant, so the source function can be divided into a reversible or elastic part proportional and with the same general shape as the load signal (assuming adiabatic conditions), and additionally a plastic work part, which is generally a steady state value through most of the crack growth close to the crack tip [23; 26; 27]. Any sources or sinks will also be contained in the function, for example if the upper and lower grip have different temperature, a gradient through the

sample might be visible.

2.3.3 Infrared thermography and fatigue

Fatigue limit

IRT has many advantages over traditional fatigue testing techniques. The fatigue limit as an example can be determined in a reliable and rapid way with a small amount of samples using the Risitano method developed in 1986 [26]. As Opara [28] explained it, the method use the fact that there is a small increase in specimen's temperature at the beginning of cyclic loading. The fatigue limit is estimated based on the fact that under a certain amount of load, the temperature does not increase. This principle can be taken even further and use a uniaxial tensile test to determine the fatigue limit [29].

Heat dissipation

Heat analysis above the fatigue limit results typically in curves presented in figure 9. Three stages are recognised, the first is the initiation stage where the temperature increases. Second stage is a steady state value, and according to Iziumova et al. [23] the following relation applies $\frac{\partial a}{\partial N_1} \sim Q_1 a_1$. In the last stage, the curve rapidly increases, and a second relation $\frac{\partial a}{\partial N_2} \sim Q_2$ was observed by the author in this region, and based on these results, the fatigue failure might be predicted.

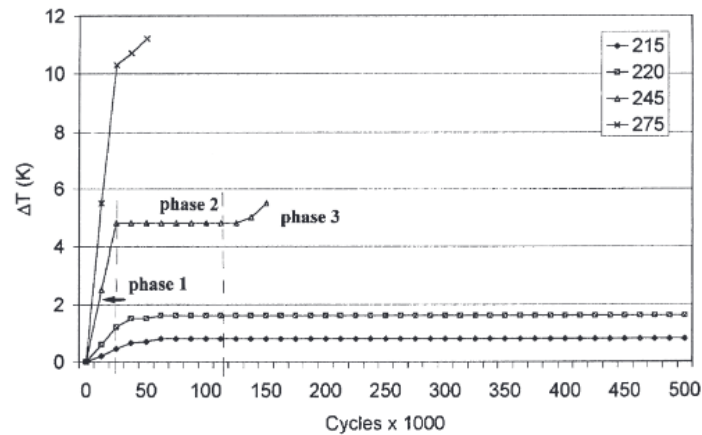


Figure 9: Maximum thermal increments in specimens under fatigue loading at different stresses, $R=0$. Three phases are shown for 245 MPa. Adopted from G La Rosa and A Risitano. Thermographic methodology for rapid determination of the fatigue limit of materials and mechanical components. *International Journal of Fatigue*, 22(1):65 – 73, 2000. ISSN 0142-1123. doi: [https://doi.org/10.1016/S0142-1123\(99\)00088-2](https://doi.org/10.1016/S0142-1123(99)00088-2). URL <http://www.sciencedirect.com/science/article/pii/S0142112399000882>

Phase shift analysis

IRT allows to measure the plastic zone in several ways. One of the methods is based on phase shift between the plastic part of the load and the load signal. When the material is in the elastic region, the heat dissipation is negligible, and the temperature variation is due to the thermoelastic effect which is in phase with the load. If the adiabatic conditions however are not met, as can be the case for heat dissipation and large stress gradients [25; 30], the adiabatic conditions are not satisfied in that region, causing a phase shift, this region corresponds to the plastic zone. A general phase shift map has three regions illustrated in figure 10a. Region A shows practically no shift, implying elastic region. Region B has a positive shift, which according to Díaz et al. [30] is caused by monotonic plasticity and high stress gradients. The last region with negative phase shift is associated with reverse plasticity, and point O is often adopted as an estimate for crack tip, as the phase map is noisy behind it, implying contact between crack faces. A phase map is illustrated in figure 10b where the plastic region and the reversed part of it is visible.

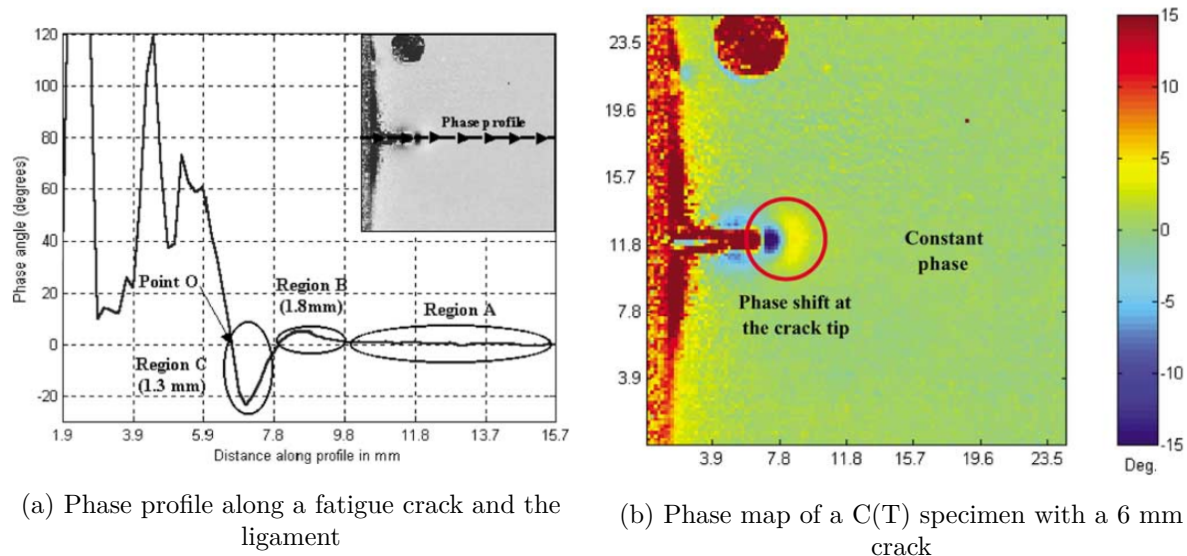


Figure 10: Illustration of the phase in a C(T) specimen. Adopted from F. A. Díaz, E. A. Patterson, R. A. Tomlinson, and J. R. Yates. Measuring stress intensity factors during fatigue crack growth using thermoelasticity. *Fatigue & Fracture of Engineering Materials & Structures*, 27(7):571–583, 2004. doi: 10.1111/j.1460-2695.2004.00782.x. URL <https://onlinelibrary.wiley.com/doi/abs/10.1111/j.1460-2695.2004.00782.x>

Ancona et al. [25] took the phase analysis a step further, and used two harmonic Fourier components. The model consisted in total of three parts, a linear term for describing the increase in the mean temperature, a harmonic term with the same frequency as the load for the thermoelastic effect, and a second harmonic term for the plastic dissipation at a frequency of twice the load frequency, since the dissipation is expected to occur both in compression and tension. The model has a potential of an even better description of the plastic zone and crack tip position, especially for low loads where the plastic zone is small and the heat dissipation is difficult to measure.

Stress intensity range and stress fields

The thermoelastic response contains information about the stress field in form of the first stress invariant, this fact can be used to calculate the stress intensity range ΔK from IRT data with help of a model for elastic stress field. Since the temperature increase is proportional to the sum of principal stresses, and the stress state is of plane stress, a stress

field model like Williams' expansion should be in agreement with the data obtained in the elastic region, and based on this, the stress intensity can be calculated [22; 30; 31]. A benefit of this method is that it shows the actual stress intensity, accounting for phenomena affecting it, like crack closure.

In the elastic region, an elastic model, like Williams' expansion, can be used to find the relation between principal stresses, and it can be combined with the first stress invariant calculated from IRT data to make a hybrid model of the stressfield based on acquired data and theoretical stress field. Thermoelasticity is also visible in the plastic region, although it is more complicated to use, because in addition to the elastic effect, heat is dissipated due to plastic work, and as mentioned, it might have the same frequency as the load in the tensile zone, or twice as high in the reversed zone [25]. The stress distribution in the plastic zone is unknown, so the ratio between principal stresses cannot be found. The stresses might still be approximated, with the following assumptions:

- A plane stress or plane strain condition is assumed.
- The temperature due to heat dissipation is assumed to be a steady state process.
- The stresses in the plastic zone are assumed to be in between a pure tensile mode, and a state occurring if the material would be elastic.
- The thermoelastic response is assumed to occur adiabatically.

Based on the last assumption a stress interval can be calculated. The first case is of pure tensile stresses, σ_2 is equal to zero, and the Von Mises stresses are equal to σ_1 , giving an upper limit of the actual Von Mises stresses. If the stresses have the same ratio as stresses occurring in an elastic material, σ_1 and σ_2 sum up to the first stress invariant, the Von Mises stresses calculated from these will have a lowest value of ≈ 0.7 of the first case, giving a lower limit. In reality the Von Mises stresses should be in between these two values. It should be noted that the model is just an approximation, and the assumptions are rough.

2.4 High-Speed Photography and Digital Image Correlation

2.4.1 Optical methods

While performing the mechanical testing of the materials, e.g. FCG tests of metallic materials, it is often useful to verify deformation mechanisms and validate the test correctness using visual inspections at the appropriate temporal and spatial resolution. The most crude observations may be made by naked eye, but it is often useful to seek for help offered by modern optical based tools. Photo or video-recording of the experiment can be used as an aid to visualise the different processes taking place during the test, for instance to observe the necking process while analysing the stress-strain curve during tensile testing [32], or to compare the crack lengths obtained using different measuring techniques. The digital images can be further processed using computer algorithms in a broad variety of ways; such action is called DIP. Some of the activities standing behind DIP are: filtering in both spatial and frequency domains, scaling, rotating, or adjusting the contrast, finding edges, and following the behaviour of the features at the surface under external influence. DIP algorithms used in this work are described in the section 2.5. The post-analysis of visual data is gaining more and more recognition for its capacity of obtaining the quantitative parameters of the observed surfaces using the digital processing methods and the numerical computing. Among the optical-based methods for investigation, many authors propose the use of digital image correlation - DIC as a non-interference, and non-contact precise measurement method to obtain the global displacement fields. These fields can be further used to determine the strains, and approximate the stresses. There are fields where it's of interest to measure, and record events of short duration, or the series of such events. One example is FCG test performed with work frequency of e.g. 10 Hz. High speed imaging, or rapid video imaging, is then a proper tool for investigation. Phrases HSI, High-Speed Photography (HSP), and RVI will be used interchangeably in this work. Using DIP methods as DIC or Particle Image Velocimetry (PIV) together with HSI makes it possible to examine the changes in the displacement or strain field at 10^{-6} second timescale [33].

2.4.2 High-Speed Photography

General about High-Speed Photography

There are many definitions of high-speed photography. One comprehensive definition was proposed by Fuller [34] :

Recording optical or photo-optical information with adequately short exposures and fast enough framing rates for an event to be evaluated with a temporal and dimensional resolution which satisfies the experimenter.

The same author proposed a division of different high-speed cameras in groups [35]:

- *High Speed* - 50 to 500 fps
- *Very High Speed* - 500 to 100,000 fps
- *Ultra High Speed* - 100,000 to 10,000,000 fps
- *Super High Speed* - in excess of 10,000,000 fps

The modern high-speed cameras use photosensitive electronic semiconductor devices as Charge Coupled Device (CCD)- or Complementary Metal Oxide Semiconductor (CMOS) sensors. CCD are able to record with extremely short exposure times, some Intensified Charge Coupled Device (ICCD) cameras as XXRapidFrame ICCD camera [36] have exposure time as low as 200 ps, and are able to capture images of high spatial resolution. Despite the superior capabilities, capturing a great number of frames is challenging for CCD. Recording larger amount of frames can be archived by using more CCD chips. This is usually not a problem for CMOS cameras. Figure 201 (after Reu and Miller [37]) in the appendix show the survey of high-speed imaging technologies.

History of HSP

It is often stated that the first instance of what we can call HSP was to settle debate on horse's gait [33]. The question was if there is the moment when all four hooves are off the ground when a horse is galloping. The photographer, Eadweard Muybridge, devised a camera system consisting of 12 (and later 24) individual cameras triggered by horse's legs. Muybridge placed cameras which were 69 cm apart, the shutter speed of cameras was less than 1/2000 s. This first series of pictures was taken June 15, 1878 and is known as *Sallie Gardner at a Gallop*. In 1892, C.V. Boys suggested a new design of rotating mirrors which could be used for high-speed imaging system, this principle is still in use nowadays, mostly on high-speed CCD cameras. The purpose of the development of this system was to film the bullet in flight [33; 38]. In 1930s, Kodak developed camera able to capture 5000 Frames Per Second (fps) [33]. The main motivation for development of HSI technology became the research on nuclear weapons during Manhattan project during the world war II, and the cold war. Rotating mirror technology was applied for imaging the thermonuclear weapons with frame rate in order of 1Mfps. The film based cameras approached their theoretical possible performance due to physical limitations around 1980s [39]. The situation changed when the photosensitive media started to be gradually replaced by electronic semiconductor devices such as CMOS and CCD.

Frame rate, exposure time, depth of field and illumination

The following section describes the importance of a proper choice of some of the most crucial parameters during high-speed imaging: frame rate, exposure time, aperture and illumination. The frame rate describes the rate of images captured for given time interval and can be given in fps or Hz. According to [33], the optimum frame rate f_r using HSP can be estimated using the equation 18

$$f_r = N_s \frac{u_e}{l_s} \quad (18)$$

where N_s is the required number of samples, at least 2 but 5-10 is a more reasonable choice, l_s is the length scale and u_e is typical velocity of an event. Knowing the size of a specimen and a velocity of an event, e.g. brittle crack propagation velocity, one can give rough estimate of the frame rate required. As an example, the cracks initiated at stress risers, as the rivet holes in aircraft industry, can travel with velocities on the order of a few hundred m/s [40].

Gao et al. [1] presents considerations about the frame rate using HSP when investigating mode I FCG using C(T) specimen, and high-frequency (90-135 Hz) resonant fatigue testing machine. Considering information extraction, computer processing capacity and data storage space, the acquisition rate was set to 3180 fps with resolution of 1280×720 pixel. This gave 24 \sim 35 images collected within one stress cycle. Yusof and Withers [41] present similar strategy choosing the frame rate. For testing of the C(T) specimen at frequency of 77Hz, the acquisition rate was set to 1000 fps, giving about 14 frames per load cycle. In both cases the images were further used in DIC, and the high pixel resolution exceeding 1 megapixel was used.

The high-speed cameras, especially cameras able to capture events with very high frame rates can be used for measuring fracturing velocity [40; 42–44]. Wright et al. [42] investigated bulk metallic glass under compression. The experiment showed ability of high-speed photography to register fracturing events which has not been detected by load cell due to low-pass filtering in the electronics of the load cell. They found velocity of the fracture propagation as well.

One of the issues in the rapid imaging is the short exposure time. To get a satisfactory photographic image, an optical image of appropriate intensity has to be exposed for the optical sensors for the appropriate length of time. To avoid the motion blur (streaking of captured object on the frame), one have to chose exposure time which compensates for sudden changes in the captured frame, e.g. a fast moving object. The four principal variables determining the camera exposure, i.e. amount of light per unit area reaching the photosensitive sensor are: the subject luminance, the film speed (films sensitivity to light),

the lens aperture, and the shutter speed. Assuming film speed, and lens aperture constant, the exposure H is proportional to the exposure time t which is the same as the shutter speed, by the following relation [45]:

$$H = E_i t, \quad E_i = \frac{d\Phi_v}{dS} \quad (19)$$

Where E_i is illuminance, also the total luminous flux Φ_v incident on a surface (e.g. photosensitive digital sensor) per unit area S .

The difficulties of lightning in high-speed photography are much more severe than the use of the camera equipment itself [46]. The lightning problem becomes much larger when the colour images are captured [33]. As shown in the equation 19, the illuminance demand rises as the exposure time is reduced [34]. There are two main methods of lighting the captured object. Either the continuous light source is used, or a pulsed light operates synchronously with the shutter opening. Various types of light sources used in the high-speed photography are presented in the table 19 in the appendix. Heat generation from a light source may cause several problems. Hertegård et al. [47] reports that for medical application trials with HSI, more specifically phoniatrics, the camera required a very strong light source (700 W) to allow image capturing with acceptable brightness. Nowadays the Light-Emitting Diodes (LEDs) are becoming popular and they are replacing the older technologies. One of advantages with the LEDs is fact that they have high luminous efficacy, which is measure of the ability of a light source to produce a visual response from its power. In other words the luminous efficacy is a ratio of luminous flux to power, quantified as lm/W. This advantage of LEDs solves some of the problems related to heat generation, and is important when performing experiments simultaneously with IRT, where the additional heat source may affect the results.

Kirugulige et al. [48] described importance of high-speed camera calibration, triggering and the light stability when dealing with the rotating mirror CCD camera. Despite differences between such camera and the CMOS HS-cam, the requirements according to the light

source remain similar. Authors claimed that a stable light source with equal light sensitivity over time is crucial for repeatability. They used a photodetector with the high-speed data acquisition system with sampling rate of 1 MHz to ensure that the light sensitivity remained unchanged during capturing the event of interest. Triggering was important since only 32 frames were captured with the frame rate of 225000, giving recording time of $145\mu\text{s}$.

Ju et al. [40] used high-speed photography and photoelastic testing techniques to capture and characterise stress-field evolution during fracture rapid propagation. In experiment, the authors used 3D printed disk made of brittle, transparent polyester. The disk was subjected to a quasi-static compressive load. The authors described the advantage of the pulsed laser light source compared to the continuous light. They used the high-speed camera synchronised with the pulsing laser light source, which gave a sharp high-quality fringe patterns, in contrast to the continuous light source producing the fuzzy fringes. Fringes have been further used to quantify the relation between the stress field in vicinity of a crack tip and the crack velocity.

Another important aspect in high-speed imaging is the depth of field. This is an important aspect when capturing the moving object as the C(T) specimen with a microscope lens. It is of interest to capture a series of the sharp focused images through the whole load cycle, even if there is some movement in axis parallel to the lens axis. The depth of field is by definition a distance between the nearest and the furthest object that are in focus in an image. According to the literature [49], the depth of field can be expressed using the following approximation:

$$\text{Depth of field} \approx \frac{2u_{ph}^2 N_{ph} C_{ph}}{f_{ph}^2} \quad (20)$$

with the circle of confusion C_{ph} , the focal length f_{ph} , the distance to subject u_{ph} , and the F-number N_{ph} . The last two quantities are of particular interest. The distance to the subject u_{ph} is crucial since the depth of field changes with the square of u_{ph} . The F-number N_{ph} is the ratio between the focal length f_{ph} , and the diameter of entrance

pupil D_{ph} , also $N_{ph} = f_{ph}/D_{ph}$. Consider a case where the lens's focal length is 5 mm and the diameter of the entrance pupil is 2.5 mm, the f-number found using the mentioned parameters is 2. The corresponding aperture would be expressed as $f/2$. The f-number is also the reciprocal of the relative aperture. If the lens has a range of aperture sizes, e.g. $f/2 - f/20$, the $f/2$ is the maximum aperture (the largest diameter of entrance pupil), while the $f/20$ is the minimum aperture (the smallest diameter of entrance pupil). It can be shown [49] that the illuminance E_i is inversely proportional to square of the f-number N_{ph} , $E_i \propto 1/N_{ph}^2$. This means that when the aperture is increased (f-number reduces), the illuminance increases as well. To get a satisfactory image after a change in the aperture, the exposure time should be reduced (faster shutter) according to equation 19. From the following series of relationships it follows that if the user wants to maximise the depth of field, the aperture has to be as small as possible. However, it has to be compensated with the stronger light source if the user wants to keep exposure time reasonably short to avoid the motion blur.

Recording memory

One of the limitations of high-speed cameras is relatively short maximum recording time compared to the traditional video cameras with maximum frame rates of approximately 30 fps. The reason for this is a fact that capturing pictures of high spatial, and temporal resolution (e.g. 20000 fps with 1024x1024 resolution) generates tens of gigabytes of data per second. Table 7 shows approximation of how fast the internal memory can be filled up with data for a given resolution. Modern high-speed cameras are equipped with the volatile memory which is overwritten in an endless loop while the camera is in recording state. To save a given event of interest, the user can employ an automated trigger or trigger it manually. When triggering, the camera stops overwriting, and keeps the wanted recording on volatile memory until the user downloads it on the computer, or other storage device. Although the camera is able to fill up the memory in seconds, it may take minutes, or tens of minutes to transfer the data to the non-volatile memory. The type of connection

with the controlling computer, or the memory used depend on the camera, cameras as Photron SA-Z uses the Ethernet connection.

Wong and Einstein [50] in their study of cracking processes in rock described some fundamentals of high speed camera, as well as the procedure of video capturing operation for the cracking experiments. They mentioned three camera features that are crucial for use in imaging of cracking process: the maximum allowable image resolution, the frame rate, and the size of internal memory within the camera. Authors postulated that it is impossible to obtain a high-speed video which can satisfy all three requirements simultaneously, and a compromise for the particular experiment has to be found. Reducing the recording frame rate, lowering the image resolution, or both, can increase the length of the recording. However it is a trade-off, since the temporal-, and spatial resolution of the recording are affected. This is an important aspect when dealing with the camera where the recording memory is limited. Three actions are proposed for preparing to capturing the cracking process.

- *Choose capturing parameters* - Selecting the image resolution and the frame rate. These values should be chosen based on expected duration of event or the series of event.
- *Set Post Trigger Value* - Determining the number of frames to be saved before, and after the camera trigger was launched. When making a choice, a reaction time lag between the human recognition of event, and the triggering on the controlling computer should be considered.
- *Trigger Camera* - This can be done by launching a proper function/tool in the software on the camera controlling computer.

Triggering

Due to limitations in available volatile memory or chips in CCD camera, it is of interest to stop memory overwriting in the proper moment. As mentioned before, this can be done by using a trigger. Depending on triggering mode, the trigger can force camera to keep images captured before, in the middle, or after the trigger signal is received. A trigger can be launched either manually, or in an automated way. Wong and Einstein [50] described the problem where the automated trigger is not an option, and the manual trigger had to be used instead. Authors postulated that for such a case, the video duration should be longer than 0.3 seconds, which is associated with the manual trigger delay caused by human reaction pace.

There are several different ways of triggering the camera in the fully automated way. This can be done using the load signal from the testing machine, or employing acoustic emission triggering. Acoustic emission triggering can be used when analysing the specific dynamic defects in solids, since the elastic waves are generated during rapid local structural transformations within the specimen. When the signal of a proper strength is recorded and surpasses the threshold value, a trigger is activated. Seleznev and Vinogradov [51] described an efficient triggering method proposed for optical imaging systems with aid from AE technique. Authors presented AE method as an attractive method for real time monitoring of deformation processes based on its high sensitivity. In the note, a broadband miniature AE sensor with 200-750 kHz operating frequency was presented. Sensor should be attached either to the specimen surface or to the grip close to the gauge part of the specimen. The pulse is registered, and if the amplitude (e.g. registered as U [mV]) surpasses the threshold value, the data acquisition board generates a standard Transistor-Transistor Logic (TTL)-compatible signal which can be used to trigger the camera. The delay between the actual signal appearance, and the threshold crossing controls the accuracy of synchronisation between the event of interest and the triggering signal. If the delay is for instance $6\mu\text{s}$ and high-speed camera frame rate is 100'000 fps corresponding to the sampling period of $10\mu\text{s}$,

the synchronisation delay of few μs is acceptable.

2.4.3 Digital Image Correlation

DIC is optical based, non-contact method to extract full-field deformation, and strain measurements using images acquired from the various optical sources. These images can be captured by wide variety of sources as: conventional CMOS-, and CCD cameras, high-speed video, macroscopes, and microscopes including atomic force microscopes, and scanning electron microscopes [33; 52]. DIC is generally divided into 2D-DIC and 3D-DIC. The former one, used in scope of this work, applies for the in-plane deformation of the nominal planar objects, while the latter one can be used for the 3D surface deformation of both planar and curved objects.

DIC algorithm

DIC measures the material deformation by image tracking. Implementation may vary, but in general, the DIC algorithm tracks the relative displacement of points between an undeformed reference image and a current image where object has undergone deformation. In what follows, a brief explanation of subset-based DIC algorithm will be given based on papers by Blaber et al.; Pan et al. [53; 54].

In order to compute displacement of a point of interest, for instance $P(x_0, y_0)$, a reference subset of n pixels centred at the point P from the reference image is chosen. Such subset is shown at figure 11 as red square with size $N \times N$ pixels. Subset is used to track the new location of point P in deformed image. In order to detect a position of a reference point P in deformed image, a criterion has to be established in order to evaluate the similarities between the selected reference subset and the target subset. This problem is solved by moving a reference subset on the searching area in deformed image and applying a selected correlation coefficient at each location. Correlation coefficient map resulting from such action can be seen in figure 11. When the correlation coefficient extreme is detected, a new

position of the deformed subset in the deformed image can be determined. The difference in the position of P in the centre of a reference, and a target subset can be further used to determine the in-plane displacement vector at P .

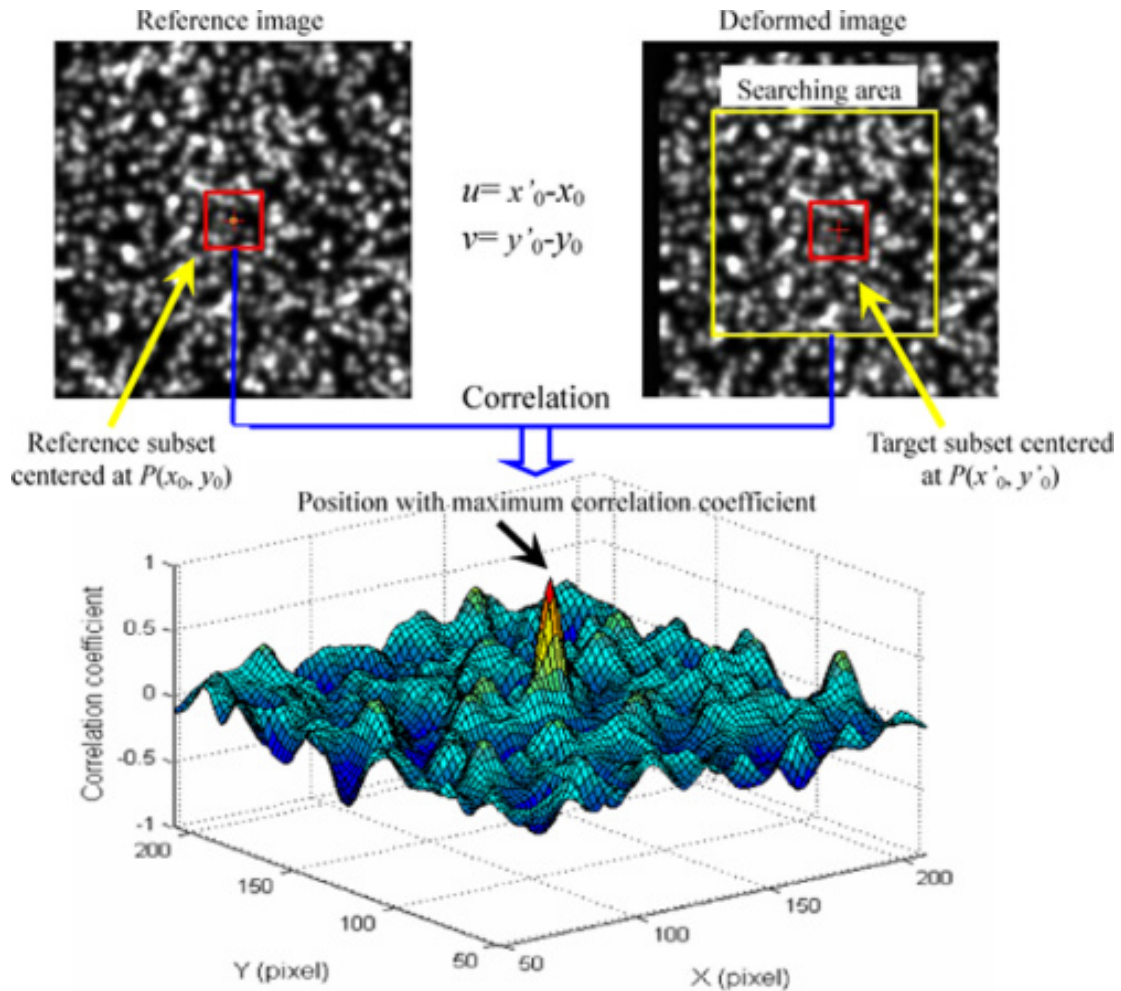


Figure 11: Example of tracking the reference subset in deformed image using DIC, adopted from Bing Pan, Huimin Xie, and Zhaoyang Wang. Equivalence of digital image correlation criteria for pattern matching. *Appl. Opt.*, 49(28):5501–5509, Oct 2010. doi: 10.1364/AO.49.005501. URL <http://ao.osa.org/abstract.cfm?URI=ao-49-28-5501>

Correlation criteria play a critical role in DIC since they are used in order to evaluate the similarity degree between the reference-, and the target subset. These correlation criteria compare grayscale values of reference-, and target subset respectively. Some of the criteria used in DIC can be divided in four categories according to their mathematical definitions:

sum of absolute difference (SAD), cross-correlation (CC), sum of squared difference (SSD), and parametric sum of squared difference (PSSD). Two commonly used criteria, Zero-mean Normalised Cross-Correlation (ZNCC) coefficient, and Zero-mean Normalised Sum of Squared Difference (ZNSSD) coefficient, will be presented in the following. Let $f(x_i, y_i)$ and $g(x'_i, y'_i)$ indicate grayscale value in the i th pixel in the reference subset, and the target subset respectively. These can for simplicity be denoted as f_i and g_i . Let also $\bar{f} = \frac{1}{n} \sum_{i=1}^n f_i$, $\bar{g} = \frac{1}{n} \sum_{i=1}^n g_i$, $\bar{f}_i = f_i - \bar{f}$ and $\bar{g}_i = g_i - \bar{g}$. The ZNCC and ZNSSD can be expressed as:

$$C_{ZNCC} = \frac{\sum \bar{f}_i \bar{g}_i}{\sqrt{\sum \bar{f}_i^2 \sum \bar{g}_i^2}} \quad (21)$$

$$C_{ZNSSD} = \sum \left(\frac{\bar{f}_i}{\sqrt{\sum \bar{f}_i^2}} - \frac{\bar{g}_i}{\sqrt{\sum \bar{g}_i^2}} \right)^2 \quad (22)$$

More details about the correlation criteria commonly used in DIC can be found in [1; 53; 54]. The deformation inside each subset is assumed to be homogeneous, and the transformation of the reference subset points to the target configuration is constrained to the linear, first order transformation [53]. Such a transformation can be represented by the generalised deformation vector \mathbf{p} :

$$\mathbf{p} = \left\{ u \ v \ \frac{\partial u}{\partial x} \ \frac{\partial u}{\partial y} \ \frac{\partial v}{\partial x} \ \frac{\partial v}{\partial y} \right\}^T \quad (23)$$

The linear transformations for subset coordinates can be seen in figure 12. For non-homogeneous deformations, the second order shape function capable to represent more complex local deformation were demonstrated to provide a high accuracy [33; 55].

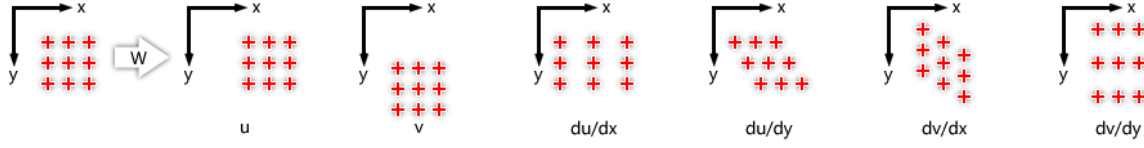


Figure 12: Linear transformation of subset coordinates by applying warp function W . Adopted from <http://www.ncorr.com/index.php/dic-algorithms>

The strains can be calculated by differentiation of the displacements. This can be done by applying Green-Lagrangian strain tensor and using the following equations:

$$\varepsilon_{xx} = \frac{1}{2} \left[2 \frac{\partial u}{\partial x} + \left(\frac{\partial u}{\partial x} \right)^2 + \left(\frac{\partial v}{\partial x} \right)^2 \right] \quad (24)$$

$$\varepsilon_{yy} = \frac{1}{2} \left[2 \frac{\partial v}{\partial y} + \left(\frac{\partial u}{\partial y} \right)^2 + \left(\frac{\partial v}{\partial y} \right)^2 \right] \quad (25)$$

$$\varepsilon_{xy} = \frac{1}{2} \left[\frac{\partial u}{\partial y} + \frac{\partial v}{\partial x} + \frac{\partial u}{\partial x} \frac{\partial u}{\partial y} + \frac{\partial v}{\partial x} \frac{\partial v}{\partial y} \right] \quad (26)$$

The specimen which is to be investigated by DIC should be prepared in order to serve as carriers of deformation information. This is typically achieved by applying a speckle pattern to the tested object. Such speckle pattern can be created using haze of black paint onto white painted background [1; 56]. Sometimes the natural surface of the component or structure has a sufficient image texture for DIC application, and additional surface preparation as painting is not necessary [52].

Use of DIC in investigating FCG

Tong et al. [57] employed DIC to find crack opening displacements as well as near-tip displacements and strains ahead of a crack tip. Displacement data and Williams' series expansion were used to find stress intensity factor K . All these together were used to investigate the crack closure impact on global crack driving force K .

Yusof and Withers [41] employed both high-speed camera and DIC in attempt to determine both the crack-tip position and stress intensity factors (K_I and K_{II}) within selected cycles using C(T) specimen made of 7010-T7651 aluminium alloy. This paper shows the influence of the quality of optics on the experiment. The displacement fields obtained in the experiment were quite noisy and as a consequence the strain fields were far too noisy to identify crack-tip position or the crack-tip strain fields. Therefore, instead of using the crack-tip stress intensity factor approach based on matching the strain, the vertical displacement vectors were used to determine K_I and K_{II} with the accuracy of around $0.2 \text{ MPa}\sqrt{\text{m}}$ from frame to frame. The acquisition rate of 1000 fps used provided 14 images per cycle.

Gao et al. [1] presented a combination of conventional photography, high-speed imaging, DIP and DIC in investigating FCG, more specifically, mode I cracking using C(T) specimen and the high-frequency (90-135 Hz) resonant fatigue tester. Authors used CCD camera, and DIP to obtain the crack path, crack length, and the crack tip position. These properties were further used for determination of strain-, and stress fields at the crack tip using DIC, and data from the high-speed camera. Acquisition rate was 3180 fps with the resolution of 1280×720 pixel giving $24 \sim 35$ images collected within a single stress cycle.

Vasco-Olmo [58] in their work present a technique for experimental determination of the crack tip plastic zone during the FCG and its comparison with the theoretical plastic zone using three different models (the Westergaard solution, Williams expansion, and the Christopher-James-Patterson model). Authors give description for obtaining the stress fields out of the displacement fields found by using DIC. The stress fields were further used to estimate the plastic zone size, this has been done by applying either von Mises or Tresca criterion to the stresses. Using mentioned techniques the authors investigated the influence of the R -ratio on the size of the plastic zone in FCG.

Vasco-Olmo [59] in another work use DIC in study of Crack Tip Opening Displacements (CTODs). An attempt to evaluate the ability of CTOD to characterise FCG was made. Authors present a methodology to measure the CTODs from experimental data employing

DIC. They have found that the plastic CTOD is directly related to the plastic deformation at the crack tip. In addition it has been presented that there is a linear relationship between growth rate da/dN and the plastic part of CTOD. Authors present also a method for determining the crack tip position with DIC using the displacement profiles.

There are fields where optical methods as DIC are more suitable for obtaining quantitative data than other well-known and widely used methods such as the potential drop DCPD method for obtaining the crack length. Hosdez et al. [60] compared two methods: DIC and DCPD for characterising long crack behaviour and identifying the Paris' law constants. The material investigated was ductile iron. For identification of the Paris' law, the crack lengths had to be found. The authors presented some concluding points where they compared DIC and DCPD as methods.

- *Measuring process* - DCPD is of interest when dealing with closed environment where it may be difficult to set up the optical equipment. Measurement using DCPD is continuous. DIC have some technical limitations as memory requirements to store the pictures, post-treatment of images.
- *Measurement accuracy* - DCPD offers higher resolution ($50 \mu\text{m}$) compared to DIC (100 to $400 \mu\text{m}$).
- *Multiaxiality* - DIC can be employed to find SIFs in all three cracking modes (K_I, K_{II}, K_{III}) while DCPD is limited to the opening cracking mode.
- *Plasticity* - DIC allows masking of the plasticity impact on the displacements at the crack tip and it's constraining its influence on identification.

Authors described DCPD as method more suitable for simple Paris' law determination, while in case of multiaxial tests or plasticity studies, DIC is preferred.

HSP and DIC combined with IRT

The paper by Crump et al. [56] concentrates on challenges faced by the use of DIC and IRT at high speeds to obtain strain-, and temperature distributions in composite materials, and using them in a synchronised manner. Authors mention additional sources of error arising from the use of high-speed camera images in DIC for high-velocity testing. One of the first problems mentioned is reducing the resolution of the sensor in order to increase the frame rate. The user has to accept a coarser strain map, and this can lead to a greater uncertainty in the strain result. The second source of error was related to illumination. It is difficult to obtain satisfactory images with high contrast, when the exposure time is strongly reduced. Authors noted two adverse effects of high light intensity: specimen heating and heat haze at the images.

The authors mention issues using IRT at higher frame rates. The main physical limitation is the fact that IR is dependent on the finite amount of energy emitted from the materials surface. Amount of photons and the sensitivity of the detectors limit the maximum frame rate in IRT, while for white light high-speed cameras the problem of reduced exposure time can be solved by increasing the illumination.

The same authors propose actions for obtaining the same temporal location of the temperature, and the strain fields. The first challenge to overcome is triggering of the equipment. The second problem is related to the frame rate. The maximum frame rates in IRT are much smaller than the frame rates that can be obtained by HSI. Authors postulate that using frame rates for HSI being a multiple of frame rates for IRT will ensure that for each IR image there will be a strain image from DIC. The final challenge is related to specimen preparation. DIC requires speckle pattern, while to obtain best results, use of black matt paint will be favourable for IR.

2.4.4 Conclusions arising from theory and literature

- HSI or conventional photography is seldom used alone for investigating the FCG. The majority of literature treats about use of HSI together DIC analysis.
- The frame rate depends on the purpose. For the use in DIC investigating FCG, the frame rate should be in the order of tens of images per load cycle, and the spatial resolution should be maximised. For qualitative analysis, and filming the brittle fracture, a high frame rates should be selected depending on the expected velocity of the event (crack jump).
- When the large magnification is used during the test, there is a risk of loss of focus. To avoid this, one can maximise the depth of field by decrease in the aperture of the lens/camera if the equipment has adjustable aperture. The other action possible is use of a larger FOV.
- Recording memory, lighting and the triggering are other important aspects that has to be considered in order to get satisfactory recording.
- Several authors used DIC for investigating the different aspects of FCG. In this work it is of interest to compare different parameters obtained using different techniques, i.e.; crack growth rate, effective SIF, crack closure and the plastic zone. For this reason, some of the ideas presented by authors mentioned in literature section are further used [1; 57–59; 61].
- The concurrent use of the HSP and IRT has been previously tested. The issues with the specimen heating, heat haze and the temporal resolution were reported.

2.5 Digital Image Processing

The digital images often require a post-processing in order to remove imperfections which can affect the results if the optical data is to be used in quantitative manner, or general reception of the image obtained. The term digital image in this work refer to image taken by conventional camera, but also IR camera. The imperfections to be treated arrive from the optics used, illumination, or the camera itself (e.g. dead pixel on the matrix).

The images obtained by HSI combined with microscope lens suffer of vignetting. This is a phenomenon revealing itself by reduction of brightness toward the periphery of an image compared to its centre. Vignetting can be removed by assuming the uneven illumination as an additive low frequency signal and removing it. Filtering may be achieved by convolving the image with a Gaussian kernel [62]. Following section describe the principle behind filters used in this work.

2.5.1 Discrete Fourier Transform

Uneven illumination interpreted as the low frequency signal can be removed in efficient way in the frequency domain. The filters such as the Gaussian filter modifies the input signal by signal convolution with proper filtering function. In this work, the Gaussian filter was applied by multiplying the Fourier transformed picture with Gaussian kernel. Convolution theorem states that

$$\mathcal{F}\{f * g\} = \mathcal{F}\{f\} \cdot \mathcal{F}\{g\} \quad (27)$$

where \mathcal{F} denotes the Fourier transform, f is a signal function and g represents a filtering function. Considering continuous input signal in time-domain as $f(t)$, its representation in frequency-domain $F(\omega)$ is given by:

$$F(\omega) = \int_{-\infty}^{\infty} f(t)e^{-j\omega t} dt \quad (28)$$

for any real number ω . This is called continuous time Fourier transform. Dealing with the samples of the digital signals the integral turns to the sum of infinite number of discrete values called Discrete-Time Fourier Transform (DTFT):

$$F(\omega) = \sum_{n=-\infty}^{\infty} f[n]e^{-j\omega n} \quad (29)$$

with periodicity 2π . When having a finite number of time samples, the discrete-time Fourier transform turns to Discrete Fourier Transform (DFT):

$$F[k] = \sum_{n=0}^{N-1} f[n]e^{-j\frac{2\pi kn}{N}} \quad (30)$$

where $k \in [0, N-1]$, and the sequence is N -periodic. The digital image can be denoted as 2D array $f(x, y)$, where f is for instance a grayscale value for given pixel position. For a digital image of size $M \times N$, where $x = 0, 1, \dots, N-1$, and $y = 0, 1, \dots, M-1$, the 2D-DFT is denoted as:

$$F[u, v] = \sum_{x=0}^{N-1} \sum_{y=0}^{M-1} f[x, y]e^{-j(\frac{2\pi ux}{N} + \frac{2\pi vy}{M})} \quad (31)$$

where the output image $F[u, v]$ has the same size $M \times N$, where $u = 0, 1, \dots, N-1$ and $v = 0, 1, \dots, M-1$, and u as well as v are the vertical and horizontal frequencies. In *MATLAB*, the 2D-DFT is performed using function `fft2`.

From the properties of DFT it follows that the DFT is infinitely periodic in u and v directions, and the periodicity is determined by the M and N . These two are typically representing the image size, but they can be arbitrary numbers. In addition, the Fourier transform of a real-valued function is the even symmetric function. For DFT of the real signals it follows that:

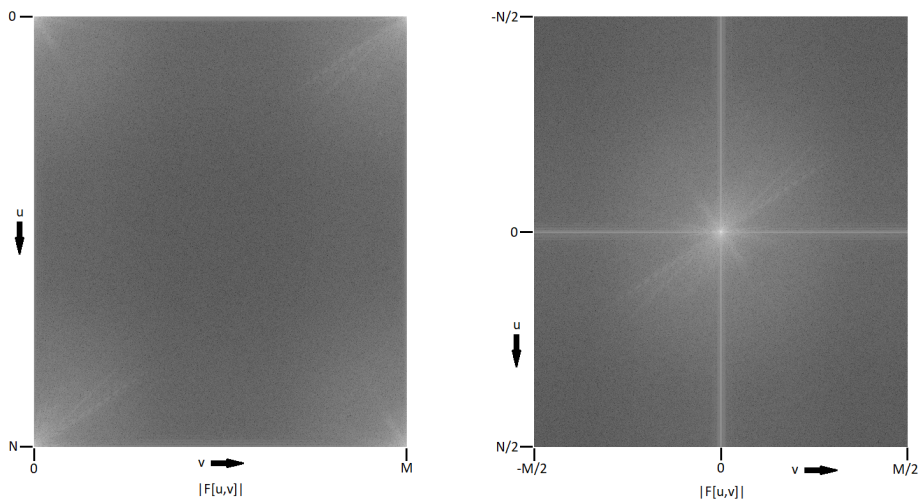
$$f_n \in \mathbb{R} \quad \forall n \in \{0, \dots, N-1\} \Rightarrow F_k = F'_{-k} \quad \forall k \in \{0, \dots, N-1\} \quad (32)$$

Where F' denotes complex conjugation. It means that for 2D-DFT, $F[u, v] = F[-u, -v]'$ and $|F[u, v]| = |F[-u, -v]'$. The fact of periodicity and symmetry can be used for interpreting the frequencies while performing DFT. It's often useful to visualise a 2D-DFT, but the transformed image is an 2D array of complex values. Thus the magnitude of the complex number z if $z = x + yi$ is to be found with following formula: $|z| = \sqrt{x^2 + y^2}$. Since the low frequency points on the array are expected to be very large compared to high-frequency content, a logarithmic plot is favourable. Now consider the DFT at log-magnitude visualisation on figure 14a. After transformation, $F[0,0]$ which is here the upper left corner is the sum of all pixel intensities of the original image in spatial domain because $e^{-j\frac{2\pi y \times 0}{M}} = e^{-j\frac{2\pi x \times 0}{N}} = 1$. Consider situation where $u = 0$ and one follow upper edge from $v = 0$ to $v = M$. Starting from $[0,0]$ and following the edge of the log-magnitude rectangle, the absolute value of F drops as frequency rises, but passing $M/2$ it starting to grow again because $F[0, M/2-1]$ is a complex conjugate of $F[0, M/2+1]$, finally reaching $v = M$ it can be seen that the $|F[0,0]| = |F[0, M-1]|$.

Analysis of the frequency content can be simplified by shifting the zero-frequency component to centre of the spectrum. In *MATLAB*, shifting can be performed using function `fftshift` which swaps the first quadrant of the 2D-array with the third, and second quadrant with the fourth. After shifting, the low frequency content of the DFT is focused on the middle of the frequency rectangle with low-frequency «rays» radiating from inside the rectangle. This can be seen as light rays on figure 14b.



Figure 13: Original picture in grayscale to be filtered



(a) Unchanged DFT

(b) Shifted DFT

Figure 14: Log-magnitude representation of DFT of the picture in figure 13

2.5.2 Gaussian low-pass filter

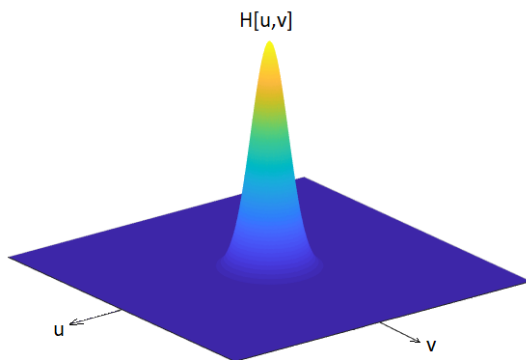
For removing the vignetting effect from the image, one may employ filtering using Gaussian kernel. This can be done by creating blurred version of the reference image containing low frequencies, and subtracting it from the reference image. One may also use Gaussian kernel

to only pass the high-frequencies directly. In this work, the former of mentioned ways of filtering is used.

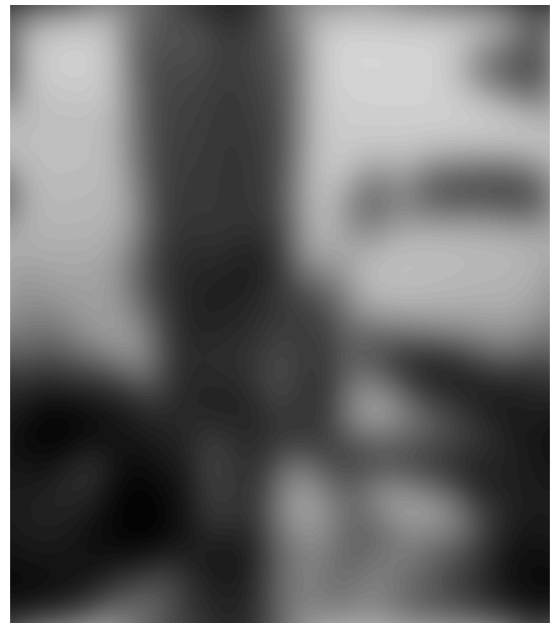
The Gaussian blur can be made by multiplying the Fourier-transformed, and shifted image with a mask containing the Gaussian curve with a two-dimensional domain. The middle of the «bell» should be aligned with the middle of the shifted frequency rectangle such that the low-frequency passes through, while the high-frequency content is reduced. The two-dimensional Gaussian function used to create filter is expressed as:

$$H[u, v] = e^{-\frac{(u-u_0)^2+(v-v_0)^2}{2\sigma^2}} \quad (33)$$

Where u_0 and v_0 determine the centre, and σ controls the spread of the blob. The σ is used to adjust the level of the image blur, since it determines how much high-frequency content passes through the mask. Gaussian kernel representing the filtering function $H[u, v]$ is shown on figure 15a, while the example picture with after filtering is shown in 15b.



(a) Visual representation of the two-dimensional Gaussian function



(b) Blurred image as a result of filtering

2.6 Acoustic Emission

2.6.1 Fundamentals of Acoustic Emission

Acoustic emission (AE) has been used as a non-destructive test method since the early 1960's, when Dunegan monitored pressure vessels using AE [63]. Acoustic Emission (AE) is a naturally occurring phenomenon where energy is released in the form of transient, elastic waves during irreversible changes in a material's internal structure, such as plastic deformation, phase transformation, and formation and propagation of cracks [63]. The elastic waves propagate through the material in four principal wave modes: longitudinal waves, shear waves, surface waves (Rayleigh waves), and in the case of thin specimens, plate waves (Lamb waves) [64]. AE is detectable once the elastic waves have travelled from the emission source to the surface of the specimen. The wave component perpendicular to the surface can be measured using a piezoelectric transducer, which converts the surface displacement produced by the wave into a voltage signal. The amplitude of the signal is small [65], so the signal must be amplified to be detectable. This is typically done in one or two steps: pre-amplification before entering the measuring system, and optional amplification before data analysis. Figure 16 shows a typical set-up of an AE system.

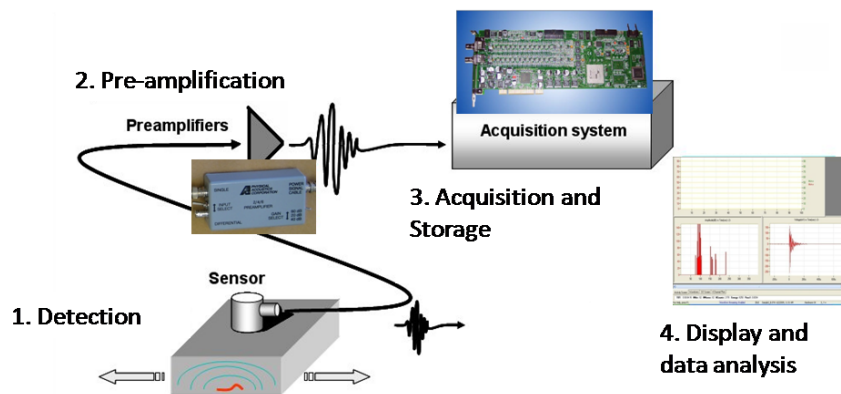


Figure 16: Typical elements of an AE system. Adopted from Haiyan Li, Jianying Li, Xiaozhou Liu, and Alex Fok. Non-destructive examination of interfacial debonding in dental composite restorations using acoustic emission. In Ning Hu, editor, *Composites and Their Applications*, chapter 7. IntechOpen, Rijeka, 2012. doi: 10.5772/51369. URL <https://doi.org/10.5772/51369>.

Two methods of performing AE monitoring exist; the traditional threshold-based method, and more modern waveform streaming.

In traditional measurements the voltage signal is continuously monitored, and if the amplitude of the signal crosses a certain threshold value, a "hit" is detected, and some parameters of the signal is recorded. These parameters could be the amplitude of the signal or the rise time, as shown in figure 17. Typically, two characteristic types of signals are detected. *Continuous signals* are an amalgam of multiple signal sources [67; 68], and have stable voltage amplitudes for long periods of time. These signals are associated with internal mechanisms like slip or phase transformation [65; 69], as well as external mechanisms like machine noise. *Discrete signals* are transient, and the signal sources are distinguishable from one another. Sources of discrete signals include crack formation and twin nucleation [63]. Accordingly, discrete signals can release order of magnitude more energy than continuous signals originating from the internal mechanisms [63; 70].

The most common discrete signal parameters are shown in figure 17 Where:

- *AE amplitude* - The largest amplitude of the signal
- *AE threshold* - The minimum value at which a signal is registered. The threshold should be high enough to remove background noise, but low enough to detect low-amplitude signals.
- *Time of hit* - The starting point of the signal count. This is where the signal first crosses the threshold.
- *Rise time* - The time it takes for the signal to reach its maximum amplitude from the hit time.
- *AE duration* - The total duration of the signal. Taken between the time of hit and the time when the signal falls below the threshold value for longer than the *Dead-time*.
- *AE counts* - Counts, or hits, are any signals that exceed the threshold value and stored as data.

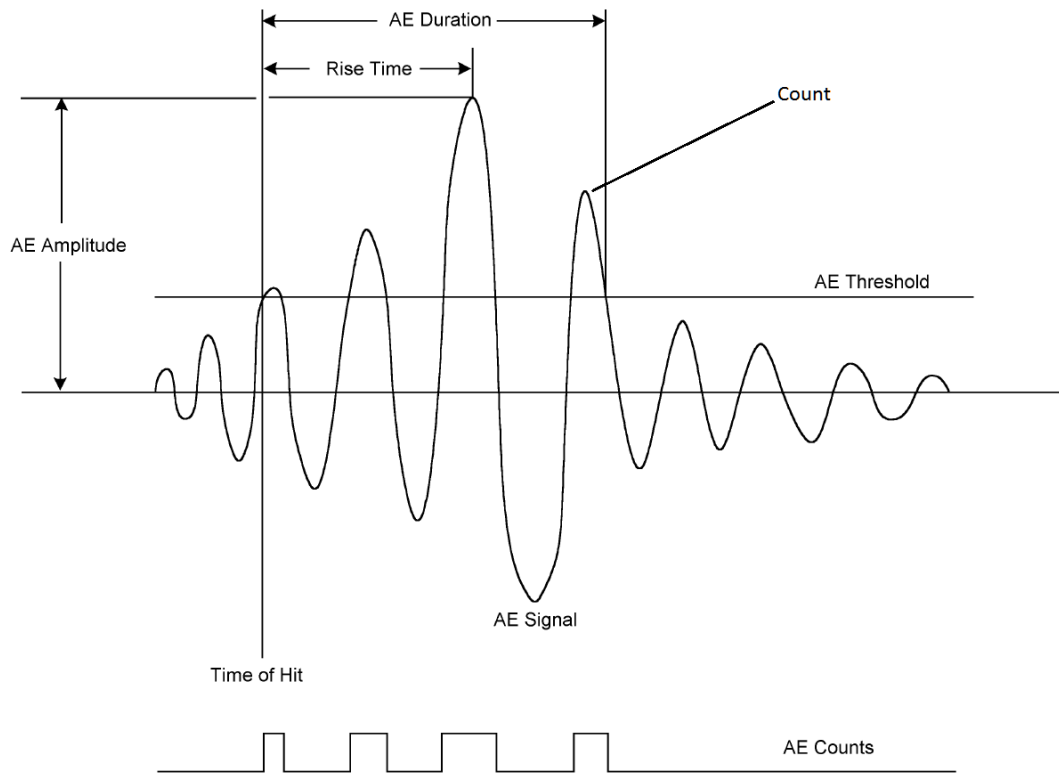


Figure 17: Common discrete signal parameters. Adopted from Physical Acoustics Corporation. *PCI-2 based AE system user's manual*. Physical Acoustics Corporation, 195 Clarksville Road, Princeton Jct., NJ 08550-5303, 2 edition, 10 2004.

Additionally there are some other common parameters not shown on the figure:

- *Dead-time* - The maximum time the signal can be below the threshold value before the signal is defined as ended.
- *Event energy* - The total energy of the event. Different formulations of the event energy exist, such as the area under the signal curve or employing the Root Mean Square (RMS). The absolute (electrical) energy is found by integrating the squared voltage signal over the instrument resistance over the entire event duration [72].

The other way of performing AE measurements is recording the voltage signal directly, through so-called *waveform streaming*, or *continuous streaming* in a threshold-less mode of operation [71]. In figure 17, this is equivalent to recording the AE signal, instead of just the AE counts. Waveform streaming avoids many of the drawbacks of the traditional method,

such as sensitivity to data loss due to improper setting of the experimental parameters like threshold value. Since the whole waveform is captured, it enables both new methods of data processing and more accurate determination of traditional AE parameters [63]. Low-amplitude signals which would be filtered out by the threshold level in traditional measurements can be analysed using waveform streaming [73], making AE more reliable and suitable for analysis of ductile materials. The main drawback of waveform streaming is the large size of the data files. For a single channel recording with a sampling frequency of 2MHz, file sizes of approximately 250MB/min can be expected [74]. For a fatigue test running for days or weeks, this becomes unreasonable. To circumvent this, periodically sampling for limited time intervals is typically done [71].

2.6.2 Acoustic emission from dislocations

Moving dislocations are considered as a major source of AE during plastic deformation. They contribute to both the continuous and transient signal, depending on the mechanism. An overview of some common dislocation mechanisms and how they typically influence the overall AE signal is given below.

The best-known source of AE is the collective motion of dislocations (i.e. dislocation slip) during plastic deformation, such as that in the localised plastic zone ahead of a crack tip. The passage of a dislocation causes a relaxation of the surrounding stress field, which releases AE. When the elastic wave reaches the surface, the associated surface vibrations can be measured as mentioned in 2.6.1. The signal strength is proportional to the surface displacement of the specimen, which can be approximated for dislocation loops in isotropic materials. For n_d dislocation loops, the peak surface displacement, a_n , becomes:

$$a_n = n_d b r_l v \frac{C_2^2}{DC_1^3} \quad (34)$$

Where b is the Burgers vector, r_l is the radius of a dislocation loop when it reaches the surface, v is the velocity of the dislocations, C_1 is the longitudinal wave speed, C_2 is the

shear wave speed and D is the distance from the surface. Heiple and Carpenter [65] calculated that for a polycrystalline aluminium alloy, the surface displacement for a single dislocation loop 4cm from the surface, moving at 200m/s would be 10^{-15} m, which is not realistically detectable. Only 1% of the released energy is in the form of detectable AE [65; 69], thus it is necessary to have the movement of thousands of dislocations in order to get reliable detection. Since the amplitude is dependent on the velocity, the strain rate is important, as they are related in the following manner:

$$\bar{v} = \frac{\dot{\epsilon}}{C_3 b \rho_d} \quad (35)$$

where \bar{v} is the average velocity of the dislocations, C_3 is a geometric constant, b is the Burgers vector and ρ_d is the dislocation density. Acoustic emission is therefore very weak in materials dominated by steady dislocation motion when measured during slow loading, and if measurable, associated with the continuous signal due to the overlapping events. That does not mean that the high-amplitude discrete AE cannot be generated by dislocation slip, however. Dislocation movement can be blocked by grain boundaries, inclusions, point defects etc., causing pile-ups. James and Carpenter [75] suggested that a stress increase at a few pinned dislocations could cause them to break away from their pins, producing a high amplitude stress wave. This stress wave could then unpin nearby dislocations, releasing more stress waves, and cause an avalanche of dislocation movement within a small volume in the material. This sudden release of a large number of dislocations could create a strong, discrete AE signal.

Dislocation annihilation is another source of low-amplitude AE. Heiple and Carpenter [65] described the calculations by Natsik and Chishko (1973, in Russian), estimating the elastic energy released during annihilation of a dislocation pair as:

$$E_{an} = \frac{\rho_d v^2 b^2}{8\pi} \ln \frac{l_c}{b} \quad (36)$$

Where E_{an} is the energy released during the annihilation, ρ_d is the dislocation density, v is

the relative velocity, b is the Burgers vector, and l_c is the characteristic size of the crystal. However, the energy released during annihilation is orders of magnitude lower than that for dislocation slip. It is therefore only under special circumstances, such as elastic twinning and the subsequent collapse of the twins, that dislocation annihilation produces detectable levels of AE [65].

One more source related to dislocations was associated a braking radiation during acceleration of dislocations. Kieseletter and Schuller [76] estimated the radiated energy released during emission of a screw dislocation from a Frank-Reed source. They assumed a periodic release of dislocations and used the energy radiation rate equation from Eshelby [77] with a frequency of $\omega_0/2\pi$:

$$E_{rad} = \frac{Gb^2l_d^2A^2\omega_0^4}{20\pi C_1^3} \quad (37)$$

Where G is the shear modulus, b the Burgers vector, l_d the dislocation length, $A = \frac{2\pi\bar{v}}{\omega_0}$ with \bar{v} being the mean dislocation velocity.

The brake radiation energy released during the entire period is then

$$E_{br} = \frac{2\pi E_{rad}}{l_d\omega_0} \quad (38)$$

For an aluminium alloy, the released energy was an order of magnitude lower than that for dislocation annihilation [63]. The contribution of braking radiation to the AE signal is therefore low in most cases. One should notice that this type of AE sources can be challenged since due to a large effective mass of dislocations, their acceleration/deceleration occurs withing a negligibly short time interval. The dynamic and relativistic effects associated with such processes are hard to account within a continuum mechanics approach. Instead, this is field of study by atomistic molecular dynamic simulations.

Deformation twinning is a very powerful source of AE [78]. The twinning process consists of three stages: nucleation of the twin embryo, rapid growth of the embryo to a macroscopic scale, and thickening of the twin in the direction normal to the initial growth direction [69].

The nucleation and growth of the twin embryo are rapid processes, and occur on the order of the velocity of sound in the material, while the thickening process is orders of magnitude slower, even under impact conditions [69]. Therefore, it is the twin nucleation process that is captured by the AE method, and not the lateral twin thickening.

A rough approximation of the surface displacement produced by nucleation of a single twin in a material with HCP structure, can be made by assuming that the dislocation reaction in equation 39 forms a pole source of twinning [79].

$$[0001] \rightarrow \alpha_t[10\bar{1}0] + [10\bar{1}0] \quad (39)$$

Where α_t is a fraction between $\frac{1}{12}$ and $\frac{1}{4}$. This is in fact equivalent to a Frank-Reed source where the screw dislocation is replaced with a twin. The surface displacement can thus be approximated as in equation 34. Máthis and Chmelík [63] estimated that for a twin of the size $40\mu\text{m}$ and a velocity of 2000m/s the surface displacement was $a_n = 10^{-14}\text{m}$, which is theoretically detectable. The equivalent calculation for twin growth (thickening), where the velocity was 10^{-3} m/s gave a surface displacement of $a_n = 10^{-22}\text{m}$ and therefore not detectable. Experimental results confirm that the emissions from macroscopic twin growth are at least an order of magnitude lower than nucleation and embryonic growth [69].

2.6.3 Acoustic emission related to cracks

Acoustic emission from crack related mechanisms has been studied experimentally for decades, and AE specific to crack initiation, crack extension and crack closure has been identified. Many empirical relations and qualitative explanations of the crack behaviour as it relates to AE have been developed, and some are described below.

Fracture mechanisms occurring during crack extension produce AE. The amplitude of the signal depends on the mechanism, with brittle fracture mechanisms producing higher amplitude signals than ductile ones [70; 80; 81]. Brittle fracture mechanisms include in-

tergranular fracture and cleavage/quasi-cleavage fracture. Ductile fracture mechanisms include micro void coalescence, tearing and shearing. Pollock [82] considered the elastic energy conversions of a system during crack growth for a characteristic ductile and brittle source event of equal magnitude. The difference in AE signal amplitude was explained by grouping the released energy into three groups: plastic deformation, surface energy and event energy (AE wave). The plastic deformation term captures the energy expended in creating the plastic zone, namely through dislocation movement and slip, while the surface energy refers to the disbonding of atoms to create the new surfaces. Pollock [82] argued that due to a larger plastic zone and increased surface energy due to a rougher crack surface, a lesser fraction of the converted (i.e. released) elastic energy is released as AE in a ductile fracture compared to a brittle fracture of the same magnitude.

During the 1970's, models and equations attempting to explain mechanisms causing AE were developed for a variety of scenarios. For the case of FCG, Morton et al.; Morton et al. [83; 84] found a correlation between AE count rate and SIF, equivalent to the Paris-Erdogan model. That is, a power law relation between AE count rate, $\frac{d\eta}{dN}$, and the stress intensity range, ΔK :

$$\frac{d\eta}{dN} = C_4(\Delta K)^n \quad (40)$$

Where C_4 is a constant and the exponent n is related to Paris' exponent, m , by the relation $n \approx m + 2$ as found by [80]. Lindley et al. [80] proposed that both energy released during crack extension, and deformation and fracture events within the plastic zone ahead of the crack, contribute to AE during fatigue crack growth. This is in line with the considerations in 2.6.2 and the review of Heiple and Carpenter; Heiple and Carpenter [65; 69], finding dislocation mechanisms, twin nucleation, and fracture of inclusions to be significant sources of AE. For a brittle material ($K_{IC} < 5\text{MPa}\sqrt{\text{m}}$), subcritical crack growth is near non-existing, and the crack propagates rapidly by brittle fracture mechanisms. Thus AE detection is limited to a time interval shortly before failure. However, the AE signal has a high amplitude due to the rapid breaking of atomic bonds [70].

For materials with a fracture toughness between 15 and 50MPa $\sqrt{\text{m}}$, such as high strength aluminium, and steel, there is significant subcritical crack growth before fracture, and thus AE. For these materials the crack can propagate by brittle mechanisms, or ductile mechanisms such as tearing, alternating shear or coalescence of voids [85]. The acting fracture mechanisms appear to change as the SIF (or SIF range) increases, causing the acoustic emission stage 2 crack growth stage to be split into two sections, 2a and 2b, characterised by a sudden increase in count rate at a SIF (range) of $(\Delta)K_o$ [70; 86]. This has been attributed to the beginning of microcleavage [70]. The power law relation in equation 40 does not account for this effect, but can be modified by making a bi-power law with one exponent for each slope.

For low strength materials with high fracture toughness, the ductile fracture mechanisms are dominant; the acoustic emission is therefore very weak, sometimes barely crossing the threshold amplitude [70]. For some materials, like AISI 316L steel, a sudden change in the count rate during the stage 2 crack growth can be observed just like for medium-toughness materials. However, the effect acts in reverse for the ductile material. AE in stage 2a is higher than for stage 2b. Moorthy et al. [86] proposed that this was due to the decrease in dislocation formation and movement due to the transition from plane strain to plane stress condition, which leads to a reduction in the cyclic plastic zone size [87]. Since the ductile fracture mechanisms produce such weak AE, this leads to a highly reduced count rate in stage 2b.

Acoustic emission can be produced during crack closure due to several mechanisms. These include such mechanisms as: rubbing of the crack faces due to local compressive stresses from plastic deformation, friction between jagged crack edges and rubbing or breaking of wedged oxides [80; 88–91]. Closure effects occur even at positive R-ratios [89]. This can be explained by the fact that plasticity can induce compressive stresses, effectively reducing the local stress level, while oxides and crack surface roughness create peaks and valleys in the crack faces which can contact. AE induced by crack closure is dependent on factors like material, environment and test frequency [89; 92]. The ductility of the material will

affect the roughness of the crack faces, and the susceptibility of a material to oxidation in a given environment will affect the presence of oxides in the crack region. According to [92], a higher test frequency increases the AE from crack closure. It was postulated that an increase in test frequency results in a more forceful closure, which would result in more severe rubbing between the crack faces.

Closure emissions are generally unwanted [88]. Several methods exist for reduction or removal of AE from crack closure. Since rubbing between the crack edges is partially responsible for AE from crack closure, applying a lubricant to the crack will reduce closure effects. Performing tests at a high R-ratio can reduce, if not remove, closure emissions. This will, of course, affect the test results. As mentioned, removing closure emissions by physical means will likely affect the test results in some manner. An alternative way is to filter the closure emissions by means of signal processing. Specific examples from literature are described in section 2.6.6.

2.6.4 Acoustic emission from miscellaneous sources

Phase transformations are another potential source of AE. During phase transformation, changes in the elastic modulus and material density causes a variable shape distortion, releasing AE [93]. While phase transformation normally occurs due to thermal changes during heat treatment etc., plastic deformation during cyclic loading can cause strain induced martensitic transformations in metastable materials like austenitic steels [85; 94]. Attempts to model and quantify the effects of phase transformation have been made by [93] and [95].

2.6.5 Source localisation using acoustic emission

One of the advantages of AE over other methods of Non-Destructive Testing (NDT) is the ability to locate the source of the damage in situ. This can be done in several ways, a common example being the Time Of Arrival (TOA) method [72]. In a setup using multiple

AE transducers, the TOA of the signal at each transducer can be utilised to triangulate the source location of the AE event. For 1D source location based on TOA, a simple setup based on two sensors as shown in figure 18, is common [96]. The sensors are placed a distance D_{1-2} from each other, and an AE source is located a distance d_{1-2} from sensor 1. The arrival time of the AE signal at sensors 1 and 2 is T_1 and T_2 , respectively. If the material is homogeneous, the wave velocity, V_w , is assumed to be constant. The distance between the AE source and sensor 1 is then:

$$d_{1-2} = \frac{1}{2}(D_{1-2} - (T_2 - T_1)V_w) \quad (41)$$

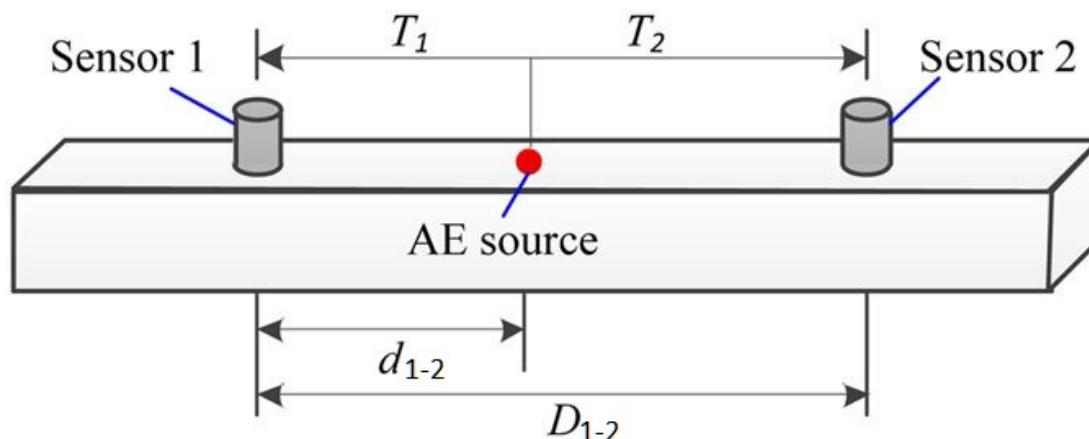


Figure 18: One dimensional source location, modified from Zi-long Zhou, Jing Zhou, Longjun Dong, Xin Cai, Yi-chao Rui, and Chang-tao Ke. Experimental study on the location of an acoustic emission source considering refraction in different media. *Scientific Reports*, 7, 2017. URL <https://doi.org/10.1038/s41598-017-07371-w>

With two AE transducers on a C(T) specimen, this can be used to locate the vertical position of the signal source. This means that signals originating from other locations than the crack (i.e. noise) can be filtered out. This can be difficult for specimens with small dimensions, however, since the TOA will be similar for both sensors regardless of the origin of the signal due to the small distances involved.

2.6.6 AE Signal Processing

The advancements in sensor technology and the computing power of modern computers have given rise to several new methods of processing data during the last decades.

Kim et al. [97] used an artificial neural network to perform stress intensity factor measurements from traditional AE parameters, and compared them to calculations done from CCD camera recordings. They found a good agreement between the predictions made by the artificial neural network and the experimental measurements.

Other researchers have attempted to move away from the traditional AE parameters. Chai et al.; Chai et al. [98; 99] and Tanvir et al. [100] explored the use of information entropy as an alternative to the typical AE parameters, arguing that information entropy is independent of test set-up parameters like threshold value or hit detection time. The premise of information entropy is that when an event has a low-probability value, it contains more information than when an event occurs which has a higher-probability value. The information content of events is therefore a stochastic variable where the expected value is its information entropy. In relation to AE, this refers to the voltage amplitude distribution of the recorded signal. In the constant presence of noises such as those from the test machine, a predictable voltage signal distribution is produced. Thus, an AE event will produce a significantly less probable distribution, and therefore information entropy. Different formulations of information entropy exists, the original being Shannon's entropy, as used by Chai et al. [99], and another example being Renyi's entropy [100].

Shannon's entropy is defined as:

$$H_S = - \sum_{i=1}^n p(x_i) \cdot \log_2(p(x_i)) \quad (42)$$

Where H_S is Shannon's entropy and p is the probability mass of the value x_i .

Renyi's entropy is a generalisation of Shannon's entropy, and defined as:

$$H_R = \frac{1}{1-a} \log_2 \left(\sum_{i=1}^n (p(x_i))^a \right) \quad (43)$$

Where H_R is Renyi's entropy, p is the probability mass of the value x_i and a is the entropy order. Due to the parameter a , Renyi's entropy is more flexible as a measure, as several measurements of uncertainty can be found within the same distribution[101]. It can be shown for the case of $a \rightarrow 1$, that Renyi's entropy equals Shannon's entropy[102]. From equations 42 and 43 it's obvious that any constantly present signal will be "absorbed" into the high-probability signal values. For the material used in this report, continuous type emissions account for the majority of the AE. This means that while predictable noise, e.g. machine noise, will produce a low entropy value, so too might the AE.

Máthis and Chmelík [63] discussed the capabilities of modern AE equipment and computer storage to store, and process, the raw AE signal using continuous signal sampling. In this manner, it is possible to run multiple analyses of the same raw signal, or compare a specific time frame with the overall data set. Loss of low-amplitude AE signals due to the setting of the threshold value is also potentially avoided by using continuous signal sampling [73]. Danyuk et al. [73] compared, for a case of low-amplitude AE signal, conventional AE measurements with continuous sampling, employing a wavelet block thresholding based algorithm to count AE events. They found a resemblance between the detections per loading cycle by the continuous sampling algorithm (300 ± 20) and manual counts by AE experts (420 ± 70), while the traditional method detected far fewer (16 ± 2). The low count rate of the traditional method was attributed to the low signal amplitude, the effect of the dead-time and the nature of the hit detection algorithms. Bhuiyan et al. [103] combined traditional AE measurements with finite element modelling and laser Doppler vibrometry to find a relation between crack tip resonance frequencies and crack geometry, suggesting a physics of materials based link between AE and geometric features of the crack.

An important part of processing the continuous waveform is extraction of the frequency content of the signal in the form of Power Spectral Density (PSD), i.e. the signal power

as a function of frequency. This can be performed in a similar manner to that described in section 2.5, except in one dimension. The DFT can be obtained using a Fast Fourier Transform (FFT) algorithm. A *periodogram*, estimating the PSD, can then be obtained by taking the square of the absolute value of the FFT. AE signals typically contain significant noise. This noise can be reduced by performing an averaging operation in addition to the FFT algorithm, trading frequency resolution for reduced variance (noise). A common way of doing this is employing Welch's method as an alternative estimator of the PSD [104]. Welch's method [105], is in principle just an average of periodograms across the sampling time. The signal is divided into overlapping data segments, and FFT is performed on each segment which is then averaged for the entire signal. By dividing the signals into smaller lengths, discontinuities are created, yielding artificial high-frequency artefacts near the edges of the segments, by nature of the DFT. This effect is negated by applying a *window function* to the signal, which is a class of normalising functions tapering from unity at its mean, to a low value at its edges. An important note with regards to using Welch's method is a side effect of the overlap. The point of the method is to reduce the variance of the FFT of a stochastic signal, but by adding an overlap, co-variance between the segments is introduced. Thus there is a limit to how much overlapping can be performed.

While the PSD is powerful, and reveals information about the signal's frequency content, it has no temporal resolution, akin to the time stream having no frequency resolution. For a stationary signal, this is not a problem. For analysis of AE, particularly of burst type signals, but also cyclic fluctuation in the continuous signal, this poses a significant shortcoming of the PSD as a tool for analysis. *Time-frequency analysis* allows for simultaneous study of the time and frequency domain. Several techniques exist for time-frequency analysis, a basic method being Short-Time Fourier Transform (STFT) and an advanced method being the *Wavelet transform*. The discrete-time STFT is performed by partitioning the time-series into overlapping, windowed, segments and performing FFT on each segment under the assumption that the signal is stationary for the short time intervals [106]. Mathematically, the STFT has its basis in the DTFT from equation 29, and can be

defined as:

$$F_{\hat{n}}(\omega) = \sum_{m=-\infty}^{\infty} f[m]W(\hat{n}-m)e^{-j\hat{\omega}m} \quad (44)$$

Where $W(\hat{n}-m)$ is a windowing function, \hat{n} is the (discrete) time index variable, and $\hat{\omega}$ is the (continuous) frequency variable. By keeping \hat{n} fixed, this is equivalent to:

$$F_{\hat{n}}(\omega) = DTFT(f(m)W(\hat{n}-m)) \quad (45)$$

It is easier in practice to consider the STFT such that the window function "slides" over the signal. The STFT can be rewritten as:

$$F_{\hat{n}}(\omega) = e^{-j\hat{\omega}\hat{n}}DTFT(f(\hat{n}+m)W(-m)) \quad (46)$$

Similar to in section 2.5.1, the STFT will in practice be sampled using a finite number of samples:

$$F_{\hat{n}}(\omega) = e^{-j\hat{\omega}\hat{n}}DFT(f(\hat{n}+m)W(-m)) \quad (47)$$

The full STFT is then found as the summed transforms for each time index:

$$F(\omega) = \sum_{\hat{n}=0}^{N-1} F_{\hat{n}}(\omega) \quad (48)$$

While the STFT yields information in both time and frequency domains, it has a significant limitation in practice due to the windowing. In order to achieve a high frequency resolution, it is necessary to observe the signal for a long time (wide window, or few time indices). The temporal resolution can then at most be equal to this "exposure time". Thus, in order to increase the temporal resolution, the exposure time will have to be lower (narrower window, more time indices), but this will result in a lower frequency resolution since the order of sines and cosines will be lower [106]. As the window length goes to infinity, the STFT will approach the FFT of the signal. Likewise, as the window length goes to 0, the STFT approaches the time-stream. The phenomenon is illustrated in figure 19. As can

be seen, the absolute resolution is the same, regardless of time or frequency focus, and is limited by the Gabor-Heisenberg limit.

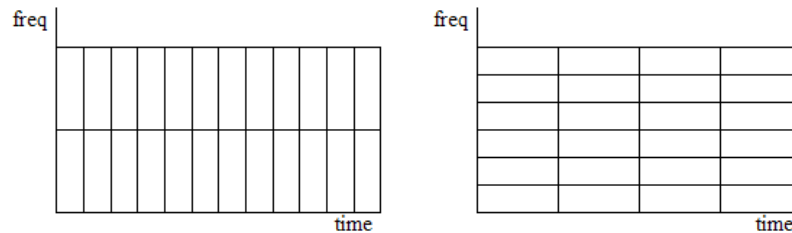


Figure 19: Narrowband (high time-resolution) vs wideband (high frequency-resolution) STFT. Adopted from Wikimedia Commons. Stft windows, 2005. URL https://en.wikipedia.org/wiki/Short-time_Fourier_transform/media/File:STFT_-_windows.png.

Common to many of the aforementioned approaches to AE signal processing, is the use of cluster analysis to identify distinct sources of AE [73; 98; 99; 103; 108; 109]. Cluster analysis consists of grouping a data set such that the data in each group, or cluster, are more similar to each other compared to the other clusters Everitt et al. [110]. Cluster analysis is general term, and a plethora of algorithms exist to achieve the clustering. Some examples include *K-means clustering*, *mean-shift clustering* and *Density-Based Spatial Clustering of Applications with Noise (DBSCAN)*. *k-means* clustering is a widely used clustering algorithm [110]. The algorithm tries to divide the data set into k clusters, where each data point is part of the cluster with the nearest mean value to the data point. Different methods exist for implementing *k-means* in practice, such as *Lloyd's* algorithm and the improved *k-means++* algorithm. *k-means++*, as developed by Arthur and Vassilvitskii [111], can be implemented as follows:

1. Choose an initial cluster centroid c_1 uniformly at random from the data set, X
2. Calculate distances $d(x_j, c_1)$ from each data point x_j to c_1 Choose the remaining centroids c_i such that c_i is selected at random from X with probability

$$\frac{d^2(x_j, c_i)}{\sum_{t=1}^n d^2(x_t, c_i)}$$

3. Centers t are chosen as:

- (a) Calculate the distance from each data point to all centroids, and then assign the data point to the closest centroid.
- (b) Choose centroid t at random from X with probability

$$\frac{d^2(x_t, c_i)}{\sum_{m; x_m \in C_i} d^2(x_m, c_i)}$$

with C_i being all data points which have the closest centroid as c_i . In other words, the centers are chosen randomly with a probability proportional to the distance between themselves and the closest center already selected

- 4. Repeat previous step until the centers no longer change, or maximum number of iterations is reached.

This implementation of *k-means* is quite simple, and computationally fast, making it an attractive choice of clustering. However, since *k-means* relies on centroids and the data's distance from a center, it fails to identify oddly shaped clusters, e.g. "snakelike", which can frequently occur using AE monitoring. There is also the drawback of having to pre-select the number of clusters when using *k-means*. To improve the accuracy of the clustering, more advanced algorithms such as *mean-shift clustering* or *DBSCAN* might be used.

It is clear that the research has gone in the direction of utilising continuous signal sampling and the capabilities of modern computers to perform advanced computer simulations and signal processing. Merging this with traditional parameters, as was done by Danyuk et al. [73] and by Kharrat et al. [112], allows comparisons with, or improvement, of previous work.

3 Methodology, materials and experimental setup

3.1 Specimens

3.1.1 Material

The material used to make all test samples used in this work was AISI 316L stainless steel. The typical chemical composition, and material properties are summarised in table 3. The excerpt from the material certificate is attached in the appendix as figure 200.

Chemical Composition [wt.%]											
	C	Si	Mn	P	S	Cr	Mo	Ni	Cu	Ti	N
Min.	-	-	-	-	-	16.50	2.00	10.00	-	-	-
Max.	0.030	1.00	2.00	0.045	0.030	18.50	2.50	13.00	-	-	0.1100
Actual	0.024	0.50	1.75	0.035	0.017	16.89	2.02	10.02	-	-	0.0520
Mechanical Properties											
Yield Strength (0.2%) [MPa]	Tensile strength [MPa]		Elongation at fracture [%]			Hardness [BHN]					
308	612		53			174-177					

Table 3: Chemical composition and mechanical properties of AISI 316L

The material certificate does not contain the proportionality limit, the Poisson's ratio, or the elastic modulus. These values were found while performing tensile tests and are presented in section 4.3.3.

3.1.2 Tensile specimen

Specimen shape and dimensions

The specimen shape, as well as dimensions are shown on figure 20. The shape was based on the standard, subsize, sheet-type test specimen shown in figure 1 in ASTM E8/E8M-16a [113]. Limitations arriving from capabilities of the testing machine and extensometer when performing the tests required reduction in gauge length, however, most of the dimensions followed the standard.

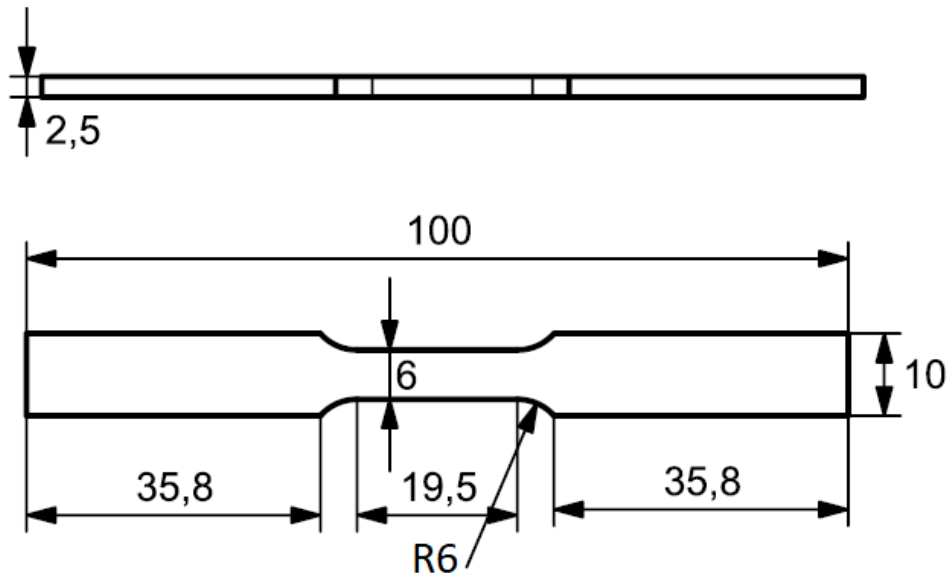


Figure 20: Tensile specimen with dimensions

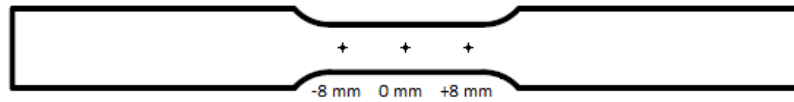


Figure 21: Points where the thickness of samples was measured

During calculation of stresses, the width of the narrow section of tensile specimens was assumed to be equal 6 mm since the edges were not polished after machining. The specimen thicknesses were measured in 3 different places on the area with reduced cross-section; on the middle of the sample, and at the distance of ± 8 mm from the middle of the sample. Points where the thickness was measured is presented on figure 21, while the values measured are presented in table 4.

Specimen nr.	1	2	3	4
Thickness at -8 mm	1825 μm	1830 μm	1800 μm	2325 μm
Thickness at 0 mm	1825 μm	1825 μm	1788 μm	2340 μm
Thickness at +8 mm	1805 μm	1795 μm	1774 μm	2345 μm

Table 4: Thicknesses of the tensile specimens

Specimen preparation

The tensile specimens were made on the CNC-milling machine, and required finishing after the machining. Since the specimens were manufactured by a third party, the authors had no control on the quality of machining, and there were some suspicions that milling with rapid tool movement could introduce imperfections in the sample, or even affect the microstructure. For this reason grinding on metallographic grinding machine was carried out. About 200 μm of the thickness from each side was removed in order to ensure that machining had no influence on the results. The thickness of the samples after first grinding was around 2.1 mm. During the preparation to the test it has been found that the test machine capability is 7 kN instead of 10 kN, and the specimen thickness had to be reduced with additional 0.3 mm in order to reach expected ultimate tensile strength of the material. The final thickness of the sample after additional grinding was approximately 1.8 mm, more accurate values are presented in table 4. The test samples were painted with speckle pattern in order to record the test and analyse the results with DIC software.

3.1.3 C(T) specimen

Specimen shape and dimensions

All test samples for FCG used were so called compact tension (C(T)) specimens, and were made according to ASTM E647-15 [114] standard. Specimen shape and explanation of symbols are shown in figure 22. All dimensions are listed in table 5. Although the thickness B should be 5 mm, its value used in calculations deviated from the value given in the table. Specimens were machined according to table values, but they were ground in order to remove traces after milling, and the thickness was reduced to around 4.85 mm. The real, measured thickness has been used in calculations instead of the table value of 5 mm. The stress intensity factor K for C(T) specimen was found using the following

formula:

$$K = \frac{P}{B\sqrt{W}} f\left(\frac{a}{W}\right) \quad (49)$$

Where P is the applied load, B is thickness, f is the calibration factor, a is the crack length and W is the specimen length. The calibration factor is a function of a/W -ratio, and can be calculated by using equation 50.

$$f\left(\frac{a}{W}\right) = \frac{\left(2 + \frac{a}{W}\right)\left(0.886 + 4.64\left(\frac{a}{W}\right) - 13.32\left(\frac{a}{W}\right)^2 + 14.72\left(\frac{a}{W}\right)^3 - 5.6\left(\frac{a}{W}\right)^4\right)}{\left(1 - \left(\frac{a}{W}\right)\right)^{3/2}} \quad (50)$$

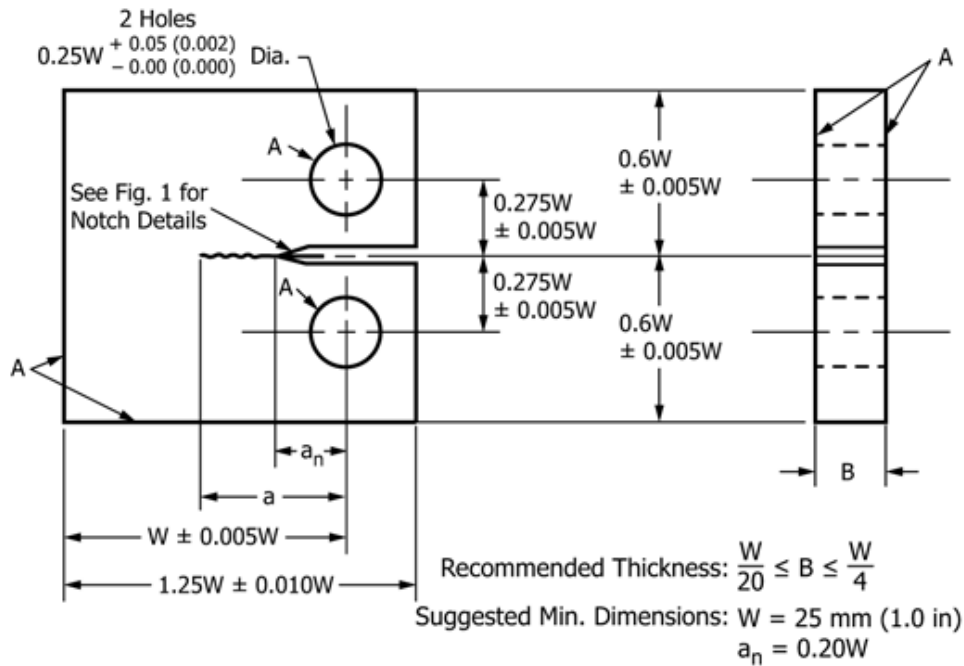


Figure 22: Standard Compact C(T) Specimen for Fatigue Crack Growth Rate Testing, adopted from: E647-15e1. Standard test method for measurement of fatigue crack growth rates. Standard E647-15e1, ASTM International, West Conshohocken, PA, 2015. URL <https://doi.org/10.1520/E0647-15E01>

W	W_1	B	L	D_1	a_{notch}
30 mm	37.5 mm	5 mm	36 mm	7.5 mm	6 mm

Table 5: Dimensions of the specimen

Specimen preparation

The samples had to be post-processed after machining to satisfy the requirements of the different methods used. IRT required grinding to remove scratches and matte black paint on one side of the specimen, while HSI-technique required different types of surface finish depending on the type of data to be acquired. For qualitative observation of crack propagation, a mirror-like polished and eventually etched surface was of interest. For DIC-analysis the pattern of random features (speckles) was desirable as mentioned in section 2.4.3, and thus the black-white painting was applied. During the testing it has been found that black-white painting is too coarse for DIC purposes when the size of FOV is less than $1 \text{ mm} \times 1 \text{ mm}$. New attempt for preparing random pattern was made, this time etching the polished sample in etchant for 1 minute. It gave rough surface with random features that could be used for DIC at much smaller scale. Both types of random pattern can be seen at figure 24. Grinding and polishing was carried out on metallographic grinding and polishing machine. For qualitative analysis with high-speed imaging, the specimens were ground, polished and eventually etched with etchant containing $\frac{1}{3}$ HCl, $\frac{1}{3}$ HNO₃, and $\frac{1}{3}$ H₂O. The specimens were submerged in Petri dish containing etchant for about 20 second or 1 minute depending on the purpose and immediately rinsed with ethanol after etching. The procedure for etching was inspired by ASTM E407-07 [115]. The results of polishing and etching are presented in figure 23. All steps of specimen surface preparation are listed in table 6. Index in parenthesis in the table correspond to average abrasive particle diameter.

Step nr.	Purpose		
	Mirror-like finish	IR-imaging/DIC	DIC
1	Grinding P80 ($200\mu m$)	Grinding P80 ($200\mu m$)	Grinding P80 ($200\mu m$)
2	Grinding P120 ($125\mu m$)	Grinding P120 ($125\mu m$)	Grinding P120 ($125\mu m$)
3	Grinding P220 ($68\mu m$)	Grinding P220 ($68\mu m$)	Grinding P220 ($68\mu m$)
4	Grinding P360 ($40\mu m$)	Grinding P360 ($40\mu m$)	Grinding P360 ($40\mu m$)
5	Grinding P500 ($30\mu m$)	Grinding P500 ($30\mu m$)	Grinding P500 ($30\mu m$)
6	Grinding P1000 ($18\mu m$)	Grinding P1000 ($18\mu m$)	Grinding P1000 ($18\mu m$)
7	Grinding P2000 ($10\mu m$)	Grinding P2000 ($10\mu m$)	Grinding P2000 ($10\mu m$)
8	Polishing ($3\mu m$)	Matte black/white painting	Polishing ($3\mu m$)
9	Polishing ($1\mu m$)		Etching (1 minute)

Table 6: Specimen surface preparation

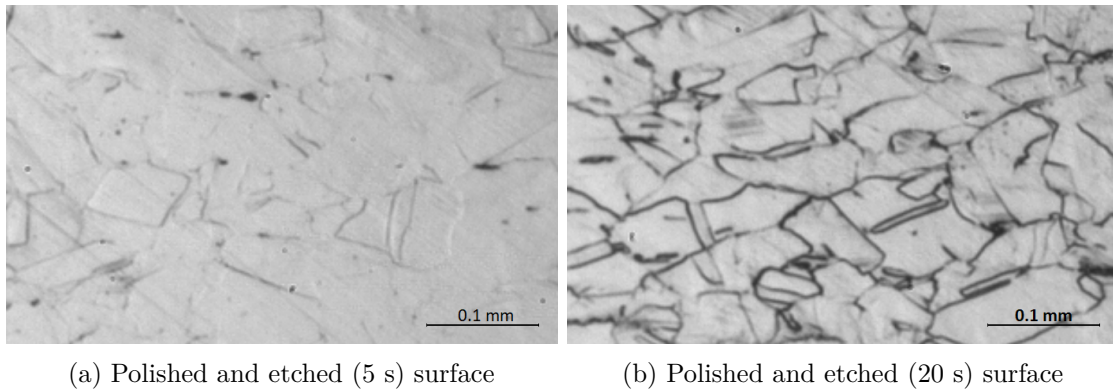


Figure 23: The specimen surface seen with the high-speed camera

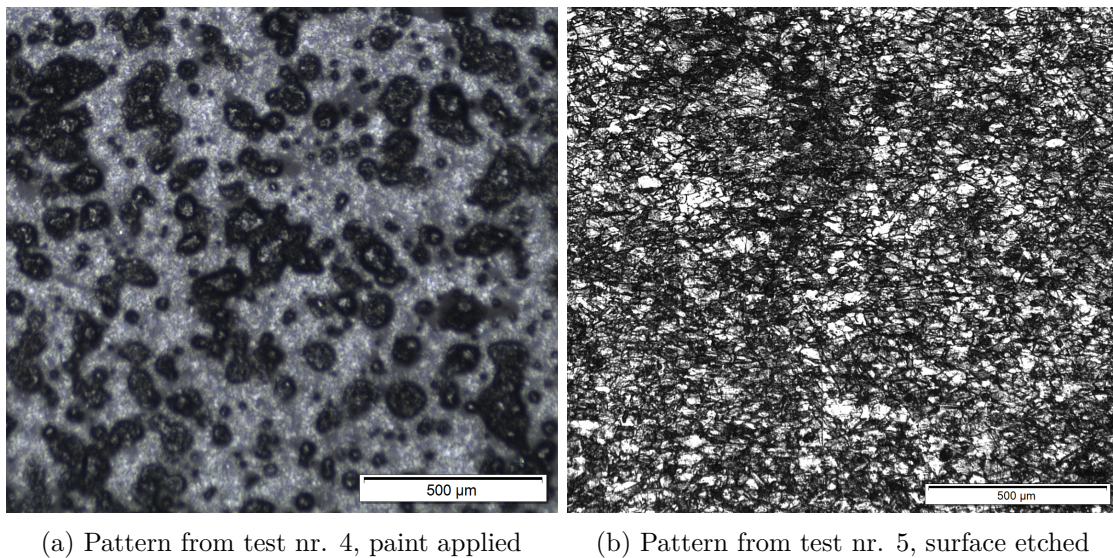


Figure 24: Random pattern used for DIC-analysis

3.2 Equipment and software used

3.2.1 Infrared thermography

IRT was performed using a Telops FAST M350 mid-wave, high-speed IRT camera, with an operating spectral range of 1.5 μm to 5.4 μm . The photodetector was of the indium antimonide (InSb) type, with a typical NETD of 20mK. The camera had a resolution of 640x512 pixels, and a maximum frame rate of 355fps. The internal memory of the camera was 16GB, with the possibility of direct transfer to an external drive. The camera was statically mounted on a tripod directly facing the test specimen. A IRC-LENS-G1-MW 1X microscope objective operating in the range of 3-5 μm and with the working distance of 26cm was used. The camera was operated using the Reveal IR software version 1.3.5. Cameras internal memory was used with a Moment Of Interest (MOI) set to external trigger.

The frame rate was set to 130 fps. A testing frequency of 10Hz gave 13 samples per cycle. Ideally, the higher frame rate would give a better representation of the sine formed temperature variation in the sample due to the thermoelastic effect, but it requires lower exposure times and increased noise. If the temperature amplitude would be calculated from maximum temperature difference with time, which is reasonable for the amount of data to process, assuming an ideal sine wave sampling rates give a worst case temperature amplitude error of under 3%, but due to the chosen sampling frequency and test frequency, the error was practically halved, as explained in section 3.4.3. For temperature amplitudes as large as 1K this error is less than the typical NETD. The sequence size was set to 65 frames corresponding to recording 5 cycles at every trigger, respectively. The camera was set up with automatic exposure control, to reach a well filling level of 60% for 90% of the sensors.

3.2.2 High-speed imaging and DIC

Hardware

In this work all rapid video imaging, and collecting data for DIC analysis was performed employing the Photron FASTCAM SA-Z 2100K CMOS high-speed camera. Depending on purpose, the high speed camera was equipped either with macro-, or microscope lens. When performing FCG tests, the Navitar microscope lens system was used, more precisely the Navitar 12X Zoom Lens System optics. This included Navitar 2X F-Mount 1-62922 adapter, 3mm F.F. zoom lens and optionally 2X 1-50015 lens attachment. Unfortunately, there was not possible to adjust the aperture in this system. In FCG tests, the camera used an external light source connected to the zoom lens. For this purpose the Hayashi LA-HDF 7010RL LED light source was used, providing up to 1800000 lx illuminance. When performing the tensile tests a larger FOV was required, and the Tamron 90mm f/2.8 SP AF Di macro lens was used then. Use of the high-speed camera in the tensile test was not necessary due to the relatively low strain rate ($\dot{\epsilon} = 0.002\frac{1}{s}$), conventional digital camera could be used instead, but due to the equipment compatibility and pace of change in setup it has been decided to use high speed camera anyway. The HSI camera used in this work has a limitations when filming with the low frame rate, the maximum exposure possible is 1/10000 second, leading to increased light demand in order to get a satisfactory images. During the tensile tests, a single HSI LED-lighting was used to provide sufficient illumination.

Photron FASTCAM SA-Z CMOS camera is capable of image recording with frame rate of 2'100'000 fps at the reduced resolution 128×8 pixels. The shortest shutter speed of this high-speed camera is of 1/6'300'000 s, this is of special interest while filming at very high frame rates. Such a fast shutter is useful when observing rapid phenomena that as crack development. Authors of earlier papers as Fukui et al. [116] had to deal with the long shutter speed (1/1000 s) forcing a reduced frequency of the fatigue testing machine of 0.1 Hz for observing opening-closing behaviour when performing FCG test. Modern CMOS

and CCD cameras as Photron SA-Z are able to overcome temporal resolution problems due to their shutter speed and frame rate capabilities.

Photron FASTCAM SA-Z 2100K			
Resolution	Frame Rate	64GB	
(h x v pixels)	Max fps	Frames	Time (sec)
1024 x 1024	20000	43682	2.18
1024 x 1000	21000	44731	2.13
1024 x 840	25000	53251	2.13
1024 x 512	40000	87367	2.18
640 x 488	60000	146663	2.44
512 x 456	75000	196195	2.62
640 x 280	100000	255615	2.56
512 x 256	120000	349475	2.91
384 x 176	200000	677772	3.39
512 x 56	480000	1597608	3.33
384 x 64	525000	1863877	3.55
256 x 56	700000	3195219	4.56
128 x 56	900000	6390440	7.10
256 x 24	1008000	7455514	7.40
128 x 32	1200000	11183272	9.32
128 x 8	2100000	44733096	21.30

Table 7: Frame rate, image resolution and memory capacity summary (from Photron FASTCAM SA-Z Datasheet)

Since the width of the FOV of interest was much smaller compared to the expected crack length, especially right before fracture, there was a need to move the camera as crack propagated. To be able to create fatigue crack propagation curves (Paris curves), there was also a need to measure the crack length very precisely. To simplify these two tasks, a Thorlabs LNR50SE motorized translation stage was brought. The translation stage is equipped with precise stepper motor and the optical encoder. It has a travel range of 50 mm sufficient for the most FCG tests. It has also minimum step size of 0.05 μm , and a backlash less than 6 μm . In addition, the stage has sufficient load capacity to handle weight of Photron FASTCAM SA-Z with lens attached, and has compatibility with *MATLAB* where a camera position can be logged during the test. Together with controlling software, the Thorlabs LNR50SE translation stage provides precise adjustment of the high-speed

camera position despite the camera weight.

Software

The high-speed camera was controlled by the *Photron FASTCAM Viewer* software installed on the controlling laptop computer. The software provided the control of camera as well as data saving, image enhancement and playback. In this work, the dataset from high-speed camera was saved either as uncompressed AVI video data, or as a series of 8-Bit TIFF images. The visual data in this work is obtained in grayscale, due to the reduced light demand compared to the RGB image [33] and its ease in post-processing in *MATLAB*.

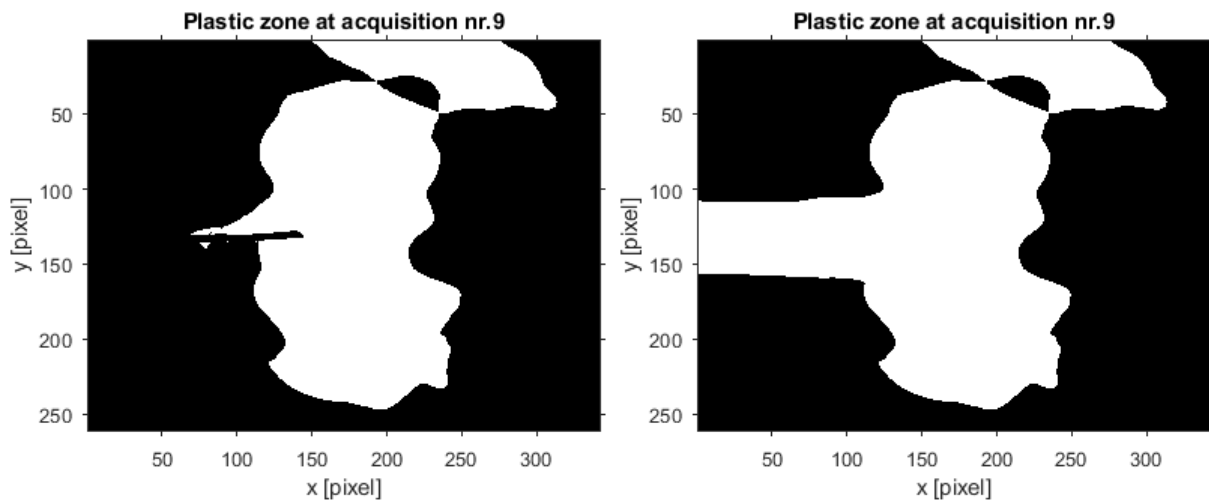
The DIC analysis in this work was performed using *Ncorr* open-source 2D-DIC program. This is a subset-based *MATLAB* program, in this work used together with *MATLAB R2018a* and *MATLAB R2019a* without any issues. More details about subset-based DIC algorithm can be found in section 2.4.3. The software has been developed by Blaber et al. [53], the result comparison with commercial DIC software has been performed by Harilal and Ramji [117]. The software has also been used for FCG experiments by others [1]. This software has advantages as being open source, and *MATLAB* based action. After analysis the displacements, and the strain fields are easily available in form of a structure array (struct) with 2D arrays of data which makes it easy to post-process the DIC results directly in *MATLAB*. For the best results, the authors of this work followed strictly the manual available on the *Ncorr* authors web page [118]. There is also an open source DIC Post-Processing Tool for *Ncorr*, *Ncorr_post* developed by Nežerka et al. [119]. However, there were several issues connected to compatibility of this tool with new versions of *MATLAB* while implementing, and it was only used for checking the reasonability of the results obtained using own made codes.

Choice of parameters in DIC analysis

In following, the considerations about influence of different parameters in DIC analysis will

be presented. There are three main DIC parameters that have a significant influence on quality of results obtained in *Ncorr*: subset radius, subset spacing and the strain radius. The main idea when choosing the subset radius is that the user should select the smallest possible subset radius (in pixels) which does not result in noisy displacement data. This may require trial and error, it's also important to mention that large subset tend to have a smoothing effect on the displacement fields. Software developer claim that the subset spacing is purely for reducing the computational load. Since the computational power of hardware used for the analysis was not a problem, the subset spacing was always set to its minimum, also 1. The last important parameter is the strain radius. As it can be seen on figure 26, the strain radius is crucial in order to remove noise and has greater influence that the subset radius. Strain radius should be selected as small as possible as long as it does not result in noisy strain data. Another important aspect when running the DIC analysis on cracked specimens with Region Of Interest (ROI) excluding the crack, is that user has to activate the subset truncation function, which is a feature that prevents subsets from wrapping around the crack tip. Subset wrapping may cause distortions in both displacement and strain fields near the crack tip. In this work, the plastic zone analysis was performed using the subset radius of 25 pixel, the subset spacing of 1 pixel and the strain radius of 20 pixel. Bitmap with the approximate plastic zone resulting from this choice of parameters is represented in the right-lower corner in figure 26. The analysis of the tensile tests and Crack Opening Displacement (COD) analysis was performed with the subset radius of 15 pixel, subset spacing of 1 pixel and strain radius of 15 pixel. In opinion of authors of this work, these parameters provide the optimal (highest possible) precision without obtaining noisy strain and stress fields. More details about the DIC algorithm can be found in section 2.4.3, more information about software and manual is to be found on its authors web page [118]. Another aspect that may have an influence on the size, and the shape of the plastic zone is the ROI used in the stress analysis. The plastic zone analysis in this work is based on papers by Vasco-Olmo [58] and Gao et al. [1]. Vasco-Olmo [58] doesn't mention anything about the shape of the ROI used in DIC analysis, but from the figures in the paper it follows that the crack was not excluded from ROI when

running the analysis. The lack of crack excluding can be clearly seen by presence of a kind of tail with large stresses present behind the crack tip when looking at stress maps and the plastic zone. This happens because the local strains across the crack are quite large. Gao et al. [1] have excluded the crack making the ROI in their work. Based on experience of mentioned authors, a comparison between the plastic zone using two different ROI has been done. Figure 25 presents results for two different ROIs. The left figure present zone where the crack was excluded from ROI, it can be seen that the white zone of plasticity is limited to the middle of the FOV. The right one presents the results where the ROI didn't exclude the crack, here the mentioned tail is visible behind the crack tip. However, the overall shape of both plastic zones is identical, and the only difference for given set of DIC parameters is a tail behind the crack tip which can be easily subtracted when calculating the size of the plastic zone. Since the manual creation of the ROI excluding the crack is time consuming, in this work the crack was uncovered and included in the ROI when running the DIC analysis.



(a) Crack excluded from ROI

(b) Crack included in ROI

Figure 25: Comparison of the plastic zone obtained using different ROIs

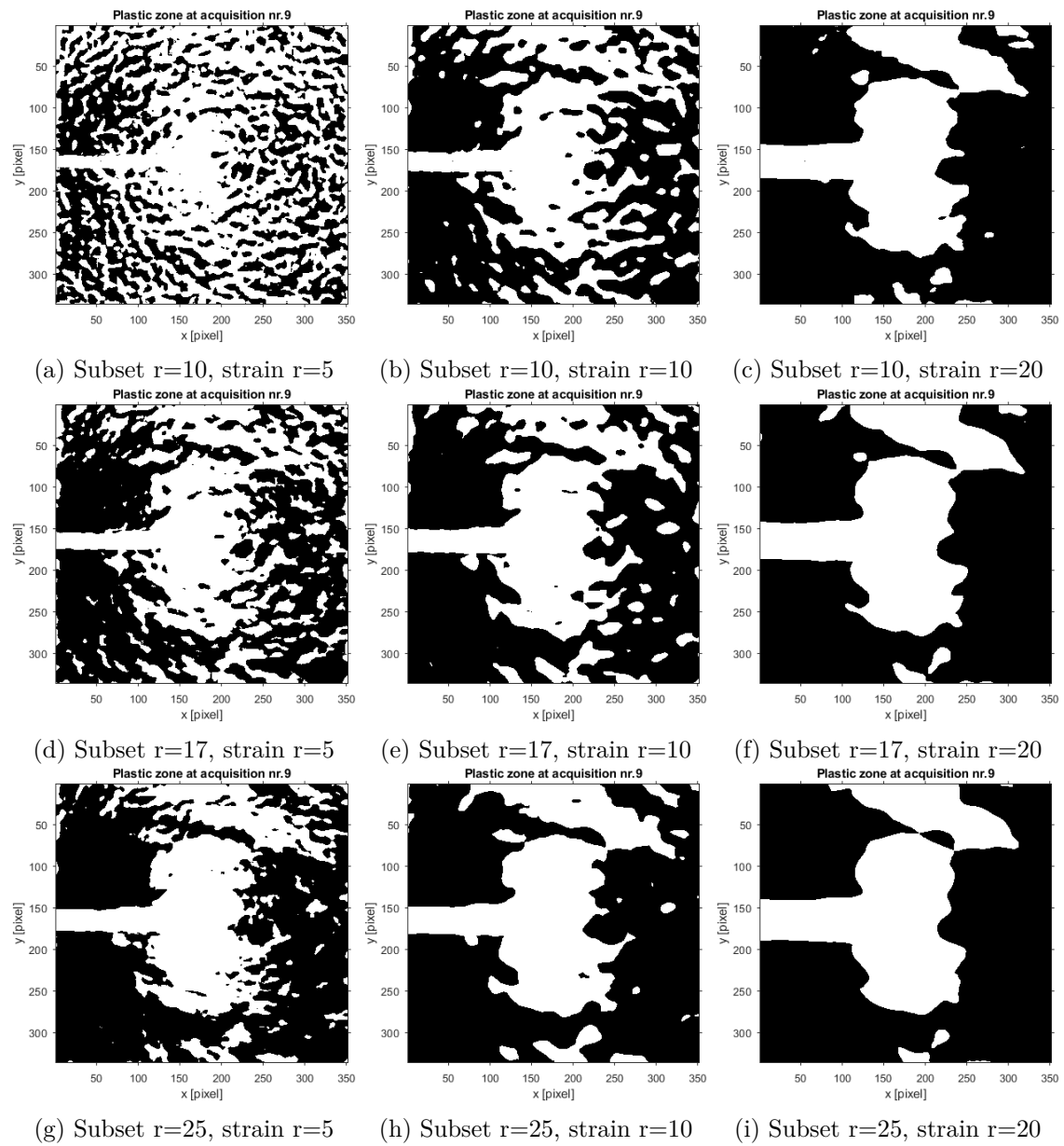


Figure 26: Comparison of the bitmap showing the area of the plastic deformation obtained using different DIC parameters

All post-processing of visual data and plotting the graphs from DIC analysis was performed using *MATLAB* if nothing else is specified.

3.2.3 Acoustic Emission

Fatigue crack growth

Acoustic emission monitoring of the fatigue crack propagation was performed using a glsPAC PCI-2 based system and the AEwin software. Two types of AE transducers were used: Physical Acoustics Corporation (PAC) Nano-30 resonant, wideband transducer and PAC Micro-30AE flat, broadband transducer. The Nano-30 transducers had resonance frequencies of 140kHz and 300kHz. The operating range of the Nano-30 transducers was 125kHz to 750kHz, and 150kHz to 750kHz for the Micro-30. The transducers were attached to the top and bottom of the specimens using custom 3D-printed clip-on devices, ensuring a consistent grip pressure across multiple tests, without blocking the view of the cameras. To provide a good acoustic impedance match, *Molykote BR2 Plus* grease was applied between the specimen and Nano-30 transducers. For the Micro-30 transducer, oil-soaked paper was used instead, as further electrical insulation was necessary. Each transducer was connected to a PAC 2/4/6 pre-amplifier, with a fixed gain set to 60dB. Band pass filters integrated in the pre-amplifiers were used, which were set to a range of 20kHz to 1000kHz. No gain was applied in the software, for a total gain of 60dB.

Electromagnetic interference (EMI) was a significant issue during early set-up and noise identification. Ensuring complete electrical isolation of the AE system from the test machine and other sources of EMI was therefore imperative. This was achieved in multiple steps. The electrical ground of the AE system was separated by using an isolation transformer. The C(T) was isolated from the test machine by the use of PTFE bushings between the grips and the specimen holes. The AE transducers were further isolated from the specimen by the combined effect of the Molykote grease or oiled paper, and the ceramic disk integrated into the transducers.

In the AEwin software, two AE-channels were enabled, one for each transducer. Default hit definition parameters were used: Peak Definition Time (PDT) of 300 μ s, Hit Definition

Time (HDT) of 600 μ s and Hit Lock-out Time (HLT) of 1000 μ s. Hit waveforms were stored for each hit, with recording sizes of 1K samples for Test 4 and 5, and 2K samples in Test 6. For Test 4, there was no pre-trigger recording, while for the remaining tests, a pre-trigger length of 256 samples was used, due to experiencing truncation of hit waveforms during Test 4. One dimensional source location was attempted using the linear source location option in AEWin[71], functioning similar to the method described in section 2.6.5. Wave propagation properties were found from the internal database entry for AISI 316L, which was assumed to be valid.

Waveform streaming was enabled for all tests, but with varying streaming parameters. For Test 4, single channel waveform streaming was enabled using the top Nano-30 transducer, with a sampling frequency of 2MHz. The recording size was 2000K samples, none of which were set to pre-trigger, resulting in a recording length of 1024ms. To trigger a recording, an external trigger signal sent from the Arduino system described in section 3.3 was used. For Test 5, waveform streaming was enabled for both the top transducer (Micro-30) and bottom transducer (Nano-30), with sampling frequency of 2MHz. The recording size was 12000K samples, with a pre-trigger length of 0, resulting in a recording length of 6144ms. Triggering was achieved using an analogue output from the test machine. In Test 6 waveform streaming was enabled for both transducers in the same manner as Test 5, but with recording parameters like in Test 4. Triggering was also done using the method of Test 4.

3.3 Triggering of the equipment

3.3.1 Hardware

To gain knowledge about the crack length analysed from the cameras and the corresponding cycle, the cameras had to be triggered at a known cycle. Additionally, trigger on a given load level was essential when capturing crack closure effect or the peak load with the rapid

video imaging, and for determination of AE source mechanisms. Since generation of a trigger pulse with the testing machine has limitations, as the waveform generation has to be stopped for a moment, and the machine takes some time to reach the wanted waveform again, a dedicated triggering system analysing the data from the load cell was developed instead.

The system was based on a Raspberry Pi 3B single board computer with Raspian, a Debian based operating system. The hardware was not equipped with an analogue to digital converter, so to overcome this issue, the processor was receiving a Boolean value from a ATmega328P microcontroller chip with a 16 MHz external oscillator about a threshold value of the load signal. The prescaling factor for the microcontroller was set to 128, it could be as low as 16, but 128 gives a theoretical sampling rate of approximately 9000Hz which is enough for a load frequency of 10 Hz, although depending on the code, the frequency changes. Benchmarking of the final code resulted in a sampling frequency of over 8900Hz. The algorithm analysing the signal was as follows:

- The load cell generated the sine-formed signal. The electric potential sent by a cell corresponds to the load and the load to potential ratio was predefined by user. The load is shown in figure 27 as the blue line.
- The microcontroller read the potential as the analogue signal, then it was converted to a digital value by Analog to Digital Converter (ADC). The ADC on the microcontroller used was a 10-bit converter meaning it had the ability to detect 1024 (2^{10}) discrete analogue levels.
- Lower and upper threshold values were selected by user. If the value received from the load cell surpassed the upper threshold, the microcontroller counted that event as a cycle and disabled the possibility for counting another cycle until the signal received load value which was lower than the lower threshold. The threshold values are illustrated as green and yellow line for the upper and lower threshold respectively in figure 27. This was because signal from the cell was not a perfect sine-wave and

this method disabled the possibility for counting the same cycle several times due to noise. Whenever a cycle was recognised, an edge signal was sent to the Raspberry Pi.

- The Raspberry Pi was set up with an interrupt, so whenever it received a signal from the microcontroller, it started a new thread where it immediately added the cycle to the total cycle count, and if the cycle number was right it told the microcontroller to trigger the equipment, seen as the red pulse in figure 27. The microcontroller might be programmed to introduce a delay in the signal if a trigger at a given point in the load curve is demanded.
- The trigger count and time of every trigger signal were logged in a file on a SD card.

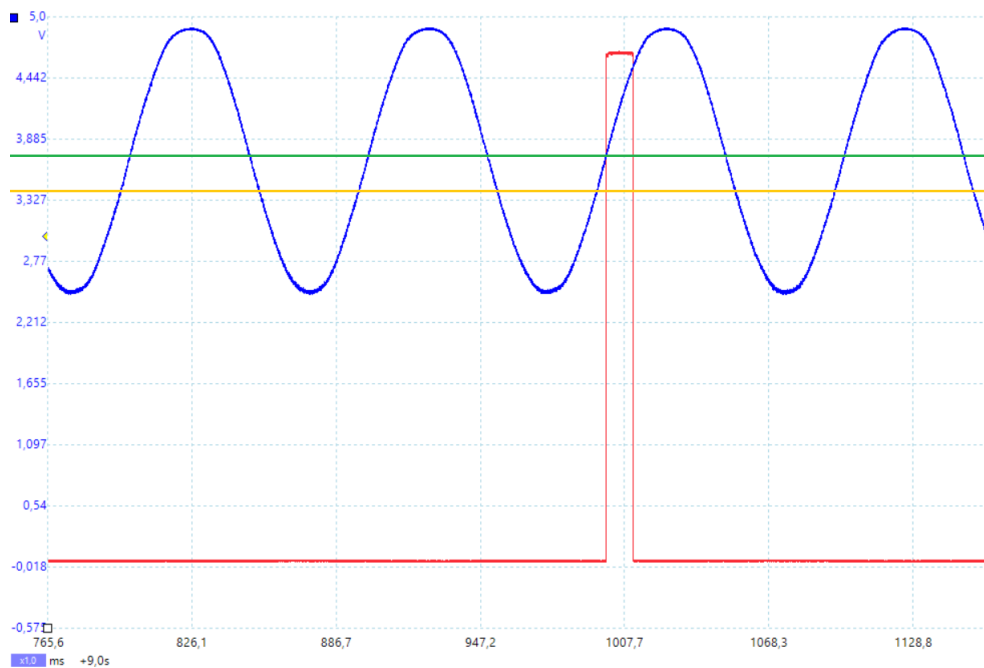


Figure 27: Figure showing the trigger algorithm

3.3.2 Software

The triggering system developed for the sake of this project had a graphical user interface, and the software was programmed in Python 3. The interface was set up for three trigger

ports, and the layout is shown in figure 28. It was possible to select the triggering time in several ways, the DCPD method might give signal about crack length and triggering at given crack length is possible. For this experiment however, the trigger used cycle intervals and manual triggering only.

The first choice was to activate given port, the second enabled cyclic trigger, the condition that activated the trigger was:

```
if((Cycle count - start trigger after)%Trigger interval == 0)
```

Where % is the modulus operator. The cycle count could be changed, the new count was typed in the window besides current cycle count and the change was applied with the red button. The "Time til trigger" was the remaining time in seconds until next cyclic trigger was fired based on the "Test freq for time calc" value. On the bottom there are three buttons for firing the trigger manually.

Whenever a trigger was fired, the time, cycle count, and what type of trigger it was, was logged in a file for the given port, so there were in total three files. Additional features were that when the software was closed, the current data were stored, so when the software was started up again, all the previous values were opened, and the software started counting cycles automatically, but no triggers were sent until a confirmation. A pop-up window asked user if a new project is to be started, if the data from last test should be loaded, or if the loaded data plus the cycles counted since start of the software should continue. The last option was added in case of unexpected errors or failures.

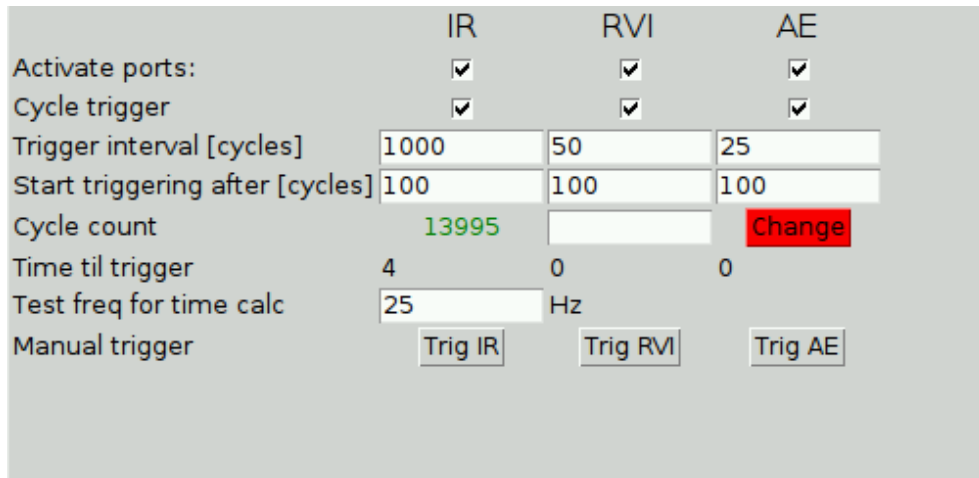


Figure 28: Figure showing the graphical interface for trigger software

3.4 Experimental procedures for IRT

The experiment resulted in a series of IRT pictures, to get useful data, the pictures had to be processed. First of all, it was important to remove the noise from the pictures, to have a clear map of temperature distribution. One of the noise sources was due to the sensors, and it was the NETD for the camera which was as 20 mK, additionally due to the large magnification the texture of the painted surface caused regular pattern of lighter and darker spots on the picture. The sample was also moving, especially when the crack has grown large, making it difficult to measure the same spot on the sample precisely.

3.4.1 Noise reduction in infrared pictures

The first thing done, was cropping of the pictures to remove the region of the picture that was of no interest regarding the results but which reduces the processing time. The next step was to filter the picture using wavelets. This is a very attractive method of filtering because it allows to tune which parts of details in the picture to keep. During such filtering, the picture was decomposed into an approximation and vertical, horizontal, and diagonal details, all described by coefficients related to wavelet manipulation. The decomposition

might be performed over several levels, and the coefficients might be further processed to keep only the details of interest. The filtering consists of three steps:

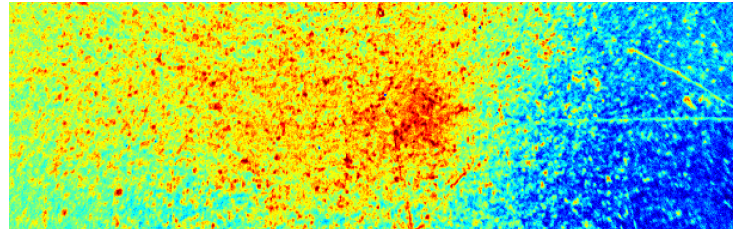
- Decomposition, where the picture is decomposed using a predefined wavelet and decomposition level into approximation coefficients and detail coefficients
- Detail coefficient manipulation, where at every level, the coefficients are adjusted, often by soft or hard threshold
- Reconstruction, where the picture is recreated from the modified coefficients

For the filtering, the decomposition was of level 5, and the wavelet type used was Symlet 14. The pictures have been denoised, using soft thresholding, using global threshold based on picture size. The criteria for determining the threshold level was simply $\sqrt{2 \cdot \log(\text{number of pixels})}$ multiplied with a constant, set to 3 for all of the analysis. Soft thresholding was used to change the coefficients.

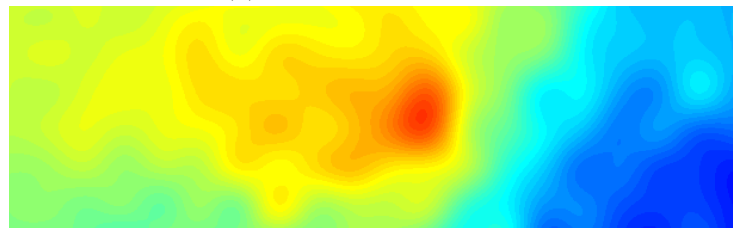
After all pictures were filtered from noise, the filtered picture was subtracted from the original to illustrate how well the filter worked. The picture should give a homogeneous temperature distribution, where only the "texture" like pattern remains, and the plastic zone is of special interest since it gives very valuable data. An example can be seen in figure 29. To measure the noise in the picture, the average value was divided by the standard deviation of the picture. The average value should not be affected much by filtering, but the standard deviation should change significantly. The signal to noise ratio defined above was approximately doubled after the filtering. Of course this number does not tell if some of the signal was filtered away, but this should be visible in the rest picture.

After the filtering, a motion compensation was performed with the algorithm described in section 3.4.2. The algorithm reduced the rotation and translation of every picture in each sequence with respect to the first picture. The transformation matrix found was based on the rest pictures, example illustrated in figure 29c, since those should be constant and temperature independent as they mostly consisted of fixed pattern noise, so the images should have the same features. A secondary cropping was done after motion compensation,

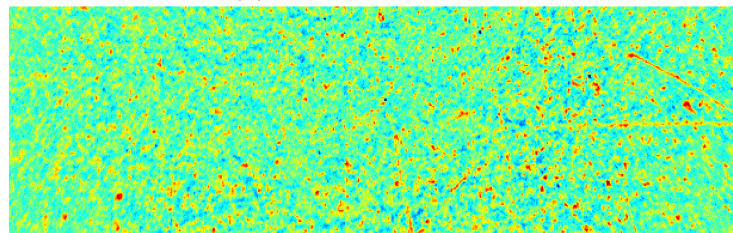
to remove the area with no data at the edge of the picture after the transformation was performed.



(a) Picture before filtering



(b) Picture after filtering



(c) Filtered picture subtracted from the original one

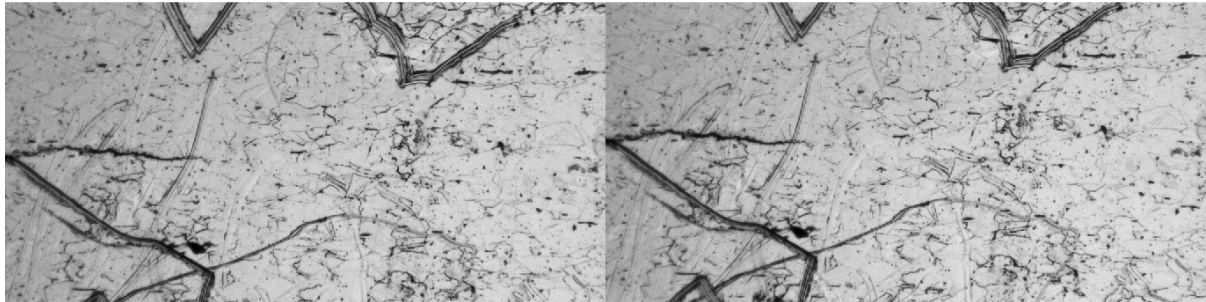
Figure 29: The temperature range in the pictures is 1,05K

3.4.2 Motion compensation

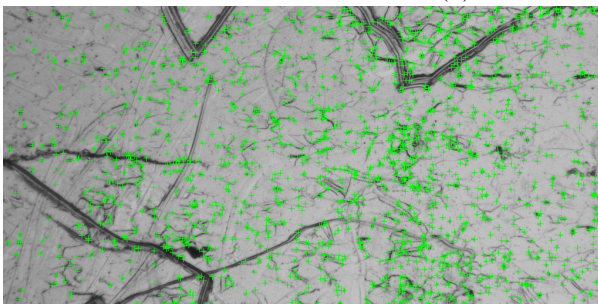
The code was developed with software and functions provided by The MathWorks. *MATLAB and Computer Vision System Toolbox Release 2018B*. The MathWorks, Inc., Natick, Massachusetts, United States., 2018.

The motion compensation function developed especially for this project, compared two pictures at a time, example given in figure 30a, and used the `detectFASTFeatures()` function provided by The MathWorks [120] to find points with specified features above a threshold value, figure 30b and 30c. The feature type detected was minimum intensity difference between corner and surrounding region. The threshold for feature detec-

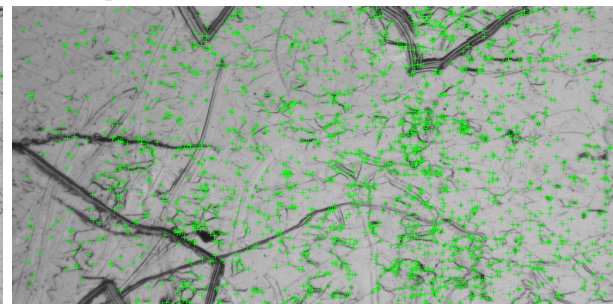
tion was adjusted depending on the pictures, to give a satisfactory amount of points. The detected features were extracted using `extractFeatures()`, and matched using `matchFeatures`. The resulting matches are illustrated in figure 31a.



(a) Two frames of a sequence



(b) Features found in the first frame



(c) Features found in the second frame

Figure 30: First stage of motion compensation

The result was a series of coordinates of the corresponding features in these two pictures. These were used to transform the picture, and the nearest transformation type provided by *The Mathworks* was a nonreflective similarity transformation consisting of translation, rotation, and scaling. Since scaling is undesired, an algorithm just for rotation and translation was developed. The scaling was not beneficial because when the crack is long, the crack opening displacement is noticeable, the features on the upper and lower half of the sample are moved away from each other. This leads to scaling of the picture, which again affects further analysis as e.g. the pixel size is changed, as well as the strains in the picture.

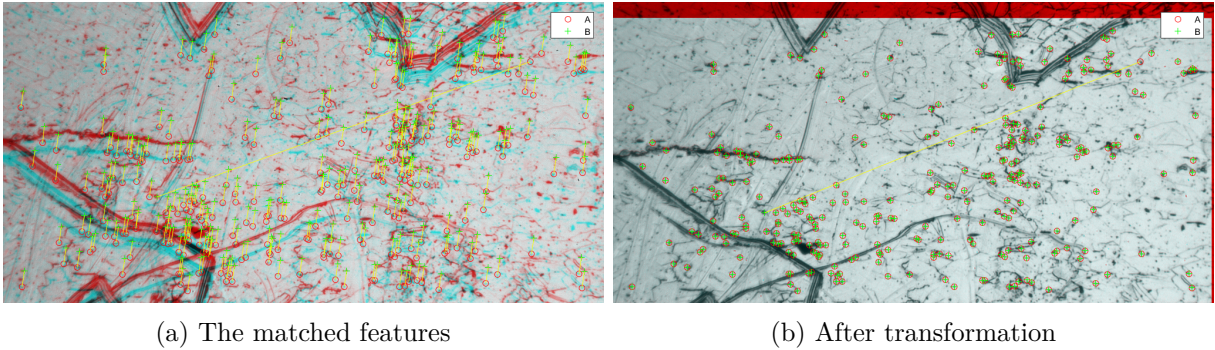


Figure 31: The two frames are superimposed with different colormaps, adding to a RGB picture

The transformation function developed, calculated the geometrical centre of the two data sets of coordinates, and the distance between these corresponded to the translation part of transformation. After this translation, the pictures had the same geometrical centre. In the next step, the algorithm took the centre point and two corresponding points from the features detected, and found the angle between two vectors starting in the centre point and ending in one of the corresponding points each. After this was done for every point pair, the mean value was computed and used as the rotating angle about the geometrical centre. The transformation is shown in figure 31b, and the final result in figure 32.

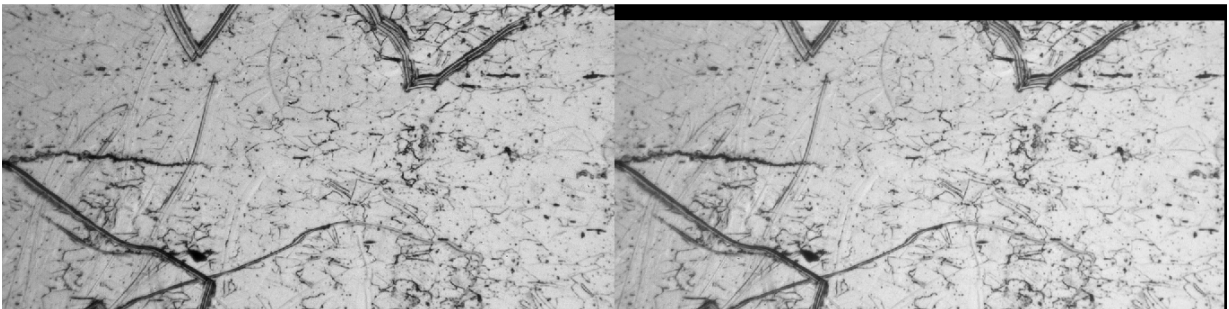


Figure 32: Final result, the second frame transformed with respect to the first.

To make the transformation more reliable, the point pairs between which the distance was far from average, were excluded. One such outlier is barely visible in figure 31. Another source of error was that points close to the geometrical centre, which was also the origin for angle calculation, were much more sensitive to noise, leading to large angle changes.

For this reason, points within a region close to the centre point were excluded. In this case, the radii was set to 60 pixels.

The algorithm was used both for the IR camera and for the HSI camera, but to make the transformation possible for the IR pictures a change was introduced. The filtered picture was subtracted from the initial picture resulting in a picture of the texture of the surface, which does not change from frame to frame as the temperature difference due to thermoelastic effect and plasticity is eliminated. The transformation matrix was found using these specially prepared pictures, but it was applied to the filtered pictures instead.

3.4.3 Temperature and phase shift analysis

To implement the concepts discussed in sections 2.3.2 and 2.3.3, the amplitude field and phase shift had to be determined. Such fields are very useful as they contain information about the first stress invariant, crack tip position, plastic zone, and stress intensity factor as described in section 2.3.

Each picture consisted of thousands of pixels containing tens of measurements for each acquisition, methods like Fourier series are in general very time consuming, and were done only on some of the data. Some pictures were affected by increase in temperature due to current caused by the potential drop method, and error due to sampling frequency of the pictures mentioned in section 3.2.1. A very important parameter to determine was the temperature amplitude field. To account for these errors, and to make the calculations rapid, every acquisition was divided into $n - 1$ equal parts (alternating red and blue in figure 33) where n was the number of cycles captured in the acquisition. Every part contained just over one cycle, and the maximal and minimal temperature in each was found, and the median value was used to determine the temperature amplitude. The whole procedure is illustrated for a single pixel in figure 33. In the figure, a Fourier fit has also been calculated, and the temperature amplitude based on the fit was 0.0794 K, while for the

algorithm described above, 0.0786 K. The ratio between these two is 0.99, additionally, the temperature amplitude near the crack tip was significantly higher, which likely reduces the noise further. A comparison of a complete picture is shown in figure 34.

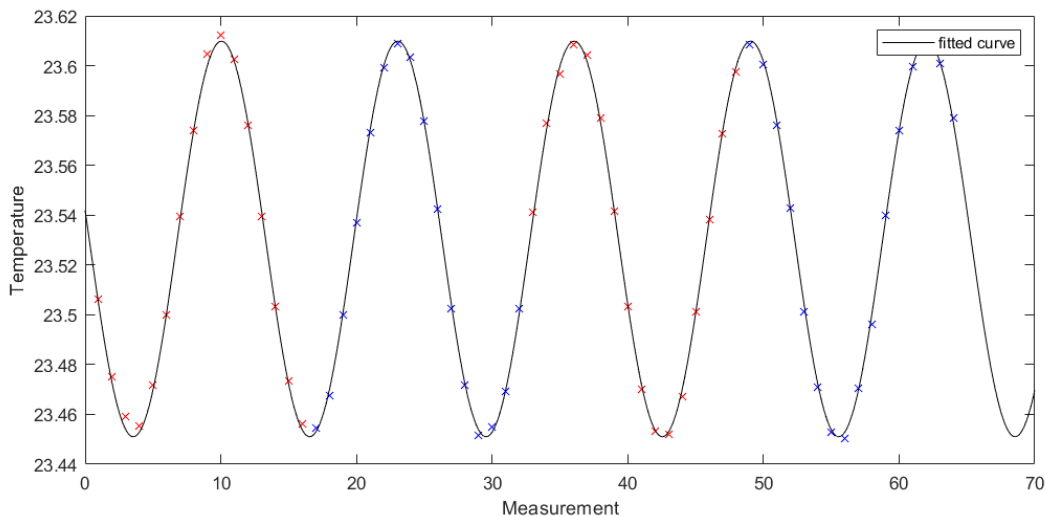


Figure 33: Temperature measurement in a single picture during one acquisition, and a first order Fourier fit

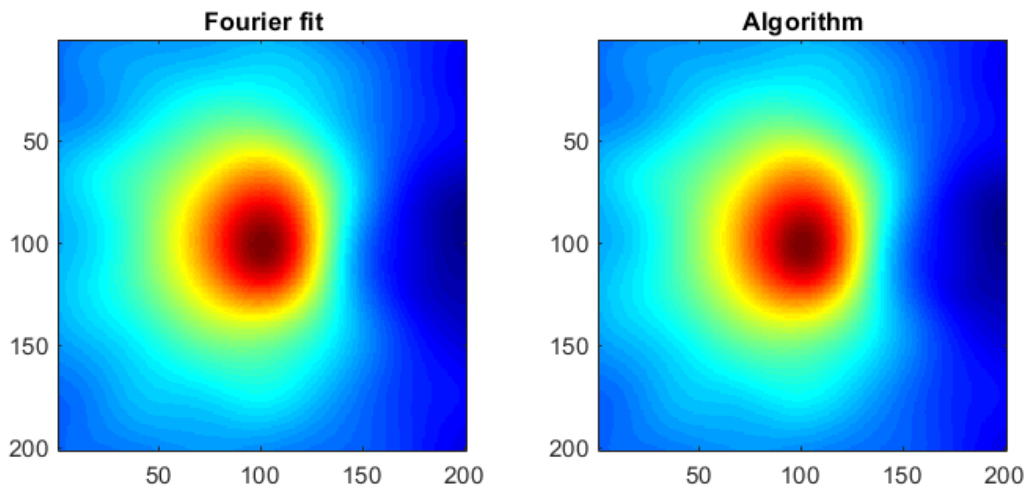


Figure 34: Temperature amplitude in a single acquisition, based on Fourier fit, and the algorithm

Since the extreme values of the temperature were used to determine the amplitude, the

calculation relied on two samples, and the noise was therefor more likely to cancel itself out, the median of these $n - 1$ values was used to represent the temperature amplitude at that pixel. The frame rate was such that there were 13 samples per cycle, because of this, if the sampling rate gave maximum error in measuring one extreme of the sin like temperature wave, it would give minimum error measuring the second extreme, which practically halved the 3% error mentioned in section 3.2.1.

The discrete Fourier fit is very time consuming, but it has been performed on some of the pictures. The fit was of second order, which in addition to the temperature amplitude due to thermoelasticity, potentially shows the reversible plastic zone, and the phase shift occurring due to heat dissipation and high stress gradients. The formula of the model is given in equation 51. T is the temperature, a_{fi} and b_{fi} are constants of the fit, ω_0 is the test frequency in rad/s, and t is time. a_{f0} corresponds to the average temperature, the total amplitudes of first and second order A_{fi} , can be calculated as in equation 52, and the phase shift ϕ_{fi} with respect to a sine wave as in equation 53. An example of the maps of calculated coefficients is shown in figure 35.

$$T = a_{f0} + a_{f1}\cos(\omega_0 t) + b_{f1}\sin(\omega_0 t) + a_{f2}\cos(2\omega_0 t) + b_{f2}\sin(2\omega_0 t) \quad (51)$$

$$A_{fi} = \sqrt{a_{fi}^2 + b_{fi}^2} \quad (52)$$

$$\phi_{fi} = \text{atan} \left(\frac{a_{fi}}{b_{fi}} \right) \quad (53)$$

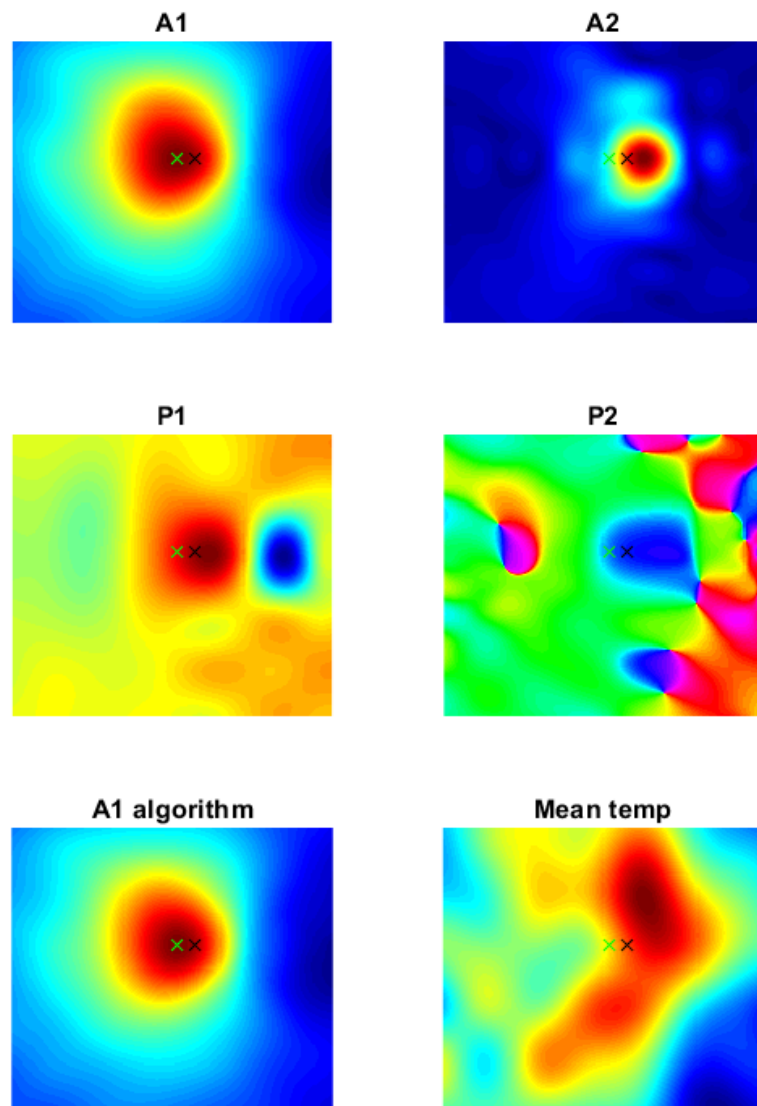


Figure 35: Second order discrete Fourier fit, A1 and P1 are the first order amplitude and phase shift respectively, and A2 and P2 are the second order terms. On the bottom left, the temperature amplitude from the developed algorithm is shown, and bottom right is the mean temperature in the region of interest. The green cross is crack tip from TSA, and the black one from fitting Williams' stress field.

3.4.4 Stress calculations and Williams' expansion

Thermoelastic constant

Assuming adiabatic conditions, the first step in any stress calculations is to determine the thermoelastic coefficient K_t . The complexity of precise determination of the relation between stresses and temperature response due to thermoelasticity, was described in 2.3.2. In the C(T) specimen, the mean stresses are varying, additionally, as soon as plasticity is introduced, and reversible plastic zone, the actual mean stresses are unknown. This could be determined in more detail by additional tests, but as a simple attempt to at least reduce the error of equation 13, a tensile specimen was subjected to an oscillating loading, and the response was measured. The load and results are presented in section 4.2.1.

Von Mises stress field

The temperature amplitude is related, and assumed to be proportional to the first stress invariant in the elastic region, and with some assumptions mentioned in section 2.3.3, the relation should be reasonable approximation in the plastic zone. To calculate the von Mises stresses in the sample, Williams' expansion was implemented. The equations for a Cartesian coordinate system are shown in equations 6-8. The principle for this was that the sum of principal stresses is measured from the thermoelastic response, and the ratio between the principal stresses was found using the Williams' stress field. Equations 6-8 and the equation 9 show that there is a linear relationship between the load and stress field for a given geometry, so the ratio should not really change. The Williams' expansion was used as it seems to represent the stress field in the elastic region well; an example comparison is shown in figure 36, and a more in depth analysis is presented in the sections 4.2.7 and 5.1.6.

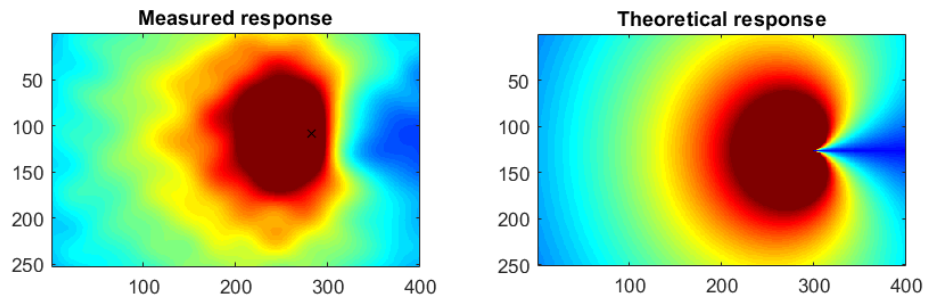


Figure 36: A figure showing the measured response and the prediction of that response by the William's expansion

The last thing needed for calculations of the von Mises stresses in the sample is the crack tip position. The position used for the calculation was the one described in section 3.4.4, because it was a crack tip position based on the stresses from Williams' expansion, and should give the most representative results. A problem occurred with the stress field calculation due to conduction. As seen in figure 36, the region behind the crack tip (black cross), should have a low response, but due to conduction, it was significant. Additionally, the ratio between principal stresses was far from 1, causing the von Mises stresses to be very high, especially compared to what they really were. To remove the error from the stress field, the stresses for ratio below a threshold value are neglected, this causes the region behind the crack to be excluded. An example of the stress field is shown in figure 37.

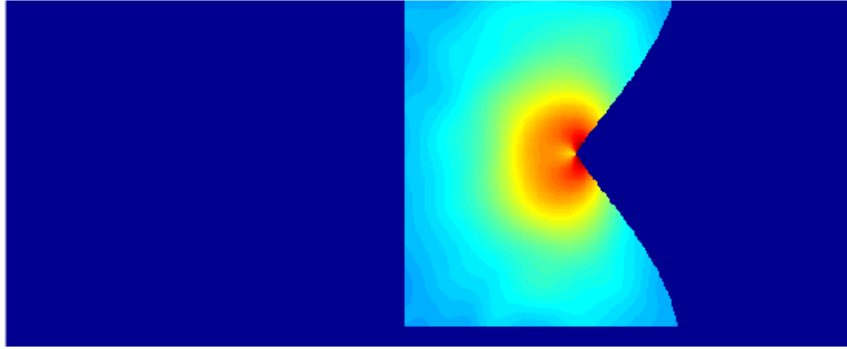


Figure 37: A figure showing the von Mises stresses based on a hybrid model combining TSA and the Williams' expansion

Stress intensity factor

The crack closure, and stress intensity were calculated from the IR data. The principle behind this was to compare the temperature response in the elastic region, with adiabatic conditions, to a theoretical temperature response at a given stress intensity factor. To do this, equations 6-8 from section 2.1.1 were used. A benefit of the implemented model, is that the stress field is linearly proportional to the load as long as the coefficients are also linearly dependent on the load, which simplifies the calculations of crack closure effect. The method has also a potential of better approximating the crack tip position in the crack plane, as described below.

Previous authors [22; 30] determined the stress intensity factor by assuming a crack tip position, but they also mention algorithms that can afterwards be used for more precise crack tip determination. The algorithm developed in this work, also needed to know the specimen geometry, and so the crack length, to calculate the theoretical stress field. The crack tip position was initially set to the crack tip from TSA (highest temperature amplitude), and was used to measure the stress intensity factor, the crack closure, and a more precise crack tip position.

The Williams' expansion based on equations 6-8, with coefficients from equation 9 seemed

to be a good choice as the general shape of it seemed to correspond well to the measured response, it is also a stress field calculated especially for a C(T) specimen. The first step in closure calculations, was to determine the maximum temperature response in planes parallel to the crack plane. The maximum value of these occurs in the crack plane, which reduced a degree of freedom in the crack tip position measurement. Some filtering of the measured stress amplitude might be required depending on the noise level, Gauss filter was used for that with a sigma value of 5. The same values were extracted from Williams' stress field with a known stress intensity. An example of these two sets of data is shown in figure 38. The advantage of this approach was that as the maximum values were used, they could be used independently of the crack tip position along the crack plane. The next step was to find the region of the data in which Williams' expansion was representative. This region has been chosen at given offsets from the peak value of the derivative of the data. This was due to that if the material would be ideally elastic, and adiabatic conditions would be met, the temperature response would be convex. The extreme values did show where the signal became concave, and an offset from the peak value was used to make sure the region was representative. An example of the values used for calculation are also visible in figure 38 (green crosses). Now that good sampling points were determined, the theoretical response could be scaled to best fit the actual response, and the scaling multiplied with the theoretical stress intensity factor of the stress field, gave the effective stress intensity factor.

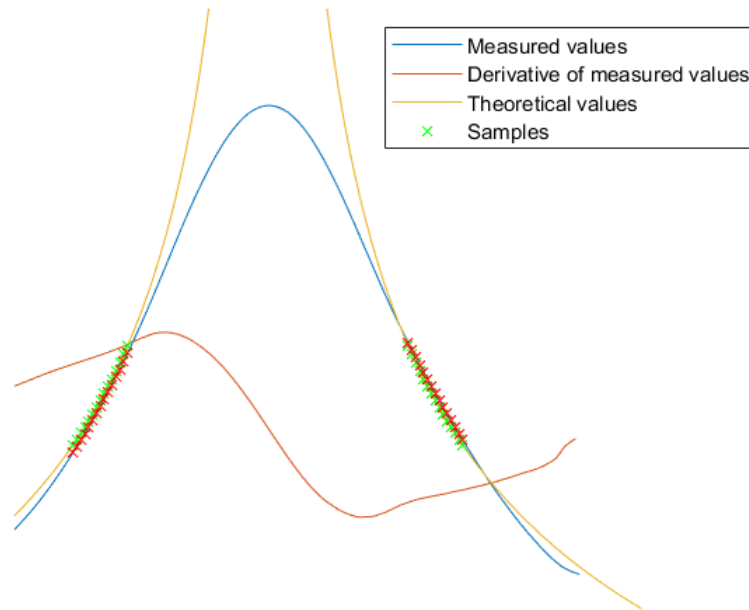


Figure 38: Max values of the stress response perpendicular to the crack plane, measured values, derivatives of those, theoretical stress response, and sampling points

Once the effective stress intensity factor was determined, the last step is to determine the crack tip position in the crack plane. The approach was similar, but this time, data from the crack plane were used. The theoretical stress field (yellow line in figure 39) was translated horizontally to best fit the actual response (blue line in figure 39), and the crack tip position was then determined. Once the crack tip position was determined, the theoretical stress intensity factor could be calculated again, and the crack closure based on the ratio between the measured, and the calculated stress intensity was found.

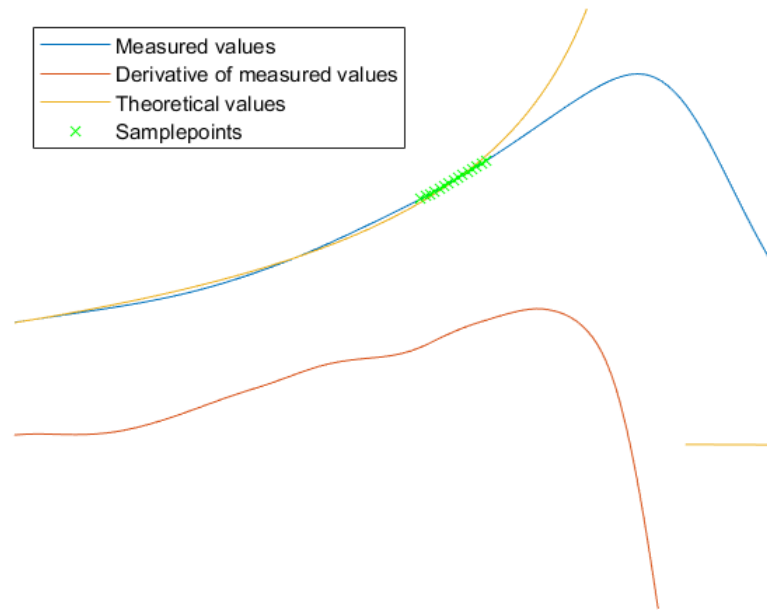


Figure 39: The temperature response, its derivative, and the theoretical response as well as sampling points, values in crack plane

3.4.5 Plastic zone size

Before explaining the calculations behind the plastic zones, it is necessary to define the plastic zone properties. The area of the plastic zone was the measured area covered by the defined zone. The size of the plastic zone was defined as the square root of the area, and finally, the radius of the plastic zone was defined as the radius of a circle with the same area as the plastic zone. Further it is important to mention that the term *plastic zone* is used in a non conventional way, as in some of the process zones, the stresses surrounding the zones do significantly exceed the initial yield strength of the material. Nevertheless, they are called plastic zones.

The common *plastic zone* is the region where yield has occurred. In this case, the calculation was simply to find the region in the von Mises stress field where the absolute stress exceeded a given stress level. The stress level might be defined as the proportionality limit,

the $\sigma_{0.2\%}$ stress, or the cyclic yield stress. This type of stress field, should be a reasonable comparison for a DIC analysis of the plastic zone. The cyclic yield stress was unknown for the material, so the monotonic plastic zones were calculated instead. To find the plastic zone from the IR data, the stress amplitude could be corrected for crack closure if it was significant, and was further divided by $(1 - R)$ to find the max stresses occurring in every pixel. This is valid only in the elastic region of the sample. Afterwards, the stresses exceeding both the proportionality limit as well as the $\sigma_{0.2\%}$ were measured.

The definition above might not be as useful for energy release calculations, as the material might be hardened in some regions, and softened in other regions. The cyclic plastic zone might have a different size or shape, some of the region might be hardened, and will not dissipate significant (measurable) heat. Another plastic zone is often defined as the area where the temperature response is not in phase with the loading. The example is shown in figure 40. The plastic zone defined here corresponds to region C in figure 10. Region B is also visible but is more challenging to measure. The analysis took a lot of time even for the relatively small FOV, which region B did already exceed, so the only region C was measured. It is the region C that is the most significant for energy dissipation. Since the region B was not included, the size of the plastic zone was not really comparable with the that of the monotonic plastic zone described above, it is rather related to the region where a hysteresis is established. The plastic zone was calculated based on data from discrete Fourier analysis described in section 3.4.3, and was defined as the region where the measured phase exceeded a threshold value.

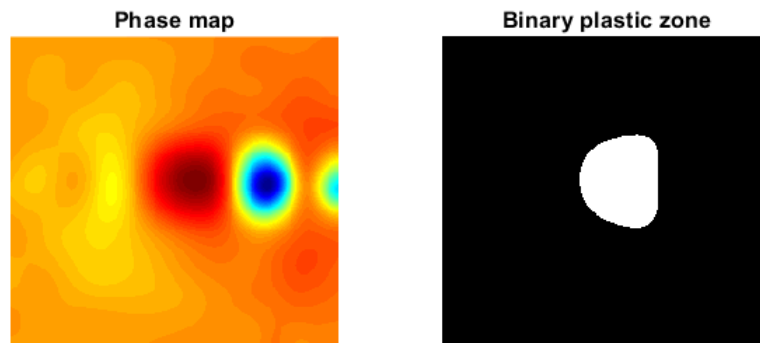


Figure 40: The phase map and a binary map of the plastic zone calculated from it

The last region of interest - the plastic zone - was defined as the area where the stress field started to deviate from the elastic stress field. For an ideal elastic material with no plasticity the cross section of the stress field in the cylindrical coordinates with the origin at crack tip is a convex function. When the stress intensity increases, the stresses are not able to follow the elastic model, and a zone is created where the stress field become concave. This phenomenon can be illustrated very well by the fact that the plastic zone becomes a sink for the gradient, so the Laplacian of the stress field, is clearly negative in such a region. It is important to keep in mind that this method was here applied to the temperature field, which not only is affected by the stress field, but also heat dissipation, and most importantly, high stress gradients which might cause conduction. In an perfect case, the zone of interest could be defined as the region where Laplacian was below zero, but due to noise, a threshold value was used instead. Additionally, since the Laplacian is very sensitive to noise, the stress field was initially filtered with a Gauss filter to remove the high frequency noise. All these steps are illustrated in figure 41. Based on the binary map, both the height and width as well as the are of the plastic zone could be calculated.

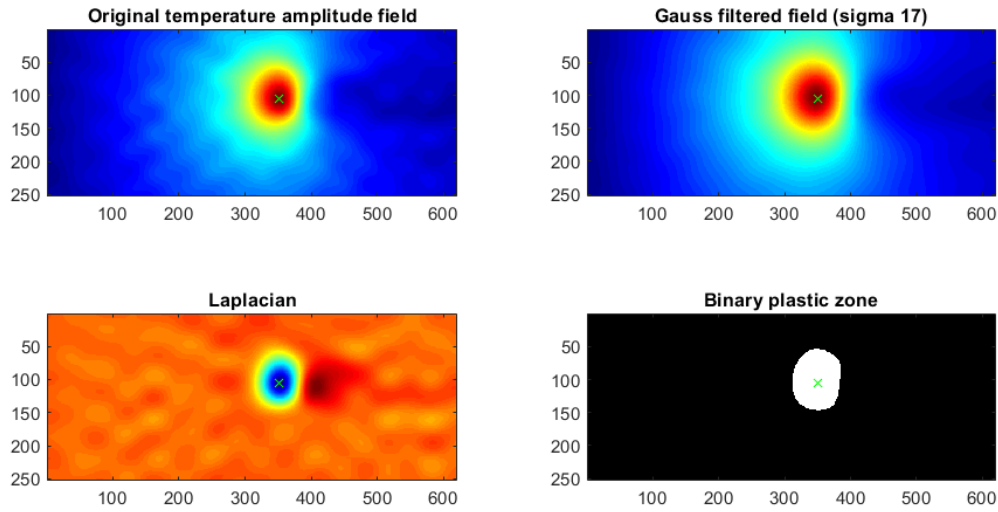


Figure 41: The plastic zone based on Laplacian of temperature amplitude

3.4.6 Heat dissipation

Once the temperature pictures were filtered from noise, stabilised and the stress analysis was performed, the *Laplace operator* was calculated. The energy release based on equation 17 was computed in several ways. The first was based on calculations over an area of interest which was defined using the stress level based on TSA analysis (sum of principal stresses) as the more conservative approach. The area was defined as the region where the stress level exceeded 80% of the max stress occurring in the current acquisition. The second method calculated the energy released per unit of volume at crack tip. The benefit of limiting the area is that the influence of temperature gradients caused by external factors like grips, or other equipment attached to the specimen were reduced without affecting the energy measurements in the region of interest. The energy dissipation outside this region of interest is omitted, so not all of the total energy will be captured if the region of interest is too small. The largest dissipation is however expected to occur in this region.

Both of the measurements were further used to make a model using a first order Fourier approximation. Based on that, the steady state energy release due to plastic work, and

the amplitude caused by thermoelasticity were calculated.

3.5 Experimental procedures for HSI and DIC

3.5.1 Crack tip detection without using DIC

Analysing the recordings from high speed camera in order to find the crack lengths a is a quite time consuming task, especially if there are hundreds of recordings to analyse. In order to reduce this time, an attempt to make crack tip detection tool was made using *Matlab*. This tool converts an uncompressed AVI video file, or series of TIFF images, into a 2D array. Since the high speed camera records in grayscale, the array itself contain different values in the range from 0 to 255, where 0 corresponds to black and 255 to white colour. The grayscale array corresponding to original image is further converted into a black-white bitmap. In this conversion a threshold value is used. This value is set manually and depends on the image contrast, the brightness, and the gamma value. Array values above the threshold are changed to 1, while all other are assumed as 0. The result can be seen in figure 42.

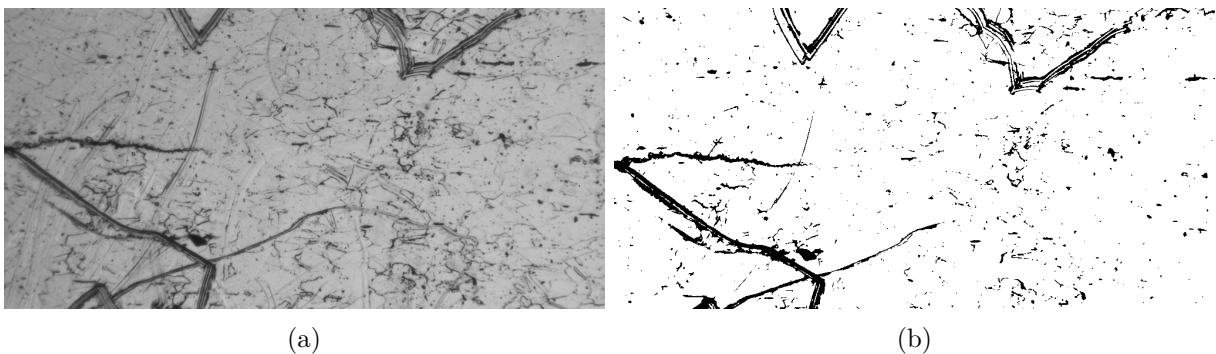


Figure 42: Original and converted image for use in crack tip detecting algorithm

The 2D array is then used in the custom `crackFinder` tool. This tool goes through the elements in 2D array (corresponding to the pixel in the image) starting from the right upper corner and moving to the left as shown in figure 43a. All these elements are checked by the core function in `crackFinder` tool in order to check if some of the neighbouring pixels

have value equal 0 (are black). This function goes through $n \times m$ nearest elements, also a $n \times m$ matrix with size determined by user, to the left of reference pixel as shown in figure 43b. If the core function detects black pixel, such pixel in nearest column is used as start point for new iteration. If there are few black pixels in nearest column, the lowest pixel is used as a start point as indicated by arrow in figure 43b. The iterations continues until left edge of image is reached, or no pixel in neighbourhood have value equal to 0. In the first case, the algorithm is interrupted and show the position of the alleged crack tip, otherwise the `crackFinder` continues the search. Due to vignetting which can occur, the left edge of image can never be reached. In this situation the tip of crack determined by longest series of iterations is assumed as crack tip. The algorithm of this tool has weaknesses, one of them is fact that if crack is very branched, or if there are many scratches present, the program loses the path of actual fatigue crack, and assumes other point as a crack tip. To solve this problem, the 2-D array is flipped upside-down and the whole procedure for crack finding is repeated. The tip of the longest crack is then assumed as the crack tip. If no problems occur during detection, the algorithm gives the same crack tip position for both flipped and non-flipped 2D-array.

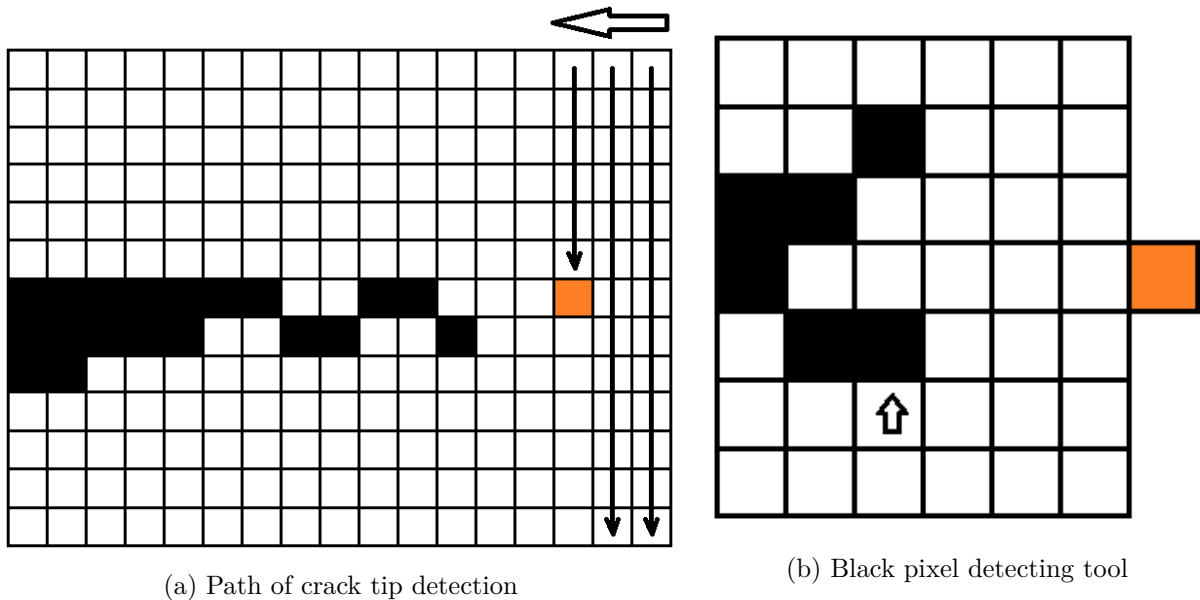


Figure 43: The principle of crack tip detecting algorithm

The final results compared with original image are presented on figure 44. It can be seen that the tool is able to find the crack tip with 2-3 pixel accuracy. Thus using the FOV with size $0.7\text{mm} \times 0.7\text{mm}$ and spatial resolution of around $0.7\mu\text{m}$ per pixel, the $1.4\mu\text{m} - 2.1\mu\text{m}$ accuracy can be obtained. `crackFinder` is able to find the tip position, even if the image contain a lot of scratches, dirt particles or grain boundary contours resulting from etching. After some trials, it has been observed that the images post-processed with edge detection tools in *MATLAB* works as well with the `crackFinder` giving satisfactory results.

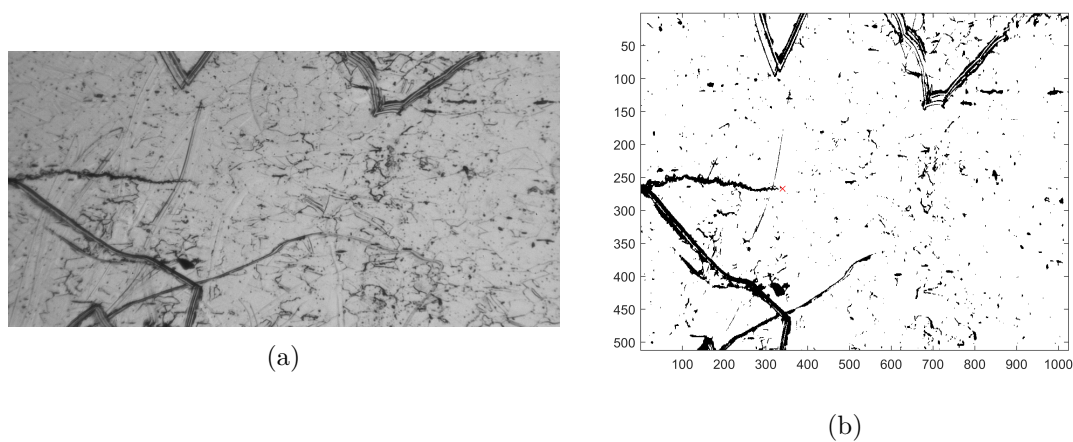


Figure 44: Image containing the crack and its bitmap representation. The crack tip is found and indicated by a red cross.

3.5.2 Determining the FCG parameters in Paris regime

The data obtained using HSI and IR contain information about the crack tip position which might be used to determine Paris constants C and m according to equation 10.

$$\frac{da}{dN} = C\Delta K^m$$

To find the crack position, the cameras were set in such way that they follow the crack propagation. That is from $0.2 \leq a/W \leq 0.7$, where 0.2 arrived from initial notch depth and 0.7 was the upper limit for use of Alternating Current Potential Drop (ACPD)-technique [114]. Final a/W can exceed 0.7 if potential drop technique is not used in the particular

test. If a width of the FOV is small compared to overall crack length, one has to move the camera as the crack tip approach the edge of FOV. For the high-speed camera the problem has been solved using motorized translation stage as mentioned in 3.2.2. Cameras had to be triggered at known temporal location to be able to assign a specific crack length to the given amount of cycles. For this purpose, an external microcontroller-based trigger analysing the signals from the load cell was used. The triggering equipment is described in section 3.3. After acquiring the data, the crack lengths from HSI and IRT could be found by looking at the actual position of crack tip and thus finding the a for given N . To create the FCG-curves, the a and N data had to be processed according to ASTM [114]. In this work, both the secant method and incremental polynomial method for computing the crack growth rate were used, both included and explained in E647 standard. The former one included calculating the slope of a straight line connecting two adjacent data points on the a - N curve. It can be expressed as shown in equation 54.

$$(da/dN)_{\bar{a}} = (a_{i+1} - a_i)/(N_{i+1} - N_i) \quad (54)$$

The average crack size \bar{a} was used for calculating ΔK , that is $\bar{a} = 1/2(a_{i+1} + a_i)$. The second technique, incremental polynomial method, involved fitting a second-order polynomial to sets of $(2n+1)$ data points. In this work $n=3$ was used. The FCG-curve was then plotted with logarithmic scale on both axis. To find the C and m constants the power regression tools were used. This includes use of equations. 55-56.

$$\begin{aligned} \text{mean : } \quad \overline{\ln x} &= \frac{\sum \ln x_i}{n}, \quad \overline{\ln y} = \frac{\sum \ln y_i}{n} \\ \text{trend line : } \quad y &= Ax^B, \quad B = \frac{S_{xy}}{S_{xx}}, \quad A = e^{\overline{\ln y} - B\overline{\ln x}} \end{aligned} \quad (55)$$

$$\begin{aligned}
S_{xx} &= \frac{\sum (\ln x_i - \overline{\ln x})^2}{n} \\
S_{yy} &= \frac{\sum (\ln y_i - \overline{\ln y})^2}{n} \\
S_{xy} &= \frac{\sum (\ln x_i - \overline{\ln x})(\ln y_i - \overline{\ln y})}{n}
\end{aligned} \tag{56}$$

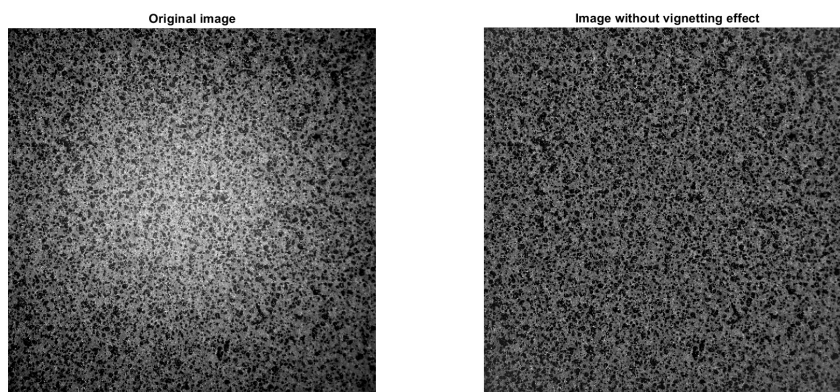
Here $A = C$ and $B = m$. The FCG-curves contain also trend lines based on the C and m values. In addition, the 95% confidence limits were plotted. To measure a quality of the fit, a coefficient of determination R^2 was calculated.

3.5.3 Investigating the vignetting effect on DIC results

During the set-up for FCG test it has been found that in some conditions the images taken by the high-speed camera have reduced brightness on the periphery of the images compared to their centre. This effect is called vignetting. For images suffering of vignetting effect, a kind of light spot is visible and fixed in the middle of the FOV. In FCG test, especially when a very small FOV is used, the specimen slightly moves in vertical direction and there is suspicion that vignetting can introduce the error to the DIC analysis. To verify the effect of this phenomenon a procedure containing two steps was established. First, the images had to be filtered. The next step is the DIC analysis, and the results comparison for both filtered, and unfiltered images.

In this work the removal of vignetting effect was performed applying the Gaussian low-pass filter in the frequency domain to the images. The theory behind the DFT and filtering in frequency domain is described in detail in section 2.5. The core of the low-pass filtering code were build-in *MATLAB* functions `fft2/iff2` and `fftshift/iftshift`. The original images affected by vignetting effect were low-pass filtered, and the smoothed out light spot (low-pass filtered image) resulting from this action was subtracted from the original images. This action was performed for all of the images in series individually. Since the 8-bit TIFF images were used, their elements in 2D array representation had

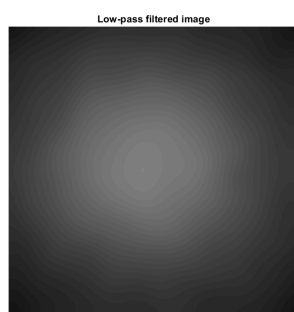
value between 0 and 255. In order to avoid any value being lower than 0 after subtraction, the minimum gray value of the low-pass filtered image was found and added to the final image (further called filtered image).



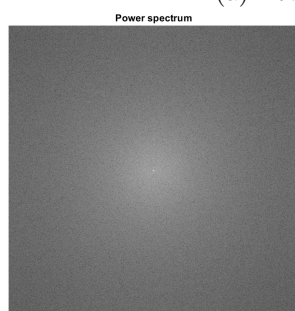
(a) Unfiltered image

(b) Filtered image

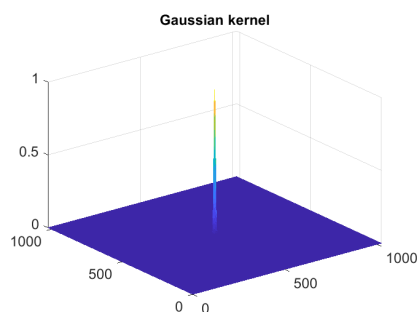
Figure 45: Comparison of both unfiltered-, and filtered image



(a) Low-pass filtered image



(b) Power spectrum



(c) Gaussian kernel

Figure 46

After the filtering, the images were analysed using *Ncorr* DIC software. The most important aspect of analysis was to hold all parameters constant during both analyses in order to avoid additional error sources. In this work, the influence of vignetting was investigated by comparing the displacement of certain points on the test sample during the sample translation. The results arising from this investigation are presented in section 4.3.1 and discussed on in section 5.2.1.

3.5.4 Post-processing the tensile test data using DIC

In order to gain knowledge about material behaviour under tensile conditions, and to get material constants as Poisson's ratio, elastic modulus or proportionality limit, a series of tensile test were performed. To create an engineering-, and a true stress-strain curves it's necessary to have a knowledge about stress and strain at any time of experiment. The stress data were extracted from the load cell. The testing machine provided force versus time data which was sufficient to find engineering stress when cross-section area is known. Accurate width and thickness of the samples was measured using micrometer. The strain data has been found using two independent methods. The first method assumed use of extensometer connected to the testing machine. In this work an Instron 2620-601 dynamic extensometer with 12.5 mm gauge length with ± 5 mm travel distance was used. The extensometer was attached to the sample using rubber bands, and the strain data was logged together with force data. It was expected that the final strain at fracture may exceed 0.4, and since extensometer had limited span it has been decided to interrupt the test, and detach the extensometer from the sample when a certain strain was reached. The other method assumed use of DIC. The visual data for DIC-analysis was captured using Photron FASTCAM SA-Z with Tamron macro lens. Two different ROIs were used in DIC analysis. One was 12.5 mm, and was supposed to correspond to span of extensometer blades. The other one was 19.5 mm and included the whole section with reduced width. 12.5 mm ROI can be seen on figure 47a. The engineering strain has been found by using

formula

$$e = \frac{\Delta L}{L} = \frac{l - L}{L} \quad (57)$$

which is expression for Cauchy strain or engineering strain. The blue and red stripe on figure 47a correspond to upper and lower displacements of the sample respectively. The ΔL in formula 57 was found by taking the average value of displacement field in its extreme, here represented by blue and red stripe and subtracting one value from the other. Finally, the engineering strain was found by dividing ΔL on the gauge length L . The 2D arrays with displacements used in calculation of strains followed Lagrangian description, all displacement were presented with reference to the image at $t = 0$. The reason for that is that in *Ncorr*, the displacement matrix following Lagrangian description doesn't change its dimension in opposition to one following Eulerian description, where the current configuration is taken as a reference. Thus the former one makes post-processing easier, while the latter one makes visualisation of displacements more intuitive.

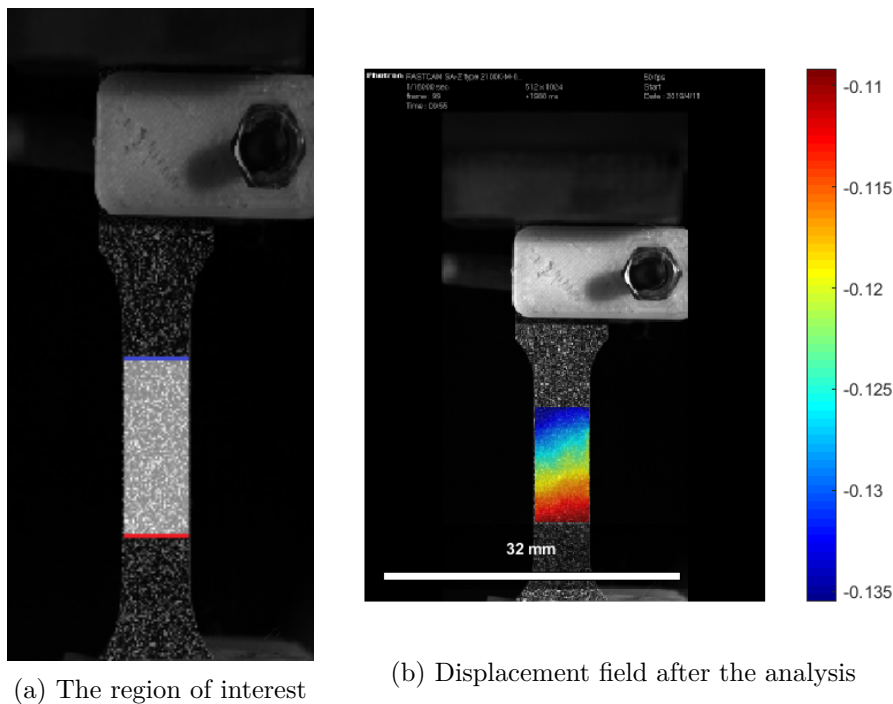


Figure 47: Procedure of finding strains using DIC

Since the testing machine used progressive time intervals when loading the sample on its

elastic region, and since the camera had a constant frame rate with equal time intervals, the sampling times for stress and strain data were different. This problem has been solved using 1-D data interpolation tool in *MATLAB*, `interp1`, and `pchip`-method which includes shape-preserving piecewise cubic interpolation of the values at neighbouring grid points. To create the true stress-strain curves, the true stresses and true strains had to be calculated. Relation between engineering and true stresses and strain is following:

$$\sigma_t = \sigma_e(1 + \varepsilon_e), \quad \varepsilon_t = \ln(1 + \varepsilon_e) \quad (58)$$

Where σ_t and ε_t are the true stress and true strain, while σ_e and ε_e are the engineering stress and engineering strain respectively.

The elastic modulus of the material was found by measuring the slope of the engineering stress-strain curve on its elastic part, assuming that the material follows the Hooke's law in this area $\sigma = E\varepsilon_e$.

The Poisson's ratio of the material was found assuming that the material is stretched along the axial direction using following equation:

$$\nu = -\frac{d\varepsilon_{e_{trans}}}{d\varepsilon_{e_{axial}}} \quad (59)$$

Where ν is Poisson's ratio, $\varepsilon_{e_{trans}}$ is transverse strain and $\varepsilon_{e_{axial}}$ is axial stress.

3.5.5 Crack tip detection using DIC

Some of the actions which can be done when investigating FCG using DIC, as determination of CODs, require a knowledge about crack tip position in order to ensure that obtained results are valid. The speckle pattern applied to the specimen to be tested using DIC may make it difficult to determine crack tip position based on visual inspection. In order to solve this problem, another method to locate the crack tip position from HSI pictures has been prepared based on paper by Vasco-Olmo [59].

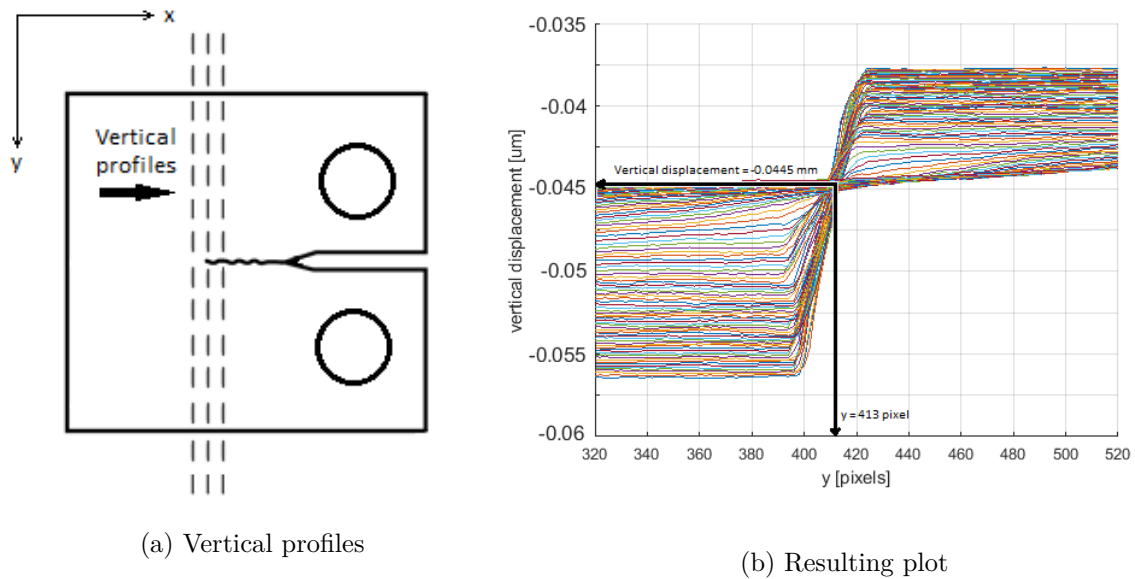


Figure 48: Determining the vertical position of the crack

Method presented here uses the 2D-array with the vertical displacements. The image to be used should come from image taken when the load was on its maximum since the displacements are largest there. First, the y -coordinate of the crack is found by plotting the vertical profiles perpendicular to the crack growth direction. The change in displacement values is visible when the profiles goes through the crack wake. This creates a crossing of the lines for different positions of vertical profiles which is further used to determine the y -coordinate, and corresponding vertical displacement.

The x -coordinate can be found by plotting the horizontal profile for the y -position found, and creating additional line corresponding to the vertical displacement found when obtaining the y -coordinate. The intersection of this horizontal profile with the vertical displacement value determine the x -coordinate of the crack tip. After some trials it was observed that this method is precise when the quality of DIC pattern is good resulting in results without significant scatter. When the quality of images used is questionable, this method may require additional visual inspection in order to ensure that user don't obtain unreasonable results.

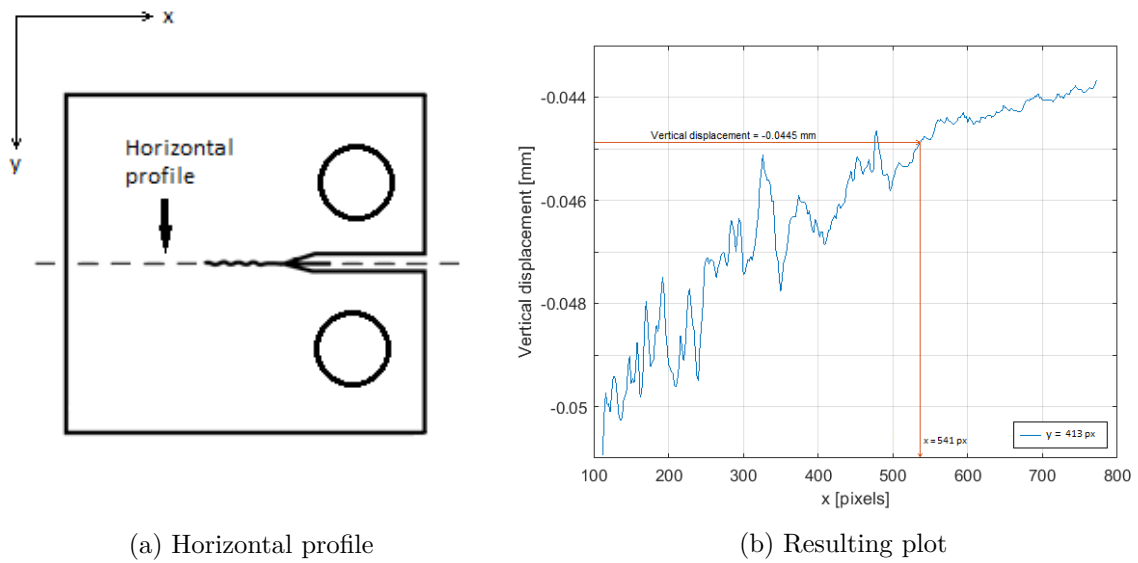


Figure 49: Determining the horizontal position of the crack

Another way of finding the crack tip position, especially when the noisiness of data is large, is the direct determination of alleged position of a crack tip by visual inspection of the vertical displacement field. *Ncorr* software provides user with a feature which allows to track the displacement value for each pixel in the displacement field. The x -position of the crack can be determined by looking at the sudden change in vertical displacement behind the crack tip.

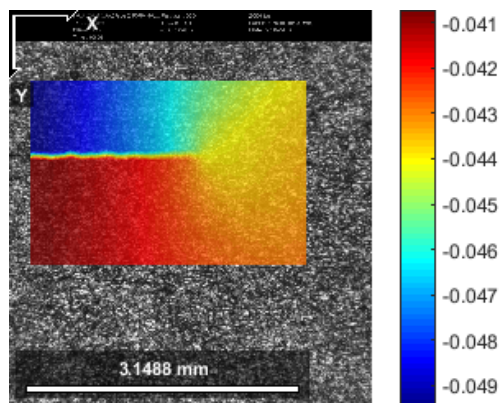


Figure 50: Vertical displacement field for use in determination of the crack position

3.5.6 Measuring crack opening displacements and the effective SIF using DIC

Following section describes a procedure of measuring the CODs using DIC. The method is inspired by work of Tong et al. [57], Vasco-Olmo [59] and Gonzáles et al. [61]. The main differences, and their influence on the results will be presented in discussion section of the report. The main goal with measuring the COD was to find the effective SIF, ΔK_{eff} . This can be achieved by using the opening load P_{op} instead of minimum load when calculating the SIF, or SIF range as described in section 2.2.4. The CODs were found by selecting few pairs of measuring points, where for each pair, one point is placed above, and the second point is placed below the crack. The difference in vertical distance between points in each pair during the whole load cycle is used to determine COD. Such pair of measuring points is presented at figure 51a.

To ensure the best quality of the results, the distance between the measuring points in each pair, the horizontal distance from measuring points to the crack tip, and the amount of measuring pairs has to be determined. In this work it has been done employing method described by Vasco-Olmo [59] in their paper. Let the $L1$ determine horizontal distance from measuring pair of points to the crack tip, let also $L2$ determine the vertical distance from measuring point to the crack. The verification of optimal location of measuring points is done by measuring the COD at the maximum load, where the COD is a function of one of the parameters, while the other parameter is maintained constant. Figure 52a shows COD as function of $L1$, while figure 52b shows COD as function of $L2$. It can be seen from figure 52a that the COD becomes larger as measuring pair of points is placed longer away from the crack tip in horizontal direction. It can be also seen that for given $L1$, the COD is increasing until it reaches a stable value which doesn't change significantly as one increases the vertical distance $L2$. The second observation can be confirmed by looking at figure 52b where the COD for given $L1$ increases until certain value of $L2$ is reached, after passing this value the COD flattens out. The choice of the $L2$ distance is clear, it should be a value in region where changes in COD are small when $L2$ increases. Choice of $L1$

distance is not so obvious, in this work, the CODs were measured at several distances to the crack tip: 5, 10, 15 and 20 pixels away from the alleged crack tip. This type of analysis was performed for all C(T) specimens for use in DIC, the $L1$ and $L2$ values are presented in result section.

For analysis of COD, a proper sampling rate should be selected. Yusof and Withers [41] and Gao et al. [1] proposed using 14 or 24-35 images per one loading cycle respectively in their works when running the FCG test. Since the high-speed camera used in this work allows using a much higher amount of images per loading cycle without any trade-off in spatial resolution, the decision of using 200 images per cycle was made. The reference image used in the DIC analysis correspond to the image when the load was at its minimum, also $P_{max} \times R$.

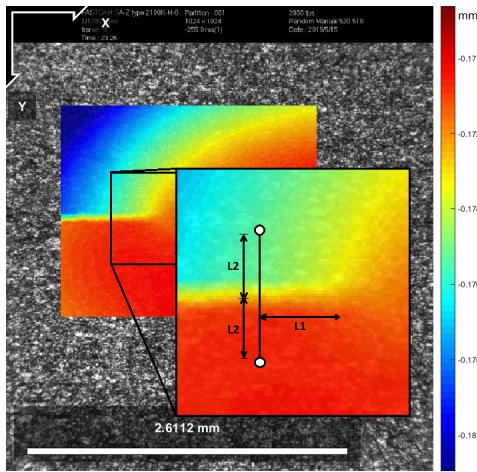
The testing machine loaded the sample with load shape corresponding to the sine-wave, and since the images were recorded with constant sampling rate, interpolation was necessary in order to fit the load at given time to the frame in the series of images. This has been done using following function:

$$P = \text{mean load} + \text{load amplitude} \times \sin(2\pi ft - \frac{\pi}{2}) \quad (60)$$

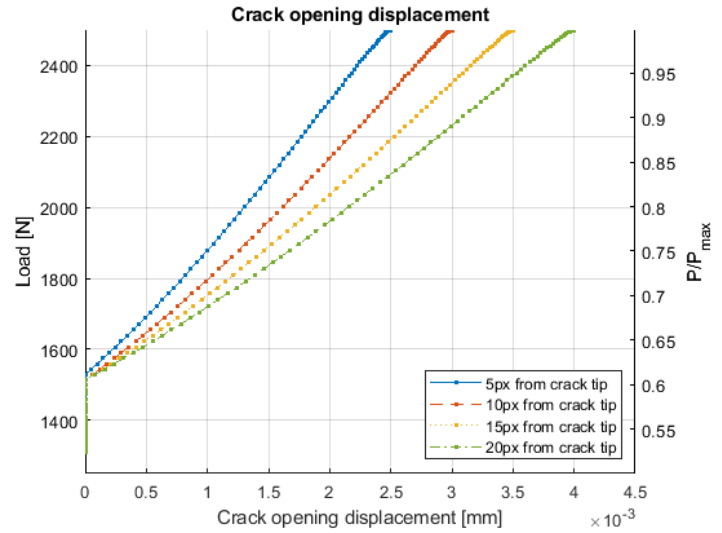
Where f is the test frequency, and t is the time. In addition, during test 5 the cameras were triggered directly from fatigue testing machine without using the triggering equipment developed for purpose of this work. Unfortunately, the delay between the triggering and the top/bottom of the sine wave was random, and the image corresponding to the maximum load P_{max} had to be found in post-processing, for DIC method by looking at the symmetry of COD curve when plotted as function of time (or images acquired). The CODs obtained using the method described in this section here are presented in figure 51b, in this example a set of artificial CODs was created. It can be seen that in the beginning of specimen loading there is no increase in the COD values even though the load increases. It changes when the specimen passes certain load value, called opening load P_{op} . The effective SIF is

found using this P_{op} value and following relation valid for the C(T) specimen:

$$\Delta K_{eff} = \frac{P_{max} - P_{op}}{B\sqrt{W}} f\left(\frac{a}{W}\right) \quad (61)$$

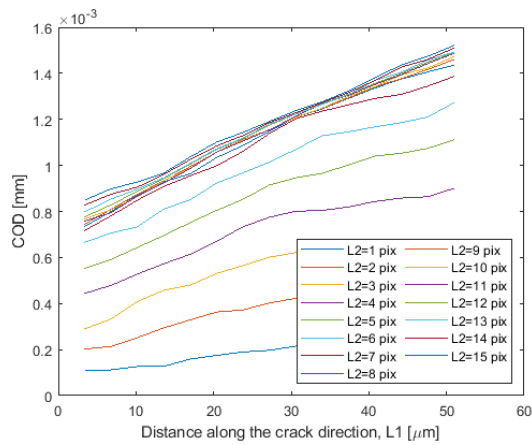


(a) A pair of measuring points with $L1$ and $L2$ indicated

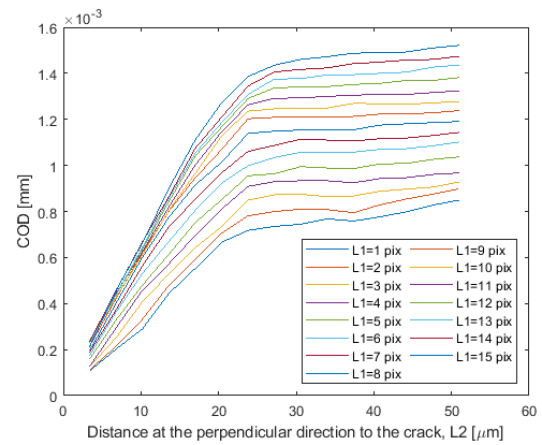


(b) Applied load as function of COD

Figure 51



(a) COD as function of horizontal distance $L1$



(b) COD as function of vertical distance $L2$

Figure 52: Determining optimal parameters for COD calculation

3.5.7 Stress analysis and plastic zone size determination using DIC

One of the major goals of this work was to estimate the size of the plastic zone based on data from FCG experiments and compare it to the theoretical models and the results obtained using IRT. Following procedure is based on the method proposed by [1] and [58], both discussed in section 2.4.3. Gao et al. [1] in their work used *Ncorr* software, which is also a case in this work.

To find the stress field out of the strain fields, the latter one can be extracted directly after the analysis in *Ncorr* in form of an 2D arrays with strain field for each image analysed. The DIC analysis for the stress analysis and the plastic zone determination was carried out using only two images, one reference image with unloaded specimen, and a target image where the specimen is loaded with maximum load P_{max} . The strains to be analysed have to follow the Lagrangian description since the dimensions of the 2D arrays remain the same for all images analysed. The problem of stress calculations is simplified to the two dimensions since the 3D analysis of FCG is out of the scope of this work. The strains provided by *Ncorr* are ε_{xx} , ε_{yy} and ε_{xy} . They follow Cartesian coordinates and correspond to strain in x-direction, strain in y-direction and shear strain respectively. The stress fields can be found using mentioned strains, and assuming either *plane stress*, or *plane strain* conditions. The former one assume situation where $\sigma_{zz} = \tau_{xz} = \tau_{zy} = 0$ which is a case at free surface, the later one assumes that $\varepsilon_{zz} = \varepsilon_{yz} = \varepsilon_{zx} = 0$. The formula for calculating stresses making *plane stress* assumption according to [121] is:

$$\begin{bmatrix} \sigma_{xx} \\ \sigma_{yy} \\ \sigma_{xy} \end{bmatrix} = \frac{E}{1-\nu^2} \begin{bmatrix} 1 & \nu & 0 \\ \nu & 1 & 0 \\ 0 & 0 & \frac{1-\nu}{2} \end{bmatrix} \begin{bmatrix} \varepsilon_{xx} \\ \varepsilon_{yy} \\ 2\varepsilon_{xy} \end{bmatrix} \quad (62)$$

While the stresses assuming the *plane strain* conditions can be calculated using:

$$\begin{bmatrix} \sigma_{xx} \\ \sigma_{yy} \\ \sigma_{xy} \end{bmatrix} = \frac{E}{(1+\nu)(1-2\nu)} \begin{bmatrix} 1-\nu & \nu & 0 \\ \nu & 1-\nu & 0 \\ 0 & 0 & \frac{1-2\nu}{2} \end{bmatrix} \begin{bmatrix} \varepsilon_{xx} \\ \varepsilon_{yy} \\ 2\varepsilon_{xy} \end{bmatrix} \quad (63)$$

Since the stresses are found according to generalised Hooke's law, the stress field is accurate only in the elastic field. While applying this method to FCG problems, the stresses in elastic regime are accurate, but once the yield strength strength is exceeded, the stresses approximated this way are overestimated. Although this limitation, the shape of the plastic zone is clear and can be defined by connecting points where the equivalent von Mises stress σ_v is equal to the yield stress of the material. The equivalent von Mises stress can be found using terms of the Cauchy stress tensor components, or using stresses in Cartesian coordinates directly:

$$\begin{aligned} \sigma_v^2 &= \frac{1}{2}[(\sigma_{11} - \sigma_{22})^2 + (\sigma_{22} - \sigma_{33})^2 + (\sigma_{33} - \sigma_{11})^2 + 6(\sigma_{23}^2 + \sigma_{31}^2 + \sigma_{12}^2)] \\ &= \frac{1}{2}[(\sigma_{xx} - \sigma_{yy})^2 + (\sigma_{yy} - \sigma_{zz})^2 + (\sigma_{zz} - \sigma_{xx})^2 + 6(\sigma_{yz}^2 + \sigma_{zx}^2 + \sigma_{xy}^2)] \end{aligned} \quad (64)$$

For 2D case and stresses in Cartesian coordinates, the formula for equivalent von Mises stress simplifies to:

$$\sigma_v^2 = \sigma_{xx}^2 + \sigma_{yy}^2 - \sigma_{xx}\sigma_{yy} + 3\sigma_{xy}^2 \quad (65)$$

Figure 53 shows the image used for determination of the plastic zone size. It's a bitmap where the white areas correspond to the points where the equivalent von Mises stress is equal to, or exceed $\sigma_{0.2\%}$. In this work, the size of the plastic zone for HSI has been determined in three ways: by taking the height, area, or the radius of the plastic zone. The radius presented in result section is a square-root of the area divided by π , not a radius measured from the bitmap. The blue contour on figure 53 shows the ROI for which

the area and maximum height is to be calculated. The size in mm was simply found by multiplying the difference in pixels with the resolution given as mm per pixel.

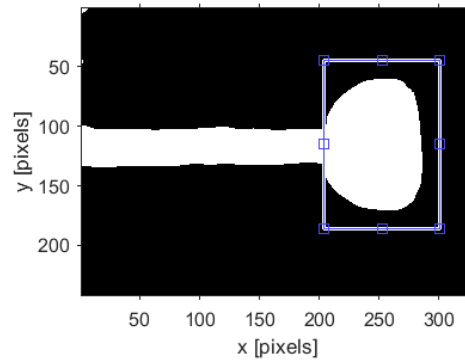


Figure 53: Zone of plastic deformation, elements where the equivalent von Mises stress exceed the $\sigma_{0.2\%}$ are represented with white colour

3.6 Experimental Procedures for Acoustic Emission

In this work, a combined approach of both traditional hit-based method, and waveform streaming is used. While waveform streaming provides superior information when compared to the traditional method, its intermittent nature during FCG means that information is lost between streaming samples. This information can (at least partially) be obtained by the hit-based approach. The validity of the hit-based data can then be evaluated by comparison of concurrent hit and streaming data.

3.6.1 Hit based procedures

Source Localisation

Linear source localisation of the hit data was attempted using the source localisation feature of the *AEwin* software. This was difficult for several reasons. For one, the small size of the specimen required very precise settings of both the wave velocity parameters,

and the event definition parameters. Wave velocities are in the order of 10^3m/s [122], while the distance from the AE transducers to the crack plane was in the order of 10^{-2}meter . Another problem was the limitation of wave velocities in the software. The AE signal consists of several wave modes with differing velocities[122], which can be scattered due to microstructural conditions, as mentioned in section 2.6.1. Accurately determining a single, averaged, wave velocity for the wave modes was difficult. In the end, tabulated values taken from the *AEwin* software were used: $5.66\text{E}6\text{mm/s}$ for longitudinal waves, $3.12\text{E}6\text{mm/s}$ for shear waves, and $2.78\text{E}6\text{mm/s}$ for surface waves. The timing parameters were selected based on recommendations in the user manual [71]. The average wave velocity was assumed to be $3.3\text{E}6\text{mm/s}$, and the event definition value was set to 100. The event lockout value was ignored, as it was not relevant for the test set up. For the other values, default settings were used. The placement of the sensors in the software were set as $\pm 20\text{mm}$ vertically and -25mm horizontally in relation to the notch position.

Importing and filtering of hit data and waveforms

From the ASCII text file output, the hit data was imported to MATLAB for processing. Due to the weak AE production in the 316L steel, the setting of the hit definition parameters proved imprecise, and the default values were used, as previously mentioned in section 3.2.3. Many hit waveforms were truncated, or consisted of a single voltage peak from the continuous signal crossing the threshold. It was therefore necessary to filter out falsely detected hits. For example, hits which had a duration less than $100\mu\text{s}$ were deemed to be due to sources other than genuine AE, and durations above $1024\mu\text{s}$ exceeded the recording length of the hit waveforms. In the 4th FCG test, the threshold was initially set too low, leading to the cyclic continuous signal crossing the threshold value of 35dB during parts of the test, leading to the threshold to be increased by 1dB while the test was running. Therefore, all hits with a peak amplitude corresponding to the initial threshold level were removed.

Due to the erroneous ASCII output settings during some tests, only a few parameters were directly recorded to the outputted data text file. In order to extract more information, it was therefore necessary to further analyse the waveform of each recorded hit. The hit waveforms corresponding to the remaining hits after filtering were identified from the timestamp in their filenames, and copied for analysis. Due to the amount of files, Windows struggled to read the folder containing the waveforms, and they were therefore split into smaller subfolders and analysed incrementally. Each hit waveform consisted of a .csv file with 1024 rows of raw voltage data. In order to obtain the true signal in the time-domain, the voltage values were converted to their pre-amplified values by dividing by the decibel to linear conversion factor, which for 60dB was $10^{60/20}$. The corresponding time stream was found by dividing the row numbers by the sampling rate to obtain time values in seconds.

Implementing Various Hit Data Parameters

Once the time-domain representation of the hit signal was obtained, it was possible to extract various signal parameters. The RMS was calculated for each hit waveform by use of the integrated MATLAB *rms* function. The signal energy was calculated by the integration of the squared voltage of each hit waveform. For simplicity, the trapezoidal rule was used for integration, with step size equal to the time stream vector increment. The absolute energy was then be obtained by dividing the signal energy by the AE system's reference resistance, which was $10\text{k}\Omega$ [71].

Several spectral parameters were also obtained from the waveform. The method of estimating the PSD of the waveform is explained in section 3.6.2.

The frequency corresponding to the maximum amplitude of the signal, *peak frequency*, was found from the maximum value of the spectral density array. Due to the large amount of hit waveform files, plotting each waveform to describe the signal was unreasonable. The statistical moments up to the fourth order were therefore calculated for each hit in order

to characterise the waveform.

The mean frequency of the waveform was calculated using an integrated MATLAB function *meanfreq*, which uses the power values of the estimated PSD to calculate the mean. The frequency variance was then estimated as

$$\sum_{i=1}^n p_i \cdot (x_i - \bar{x})^2$$

where p_i was the probability mass of each frequency based on the PSD for each frequency, analogous to using a histogram to estimate the probability of a voltage value. x_i was the frequencies and \bar{x} the mean frequency, as calculated previously.

The *skewness* of the frequency distribution was calculated as

$$\frac{\frac{1}{n} \sum_{i=1}^n (x_i - \bar{x})^3}{[\frac{1}{n-1} \sum_{i=1}^n (x_i - \bar{x})^2]^{3/2}}$$

To measure the "peakedness" of the PSD, the fourth order moment, *kurtosis* was calculated. For easier comparison to other statistical parameters, the *excess kurtosis* was used in specific:

$$\frac{\frac{1}{n} \sum_{i=1}^n (x_i - \bar{x})^4}{[\frac{1}{n} \sum_{i=1}^n (x_i - \bar{x})^2]^2} - 3$$

In addition to these conventional parameters, information entropy, as described in section 2.6.6 was implemented. Different approaches to determine the probability mass function, p . A first order estimate was made assuming a Gaussian distribution of the signal voltage. Visual inspection of the voltage distribution for selected hit waveforms suggested that this was reasonable. To improve the probability mass estimate, high resolution (low bin width) histograms were used to estimate the discrete probability mass function, inspired by the methods used in Chai et al. [99] and Tanvir et al. [100]. The bin size was set to be twice the inverse of the number of sampling points. This provides close to the maximum resolution, but reduces the effect of anomalies, since there's some averaging performed. Figure 54

shows an example of the resulting histogram for a hit waveform.

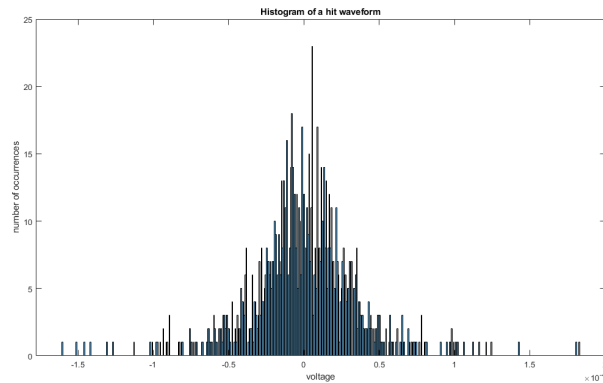


Figure 54: Example of histogram used for estimation of hit voltage probability mass function

The information entropy could then be calculated for each hit based on equations 42 and 43 in section 2.6.6.

Hit Data Clustering

Cluster analysis was attempted based on the hit data. Different approaches were used, one based on the time stream of the signal, several mono-variable analysis using individual hit parameters, and a multi-variable approach where multiple hit parameters were applied. Additionally, several cluster algorithms were tested: from the simple *k-means*, to brief attempts at the more advanced mean-shift clustering and *DBSCAN* were also performed. Due to problems analysing the Test 4 data, the use of clustering was largely abandoned until after Test 6, at which point the remaining time to perform analysis was limited. For this reason, the cluster analysis was mostly limited to the k-means algorithm.

Implementation of k-means clustering was trivial, and consisted of using the internal *MATLAB* function *kmeans*, which utilises the algorithm described in section 2.6.6. The data to be clustered (rows) and the variables to cluster by (columns) are inputted into the function, along with the requested number of clusters. The function then outputs a row vector containing the cluster number which each corresponding row of data belongs to. Selection

of variables to perform clustering, by was more difficult. The initial choice was using the timestream of the hit waveforms. However, this proved unfruitful in practice. This might have been due to the fact that the timestream consisted of at least 1024 individual values, and was therefore treated by *kmeans* as 1024 or more individual columns of variables, making it difficult to group them into meaningful patterns. Another problem was the size of the matrix which *kmeans* had to analyse. For Test 4, there was more than 300 000 hits, and the resulting 300 000 by 1024 array was unwieldy.

Another approach was the use of one, or more, of the calculated hit parameters. An advantage of this method was the fact that the array size was greatly reduced, since there is only one column for each parameter. A disadvantage was that since the signal was transformed into a single value, the data no longer directly represented the physical signal. The use of multiple variables describing different characteristics of the signal, such as an energy measurement (RMS together with a measure of the temporal distribution (e.g rise-time), and information content such as Shannon entropy was thought to alleviate this.

The final approach to data selection was the PSD of hit waveforms, as used by previous researchers [123–125]. This had the advantage of fully representing the signal with far fewer data points than the timestream, and distinguishing patterns is easier in the spectral domain[124], since the spectral data is not influenced by small fluctuations in the temporal location of the waveform. However, due to strong resonant behaviour near resonance frequencies, in particular of the Nano-30 transducer, the spectral content of most hit waveform was very uniform or dominated by the resonance frequencies. The accuracy of the clusters, as determined by the PSD, could therefore be reduced.

In order to evaluate the quality of the clustering, the silhouette method was used. The silhouette value is a measure of similarity of the data in each cluster compared to data of other clusters, ranging from -1 to 1. The higher the value, the more the point matches its cluster and the poorer it matches other clusters, and vice versa for a lower value. The silhouettes were calculated using the *MATLAB* function *silhouette*. *silhouette* uses the

data set and the corresponding cluster as input, and returns the silhouette value and plot. For evaluation of the silhouettes, the *MATLAB* function *evalclusters* was used, with the method specified as silhouette. The distance calculation was performed using the squared Euclidean.

For tests with more than around 50 000 hits, the processing time became too great for the computer available for use, and quantification of the cluster quality was not possible. For these cases, only visual inspection of the waveform, PSD, and STFT was used. In order to select representative examples from each cluster, 5 random samples from each cluster as obtained from each analysis performed, were inspected.

AE Count Rate vs Stress Intensity Range

In a method similar to the one described in section 3.5.2 for obtaining Paris' FCG parameters, it is possible to find the constants C_4 and n , describing the relation between the AE count rate and ΔK as in equation 40:

$$\frac{d\eta}{dN} = C_4(\Delta K)^n \quad (40)$$

The crack length measurements were taken from the IR recordings. As a result, there was a huge discrepancy in the amount of data points between the hit data and crack length data. For example, in Test 4 there was around 305 000 recorded hits after filtering, and 101 crack length measurements. In addition, the hits were not evenly distributed along the crack length measurements due to the irregular nature of AE and the variable recording frequency of the IR-camera. In order to overcome this issue, the hits corresponding to each crack measurement interval were grouped together in a cell array. Two methods of determining hits and cycles were then employed.

Method one was using the average values of the hit numbers and cycle numbers for the hits in each cell corresponding to a crack measurement. Method two was using the maximum

hit and cycle numbers for each cell. In both cases the count rate was calculated using the secant method as:

$$\left(\frac{d\eta}{dN}\right)_{\bar{\eta}} = (\eta_{i+1} - \eta_i) / (N_{i+1} - N_i) \quad (66)$$

Where $\left(\frac{d\eta}{dN}\right)_{\bar{\eta}}$ is the average count rate between the given crack length measurement intervals, η_i the calculated total counts corresponding to crack length measurement i and N_i the calculated cycles elapsed at crack length measurement i . Due to the averaging used for establishing the count rates, there was a surplus ΔK value. To fix this, the ΔK values were averaged as well. The constants C_4 and n were then found by linear interpolation of the logarithmic representation of equation 40 using the *MATLAB* statistics toolbox.

3.6.2 Waveform streaming procedures

PSD estimation

The spectral characteristics were extracted for both the streamed waveforms and hit waveforms by estimating the signals' PSD. This was done by employing Welch's method, as described in section 2.6.6. *MATLAB* has an internal function, *pwelch*, for employing Welch's method. By default, the function tries to use as close to 8 Hamming-type windows as possible with 50% overlap, with the number of DFT points being the highest of 256 or the next power of 2 larger than the window size. If the data does not fit to an integer number of elements, the data set is truncated. It is not possible to change the window function used in the *pwelch* function to something other than Hamming window, which is a good general purpose window function. Due to the unpredictable nature of the AE signal, this is not necessarily a problem. But since the Hamming window does not reach zero at its edges, some spectral leakage will occur with some edge discontinuity. For the hit waveforms with length 1024, this would result in 7 window segments of 256 elements and 512 DFT points. The resulting spectrum using these values has a low resolution, and the PSD is thus very coarse. In order to increase the resolution, the number of DFT points must be increased. The maximum window size is the sample length of 1024, but the data

is known to be noisy, so the averaging effect of Welch’s method is desirable. Fitting a window size and overlap without resulting in truncation of the data was imperative due to the already small data length and improper hit detection settings. After trial and error, a window size of 1/2 the sampling length, and overlap of 50% was found to work well for the hit waveforms. This resulted in 3 windows of 512 elements and 1024 DFT points. For the streamed waveforms, it was more difficult to select the parameters of the Welch transform. It was sometimes of interest to focus on a small part of the signal, such as near the peak of the load curve, while other times a whole cycle was analysed. It was also desirable to keep the scale similar to that of the hit waveform, if possible, so that the data could be compared to each other.

STFT

STFT was performed for both streamed waveforms and hit waveforms. This was done by employing a custom *MATLAB* code based on the STFT theory from section 2.6.6, as there were no *MATLAB* function for performing STFT until version 2019a. Unlike the *MATLAB* function *pwelch*, the window function was not fixed, and different window functions were therefore tested. By trial and error it was found that a Blackman window worked better than the Hamming window of *pwelch*, which might be due to the increased side-lobe attenuation which reduces the spectral leakage. As mentioned in section 2.6.6, there is a trade-off between temporal and frequency resolution in employing STFT. Additionally, it is difficult to obtain the correct window length for such a complex and erratic signal as AE. Therefore, both a wideband (high frequency resolution) and narrowband (high temporal resolution) were used in the analyses of the same data. In this manner it was possible to achieve a ”higher” resolution by deductions from comparison of the wideband and narrowband STFTs, and be more likely to obtain a good window size for the specific signal being analysed. For the hit waveforms, the window sizes used were 256 (1/4 of the signal length) for the wideband and 16 for the narrowband. These were found by trial and error after approximations based on the procedure used by Röbel [126]. The fundamental frequency

was estimated as 125kHz, which gave a window length of 50 μ s, or roughly 1/10 of the signal length.

For the waveform streams, the primary interest was to analyse the signal near peak load, as this is the most likely temporal location of emissions, as mentioned in section 2.5.2. A common range used by researchers is the top 20% of the load [80], which for the load case used in this report was ± 0.02180 s from the peak load, i.e. almost half the signal. This would result in a cropped signal of 87181 frames, which is an inefficient number for STFT, as it is not a power of 2. In addition, using this width proved too computationally intensive to perform on each acquisition. Therefore, 32768 frames were used instead, which is roughly equal to the top 15% of the sine load, or top 7% of the total load. By similar considerations as for the hit waveforms, window lengths for the wideband and narrowband were 128 and 1024 frames, respectively. Since a lot of emissions during some of the FCG tests occurred at mean or minimum load, the STFT was performed with the same parameters on these loads as well.

Waveform Stream Decomposition

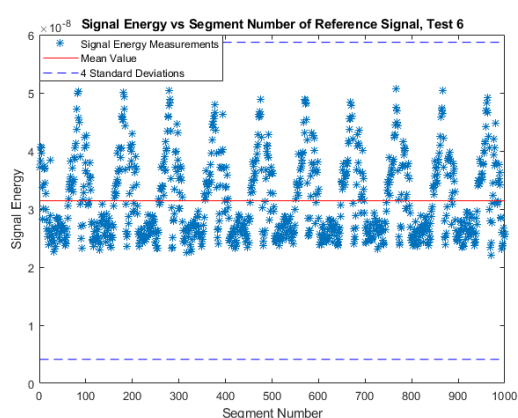
As mentioned in previous sections, the hit-based method's main weakness is the fact that the signal needs to cross a voltage threshold value to be recorded. Valuable data from AE signals which don't cross the threshold might therefore be lost. A method of decomposing the streamed waveforms into smaller segments attempting to extract and quantify signals associated with crack growth, was therefore implemented. This was done in a manner based on the work of Zhang et al. [127], but with a slight improvement. Instead of comparing a segment with the mean and standard deviations of its parent stream, they were compared with the values of The method was implemented as follows:

Each streamed waveform was divided into a series of "quasi-hit waveforms" with a length of about 1ms (2048 datapoints), which is the same length as the hit waveforms of Test 6. Then various signal parameters were extracted from the waveform segments, in the same

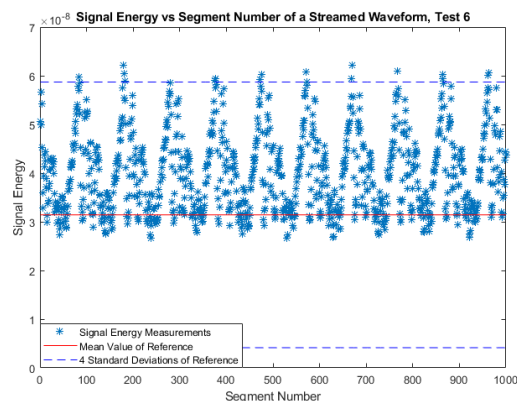
manner as for the hit waveforms discussed previously.

The parameters from each segment were then compared to values obtained from a reference stream representing noisy data. If the parameter value for a given segment exceeded $\bar{x} \pm 3\sigma$, where \bar{x} was the parameter's mean value in the reference stream, and σ the corresponding standard deviation, it was deemed an outlier, and therefore presumed to be related to plasticity or crack propagation rather than noise. Only the data corresponding to these outliers was then saved. For squared parameters, such as signal energy, a higher σ -count was used.

An example result of the procedure applied to a waveform stream's signal energy (in arbitrary units), is shown in figure 55. From the figure it can be seen that 16 outliers were identified from the segments of this stream.



(a) Signal energy of each segment of the reference signal, with mean and 4σ values



(b) Signal energy of each segment of a streamed waveform signal, with mean and 4σ values of the reference signal

Figure 55: Waveform stream decomposition method applied to signal energy.

It could be argued that this method is just roundabout way of thresholding the signal. But since it is based on the full streamed signal, deviations from the background signal can be obtained on other bases than just voltage. Another advantage is that since it is based around partitioning the signal into lengths similar to those of the hit waveforms, the data may more directly be compared.

4 Results

4.1 Test summary

4.1.1 Tensile tests

Four tensile specimens were tested in addition to the FCG tests in order to find material properties, and observe the material behaviour necessary in analysis, and discussion of FCG tests. The tensile tests were displacement controlled with displacement rate (velocity) of $\dot{y} = 0.039$ mm/s which was supposed to correspond to the strain rate of $\dot{\epsilon} = 0.002$ 1/s on the region of reduced cross section with length of 19.5 mm.

4.1.2 Test 1

Test 1 was an initial test and was supposed to evaluate if all the equipment, and triggers work correctly, and evaluate the possible sources of error. It was performed with a maximum load of 1500N, a R of 0.1 and frequency of 10 Hz. During this test, the potential drop method was used to create FCG-curves. However, the results from ACPD are not in the scope of this work, and are not presented.

4.1.3 Test 2

The test 2 has failed immediately after start. It happened when the large load was suddenly applied while tuning the PID controller in the testing machine.

4.1.4 Test 3

Test 3 was used to determine the fatigue threshold, and it was performed using low maximum loads of 840 N, 880 N and finally 920 N with R of 0.1 and test frequency of 10 Hz.

The potential drop method was used for controlling the crack growth. The precracking of specimen 3 was also captured and used to qualitatively describe the crack initiation process.

4.1.5 Test 4

Test 4 was performed with a maximum load of 2500N, and a R of 0.5 to avoid closure as it causes more noise in AE data. The test was performed using potential drop monitoring, but only for an intuitive quantification of crack growth to adjust the sampling rate of the equipment. This was the last test where the potential drop method was used. The test itself went as planned, with the only exception, that due to improper limits in the test machine, the test stopped early in stage 3, but it seems like the beginning of stage 3 was captured. The cyclic load was applied without any breaks.

4.1.6 Test 5

Test 5 was performed with the same setup as test 4, so that the same max load of 2500N, and an R of 0.5 was used. The sampling rate was based on experience from test 4. The test itself went until failure, but the sampling frequency was not set up high enough, so no data were captured in stage 3. The last measurement was taken 5196 cycles before failure, and it looks like that was just before stage 3. The test was stopped after every measurement with the cameras, the load was decreased down to zero load, and a reference picture for the DIC analysis was captured.

4.1.7 Test 6

Test 6 was performed with the same loading condition as test 4, a max load of 2500N, and an R of 0.5. The idea behind the test was to capture stage III, so the sample was pre-cracked

to a total crack length of 14mm to reduce the test time. The test was continuous, and was stopped only once, just before stage III, to change the setup of the equipment.

4.2 Infrared Thermography

In this section, the results from IRT are shown. The results are only given for tests 4-6, as tests 1-3 were from an earlier project, and not this work. The methods and experimental setup have improved since then.

4.2.1 Thermoelastic parameter

A tensile specimen was subjected to an oscillating load. The maximum stress was set to 250MPa, and the R was set to 0.1. A first order discrete Fourier fit was made for each recording consisting of four loading cycles, at a frequency of 10Hz. A total of 25 measurements, shown in figure 56, were taken. This resulted in a K_t of $4.254 \times 10^{-6} \text{MPa}^{-1}$ and a standard deviation of $1.6334 \times 10^{-8} \text{MPa}^{-1}$ for that stress level. The value according to equation 13 (for $R=-1$) should be $4.005 \times 10^{-6} \text{MPa}^{-1}$. The difference in these values is 6.22%.

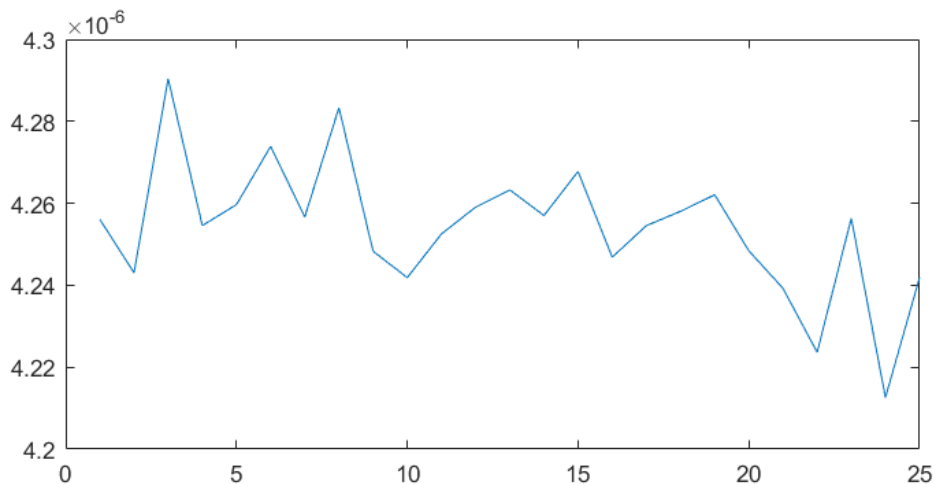


Figure 56: The values of K_t from the 25 measurements in MPa^{-1}

4.2.2 Filtering evaluation

This section shows some of the filtered pictures, to illustrate the filter performance. The figures consist of four pictures, the raw picture, the filtered picture, the resulting rest picture created by subtracting the filtered picture from the original one, and the Laplacian of the filtered picture. Every picture has a red circle, showing the crack tip position based on the Williams' series. Only test 6 is shown here, as it captured most of stage III, where the filtering was most challenging.

Test 6

In all of the pictures, the axes show pixel coordinates, and the colorbar shows temperature in °C for the original, filtered, and the rest pictures. The unit of the Laplacian picture is °C/pixel². Figure 57 shows a picture from mid stage II in the test and figure 58 from late stage II. The transition to stage III, or early stage III is shown in figure 59, and the well established stage III in figures 60 and 61, where the last one is a magnified view.

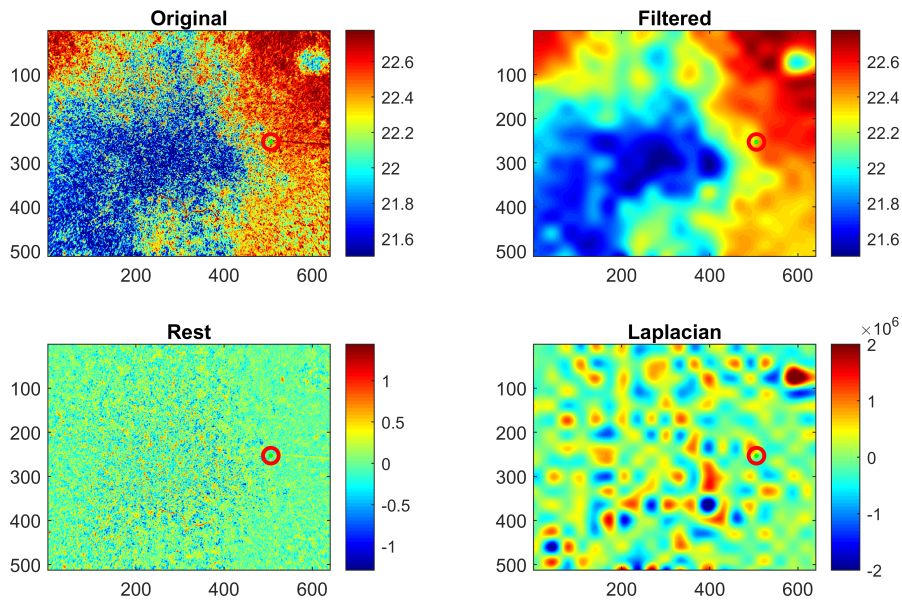


Figure 57: Filter performance from test 6, acquisition 1, frame 1, axis in pixel coordinates, and crack tip from Williams' expansion marked with red circle. The colorbar shows temperature in $^{\circ}\text{C}$ for the original, filtered, and the rest pictures and in $^{\circ}\text{C}/\text{pixel}^2$ for the Laplacian picture.

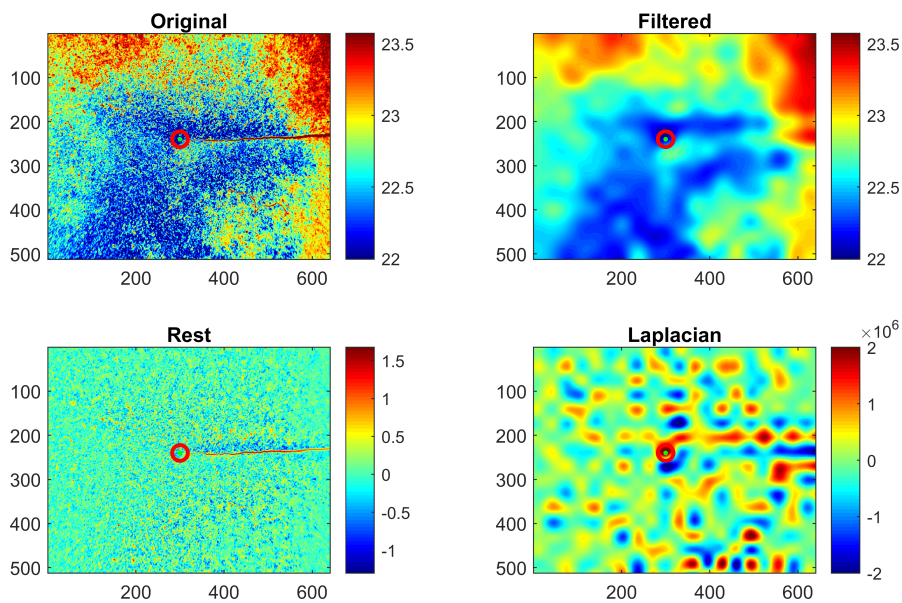


Figure 58: Filter performance from test 6, acquisition 130, frame 1, axes in pixel coordinates, and crack tip from Williams' expansion marked with red circle. The colorbar shows temperature in $^{\circ}\text{C}$ for the original, filtered, and the rest pictures and in $^{\circ}\text{C}/\text{pixel}^2$ for the Laplacian picture.

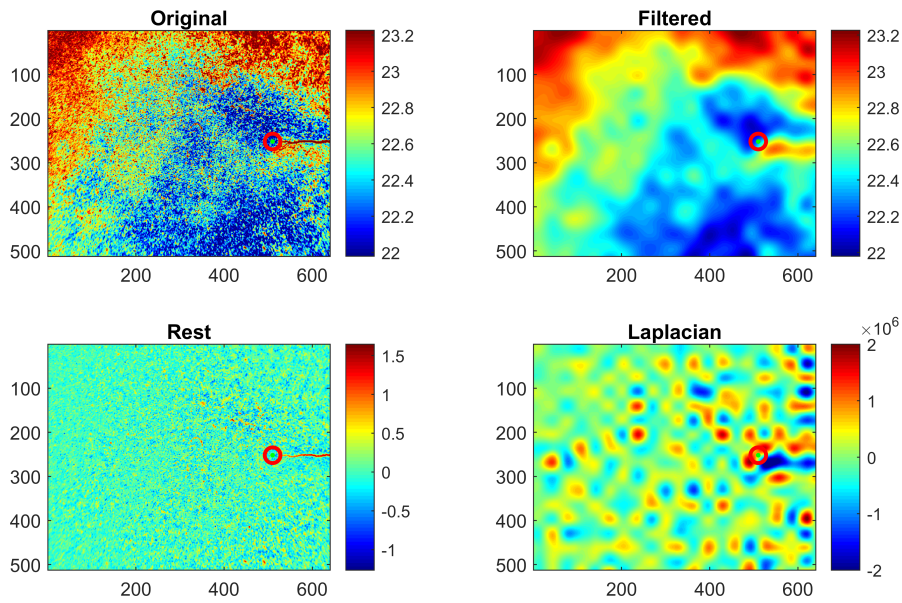


Figure 59: Filter performance from test 6, acquisition 140, frame 1, axes in pixel coordinates, and crack tip from Williams' expansion marked with red circle. The colorbar shows temperature in $^{\circ}\text{C}$ for the original, filtered, and the rest pictures and in $^{\circ}\text{C}/\text{pixel}^2$ for the Laplacian picture.

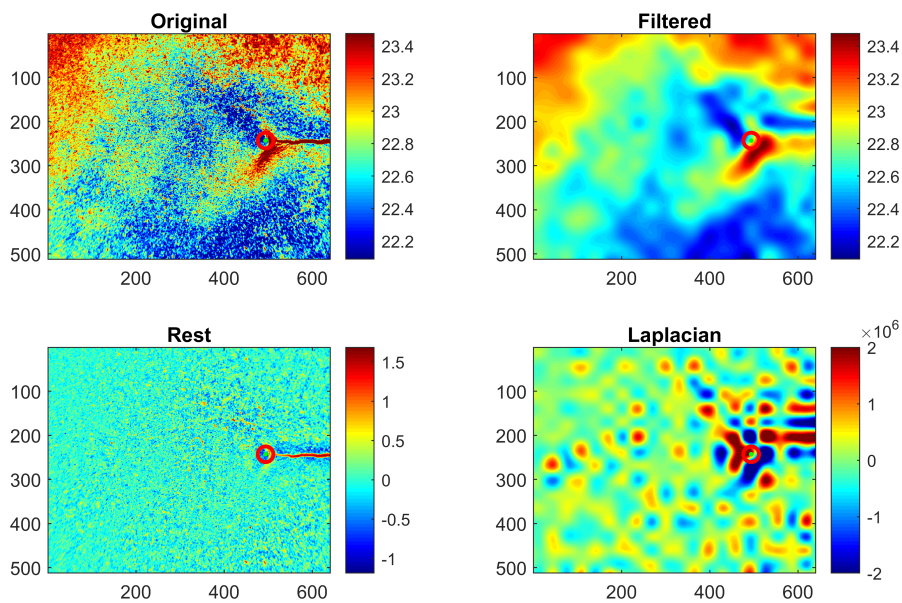


Figure 60: Filter performance from test 6, acquisition 143, frame 1, axes in pixel coordinates, and crack tip from Williams' expansion marked with red circle. The colorbar shows temperature in $^{\circ}\text{C}$ for the original, filtered, and the rest pictures and in $^{\circ}\text{C}/\text{pixel}^2$ for the Laplacian picture.

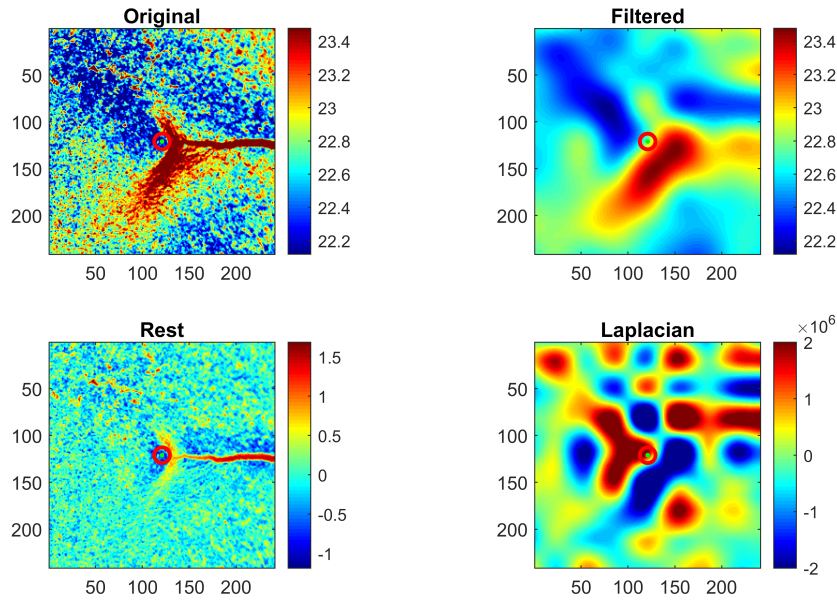
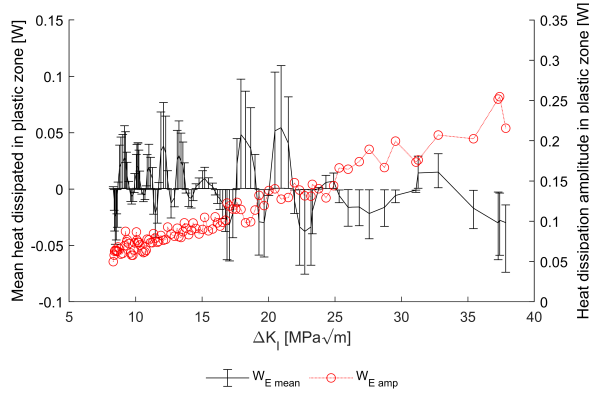


Figure 61: Filter performance from test 6, acquisition 143, frame 1, magnified to show the region close to crack tip. Axes in pixel coordinates, and crack tip from Williams' expansion marked with red circle. The colorbar shows temperature in $^{\circ}\text{C}$ for the original, filtered, and the rest pictures and in $^{\circ}\text{C}/\text{pixel}^2$ for the Laplacian picture.

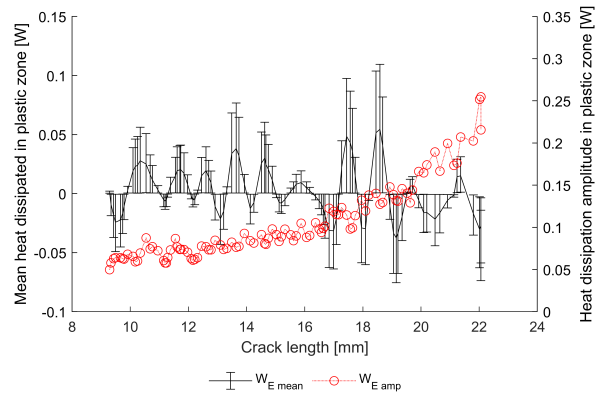
4.2.3 Energy dissipation

The heat dissipation is measured in three different ways. As heat dissipated per volume at crack tip, as heat dissipated per volume in a region around the crack tip defined in section 3.4.6, and as total heat dissipated in the same region. To make comparison with other techniques the plots are made both versus cycle count, and the theoretical stress intensity factor range. The temperature in the sample, and plastic zone, are also shown. Finally, since the test was stopped after every trigger in test 5, the temperature behaviour near the crack tip (a 11 by 11 pixel window surrounding the crack tip) is illustrated. These graphs are based on raw data, with no filtering or post processing at all.

Test 4

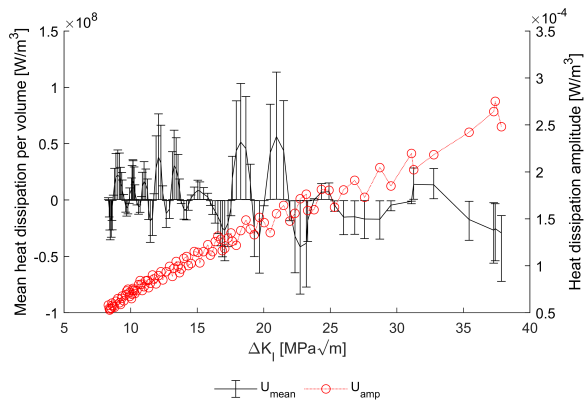


(a) Vs. stress intensity range

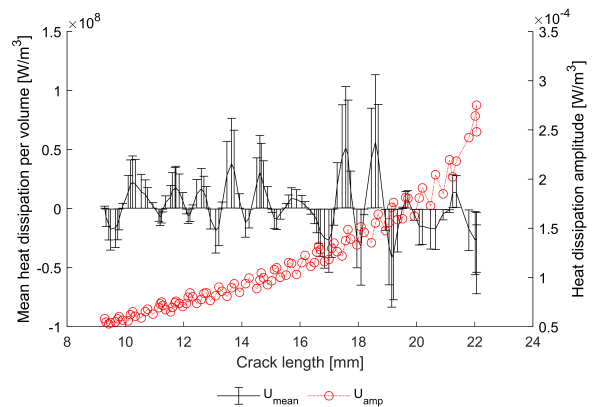


(b) Vs. crack length

Figure 62: Total heat dissipated in plastic zone. Black line is the average value with error bars, and the red line is the amplitude.

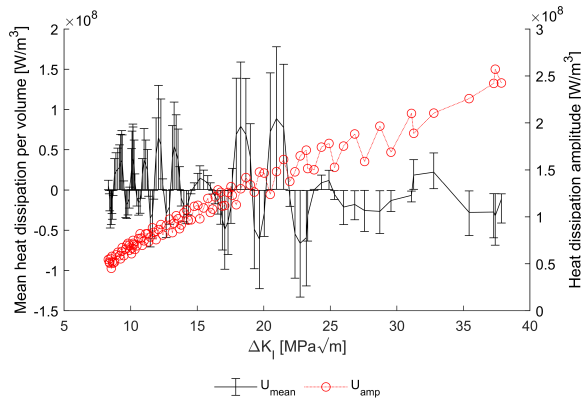


(a) Vs. stress intensity range

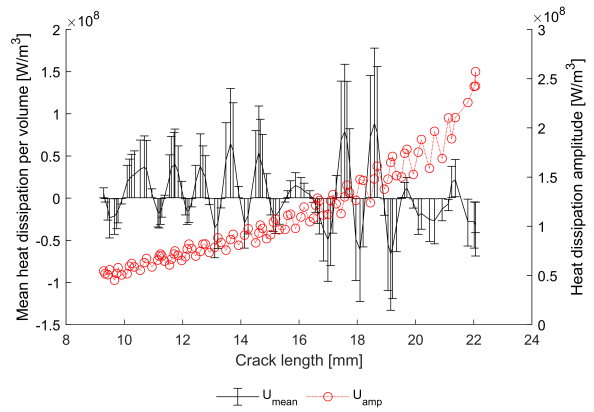


(b) Vs. crack length

Figure 63: Total heat dissipated in plastic zone per volume. Black line is the average value with error bars, and the red line is the amplitude.

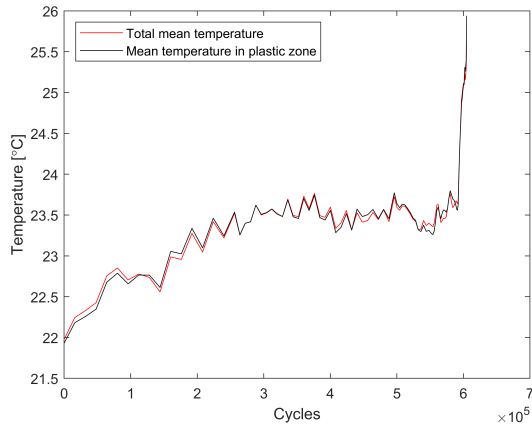


(a) Vs. stress intensity range

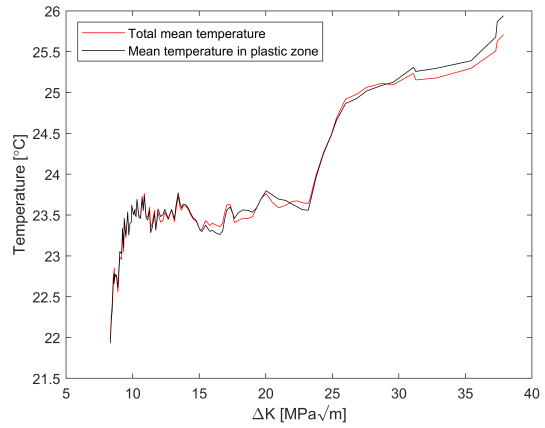


(b) Vs. crack length

Figure 64: Heat dissipated at crack tip per volume. Black line is the average value with error bars, and the red line is the amplitude.



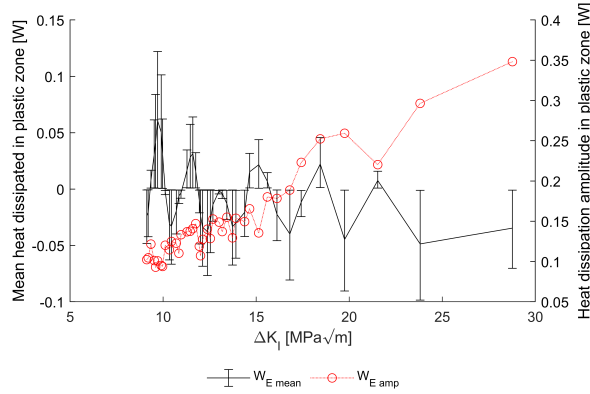
(a) Vs cycle count



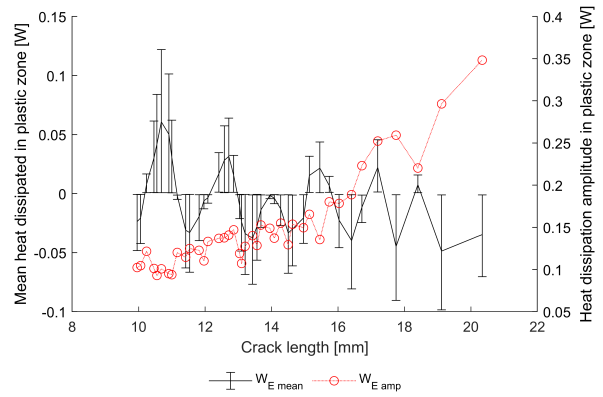
(b) Vs. stress intensity range

Figure 65: Temperature measured in the sample and the region of interest for energy calculation.

Test 5

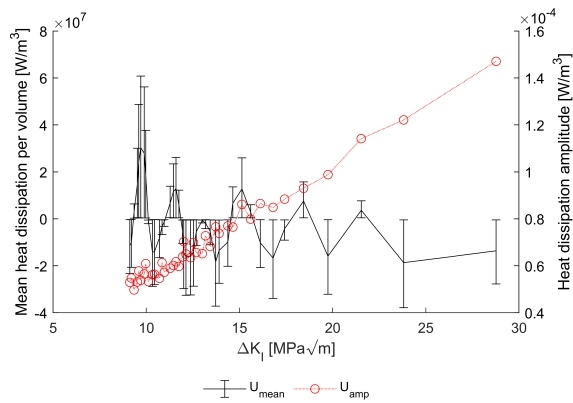


(a) Vs. stress intensity range

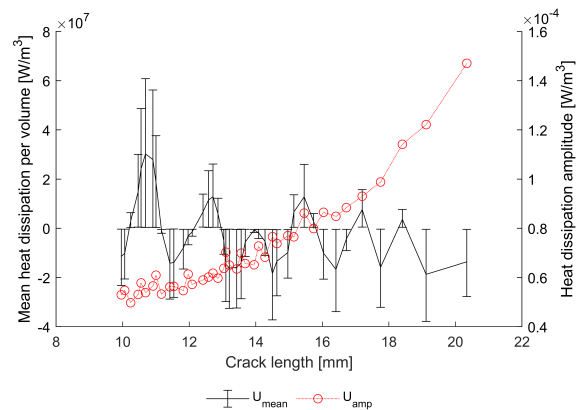


(b) Vs. crack length

Figure 66: Total heat dissipated in plastic zone. Black line is the average value with error bars, and the red line is the amplitude.

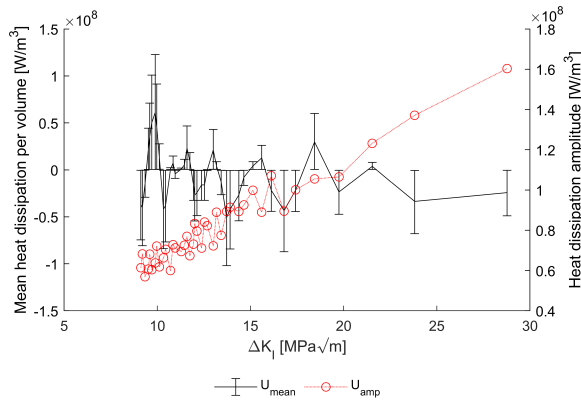


(a) Vs. stress intensity range

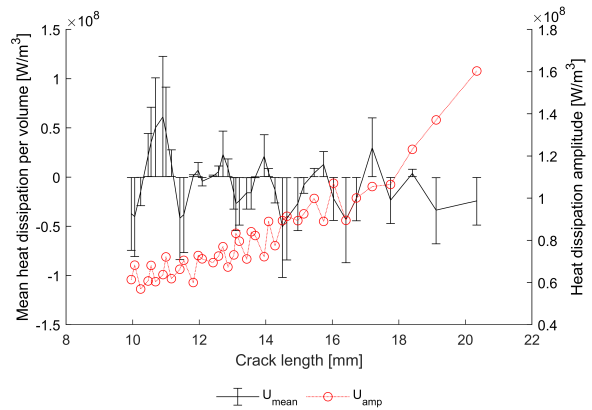


(b) Vs. crack length

Figure 67: Total heat dissipated in plastic zone per volume. Black line is the average value with error bars, and the red line is the amplitude.

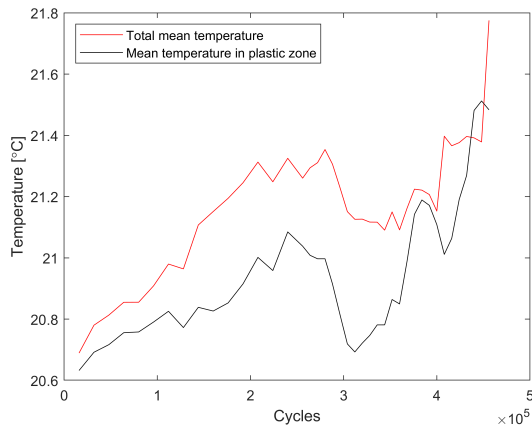


(a) Vs. stress intensity range

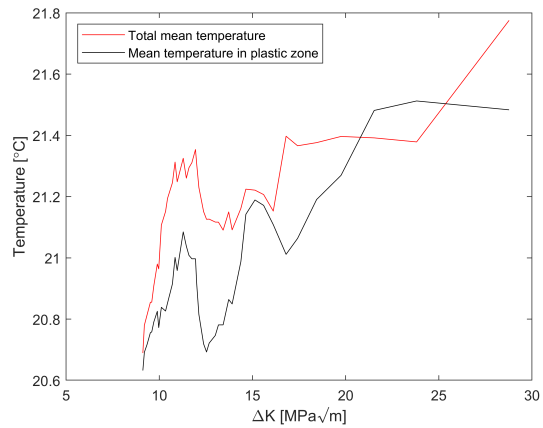


(b) Vs. crack length

Figure 68: Heat dissipated at crack tip per volume. Black line is the average value with error bars, and the red line is the amplitude.



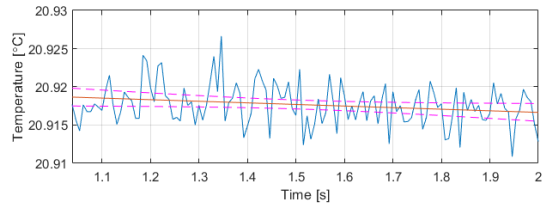
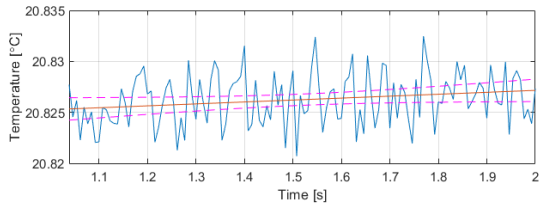
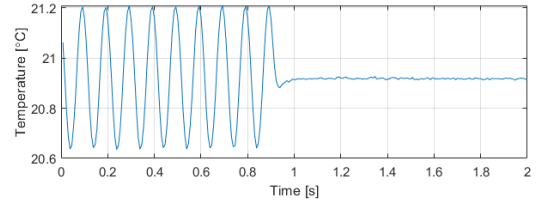
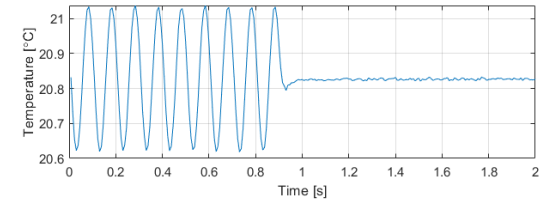
(a) Vs cycle count



(b) Vs. stress intensity range

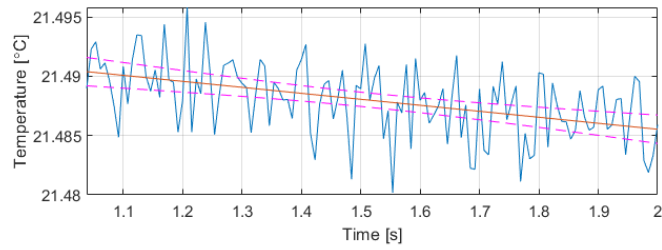
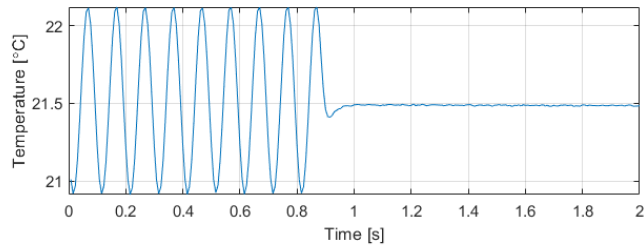
Figure 69: Temperature measured in the sample and the region of interest for energy measurements

Figure 70 show the average temperature behaviour in a 11 by 11 pixel rectangle surrounding the crack tip. The first second the test was running, and the last second, the waveform generator was stopped, and the load was kept at mean load. Figure 71 plots the slopes from the fit of the flat part with 95% confidence bars versus stress intensity range.



(a) Acquisition 10 of 41

(b) Acquisition 30 of 41



(c) Acquisition 41 of 41

Figure 70: The average temperature in a small region at crack tip, while running and after the test was paused. Additionally, a magnification of the flat part where test stopped, with a linear fit.

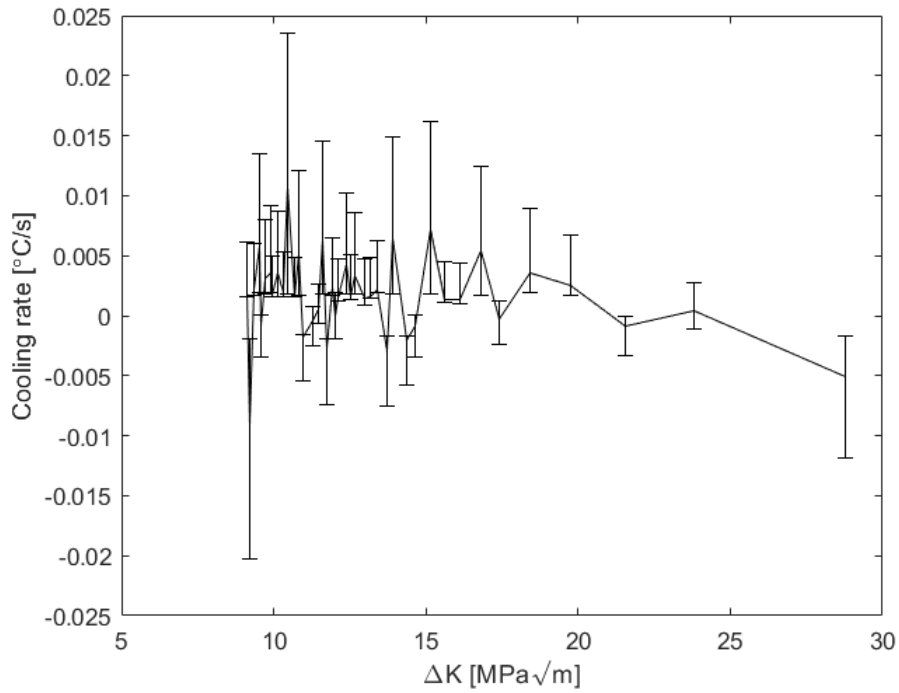
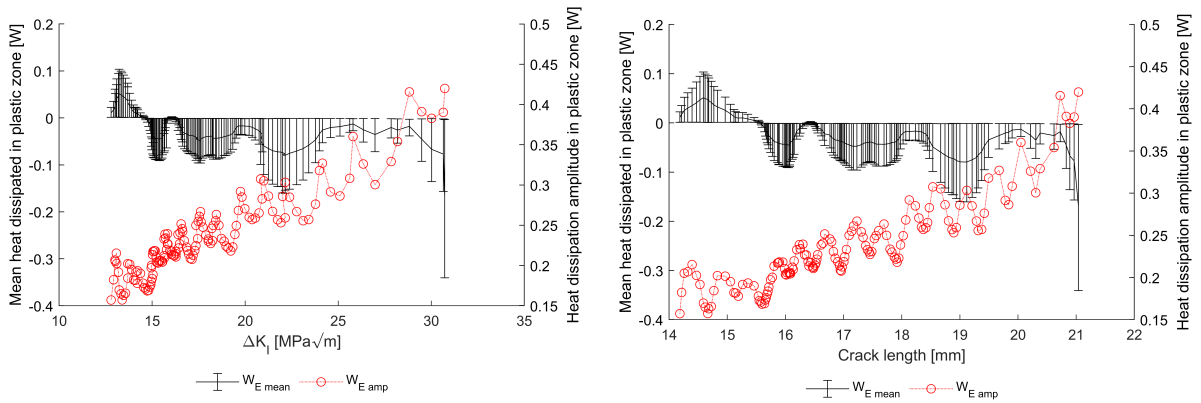


Figure 71: Cooling rate of a small region surrounding the crack tip versus stress intensity range.

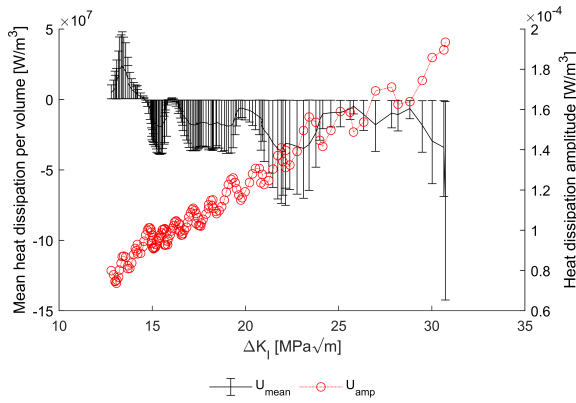
Test 6



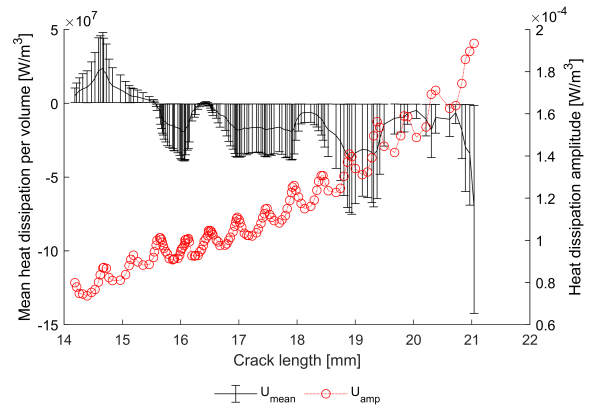
(a) Vs. stress intensity range

(b) Vs. crack length

Figure 72: Total heat dissipated in plastic zone. Black line is the average value with error bars, and the red line is the amplitude.

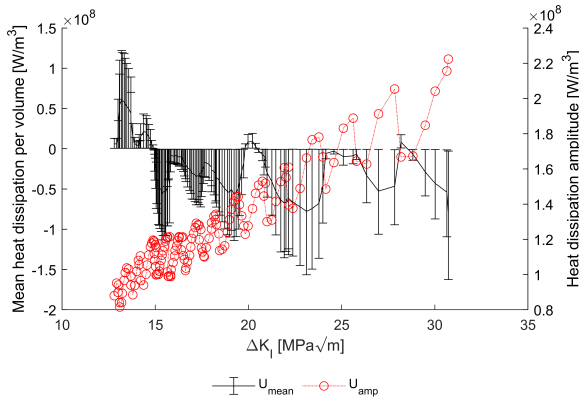


(a) Vs. the stress intensity range

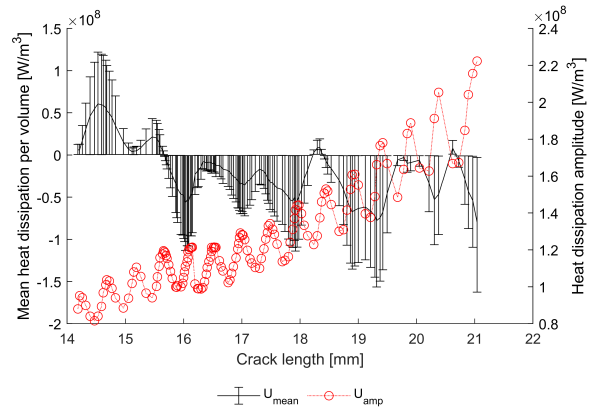


(b) Vs. crack length

Figure 73: Total heat dissipated in the plastic zone per volume. Black line is the average value with error bars, and the red line is the amplitude.

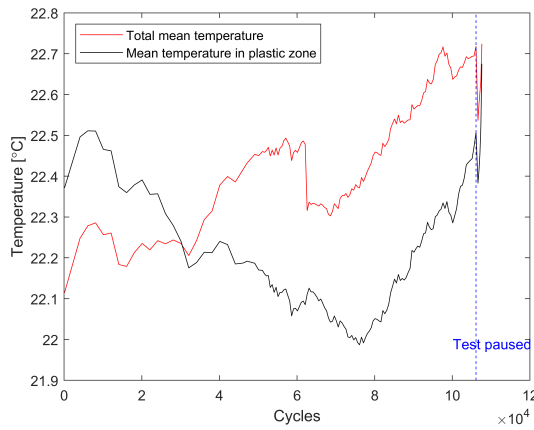


(a) Vs. stress intensity range

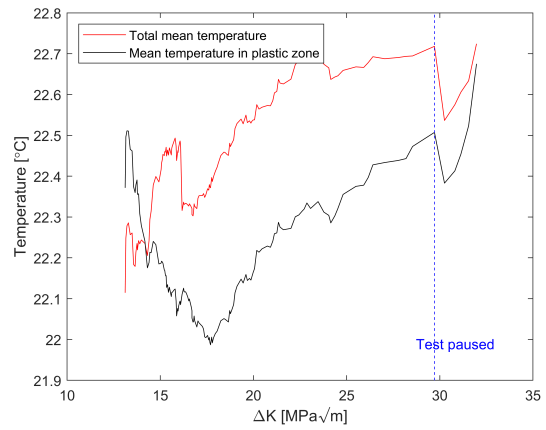


(b) Vs. crack length

Figure 74: Heat dissipated at crack tip per volume. Black line is the average value with error bars, and the red line is the amplitude.



(a) Vs cycle count



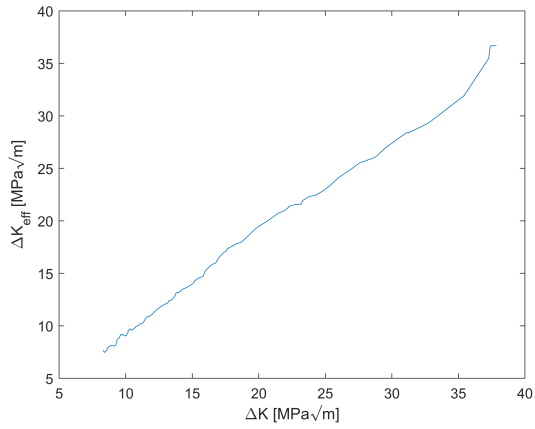
(b) Vs. the stress intensity range

Figure 75: Temperature measured in the sample and the region of interest for energy calculations.

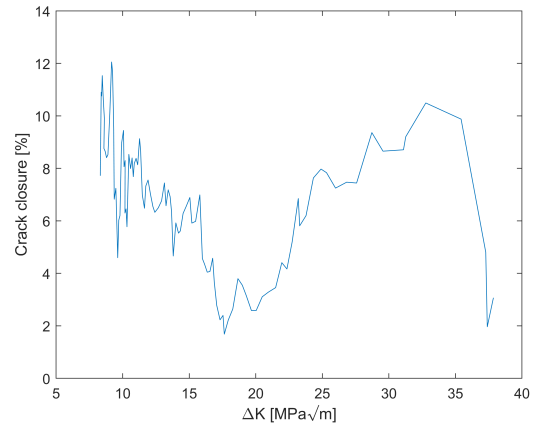
4.2.4 Stress intensity factor

The stress intensity factor was first of all calculated from crack length using the usual LEFM formula, but the effective stress intensity has also been measured from IR data. The measured one versus the theoretical one are plotted, and based on the ratio between them; the potential crack closure is also plotted.

Test 4



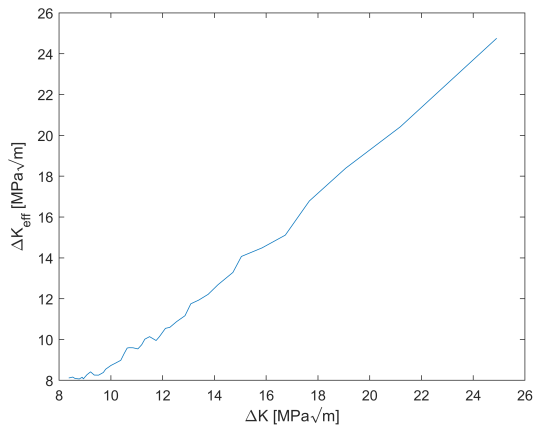
(a) Measured stress intensity factor on y-axis vs the theoretical stress intensity factor on x-axis



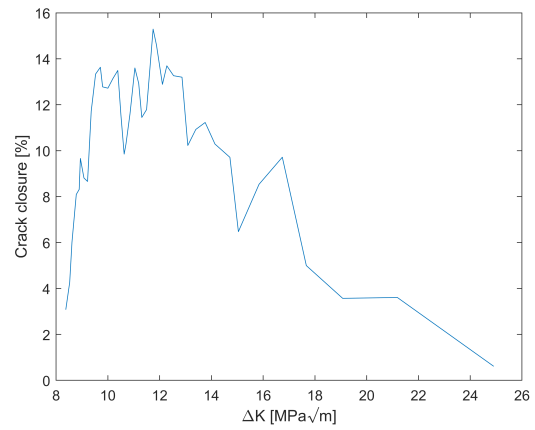
(b) Crack closure based on the stress intensity factor

Figure 76: Stress intensity and crack closure

Test 5



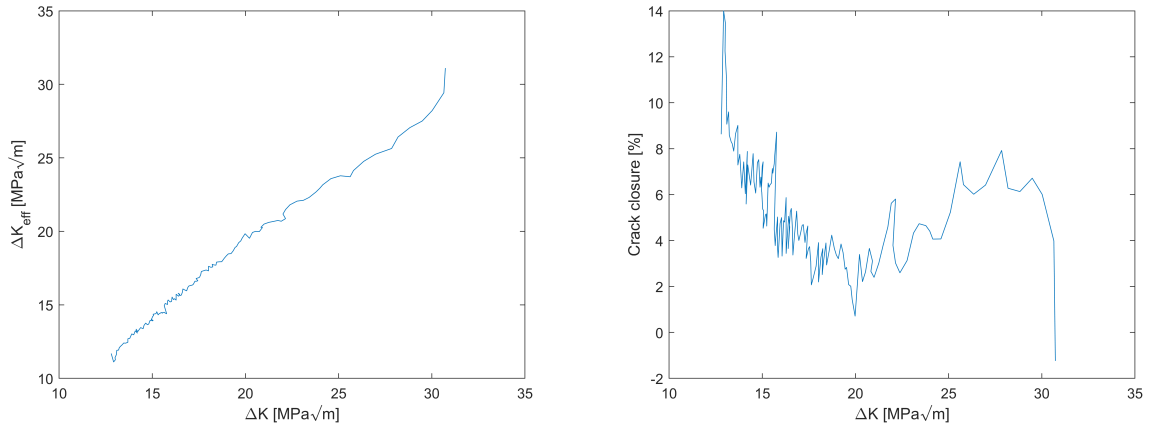
(a) Measured stress intensity factor on y-axis vs the theoretical stress intensity factor on x-axis



(b) Crack closure based on the stress intensity factor

Figure 77: Stress intensity and crack closure

Test 6



(a) Measured stress intensity factor on y-axis vs the theoretical stress intensity factor on x-axis

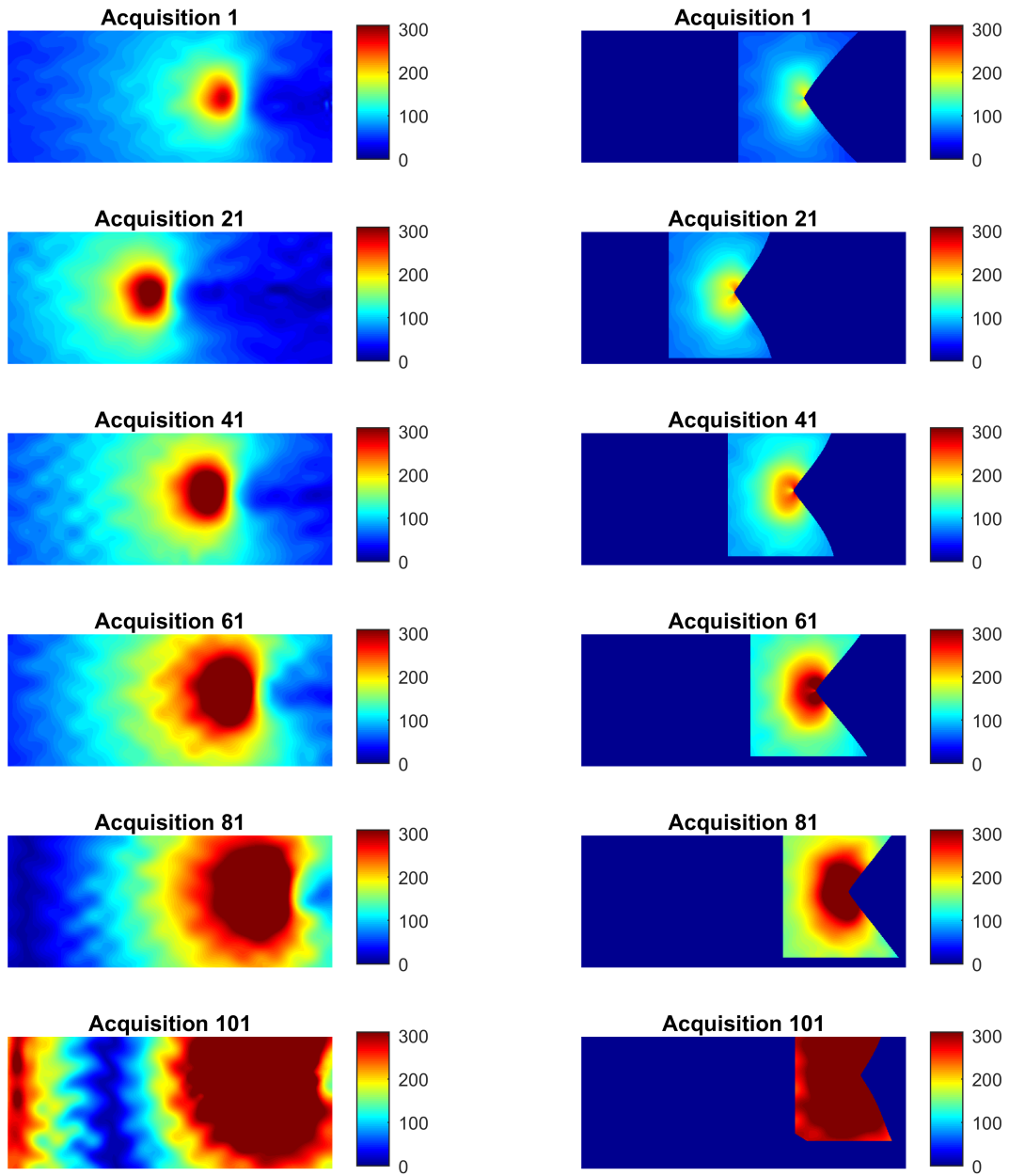
(b) Crack closure based on the stress intensity factor

Figure 78: Stress intensity and crack closure

4.2.5 Stress fields

The stress fields of first stress invariant as well as the von Mises stresses were calculated, and the illustration of the stress fields is shown for test 4 in figure 79. Curves showing the peak stresses versus both measured, and the theoretical stress intensity factors are plotted in figures 80, 81, and 82.

Test 4



(a) First stress invariant amplitude, axis limited to 308 MPa (b) Von Mises stress amplitude, axis limited to 308 MPa

Figure 79: Example of stress amplitude fields; window size is of 620 by 252 pixels

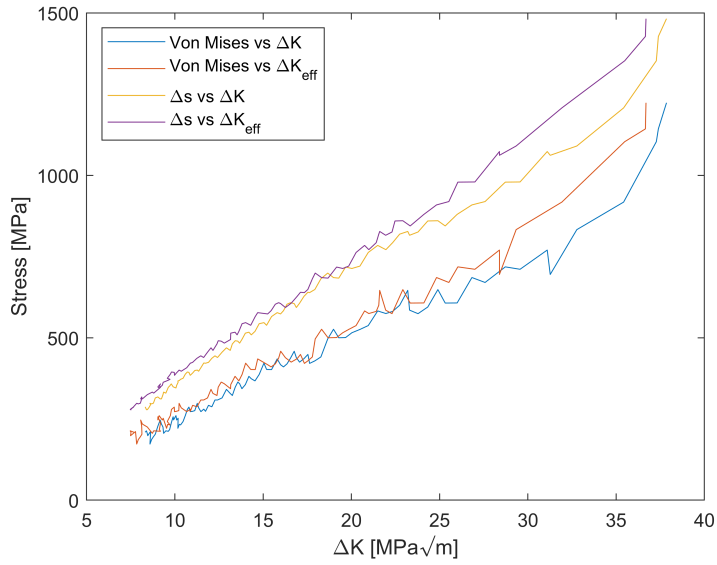


Figure 80: Maximum stresses measured in the sample, both versus the theoretical stress intensity and the measured stress intensity

Test 5

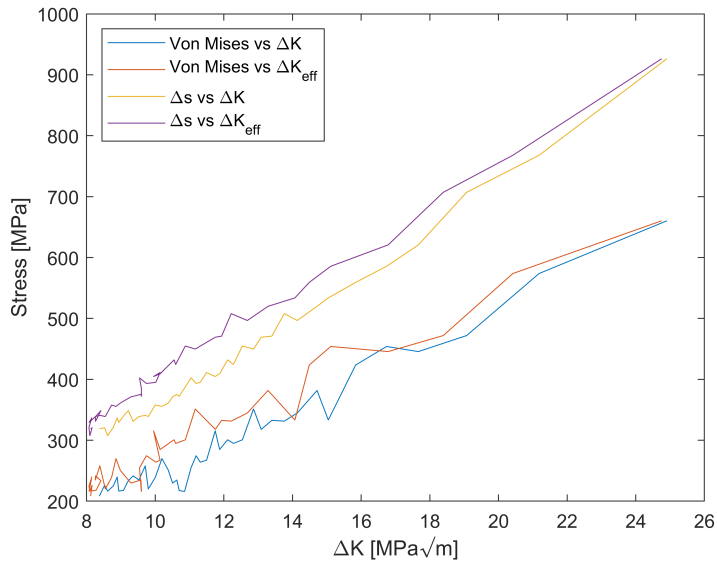


Figure 81: Maximum stresses measured in the sample, both versus the theoretical stress intensity and the measured stress intensity

Test 6

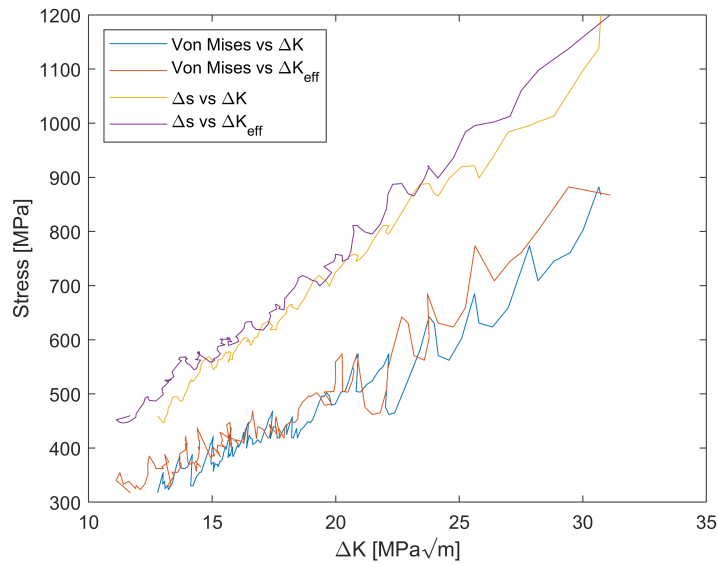
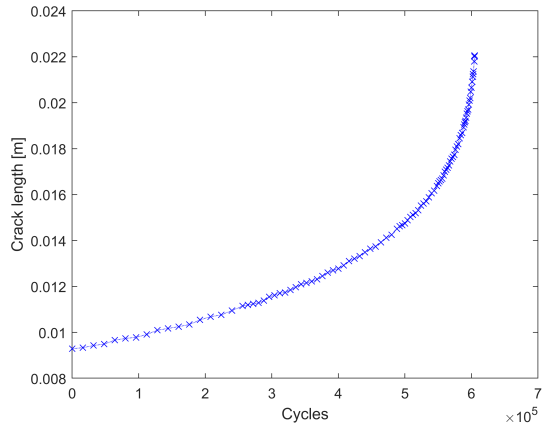


Figure 82: Maximum stresses measured in the sample, both versus the theoretical stress intensity and the measured stress intensity

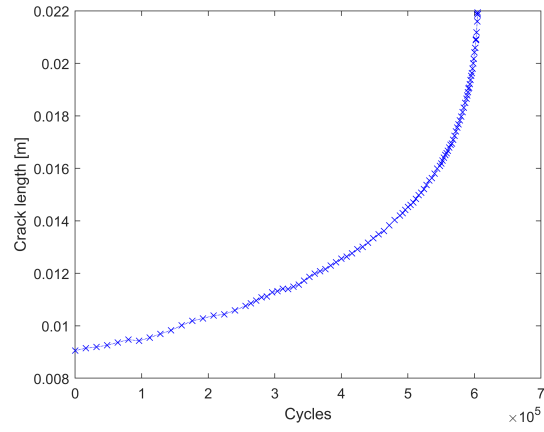
4.2.6 Crack growth curves

The crack growth curves are based on crack tip detection. The crack tip was defined in two ways, as the point with highest temperature amplitude from TSA, and as the crack tip of Williams' stress field after fitting it to measured stress field. Both of these methods are plotted. The first plot is crack length versus cycle count, further the crack growth rates are plotted together with fit, and Confidence Bands (CBs). Finally, the parameters of the fit are listed. The method for the crack growth curves is described in section 3.5.2. The crack growth rate is also plotted versus the measured stress intensity factor range.

Test 4

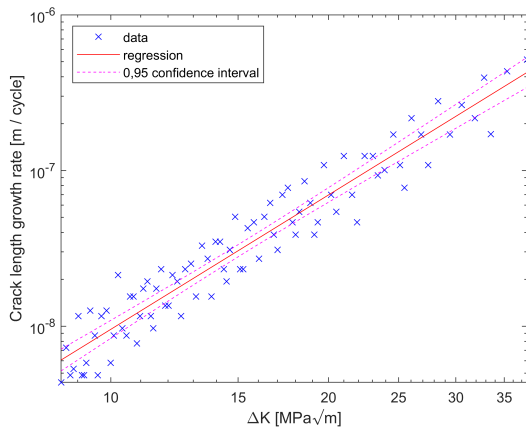


(a) Based on max value from TSA

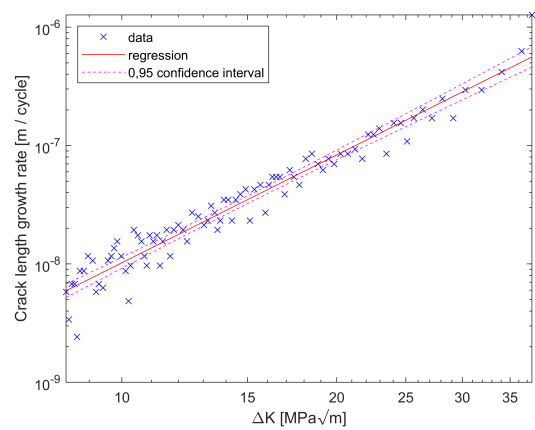


(b) Based on Williams fit

Figure 83: Crack length versus cycles

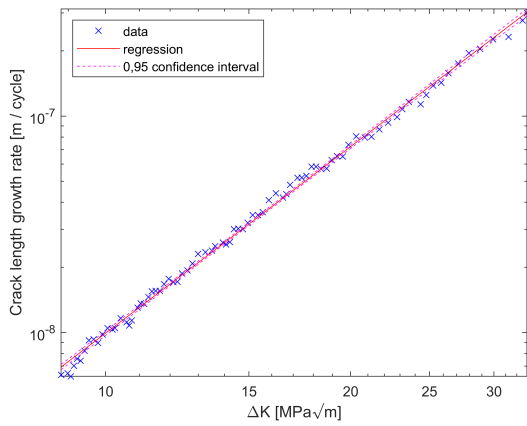


(a) Based on crack tip from max value of TSA

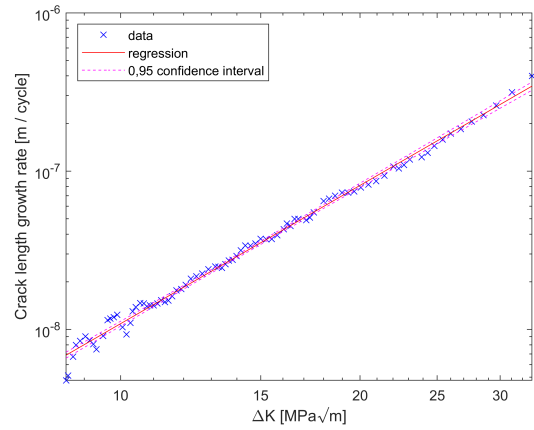


(b) Based on crack tip from Williams' stress field fit

Figure 84: Paris curves based on the theoretical stress intensity factor with the results of linear curve fitting and confidence bands (secant method).

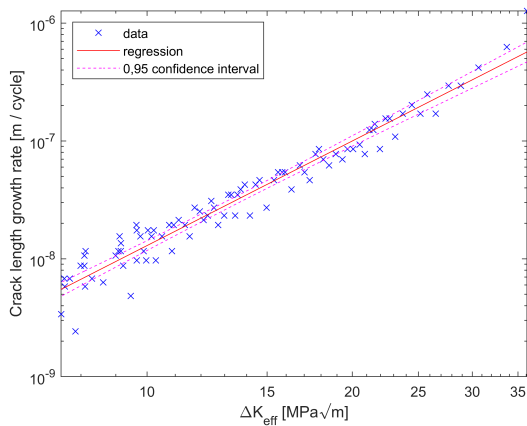


(a) Based on crack tip from max value of TSA

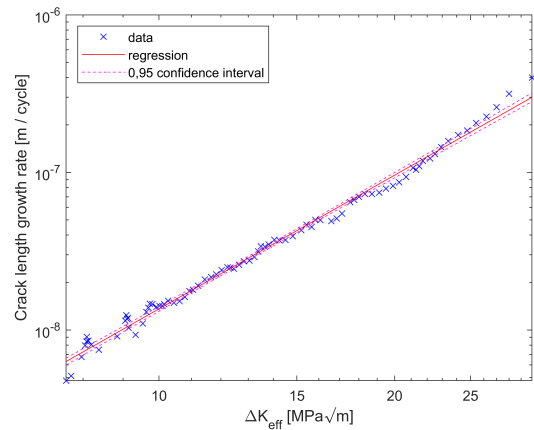


(b) Based on crack tip from Williams' stress field fit

Figure 85: Paris curves based on polynomial filtering and the theoretical stress intensity factor range, with the results of curve fitting and confidence bands



(a) Secant method



(b) Polynomial filtering

Figure 86: Paris curves based on crack tip from Williams' stress field fit and the measured stress intensity

Test 5

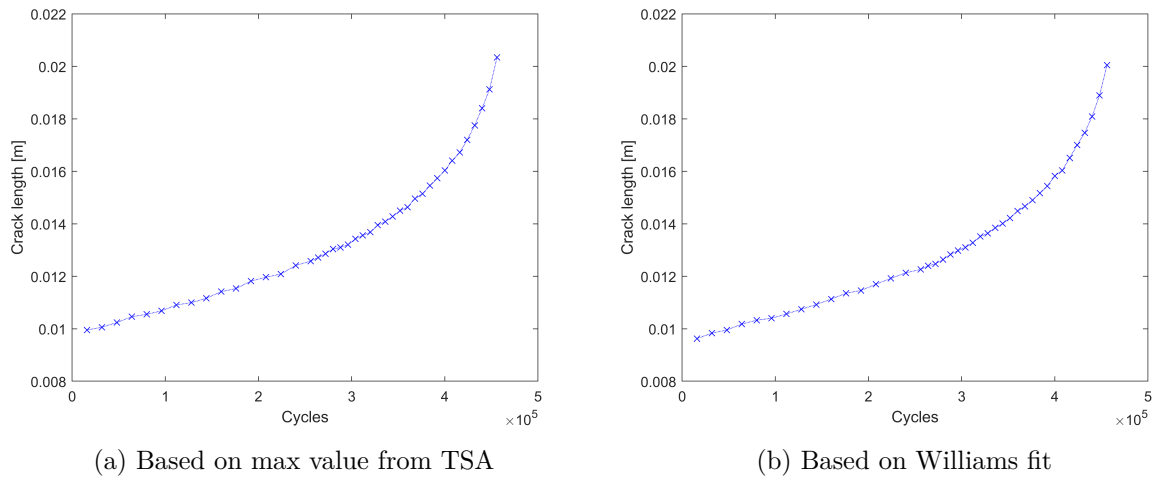


Figure 87: Crack length versus cycles

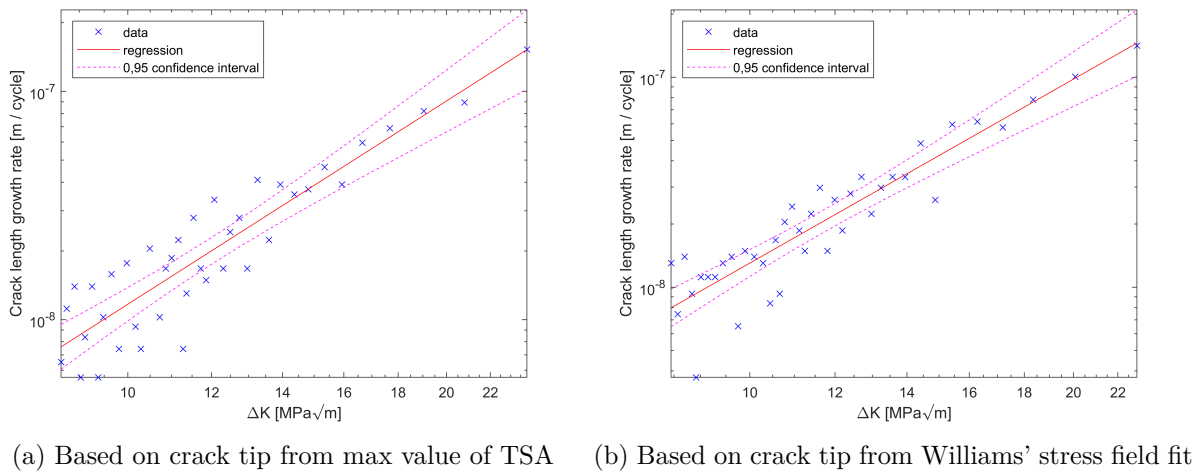
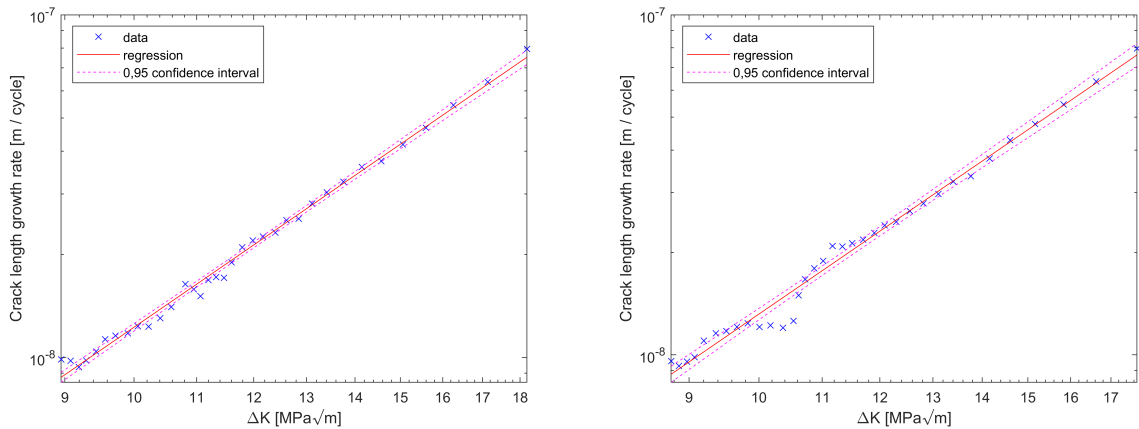
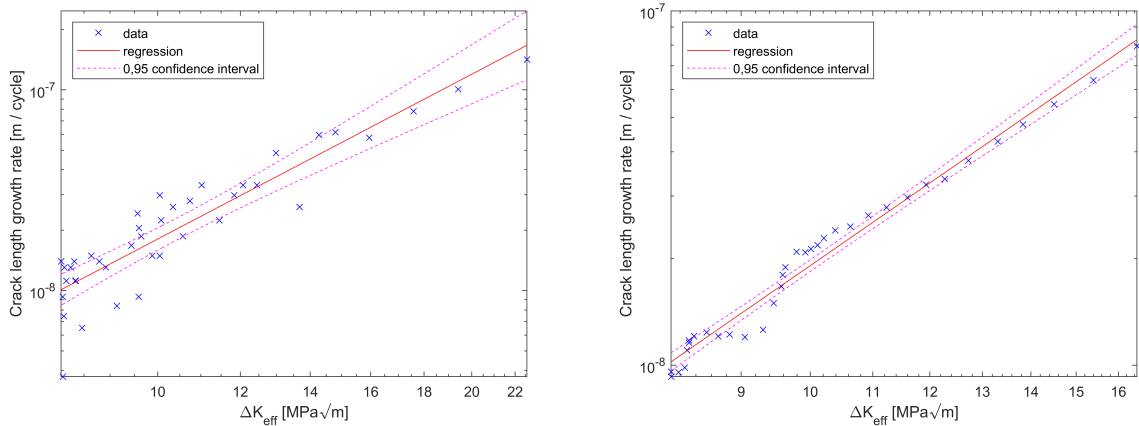


Figure 88: Paris curves based on the theoretical stress intensity factor and the secant method, with the results of linear curve fitting and confidence bands



(a) Based on crack tip from max value of TSA (b) Based on crack tip from Williams' stress field fit

Figure 89: Paris curves based on polynomial filtering and theoretical stress intensity factor range, with fit and confidence bands



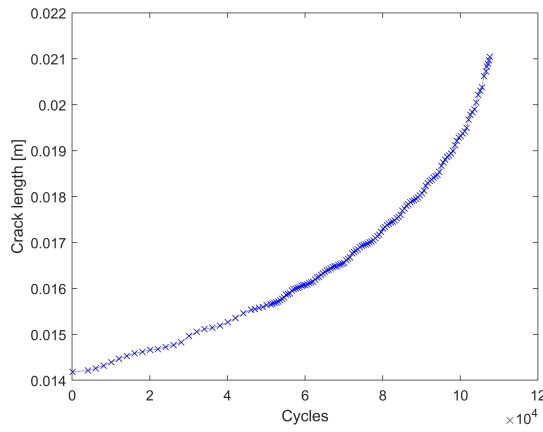
(a) Secant method

(b) Polynomial filtering

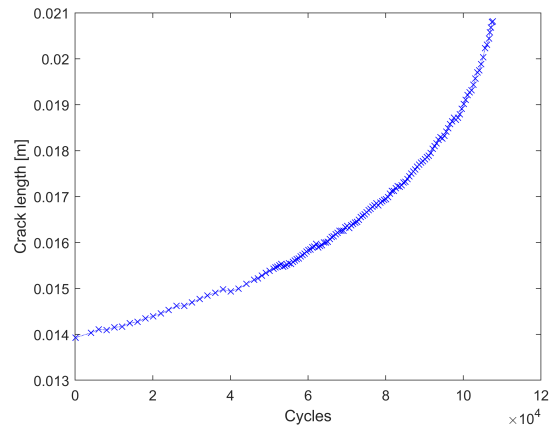
Figure 90: Paris curves based on crack tip from Williams' stress field fit and measured stress intensity

Test 6

This test had many acquisitions, spread over a short crack length as the sample was pre-cracked to a much longer initial crack length, and the test had many measurements. To reduce the scatter caused by the spatial resolution, the points where the crack grew less than 4 pixels were skipped, which improves the quality of the data.

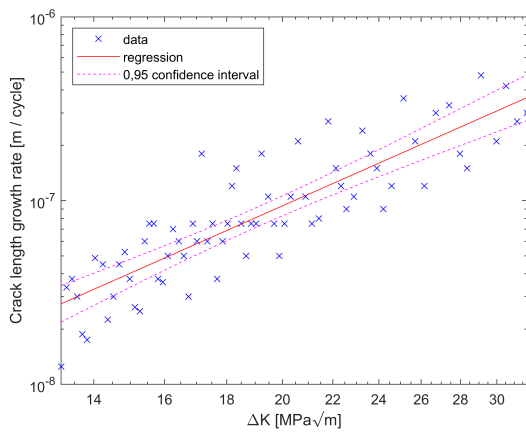


(a) Based on max value from TSA

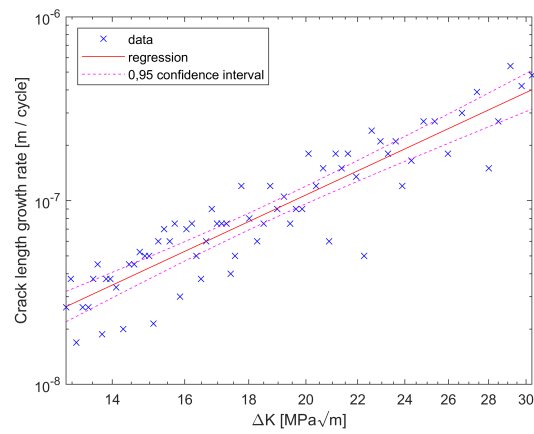


(b) Based on Williams fit

Figure 91: Crack length versus cycles

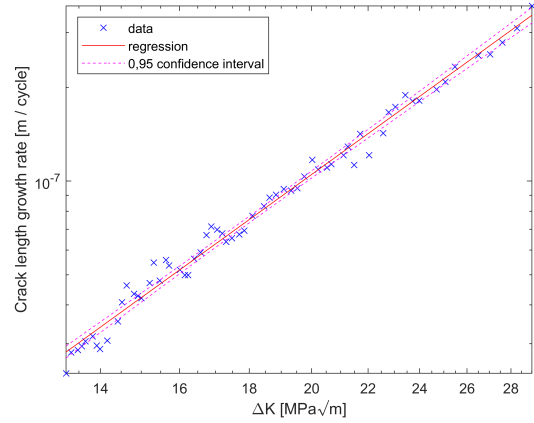
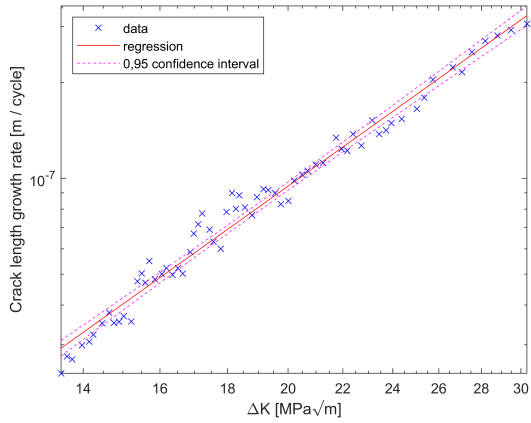


(a) Based on crack tip from max value of TSA



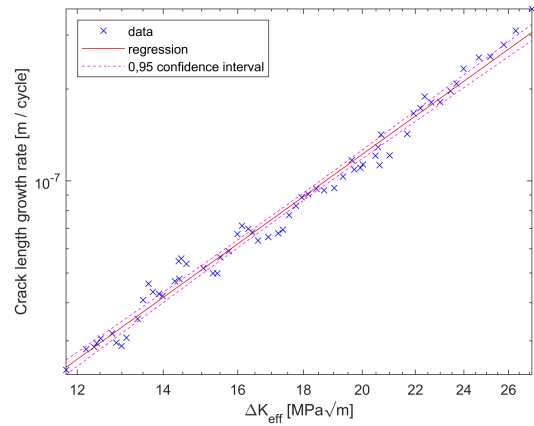
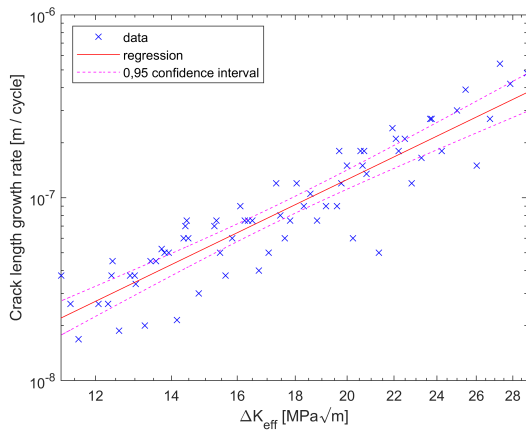
(b) Based on crack tip from Williams' stress field fit

Figure 92: Paris curves based on theoretical stress intensity factor and secant method, with the results of the linear curve fit with the corresponding confidence bands



(a) Based on crack tip from max value of TSA (b) Based on crack tip from Williams' stress field fit

Figure 93: Paris curves based on polynomial filtering and theoretical stress intensity range, with the results of the linear curve fit with the corresponding confidence bands



(a) Secant method

(b) Polynomial filtering

Figure 94: Paris curves based on crack tip estimated from the Williams' stress field fit and the measured stress intensity

Coefficients

Test	Method	$\log_{10}C$ (95% CBs)	m (95% CBs)	R^2
4	IRT, secant m.	-10.89 (-11.11, -10.67)	2.868 (2.686, 3.05)	0.9203
	IRT, incr. poly. m.	-10.87 (-10.91, -10.82)	2.863 (2.827, 2.898)	0.9970
5	IRT TSA, secant m.	-10.89 (-11.37, -10.42)	2.959 (2.52, 3.398)	0.8307
	IRT, incr. poly. m.	-10.94 (-11.03, -10.86)	3.032 (2.951, 3.113)	0.9943
6	IRT, secant m.	-10.85 (-11.37, -10.32)	2.933 (2.524, 3.342)	0.7479
	IRT, incr. poly. m.	-10.88 (-11.02, -10.74)	2.965 (2.856, 3.074)	0.9787

Table 8: Summary of fatigue crack growth parameters and R^2 values, based on TSA and the theoretical stress intensity

Test	Method	$\log_{10}C$ (95% CBs)	m (95% CBs)	R^2
4	IRT, secant m.	-11.01 (-11.2, -10.83)	3.024 (2.871, 3.178)	0.9463
	IRT, incr. poly. m.	-10.87 (-10.93, -10.8)	2.902 (2.848, 2.956)	0.9929
5	IRT, secant m.	-10.79 (-11.23, -10.36)	2.909 (2.504, 3.315)	0.8475
	IRT, incr. poly. m.	-10.96 (-11.1, -10.82)	3.079 (2.947, 3.211)	0.9855
6	IRT, secant m.	-11.09 (-11.54, -10.64)	3.167 (2.815, 3.518)	0.8286
	IRT, incr. poly. m.	-11.1 (-11.21, -10.99)	3.168 (3.077, 3.258)	0.9875

Table 9: Summary of fatigue crack growth parameters and R^2 values, based on Williams' stress field fit, and theoretical stress intensity

Test	Method	$\log_{10}C$ (95% CBs)	m (95% CBs)	R^2
4	IRT, secant m.	-10.84 (-11.01, -10.66)	2.948 (2.799, 3.096)	0.9472
	IRT, incr. poly. m.	-10.69 (-10.75, -10.62)	2.819 (2.761, 2.877)	0.9912
5	IRT, secant m.	-10.47 (-10.87, -10.07)	2.728 (2.34, 3.117)	0.8419
	IRT, incr. poly. m.	-10.67 (-10.82, -10.51)	2.947 (2.791, 3.103)	0.9783
6	IRT, secant m.	-10.8 (-11.22, -10.38)	3 (2.662, 3.337)	0.8246
	IRT, incr. poly. m.	-10.84 (-10.97, -10.72)	3.021 (2.923, 3.119)	0.9840

Table 10: Summary of fatigue crack growth parameters and R^2 values, based on Williams' stress field fit, and measured stress intensity

4.2.7 Plastic zone

Three ways of calculating the plastic zone, or process zone, are presented in this chapter. The first method is based on phase shift, and is created in regions of high stress gradients

and heat dissipation. This method was used only for test 4 as it is very time consuming. The second method is based on Laplacian, and is the region in which stresses deviate from the ideally elastic stresses. Both area and size are presented, and the definitions are as explained in section 3.4.5. The monotonic plastic zone radius is also shown and compared to theoretical models as well as the contours of these zones. The contours of the theoretical plastic zones were also corrected for closure, just to give an approximation of how much the closure effect might affect the results. The contours of the plastic zones for the phase shift and the Laplacian methods are also compared.

Test 4

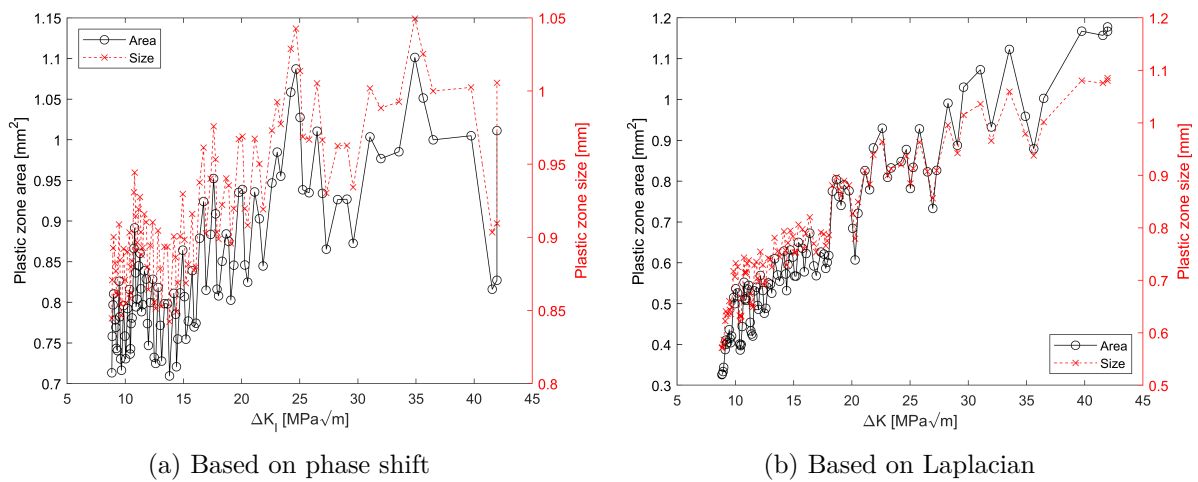


Figure 95: Plastic zone size and area vs stress intensity factor range

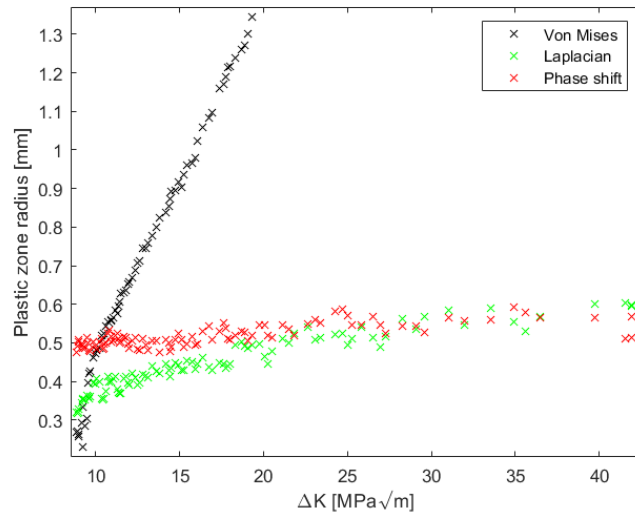


Figure 96: Comparison of radius for the three types of plastic zones.

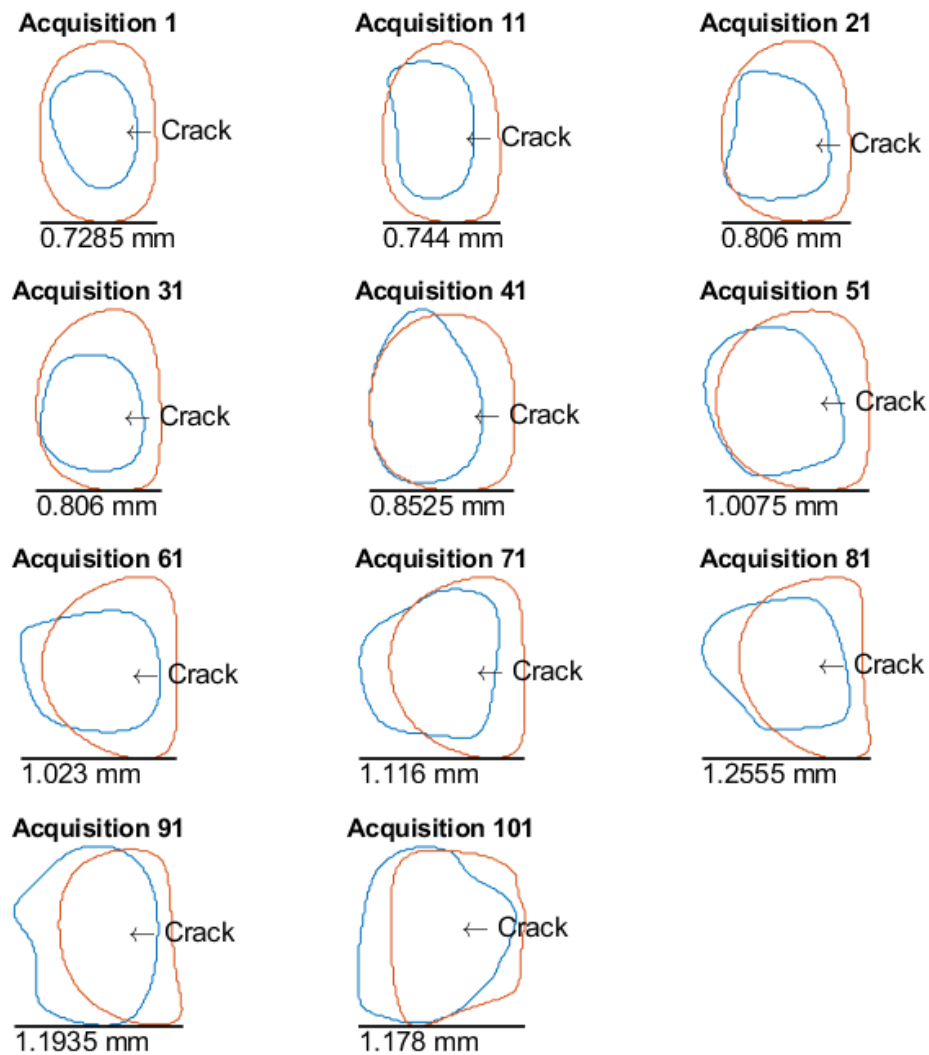


Figure 97: Contours of plastic zones for given acquisitions, based on the Laplacian (blue), and phase shift (orange)

Figure 98 shows the plastic zone radius for a monotonic plastic zone based on both the proportionality limit, and the 0.2% yield stress. The values are compared with the theoretical size based on LEFM explained in sections 2.1 and 2.1.1 both for plane stress and strain conditions, and Williams' stress field explained in section 2.1.1. The models have been based on the stress intensity factor calculated based on crack length from equations

49 and 50, but they are also plotted based on the measured stress intensity factor, named with "Corrected" in figure 99 as well as adequate figures for the other tests. The plastic zone comparison was done assuming the crack closure was minimal, and that the measured stress field could be divided by $(1 - R)$ and give valid stress field for maximum monotonic stresses in the elastic region. The radius is plotted on the y-axis and the ΔK on the x-axis. The x-axis was restricted only to the values where the whole plastic zone was within the FOV. A comparison for the differently estimated plastic zones is shown in figure 99.

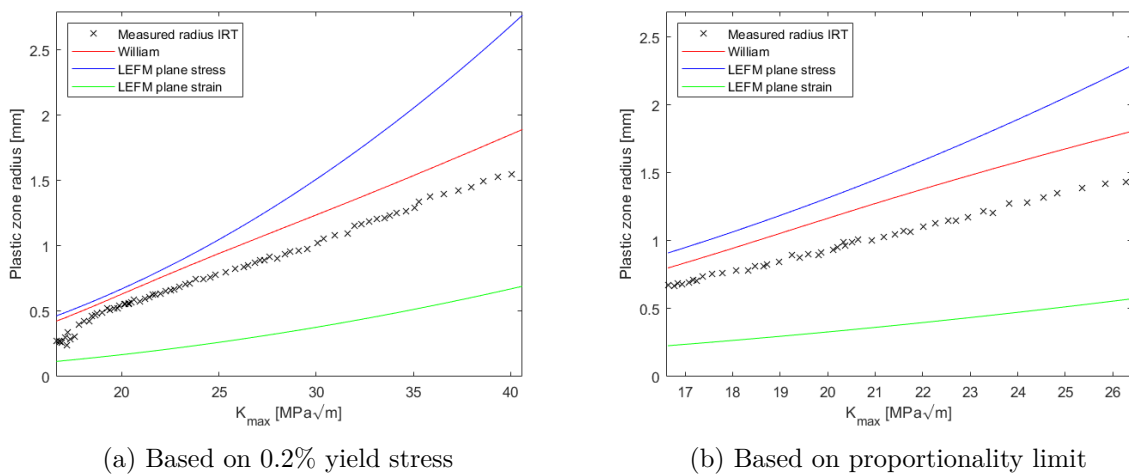


Figure 98: Monotonic plastic zone size plotted versus theoretical K_{max}

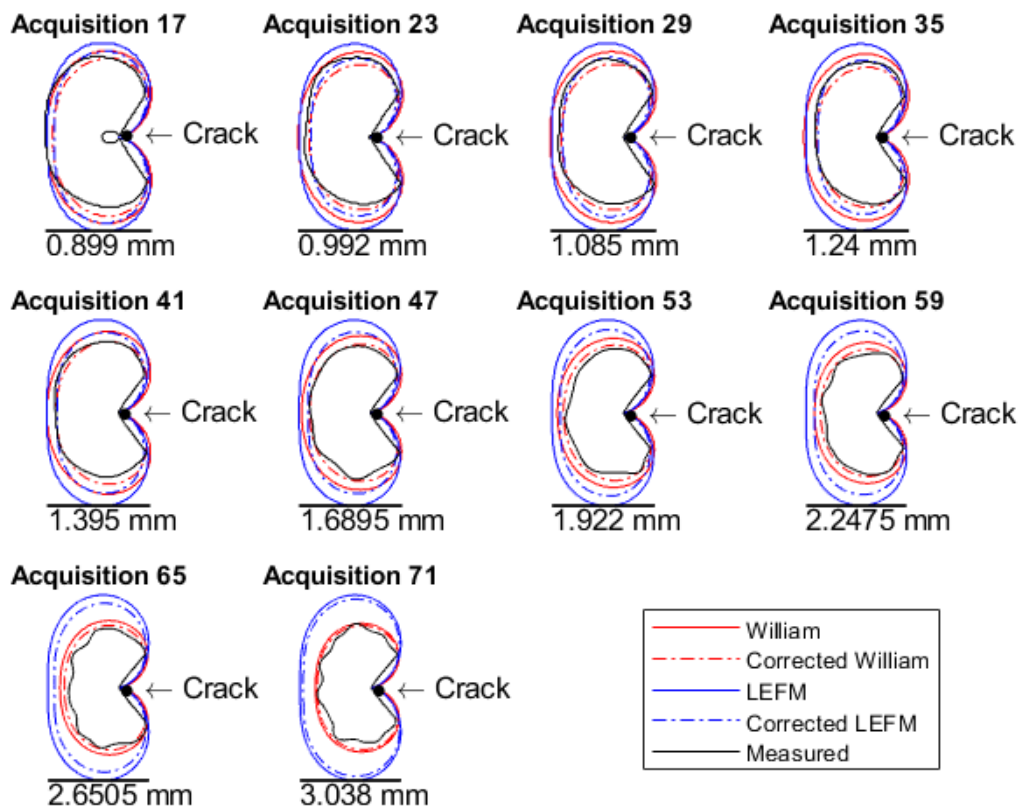


Figure 99: Contours of plastic zones for given acquisitions at the stress level of $\sigma_{0.2\%}$

Test 5

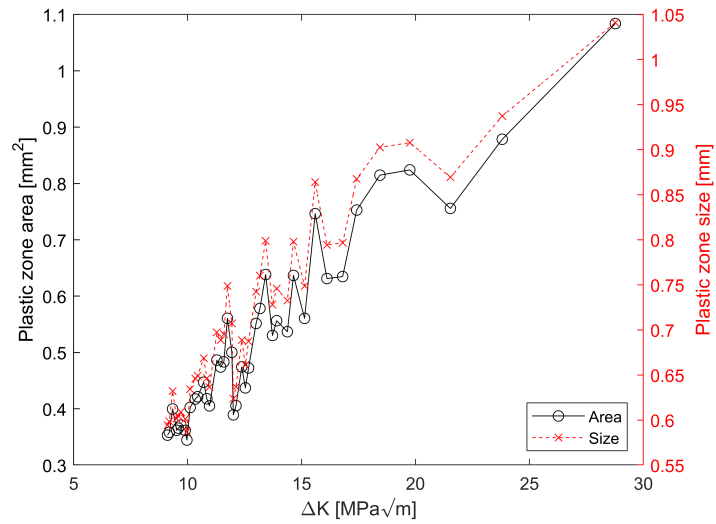
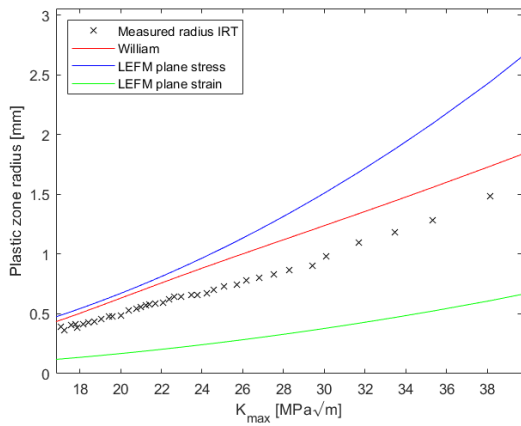
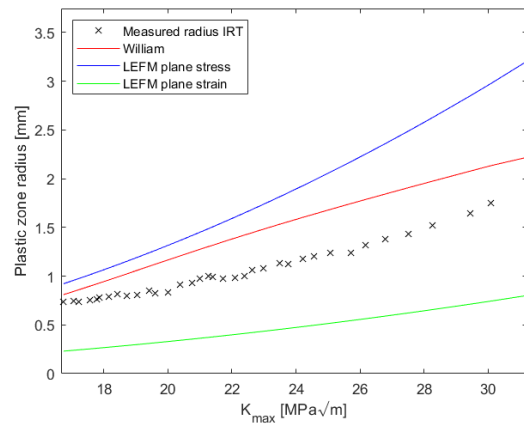


Figure 100: Plastic zone based on the Laplacian method



(a) Based on the 0.2% yield stress



(b) Based on the proportionality limit

Figure 101: Monotonic plastic zone size plotted versus theoretical K_{max}

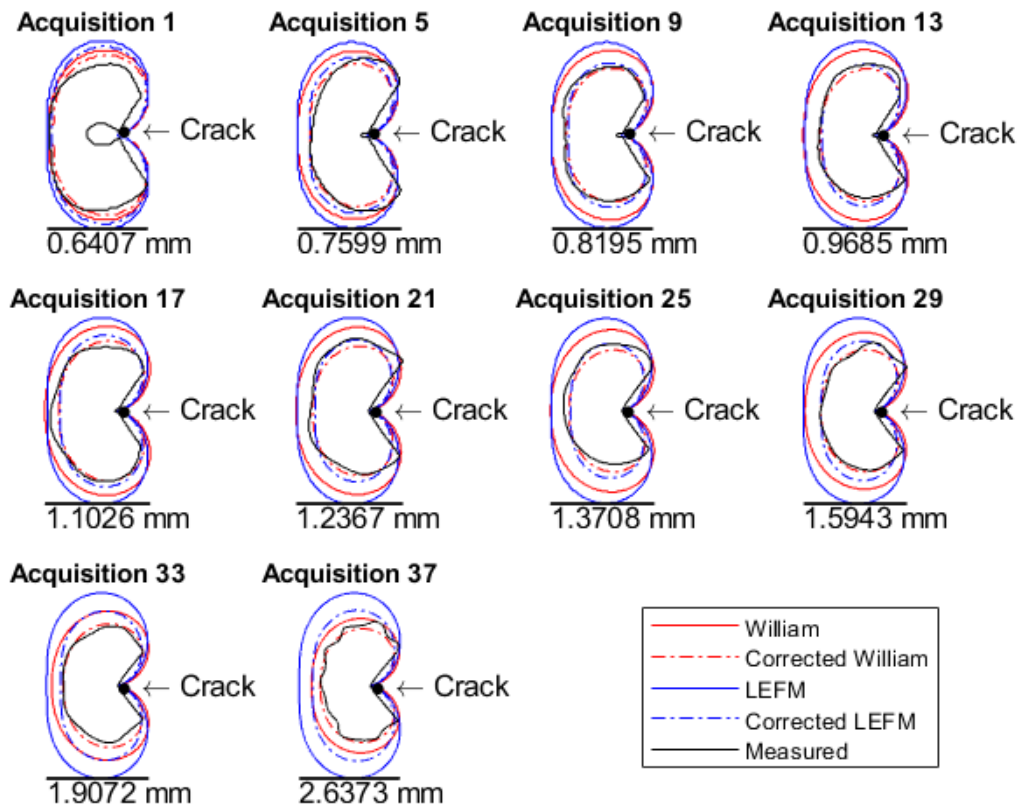


Figure 102: Contours of the plastic zones for given acquisitions at the stress level of $\sigma_{0.2\%}$

Test 6

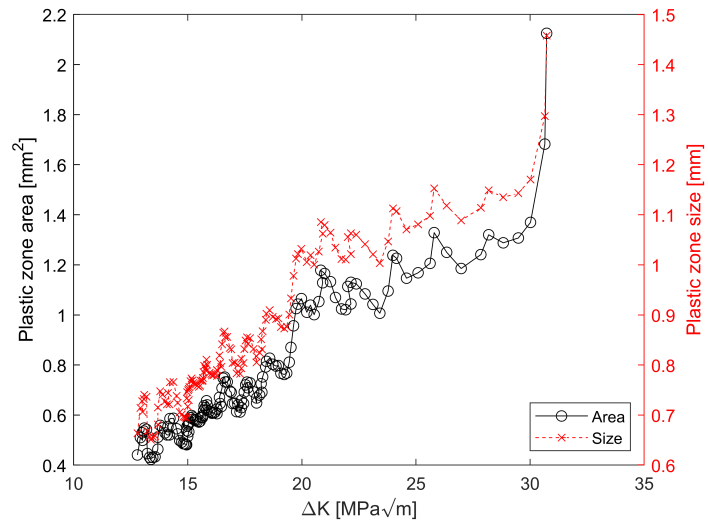
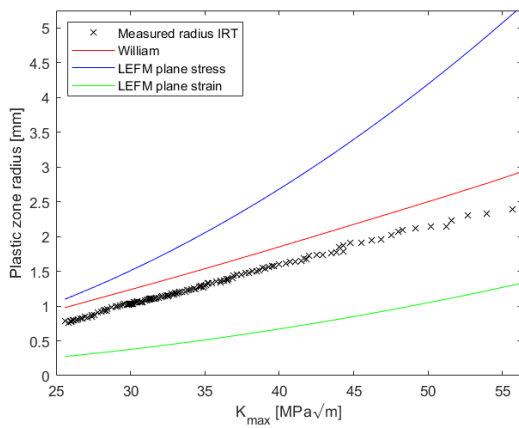
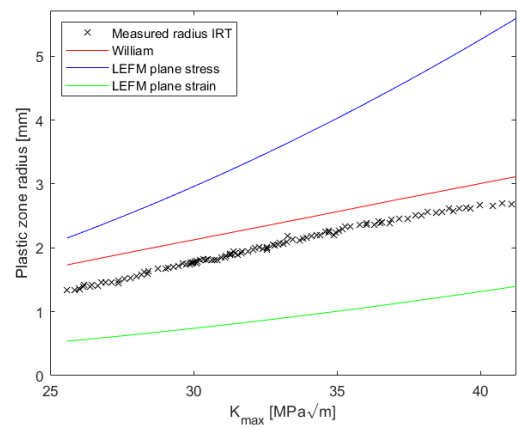


Figure 103: Based on the Laplacian method



(a) Based on the 0.2% yield stress



(b) Based on the proportionality limit

Figure 104: Monotonic plastic zone size plotted versus theoretical K_{max}

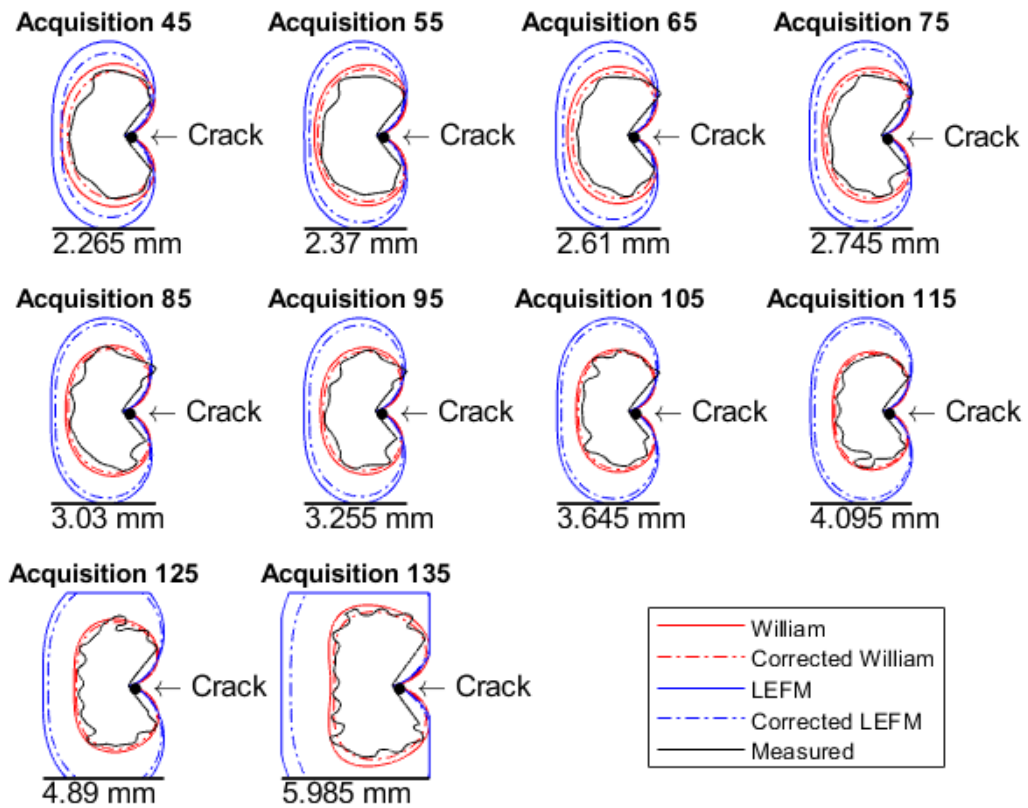


Figure 105: Contours of plastic zones for given acquisitions at the stress level of $\sigma_{0.2\%}$

4.2.8 Fourier analysis of test 4

This section shows some of the results obtained from the second order Fourier analysis. The load signal was not logged, the data are shown relative to a sine wave with zero shift. The manual triggers were likely to be significantly out of phase, so the values for phases should be considered relative within the picture. The **Mean temp** column in figures 106 and 107 is the constant in the Fourier analysis, and represents the mean temperature distribution. **A1** and **A2** are the amplitudes of the first and second order sine waves, and **P1** and **P2** are the phase shifts of the first and second order terms when compared to the sine wave without any shift.

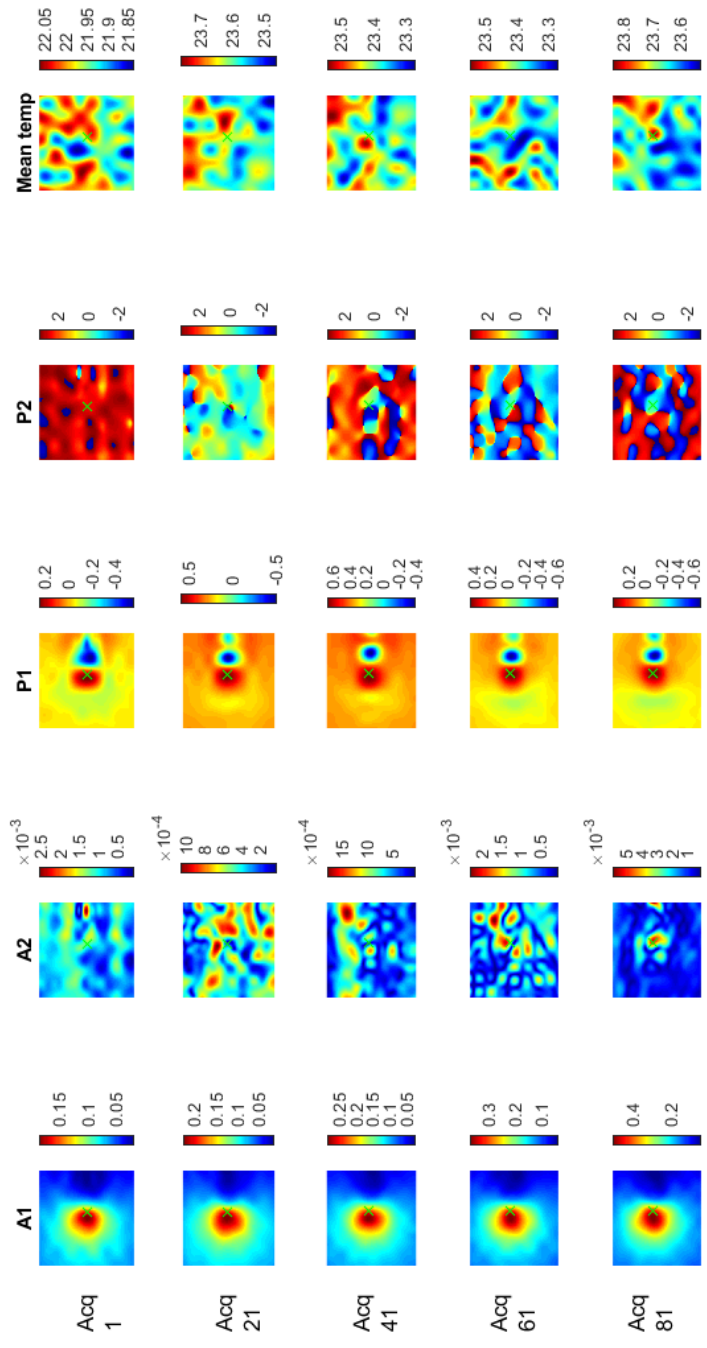


Figure 106: Samples in stage II. Discrete Fourier analysis of second order, amplitudes A1 and A2 as well as mean temperature are given in $^{\circ}\text{C}$, and phase shift of first and second order P1 and P1, in radians.

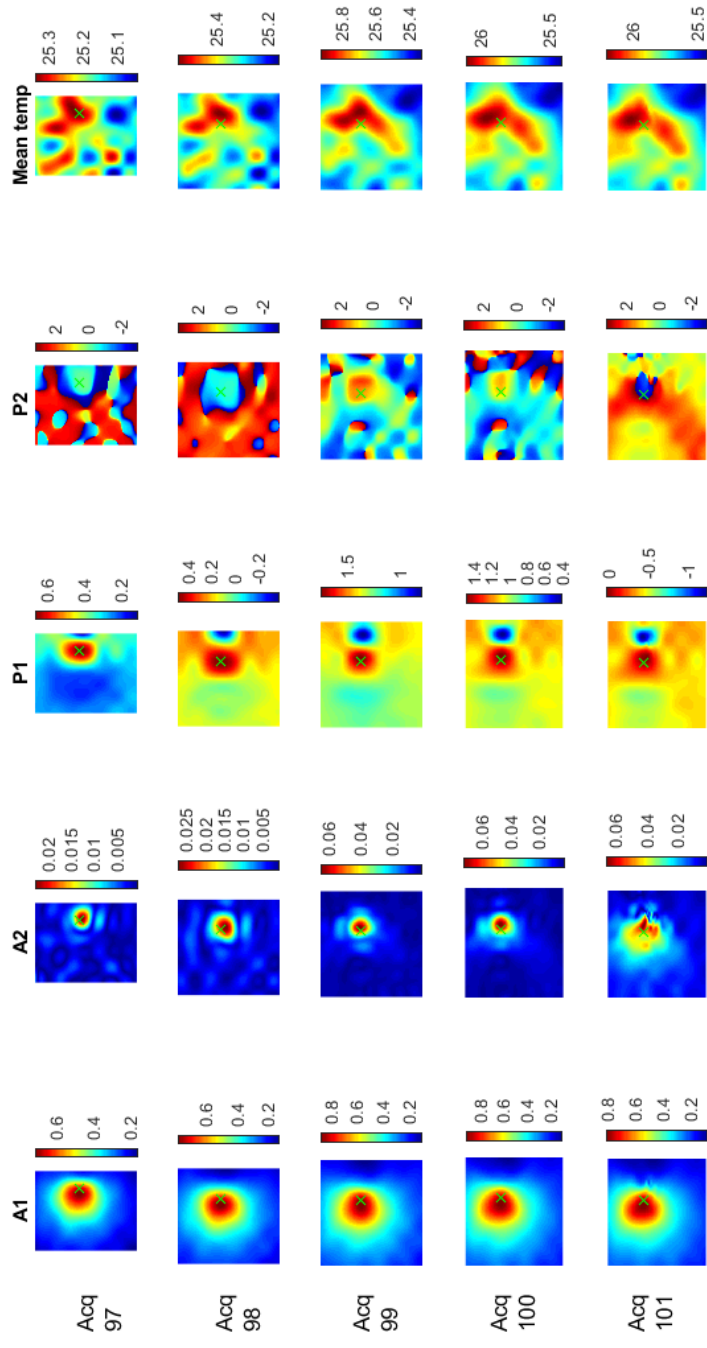


Figure 107: Discrete Fourier analysis of second order, amplitudes A1 and A2 as well as mean temperature are given in $^{\circ}\text{C}$, and phase shift of first and second order P1 and P2, in radians. Five last measurements.

4.2.9 Qualitative data for stage III of test 6

The unstable crack growth stage III of test 6 was continuously monitored and recorded by all the techniques employed, and some raw data are presented, as the filtering did not allow for any reasonable calculations so far. Figure 108 shows what is considered to be either the transition to stage III or the very early stage III (notice that the border between these two states is only vaguely defined, of course), where the crack opening seems to be small, relatively speaking, and the crack shape seem to be a V shape. The magnified view (figure 108b) shows creation of a butterfly shaped process zone, seen clearly in the well established part of stage III, as in figure 109. The process zone in the early stage III seems to appear at the angle larger than 45° with the crack plane, and in late stage III, below that angle, which is seen respectively in figures 109 and 110. Figure 112 takes a closer look at the process zone, and illustrates that it occurs behind the crack tip, and continues at approximately 45° angle with respect to the crack plane from the crack tip.

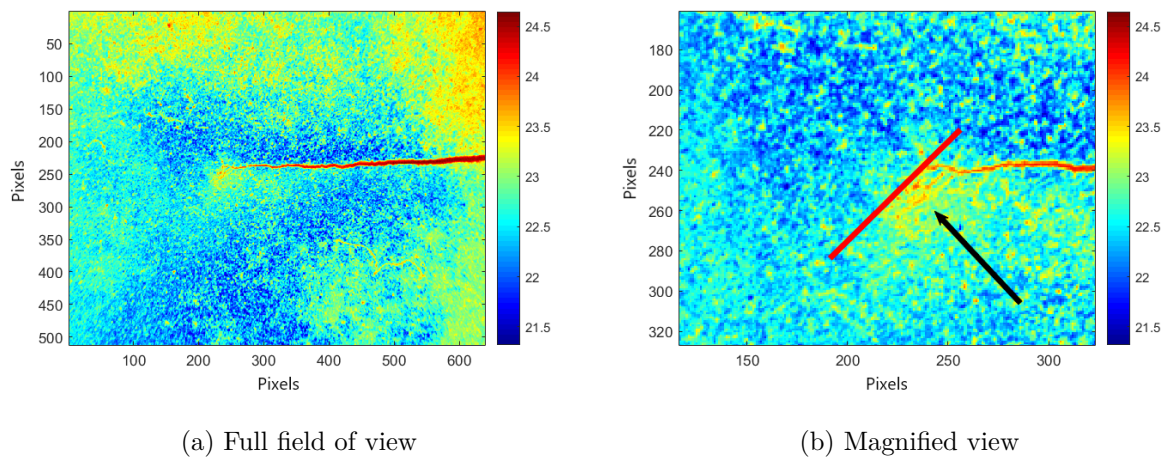


Figure 108: Transition to stage III, temperature in $^\circ\text{C}$

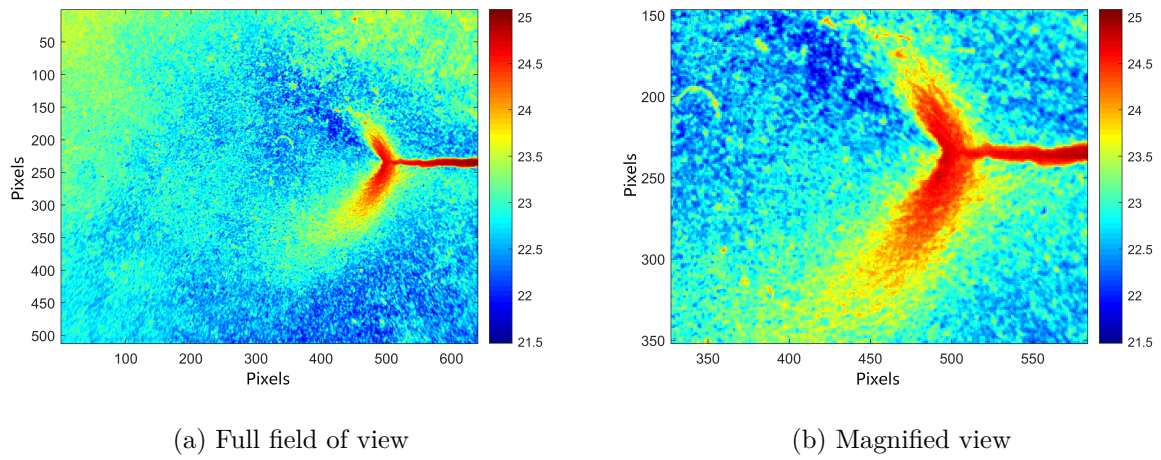
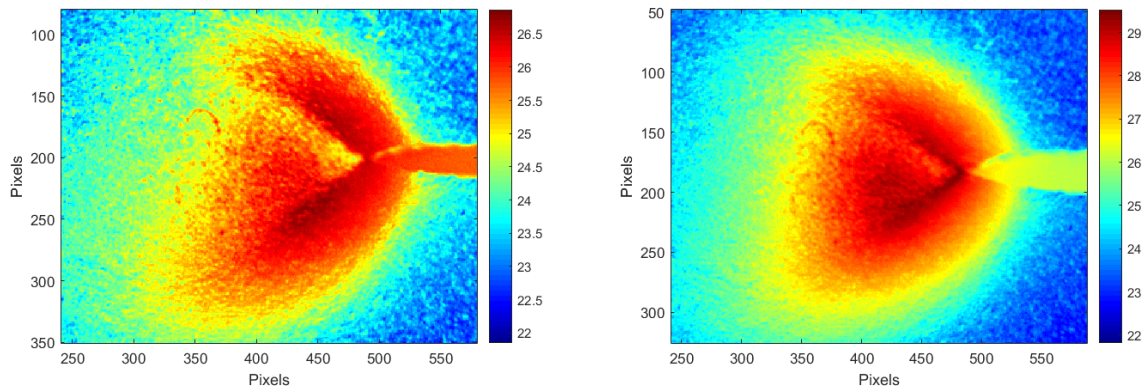


Figure 109: Stage III, temperature in °C

Figure 110 shows two pictures, with one cycle in between, it was the last full cycle before failure, and the crack jumped approximately 5 pixels, which is roughly 0.075mm. The jump resulted in a lot of heat dissipation, seen in figure 111. The heat dissipated during the crack growth, occurred in front of the crack tip, and in the region between the butterfly process zone wings described above. The temperature reaches levels as high as 46°C. The maximum temperature and mean temperature measured during the last cycles is illustrated in figure 113, the mean temperature seem to be increasing steadily in stage III until the very last cycles, where it grows very rapidly. The crack opening is much larger than in figure 108, and the crack seem blunted, or U shaped.



(a) Magnified view on crack tip before the last cycle (b) Magnified view on crack tip before the last cycle

Figure 110: The crack jump of the last cycle before failure, temperature in $^{\circ}\text{C}$

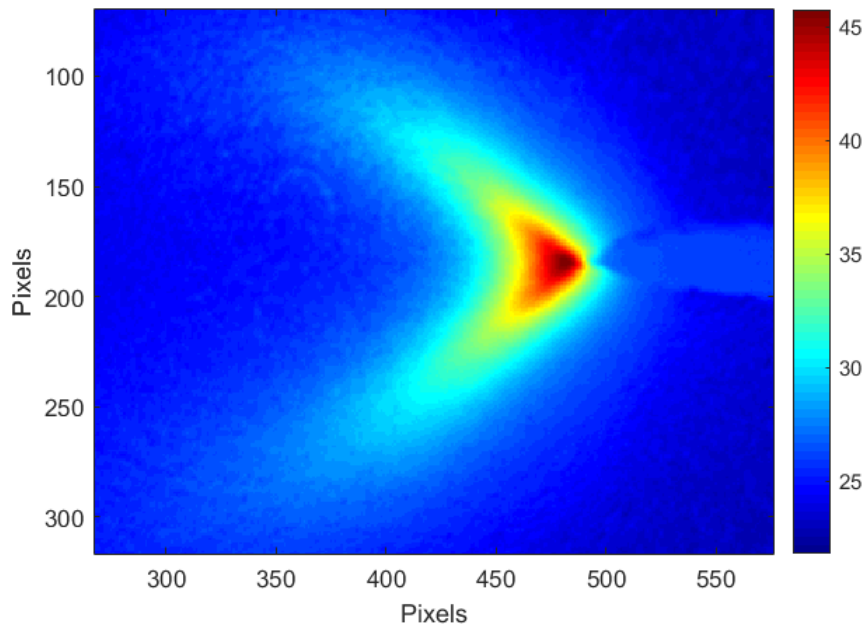


Figure 111: The temperature distribution during the crack growth in the last cycle, temperature in $^{\circ}\text{C}$

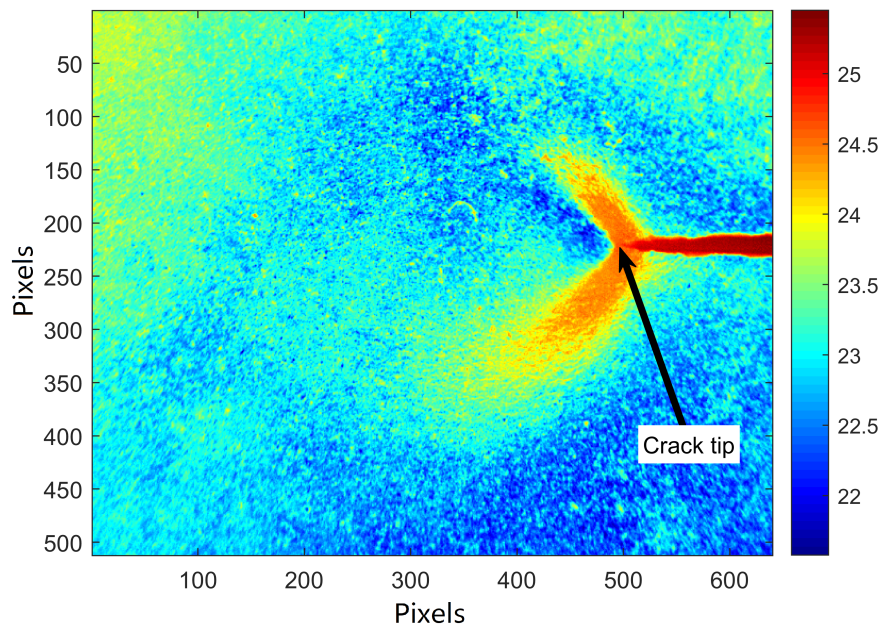


Figure 112: The process zone with respect to crack tip, temperature in °C

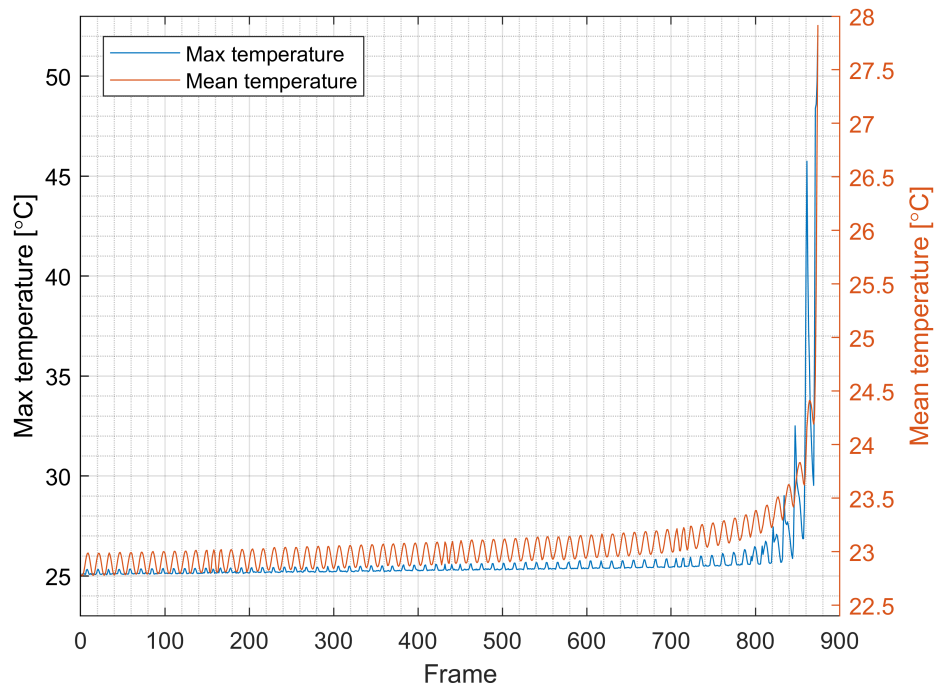


Figure 113: The maximum (left y-axis) and mean (right y-axis) temperatures occurring in the field of view during the last cycles before failure

4.3 High-speed imaging and DIC

The following section presents the experimental results obtained using high-speed camera. For all tensile specimens, as well as FCG tests 4 and 5 the additional DIC analyses were performed.

4.3.1 Influence of vignetting on DIC analysis

The following section presents results from analysis which show the influence of vignetting effect on DIC results. For this purpose, as a series of images were taken when the C(T) specimen was moved about 0.3 mm in vertical direction. The original images had very visible signs of vignetting, this effect was created artificially by choosing a proper combination of focal length and illumination. Totally 49 images were analysed. The FOV had a size of about 10 mm \times 10 mm, while ROI had a size of 7 mm \times 7 mm.

Both DIC analyses were run with exactly the same DIC parameters. The subset radius was set to 15 and subset spacing was set to 1 in both cases. The spatial resolution was 0.0098 mm/pixel.

The influence of vignetting and filtering on the images was investigated by tracking both vertical and horizontal displacement in 3 different points along the whole series of images. Additionally, for the last frame analysed, the vertical displacement profile was plotted for the 3 different lines used. In both cases, the displacements from low-pass filtered and unfiltered images were plotted and compared. Figure 114 present FOV, ROI, points, and lines used. Figure 115 show comparison of the horizontal-, and the vertical displacement fields at the last image analysed for both filtered, and unfiltered images. The first 3 sub-plots on figure 116 show horizontal displacement for each of 3 mentioned points, the results for filtered and unfiltered images are plotted at the same graph. The last sub-plot, 116d, show the Δ horizontal displacement, also the difference in horizontal displacement obtained using both filtered and unfiltered images. Similar strategy has been applied to

vertical displacements which can be seen on figure 117. Finally, the displacement profiles along the 3 different lines (according to figure 114) are presented for the frame number 49 which was the last frame. The results and the need for filtering are discussed in section 5.2.1.

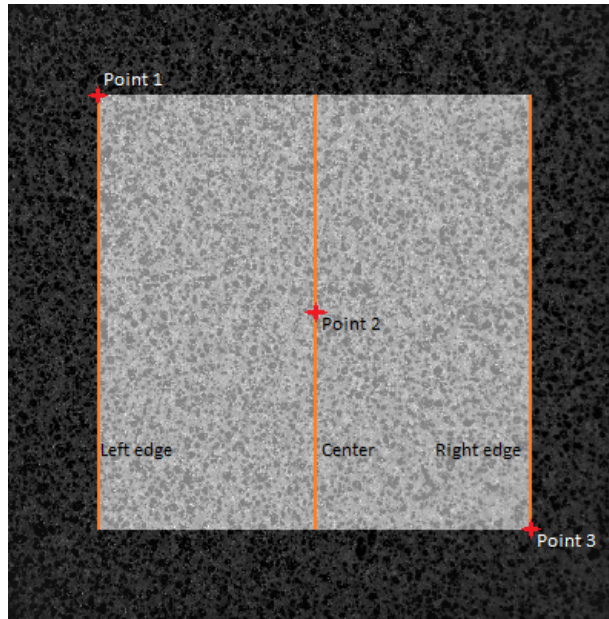


Figure 114: The FOV, ROI, measuring points, and the lines used in investigation

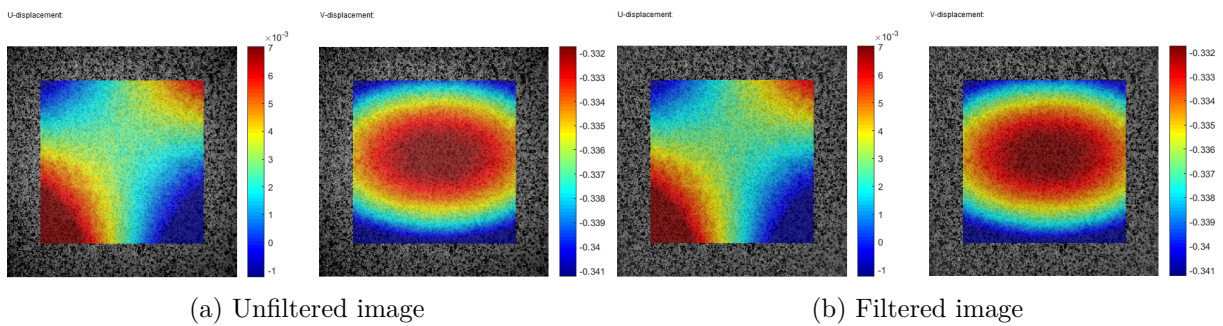
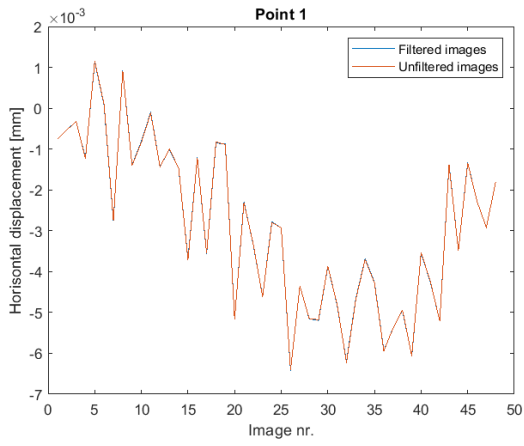
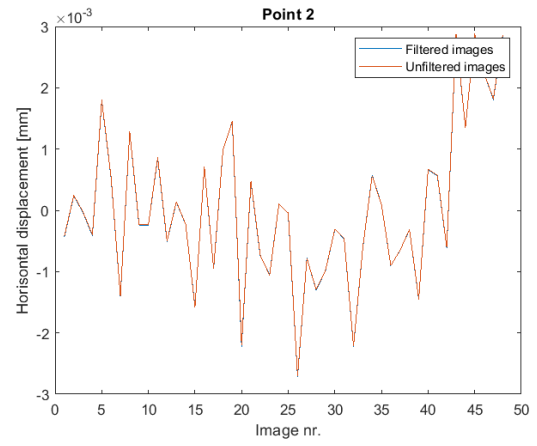


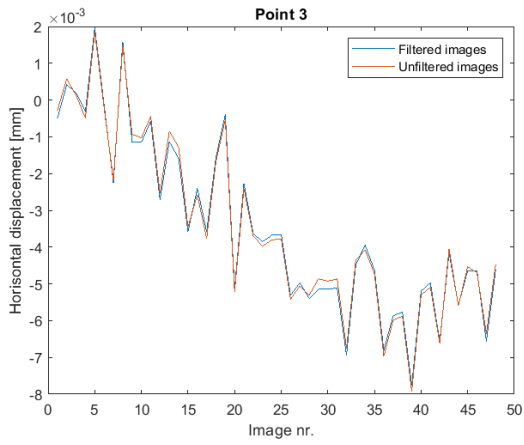
Figure 115: Vertical and horizontal displacements at the last image analysed



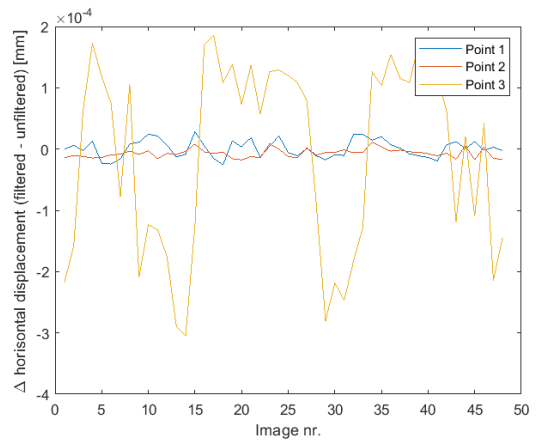
(a) Point 1



(b) Point 2

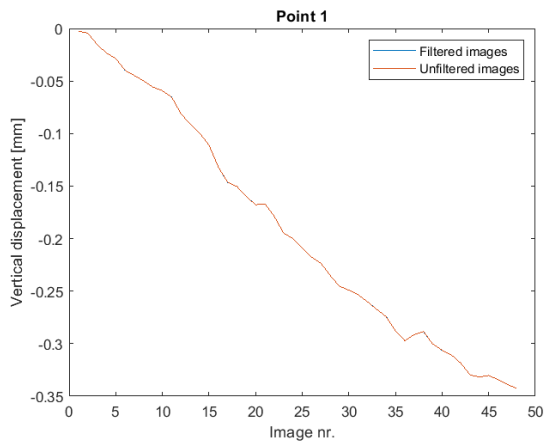


(c) Point 3

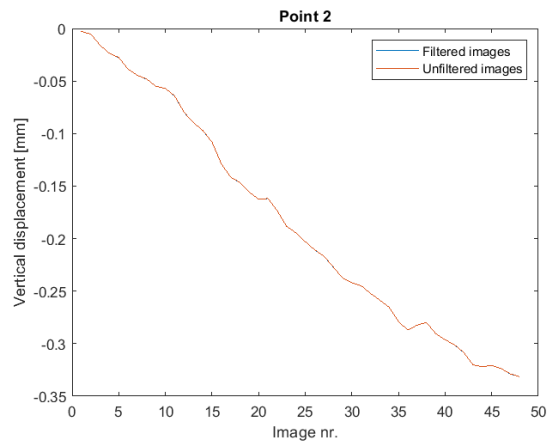


(d) Δ horizontal displacement

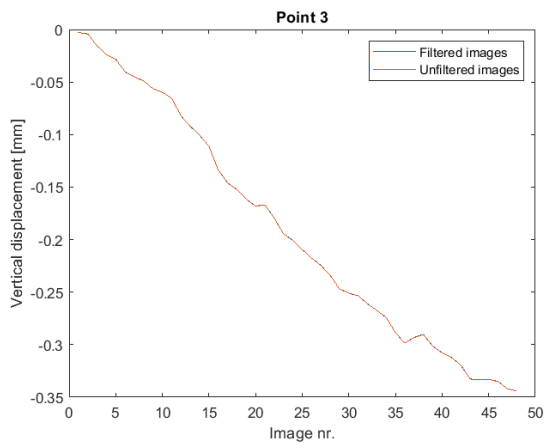
Figure 116: Comparison of horizontal displacements from the filtered and the unfiltered images



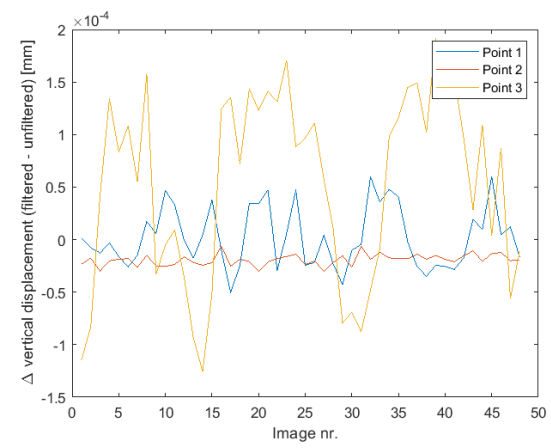
(a) Point 1



(b) Point 2



(c) Point 3



(d) Δ vertical displacement

Figure 117: Comparison of vertical displacements from the filtered and the unfiltered images

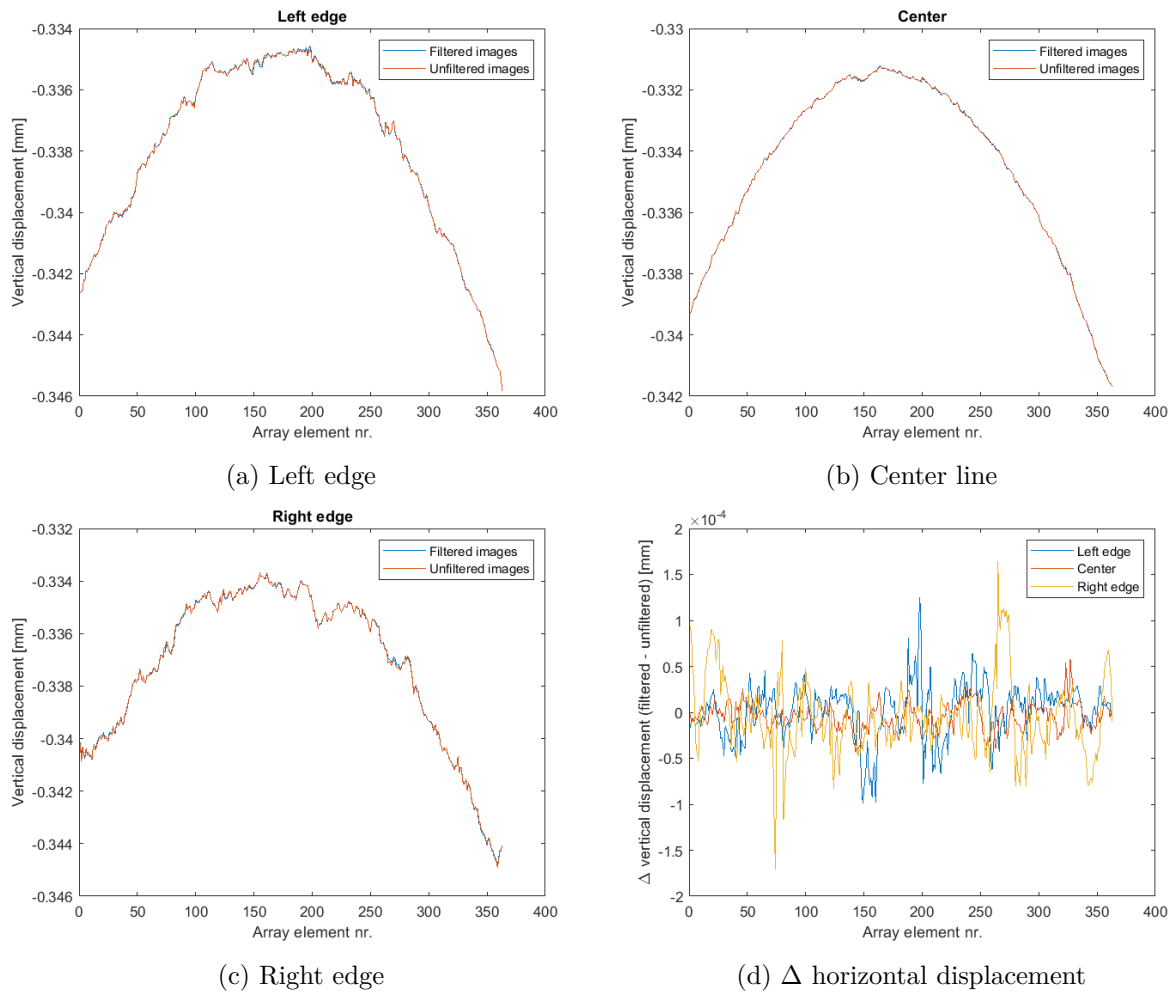


Figure 118: Comparison of the displacement along selected lines from the last of filtered, and unfiltered images

4.3.2 Comparison of strain from DIC and extensometer

Following section presents comparison of the strains obtained using both extensometer, and DIC, the latter one was found using procedure described in section 3.5.4. Figure 119a presents raw data from both DIC and extensometer for tensile specimen number 4. As it can be seen, the strains found using extensometer are unreasonably small giving elastic modulus around 466 GPa when using linear regression tool. An attempt to normalise the strains was made, the strains from extensometer were simply multiplied to get elastic

modulus of 200 GPa, this gave a factor of 2.328 which was used in graphs 119b and 120b. It can be seen that the trend of the strain using both techniques is quite similar after mentioned multiplication. The possible sources of error are discussed in section 5.2.2. The data from testing specimen 4 was also used to validate the material properties obtained using *Ncorr* DIC software. The elastic modulus value presented in section 4.3.3 was used to create the 0.2% offset line. As it can be seen in figure 120b, the intersection of the offset line with the stress-strain curve falls on stress of 307 MPa which is close to $\sigma_{0.2\%}$ of 308 MPa claimed by material supplier.

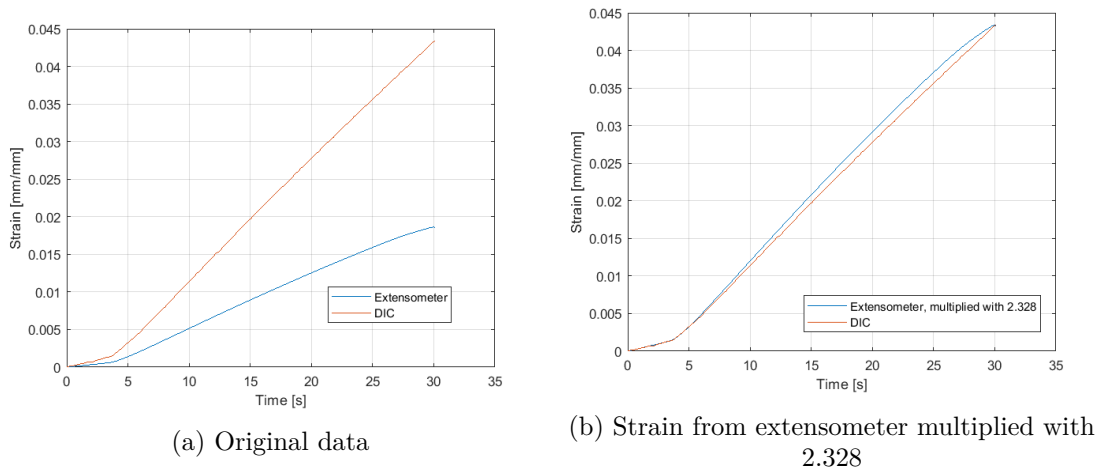


Figure 119: Measured strains as function of time

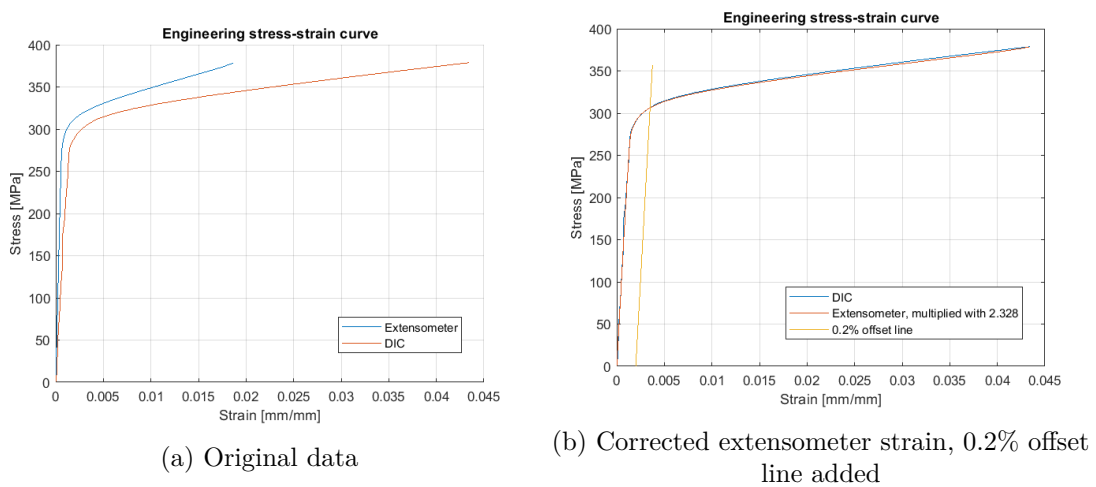


Figure 120: Engineering stress-strain curves

4.3.3 Engineering and true stress-strain curves

Following section present the stress-strain curves obtained during the tensile test. Figure 121 present the results from analysis of first 5 seconds of the tensile tests for specimen 1 and 2. Since the camera was recording with 50 fps, totally 250 images were used for creating both plots. Plots contain a regression line, its slope correspond to the elastic modulus of the material. Values of elastic modulus were found to be 193.0 GPa and 191.3 GPa for specimen 1 and 2 respectively. Possible sources of error are discussed in section 5.2.2.

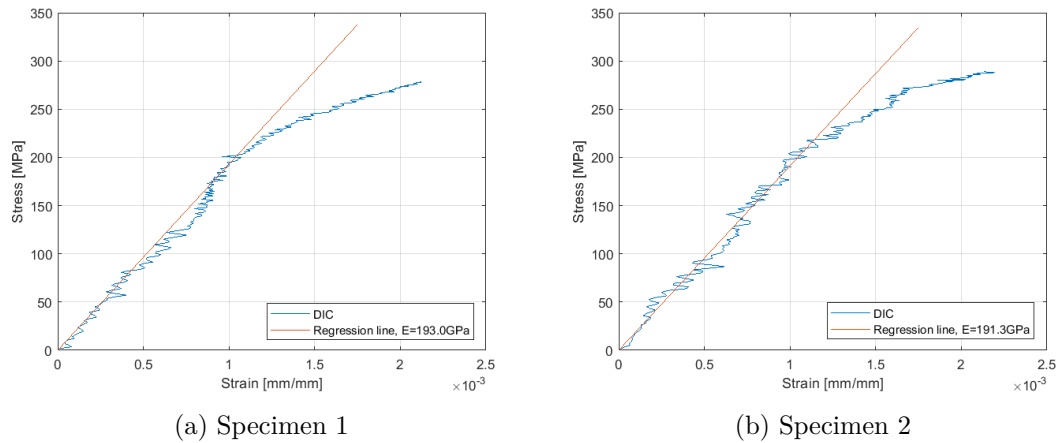


Figure 121: Analysis of the stress-strain behaviour in the elastic regime, regression line added

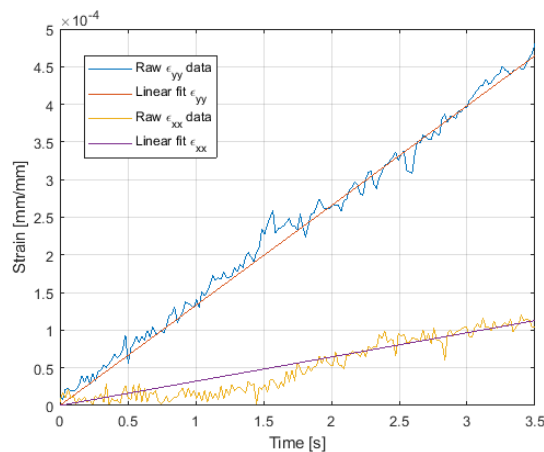


Figure 122: Strains ε_{xx} and ε_{yy} used to find the Poisson's ratio, data from specimen 3

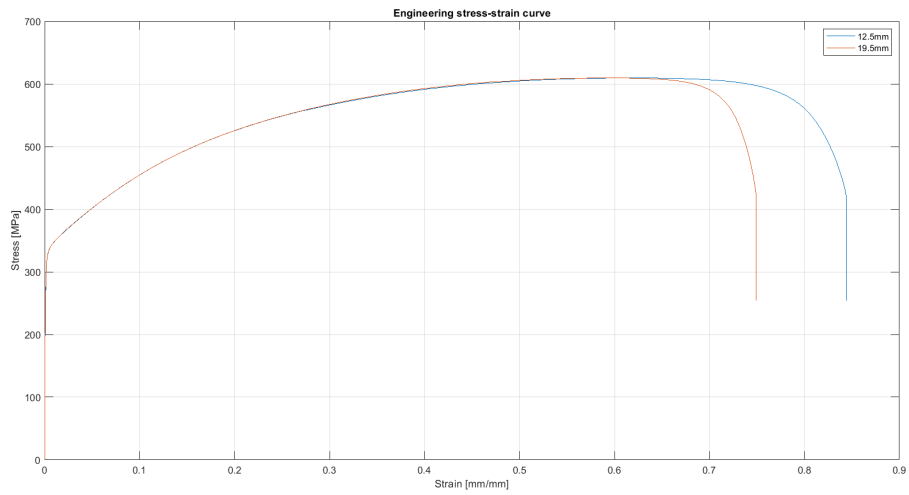
An attempt to estimate the proportionality limit can be made by looking at figure 121. Even though the scatter is significant it can be seen that the stresses starts to deviate from linearity around 210 MPa for specimen 1, and around 220 MPa for specimen 2.

Data from test 3 was useless for making the stress-strain curves due to peeling off the painting with speckle pattern during the test. However, the part of data representing the elastic region was not affected by this problem, and was used to determine the Poisson's ratio. Since the strains for the first 3 seconds of test include significant scatter, the Poisson's ratio was determined using the ratio between linear regression fit lines for ε_{xx} and ε_{yy} . The Poisson's ratio was found to be $\nu = 0.243$, and the data used for determination of this parameter are presented on figure 122. Tables 11 and 12 summarises the findings from the DIC analysis of the tensile test data.

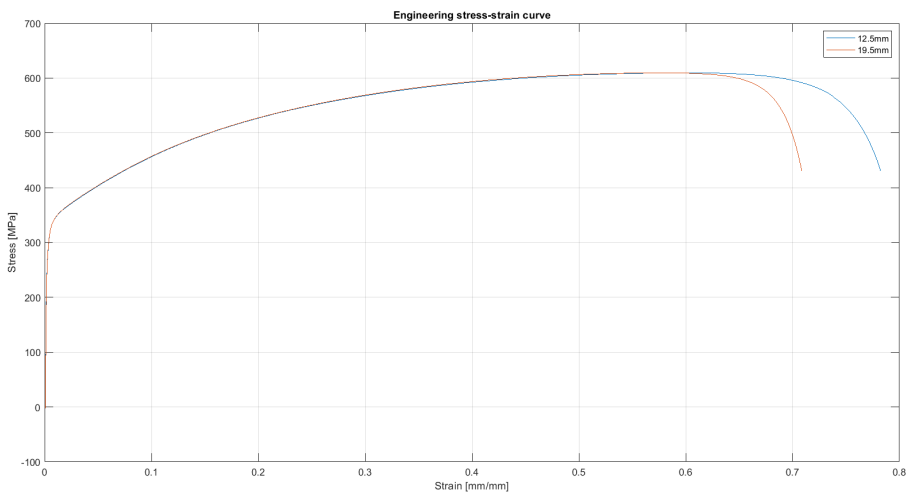
Specimen number	Elastic modulus	Proportionality limit	Poisson's ratio
1	193.0 GPa	210 MPa	-
2	191.3 GPa	220 MPa	-
3	-	-	0.243
4	-	-	-

Table 11: Parameters found using tensile tests

Figures 123 and 124 show the whole engineering stress-strain curves from start of the test to the final fracture. As mentioned in section 3.5.4, two different ROI with lengths of 12.5 mm, and 19.5 mm were used while calculating the strains. Figures 123a and 123b show comparison of engineering stress-strain curves using both ROIs for the same specimen, while figures 124a and 124b show comparison of results from different specimens using the same ROI. In opposition to the results presented in figure 121 where 250 images were used only for the elastic region, here 320, and 300 images were used to find strains for the whole stress-strain curves for specimen 1 and 2 respectively.

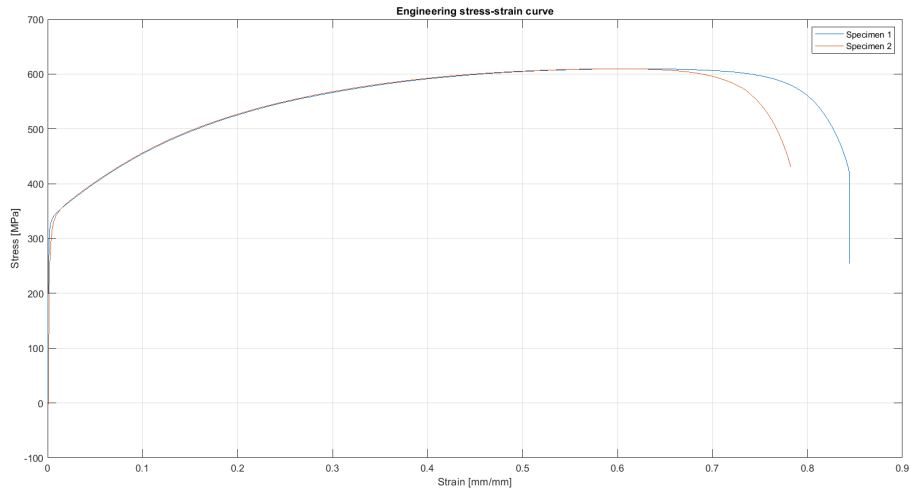


(a) Specimen 1, gauge lengths of 12.5 mm and 19.5 mm compared

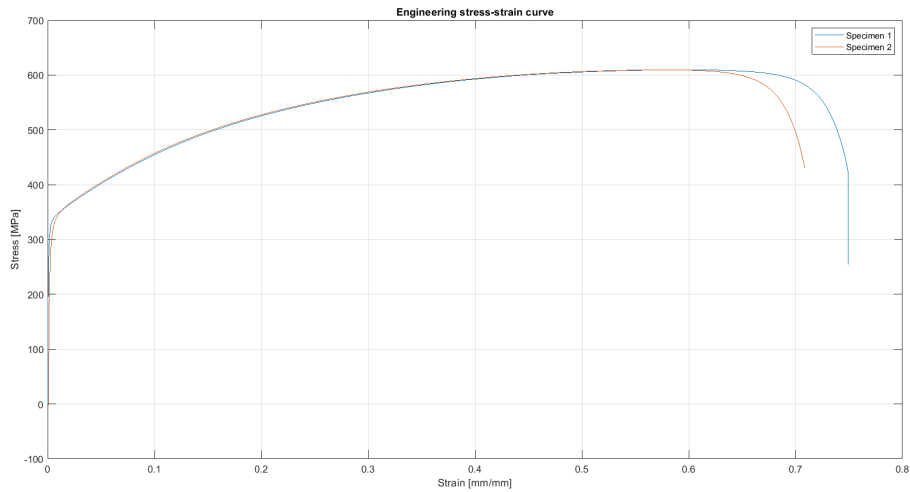


(b) Specimen 2, gauge lengths of 12.5 mm and 19.5 mm compared

Figure 123: Engineering stress-strain curves



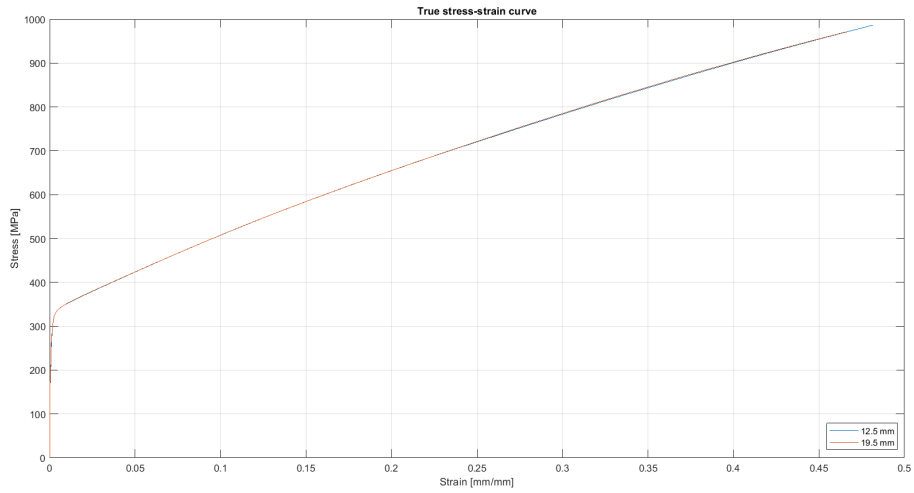
(a) Specimen 1 and specimen 2 compared, gauge length 12.5mm



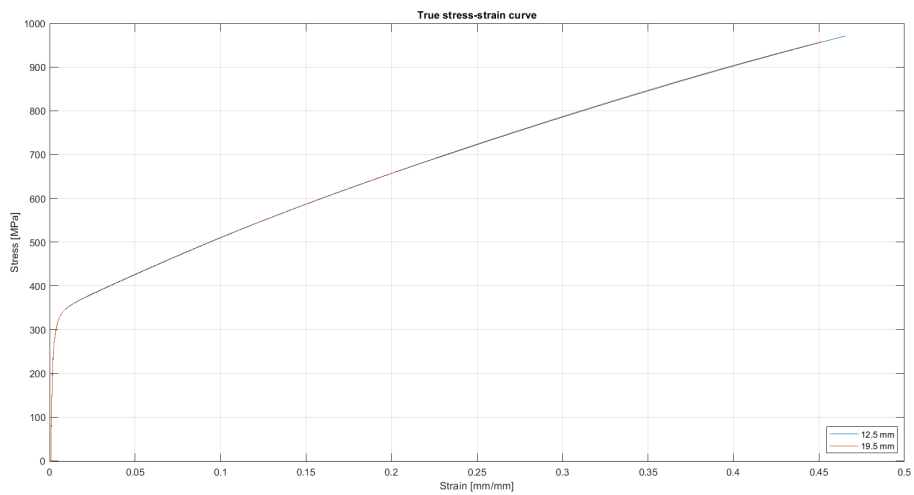
(b) Specimen 1 and specimen 2 compared, gauge length 19.5mm

Figure 124: Engineering stress-strain curves

Finally, the true stress-strain curves were made using the true strains and stresses calculated from engineering strains and stressed using method described in section 3.5.4. The maximum stress values on the true stress-strain curves correspond to the stress values on engineering stress-strain curves where the ultimate tensile strength was reached. Table 12 presents these true stress values and the corresponding true strains.



(a) Specimen 1, gauge lengths of 12.5 mm and 19.5 mm compared



(b) Specimen 2, gauge lengths of 12.5 mm and 19.5 mm compared

Figure 125: True stress-strain curves

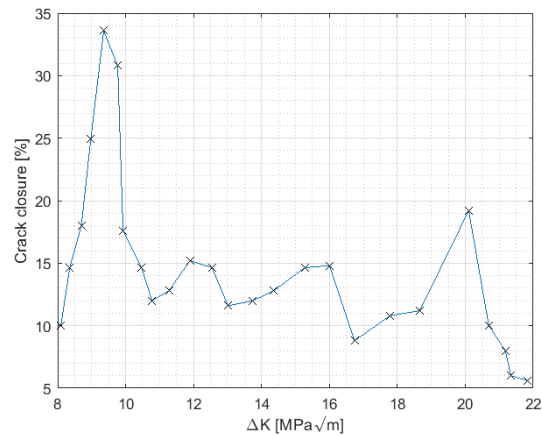
Specimen number	1		2	
Gauge length	12.5 mm	19.5 mm	12.5 mm	12.5 mm
True stress at UTS [MPa]	986.6	971.6	971.4	957.5
True strain at UTS [mm/mm]	0.4816	0.4662	0.4659	0.4516

Table 12: True stress and true strain values at UTS

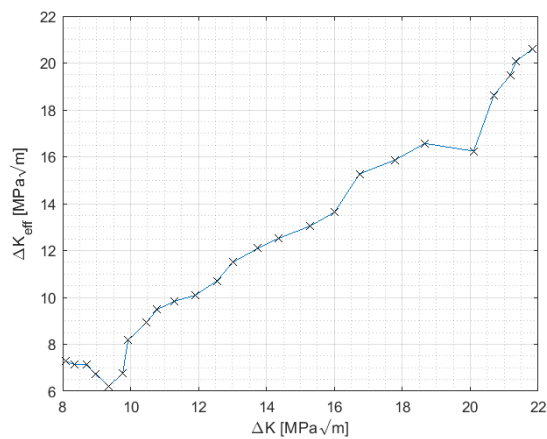
4.3.4 Stress intensity factor and crack closure

The following section presents the main findings from the FCG tests. Figures 126 and 127 present the crack closure level, and the effective SIF range as function of theoretical SIF, ΔK , both found performing the analysis of CODs according to the method described in section 3.5.6. The $L1$ used for both test 4 and 5 were: 5, 10, 15 and 20 pixels, while the $L2$ value was 10 and 12 pixels for test 4 and 5 respectively.

Test 4



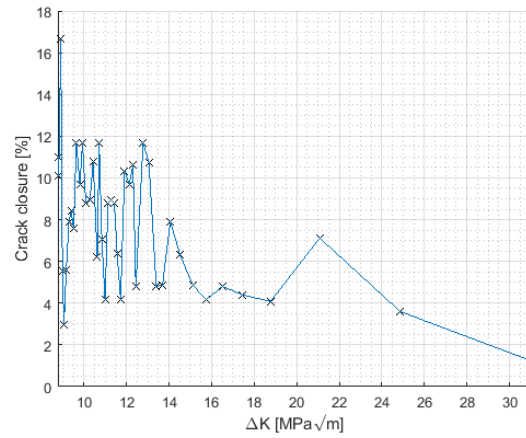
(a) Crack closure



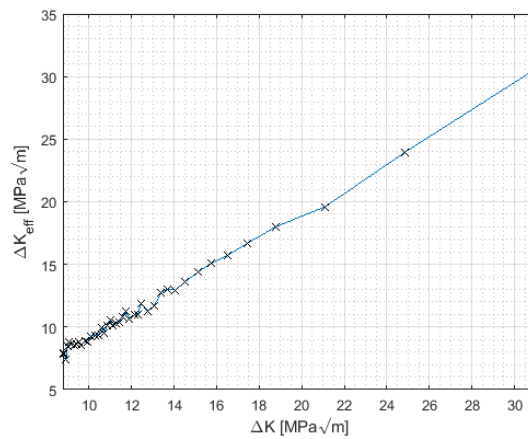
(b) Effective SIF, ΔK_{eff}

Figure 126: ΔK_{eff} , and crack closure as a function of the SIF, ΔK

Test 5



(a) Crack closure



(b) Effective SIF, ΔK_{eff}

Figure 127: ΔK_{eff} and crack closure as a function of the SIF, ΔK

Figure 128 presents four selected plots used to determine P_{op} and thus the crack closure level, and the effective SIF range for specimen 5. Remaining plots for test 5 will be attached to the thesis. For specimen 4, 25 P_{op} values were measured, while for specimen 5, 18 P_{op} values were measured.

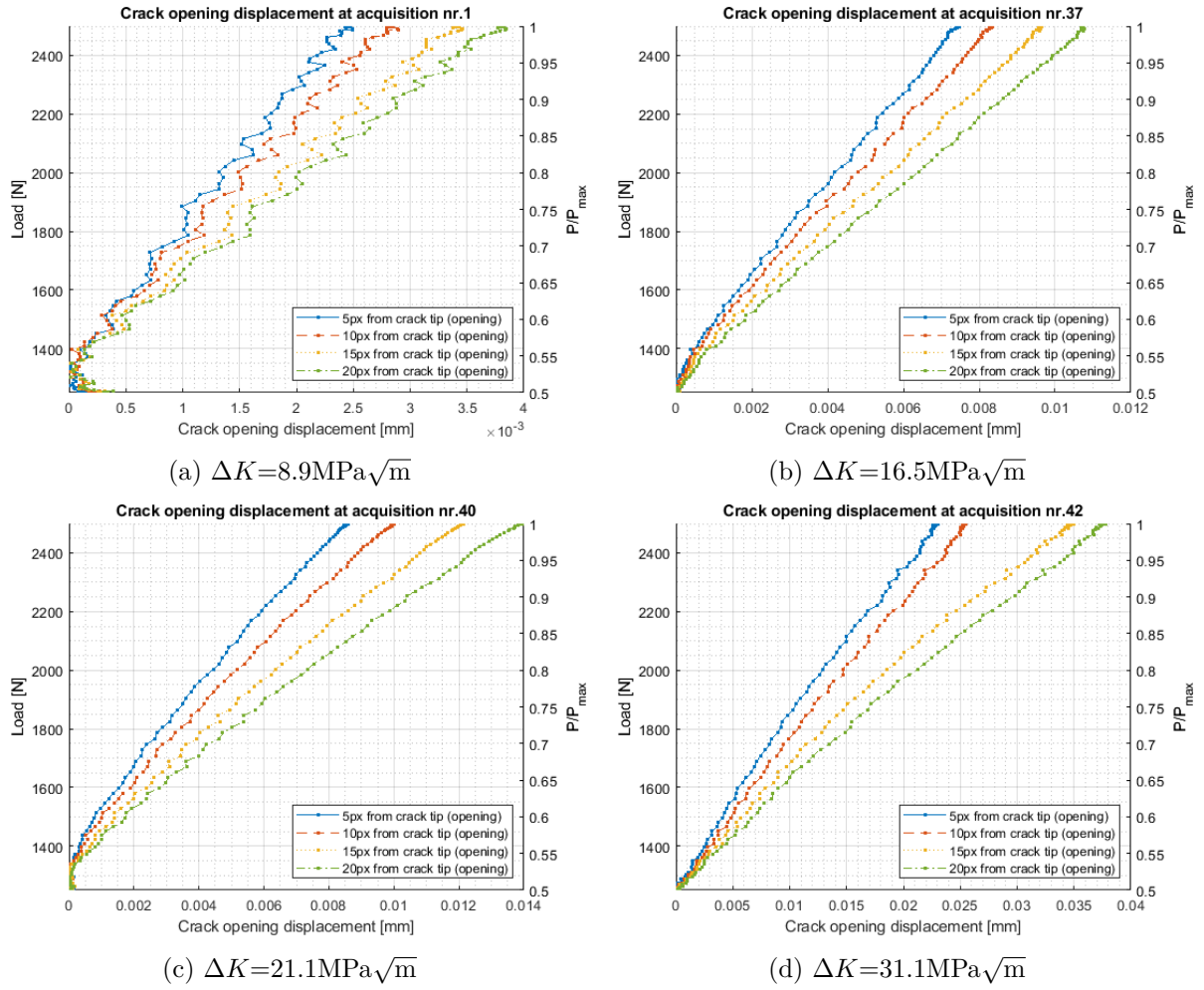


Figure 128: Applied load as function of COD

4.3.5 Strain and stress fields

Following section presents the strain-, and the stress fields used to determine the plastic zone. Figures 129 and 130 present selected strain fields directly exported from the *Ncorr* DIC-software. The left ones are the ε_{xx} , in the middle the ε_{xy} , and the right ones are the ε_{yy} . The colorbars for ε_{xx} and ε_{xy} are scaled from 0 to 1.5×10^{-3} , while the ε_{yy} -strains are scaled from 0 to 3×10^{-3} .

Test 5

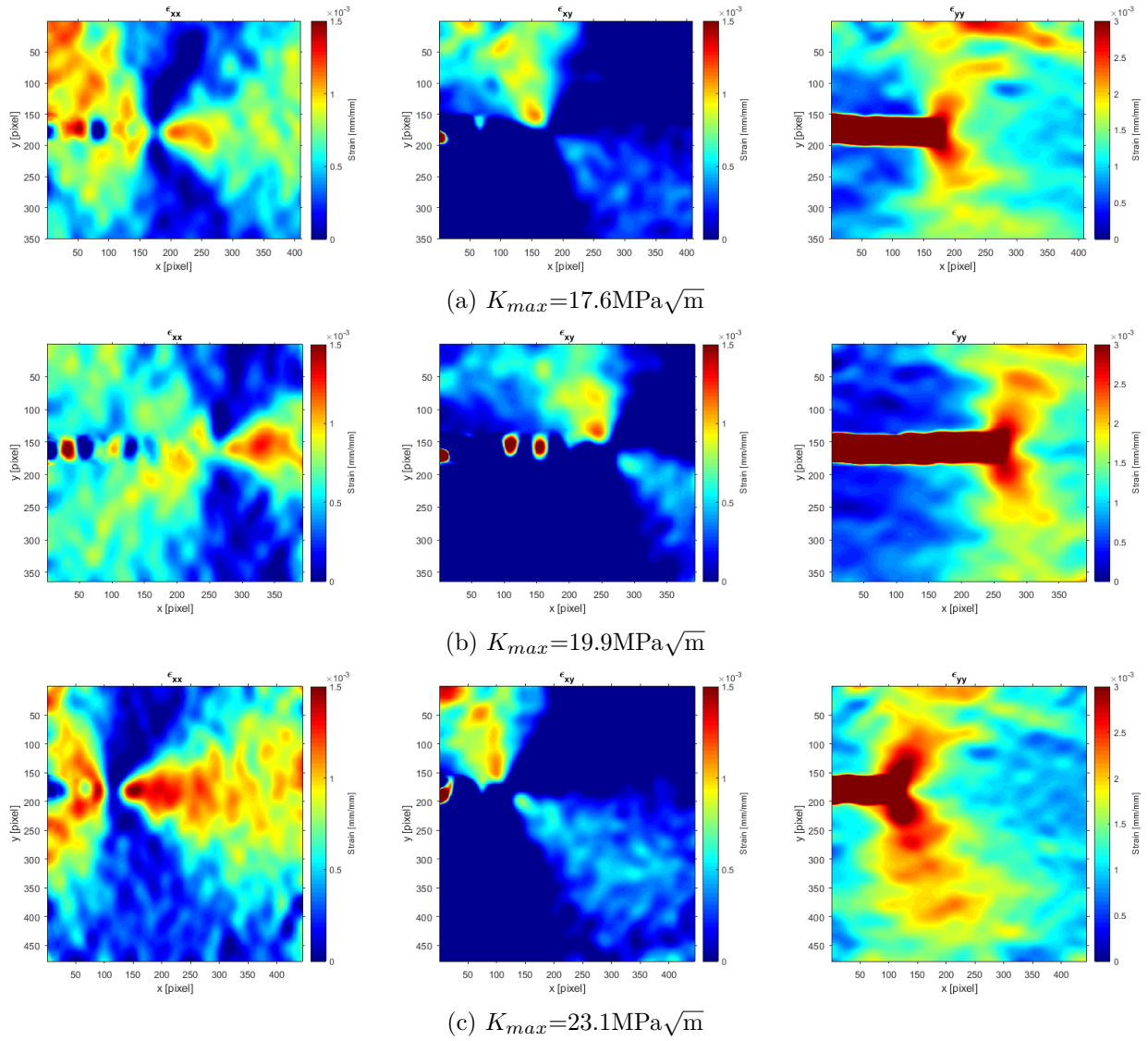


Figure 129: The strains ε_{xx} , ε_{xy} , and ε_{yy} for different K_{max}

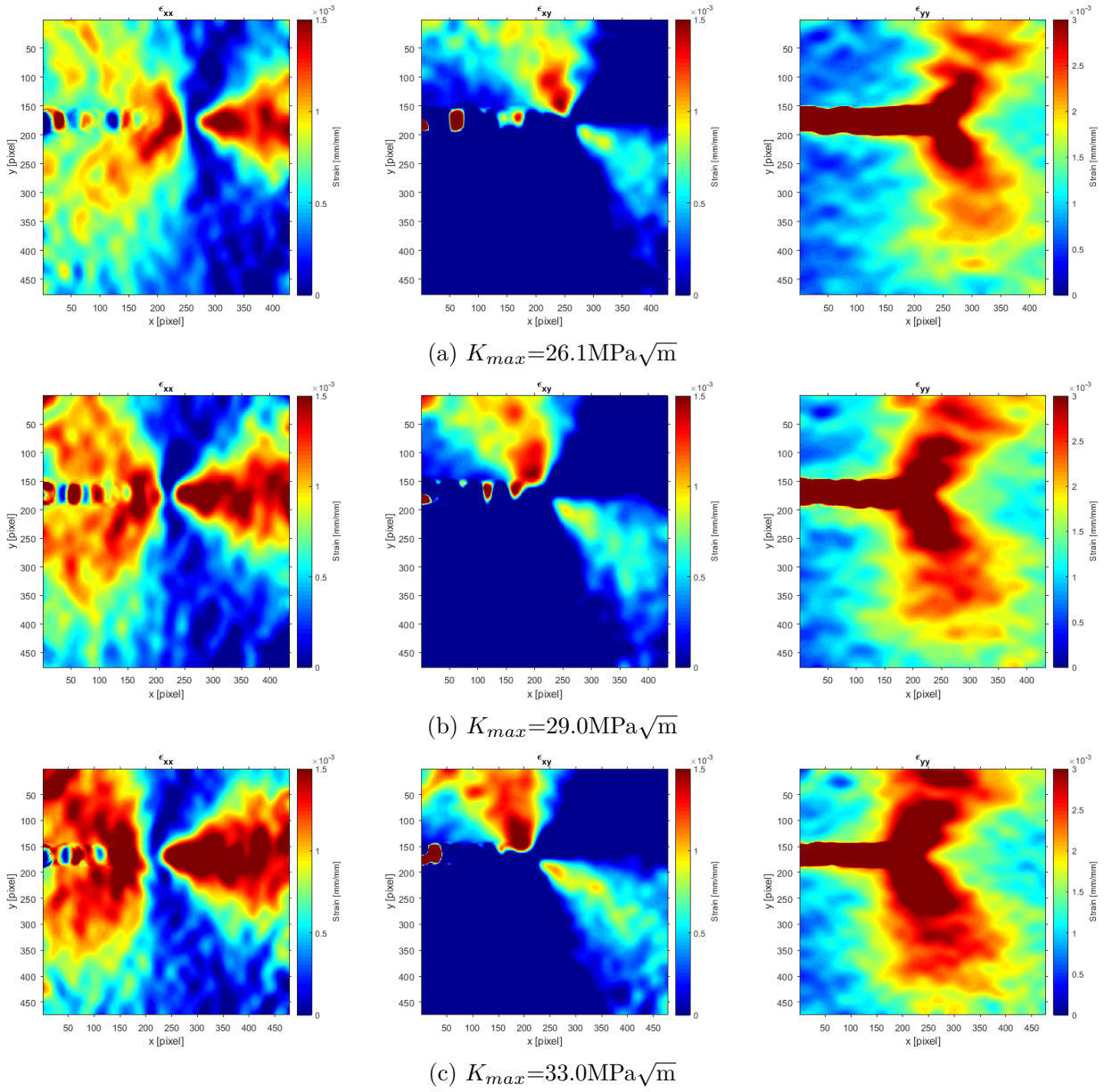


Figure 130: The strains ε_{xx} , ε_{xy} , and ε_{yy} for different K_{max}

These strain fields were further used to determine the elastic stress fields, also the equivalent von Mises stresses. These stresses assume the Hooke's law, and are only valid in the elastic regime. Since the tool for calculation of stresses employs the stiffness tensor and the plane stress assumption, the stress are scaled from 0 to 308 MPa, where the plastic deformation is assumed to be inside the zone where the stress of 308 MPa is exceeded.

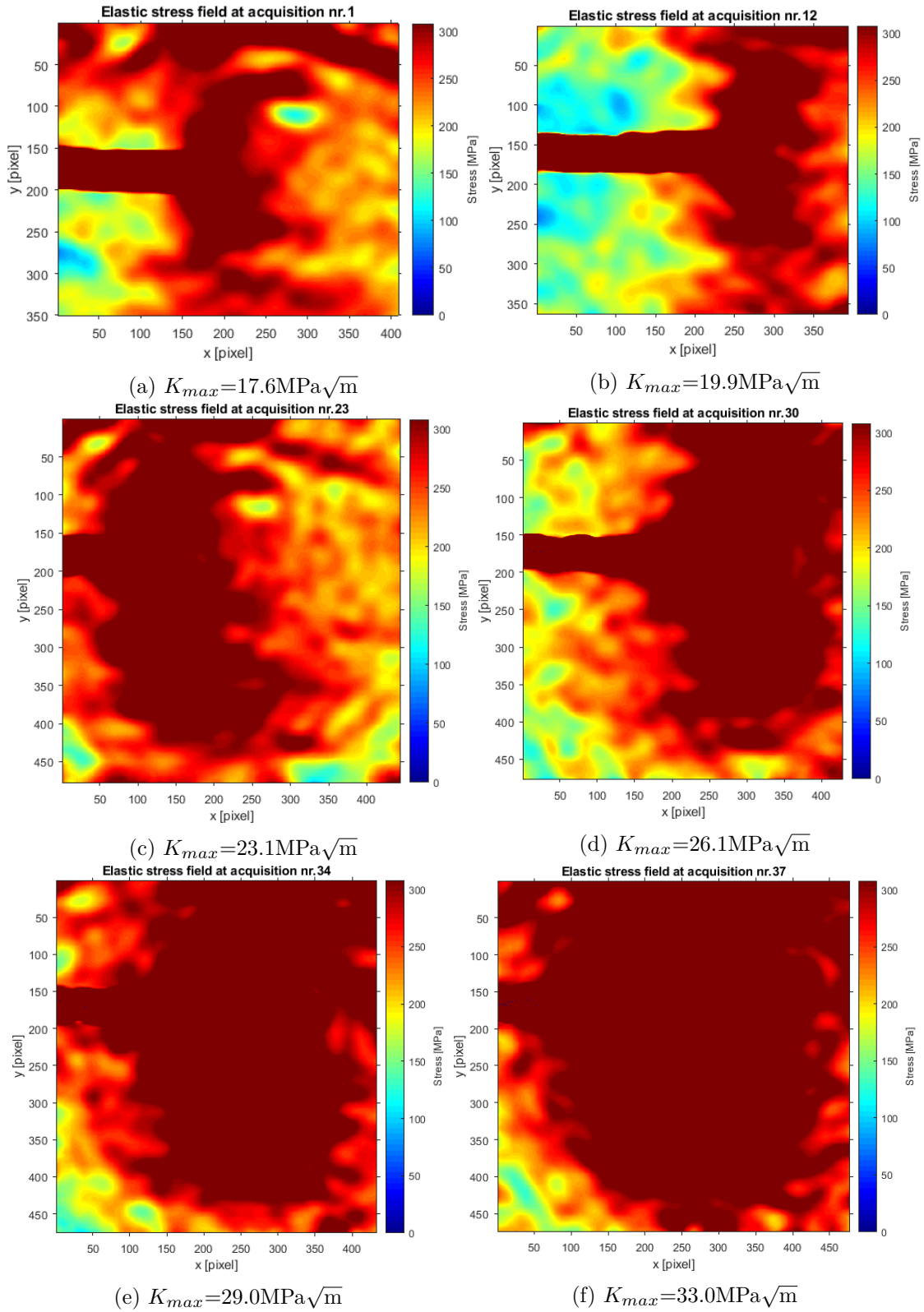
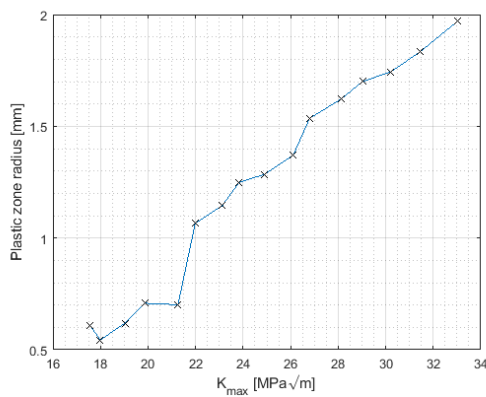


Figure 131: Elastic stress fields (equivalent von Mises stresses) for different K_{max}

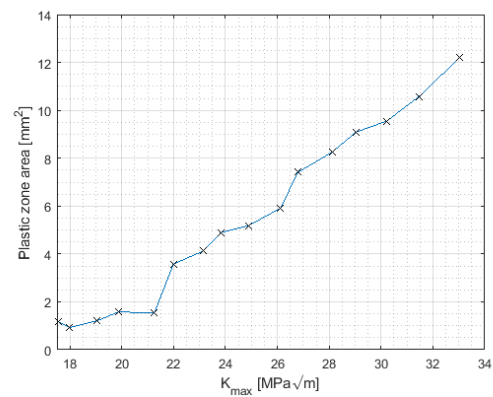
4.3.6 Plastic zone

The equivalent von Mises stress fields presented in section 4.3.5 were further used to estimate dimensions of the plastic zone. As mentioned earlier, the zone of plastic deformation is assumed to occur where the stress level of 308 MPa is exceeded. Figure 133 show the selected bitmaps, the white areas correspond are the areas where the yield strength is exceeded. These were further used to quantify a supposed area of the plastic zone. Figure 132 presents the sizes (radius, area and height) plotted against K_{max} .

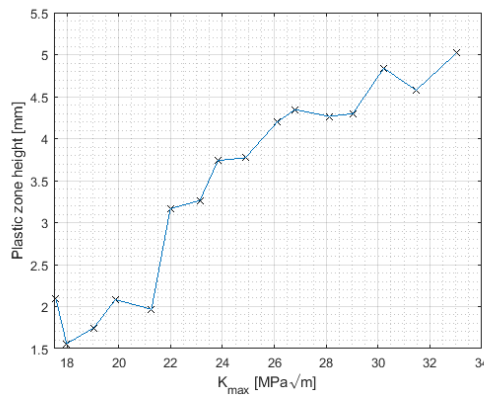
Test 5



(a) Plastic zone radius



(b) Plastic zone area



(c) Plastic zone height

Figure 132: Plastic zone sizes as function of K_{max}

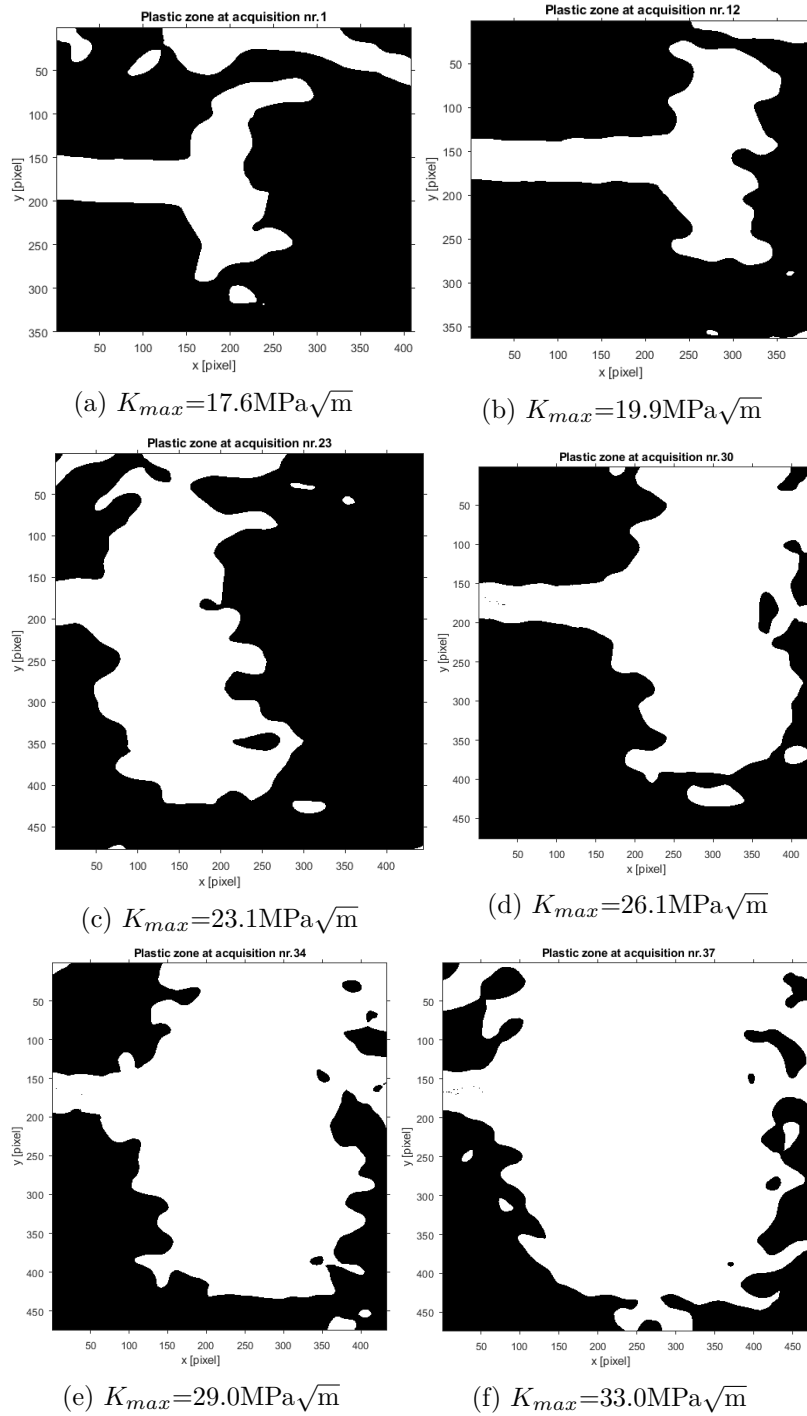


Figure 133: Bitmaps showing approximate plastic zone for different K_{max}

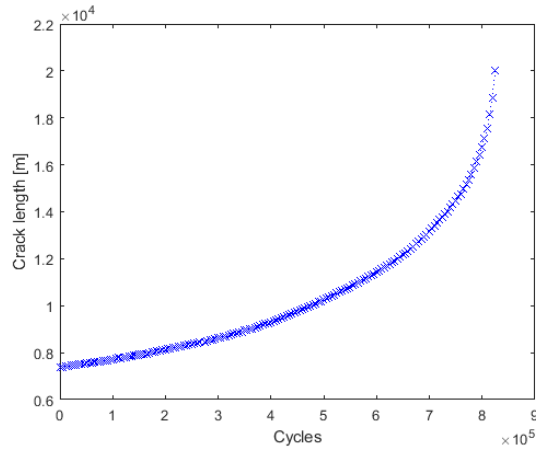
4.3.7 Fatigue crack growth parameters in Paris regime

Following section presents the fatigue crack growth curves, and lists the fatigue crack growth parameters in Paris regime (C and m). The procedure for creating the fatigue crack growth curves was described in section 3.5.2. For the high-speed camera the constants were obtained using the ΔK rather than ΔK_{eff} because the procedure of measuring the latter one is quite time consuming, and only selected ΔK_{eff} were analysed for tests 4 and 5. For the test 1 none ΔK_{eff} were found since the specimen was unprepared for the DIC analysis. The crack tip positions for test 1 were found using visual inspection of the raw images, while for specimen 4 and 5, the vertical displacement fields were used to determine the crack tip position. Constants with 95% CBs and R^2 are presented in table 13. The a-N and the FCG curves for HSI are presented on figure 134, 135 and 136.

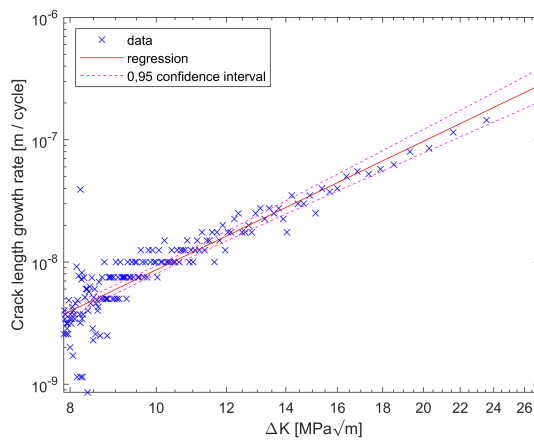
Test	Method	$\log_{10}C$ (95% CBs)	m (95% CBs)	R^2
1	HSI, secant m.	-11.56 (-11.81, -11.31)	3.494 (3.247, 3.741)	0.8276
	HSI, incr. poly. m.	-32.95 (-33.59, -32.3)	3.556 (3.464, 3.649)	0.9736
4	HSI, secant m.	-11.0 (-11.4, -10.6)	3.069 (2.703, 3.436)	0.8115
	HSI, incr. poly. m.	-10.94 (-11.07, -10.81)	3.019 (2.898, 3.139)	0.9767
5	HSI, secant m.	-11.32 (-11.63, -11.02)	3.377 (3.096, 3.659)	0.938
	HSI, incr. poly. m.	-11.45 (-11.54, -11.37)	3.530 (3.452, 3.607)	0.996

Table 13: Summary of fatigue crack growth parameters and R^2 values.

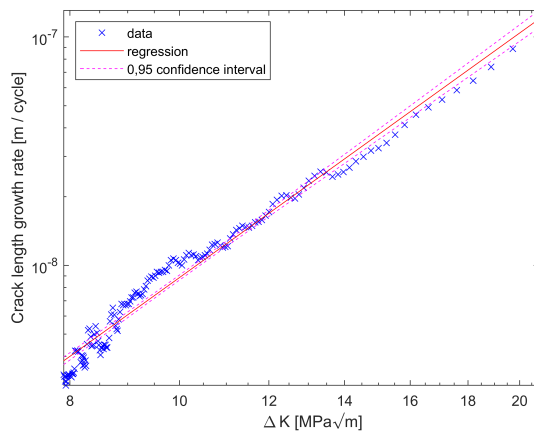
Test 1



(a) a - N curve



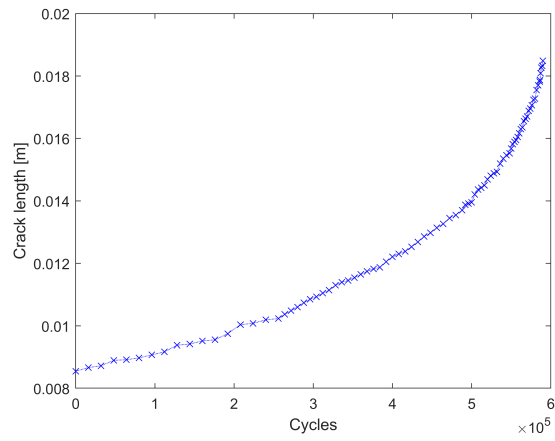
(b) FCG curve, secant method



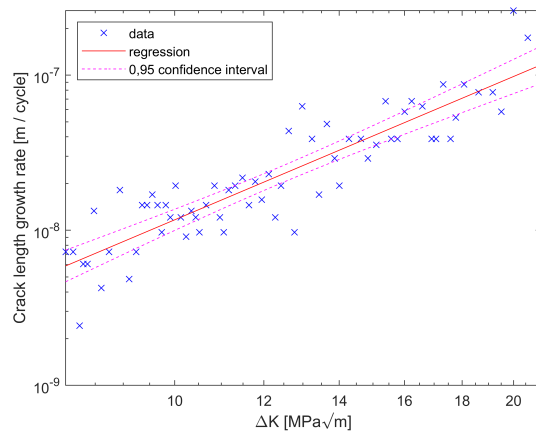
(c) FCG curve, incremental polynomial method

Figure 134: Fatigue crack growth curves obtained using high-speed camera, data from Test 1

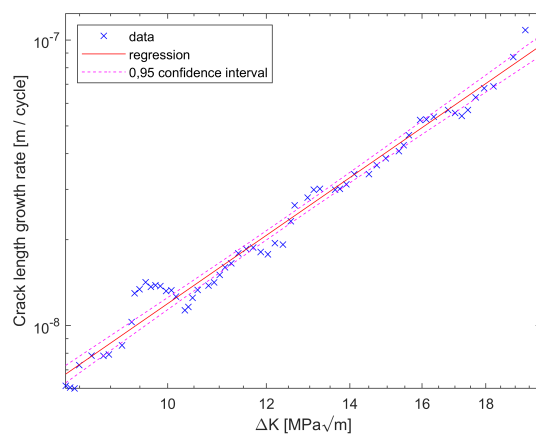
Test 4



(a) a - N curve



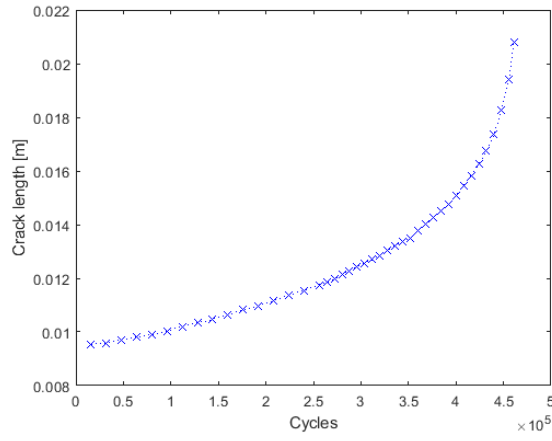
(b) FCG curve, secant method



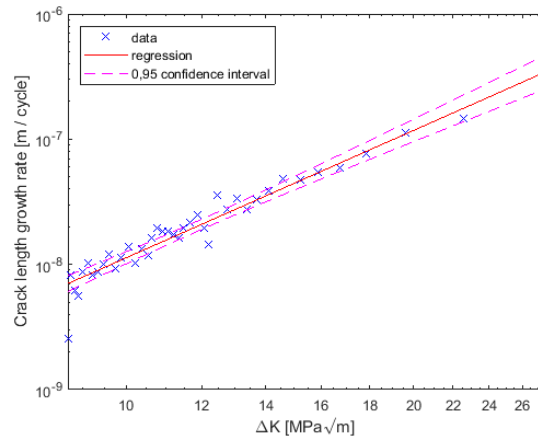
(c) FCG curve, incremental polynomial method

Figure 135: Fatigue crack growth curves obtained using HSI and DIC, data from Test 4

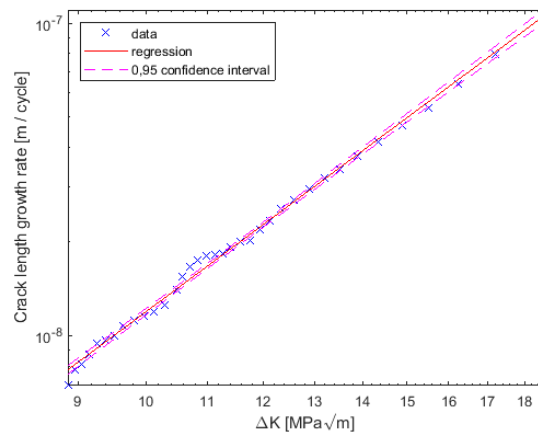
Test 5



(a) $a-N$ curve



(b) FCG curve, secant method



(c) FCG curve, incremental polynomial method

Figure 136: Fatigue crack growth curves obtained using HSI and DIC, data from Test 5

4.3.8 Qualitative observation of crack initiation and propagation

One of the goals in this work was qualitative observation of cracking, especially when the cracking process moves from the Paris regime (stage II) to the high growth regime (stage III). This transition was captured in test 6. The precracking process was also of interest, the whole crack initiation process for specimen 3 was captured.

Test 3 - Precracking

The crack initiation was captured when the P_{max} , and R were 3.5kN, and 0.1 respectively. As it can be seen on figure 138, the initiation was a process where the crack slowly appeared with length of 35 μm . This 35 μm portion of the crack seem to occur at the grain boundary. The crack initiated at the machined notch tip and continued until it met another grain boundary at angle of 45° , where it was arrested. A precise determination of cycle when the crack was initiated is challenging since the 35 μm crack was initially similar to the typical grain boundary, and become visible when it got darker as seen on figure 138b. After the initiation a crack continued the growth in transgranular manner perpendicularly to the applied load, and following a zigzag path.

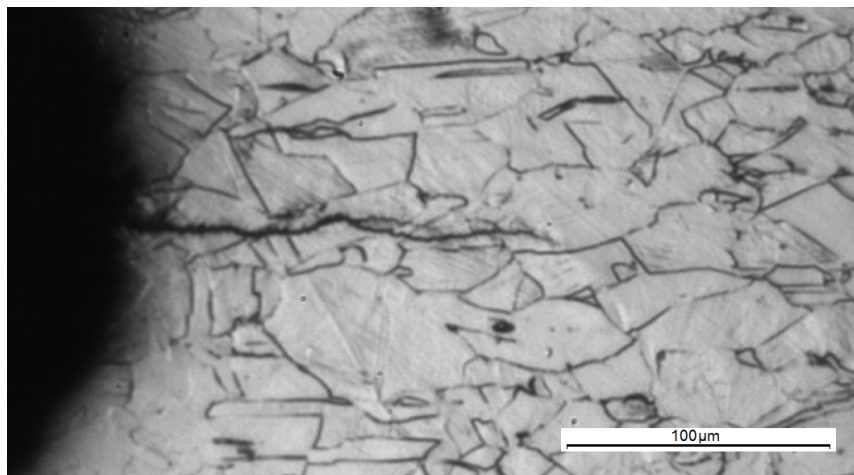
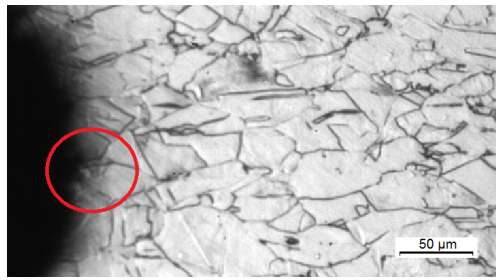
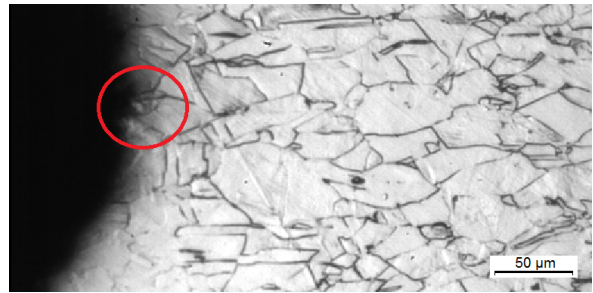


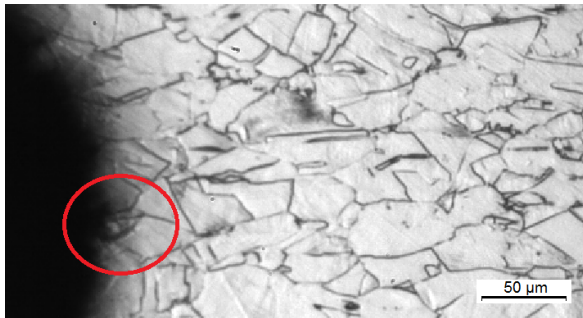
Figure 137: Precracking of specimen 3



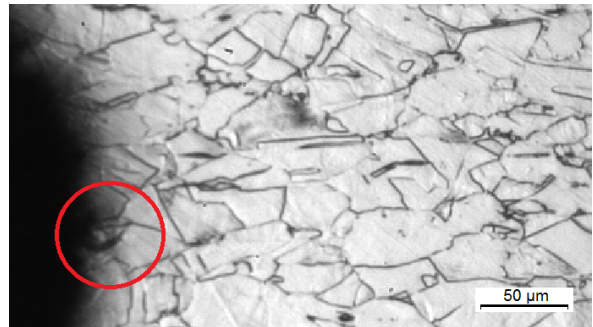
(a) Just before the crack initiation



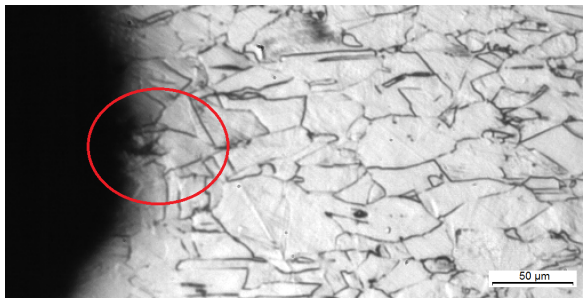
(b) 10 cycles after initiation



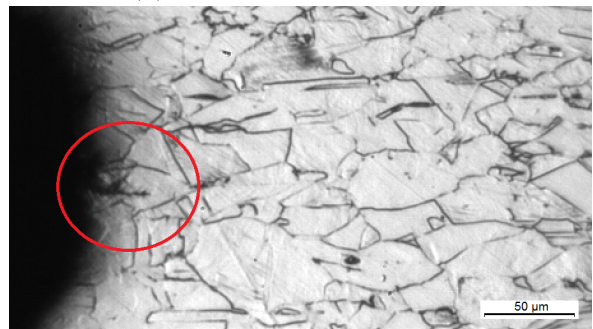
(c) 80 cycles after initiation



(d) 140 cycles after initiation



(e) 530 cycles after initiation



(f) 900 cycles after initiation

Figure 138: Precracking of the specimen number 3

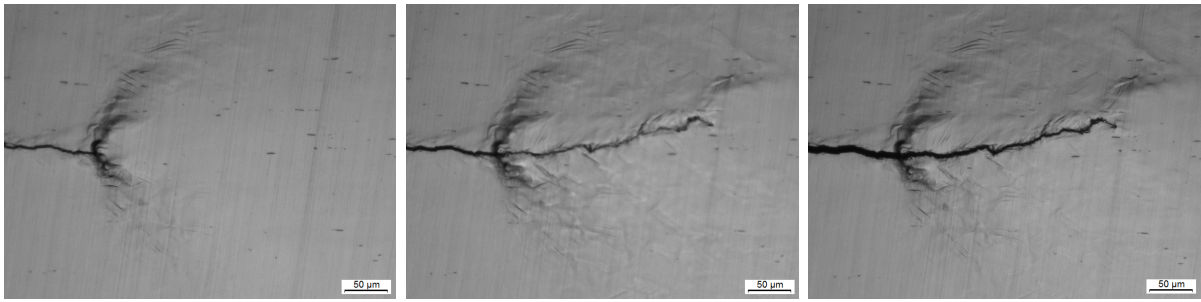
Test 6 - Crack propagation and transition from stage II to stage III

In the following, the qualitative results from test 6 are presented. Figure 139 show start of the test, and the zone of plastic deformation which occurred when the load was removed after the precracking was done. There are no signs of crack closure behind this zone even though the image 139a was captured when the load was P_{min} . In opposition, the closure is present between the crack tip and mentioned zone as it can be seen in figure 139b.

Set of images 140 present an example branching of the crack. It can be observed that for presented acquisition, the crack started to grow in two directions simultaneously; almost parallel to the existing crack, and at very sharp angle. However, the crack propagated parallel as it follows from figure 139c.

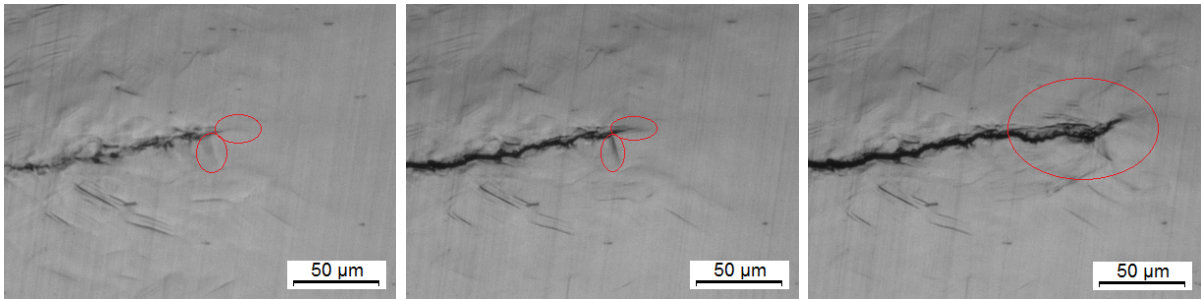
What can be seen for all figures presented in this section is that the surface areas left by the "active" plastic zone are uneven and deformed. The figure 141 present this phenomenon. As the crack propagated, and ΔK increased, the surface was more, and more affected. This behaviour is very clear at stage III of FCG. The slip bands resulting from the plastic deformation can be seen at figure 142.

During test 6 the majority of stage III was captured, some of moments are presented at figure 143. A movie from stage III follows as attachment to the thesis. There were several issues when capturing the stage III. The zone of deformation left by the process zone ahead of the crack tip was more, and more pronounced, while the surface ahead of the crack tip has raised towards the lens. Rising of the process zone ahead the crack tip led to a slope in the surface right behind the process zone, this is visible as a dark transition between the two different areas of a surface. These two facts made it impossible to observe crack growth itself for a few moments before the final failure, since the rise of the process zone lead to a loss of focus, while the slope between the areas of surface created a shadow hiding the crack tip.



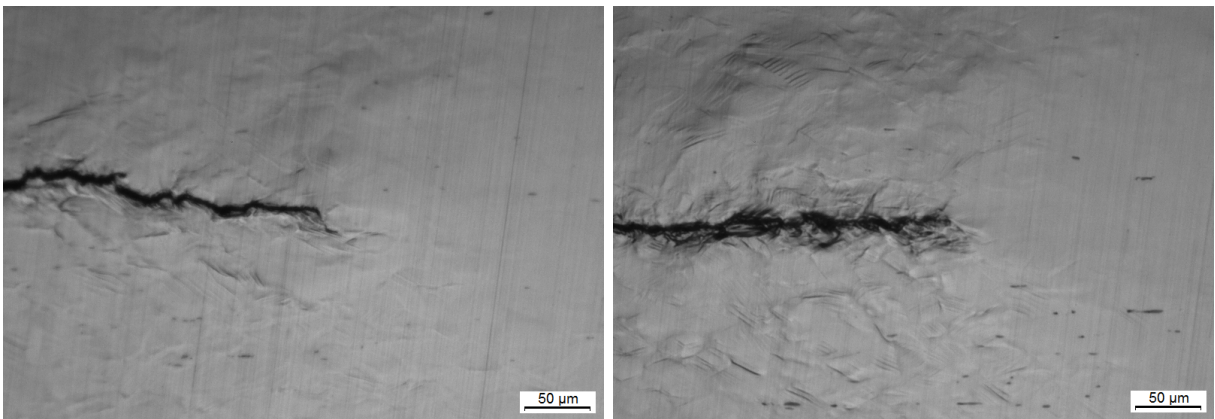
(a) Start of the test, at P_{min} (b) +6400 cycles, at P_{min} (c) +6400 cycles, at P_{max}

Figure 139: Start of the test 6



(a) +22000 cycles, at P_{min} (b) +22000 cycles, at P_{min} (c) +24000 cycles, at P_{max}

Figure 140: Branching of the fatigue crack, branches marked in red circles, the cycles are counted from the test start



(a) +75500 cycles after the test start (b) +102000 cycles after the test start

Figure 141: Uneven specimen surface left by the plastic zone, the cycles are counted from the test start

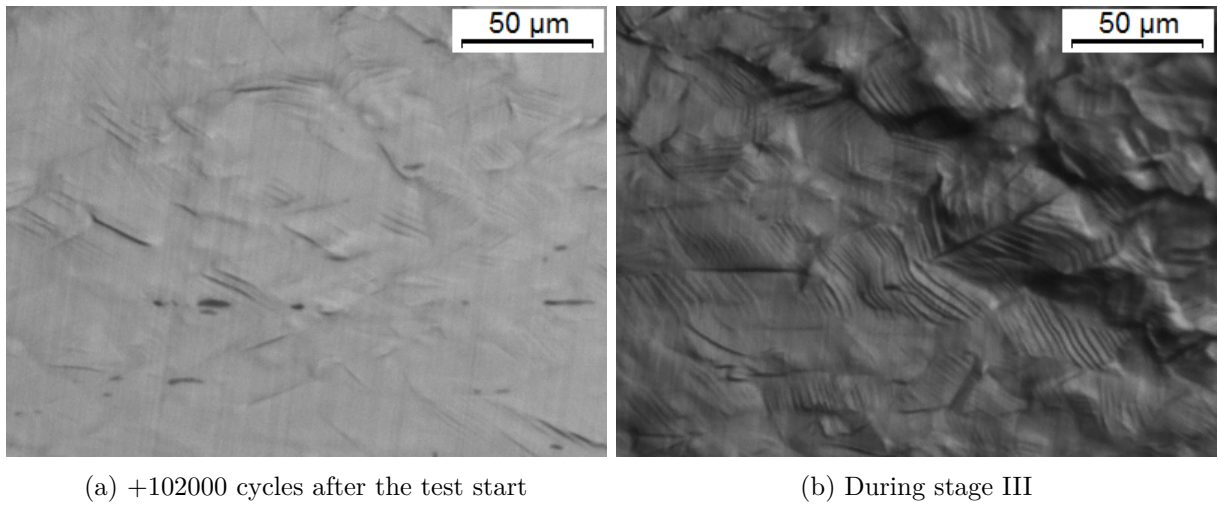


Figure 142: Slip bands present on the grains affected by the plastic deformation

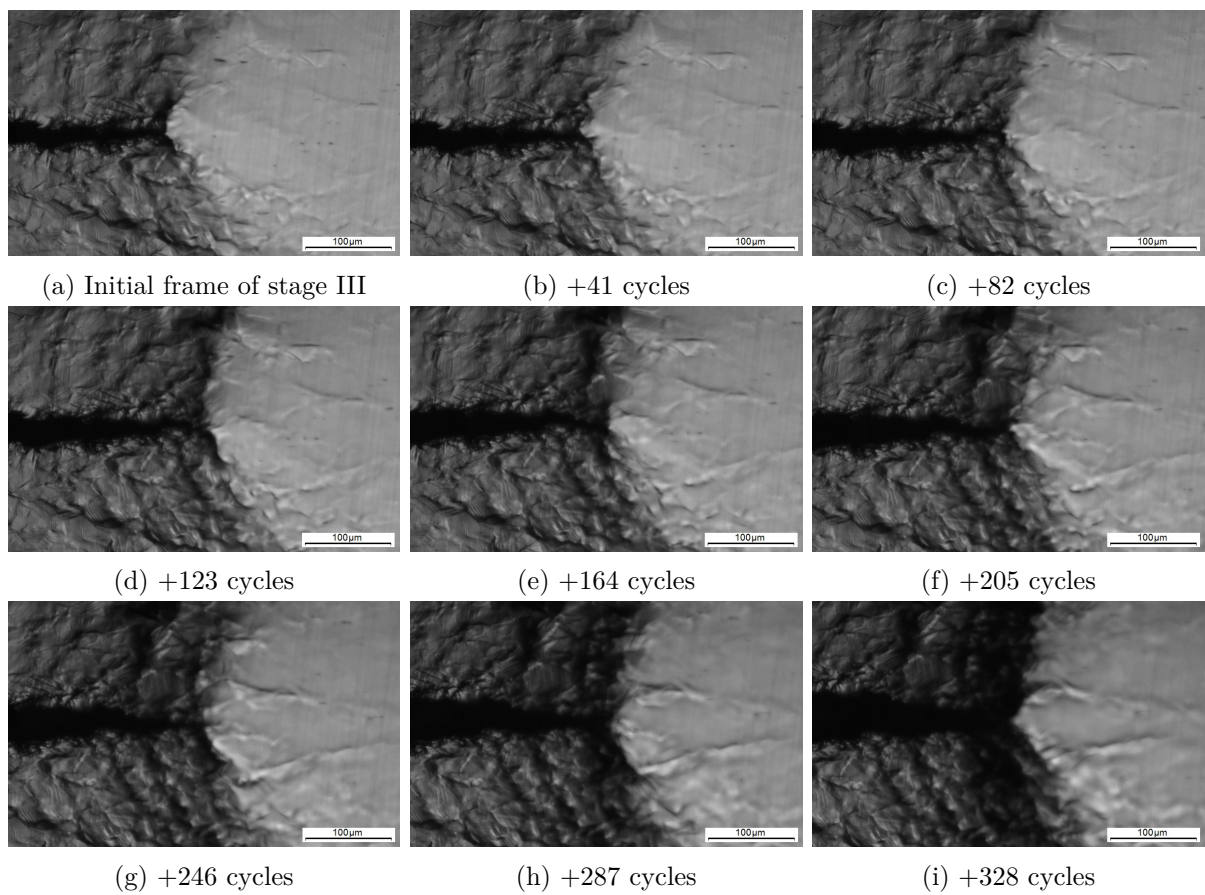


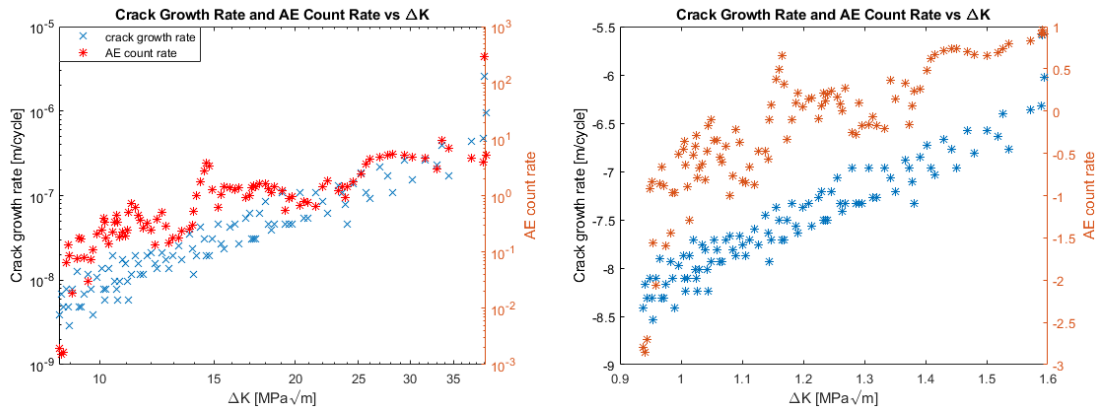
Figure 143: Stage III of FCG

4.4 Acoustic Emission

4.4.1 Count rate curves

Test 4

Figure 144 shows the AE count rate, and crack growth rate based on IR recordings, plotted against ΔK from Test 4. Figure 144a shows AE count rate calculated based on the mean method, while the peak method was used in figure 144b, where the methods are as described in section 3.6.1.



(a) Comparison of crack growth rate and AE count rate versus ΔK from Test 4 using mean cycles and count rate

(b) Comparison of crack growth rate and AE count rate versus ΔK from Test 4 using peak values of cycles and count rate

Figure 144: Crack growth rate and AE count rate versus ΔK from Test 4 using two different count rate procedures

For estimating the constants C_4 and n in the Paris regime, the first 4 and last 3 measurements were ignored. The resulting values are shown in table 14. The equivalent calculations for the Paris constants C and m can be found in section 4.2.6.

Test	Method	$\log_{10} C_4$ (95% CBs)	n (95% CBs)	R^2
4	mean counts	-3.653 (-4.079, -3.227)	2.921 (2.565, 3.277)	0.7426
	peak counts	-3.638 (-4.088, -3.188)	2.910 (2.536, 3.283)	0.7221

Table 14: Summary of AE count rate parameters and R^2 values, based on mean and peak count rate calculations

Test 5

The count rate curves from Test 5, as calculated based on hits from each sensor, is shown in figure 145.

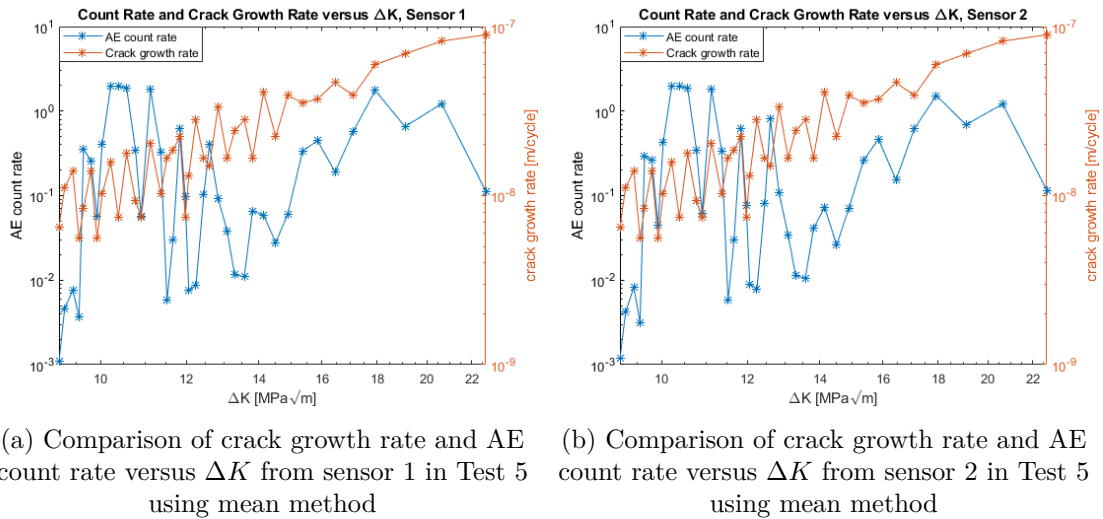


Figure 145: Crack growth rate and AE count rate versus ΔK from Test 5 from each sensor in Test 5

Count rate curves from Test 5, as calculated by the mean-method and peak-methods are shown in figure 146, based on the total data taken from both sensors. The corresponding parameters, C_4 and n are found in table 15 with 95% confidence bands.

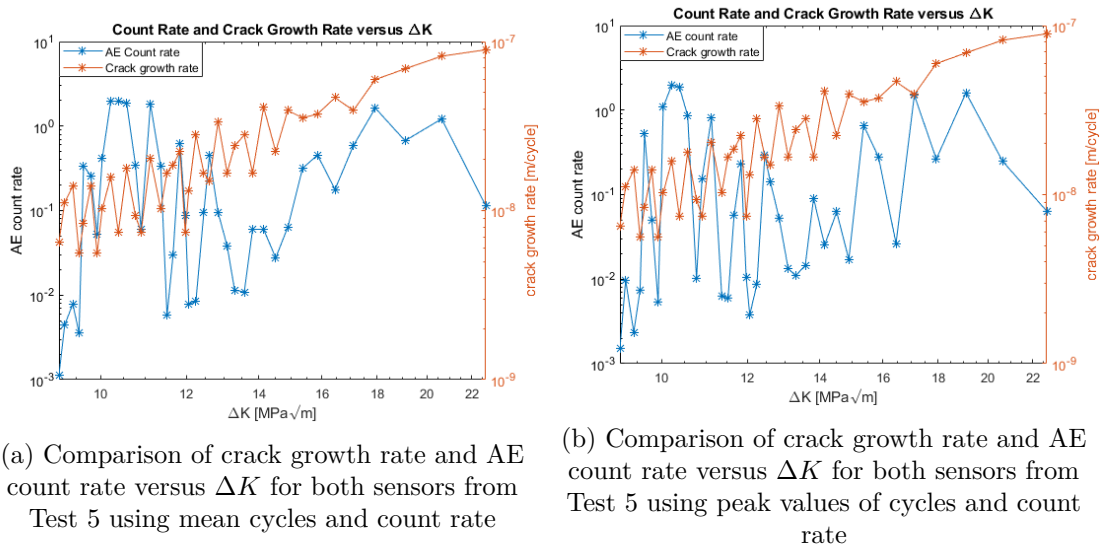


Figure 146: Crack growth rate and AE count rate versus ΔK from Test 5 using two different count rate procedures

Test	Sensor	Method	$\log_{10} C_4$ (95% CBs)	n (95% CBs)	R^2
5	1,2	mean counts	-4.402 (-7.234, -1.571)	3.031 (0.4904, 5.571)	0.1531
	1,2	peak counts	-4.952 (-7.924, -1.980)	3.310 (0.6448, 5.974)	0.1621

Table 15: Summary of AE count rate parameters and R^2 values, based on mean and peak count rate calculations

Test 6

Based on the results of Test 5 showing minimal difference between the count rates as obtained by either sensor, only the count rates calculated using both sensors were calculated for Test 6. Figure 147 shows the count rate based on IR crack length measurements, plotted against the corresponding crack growth rate.

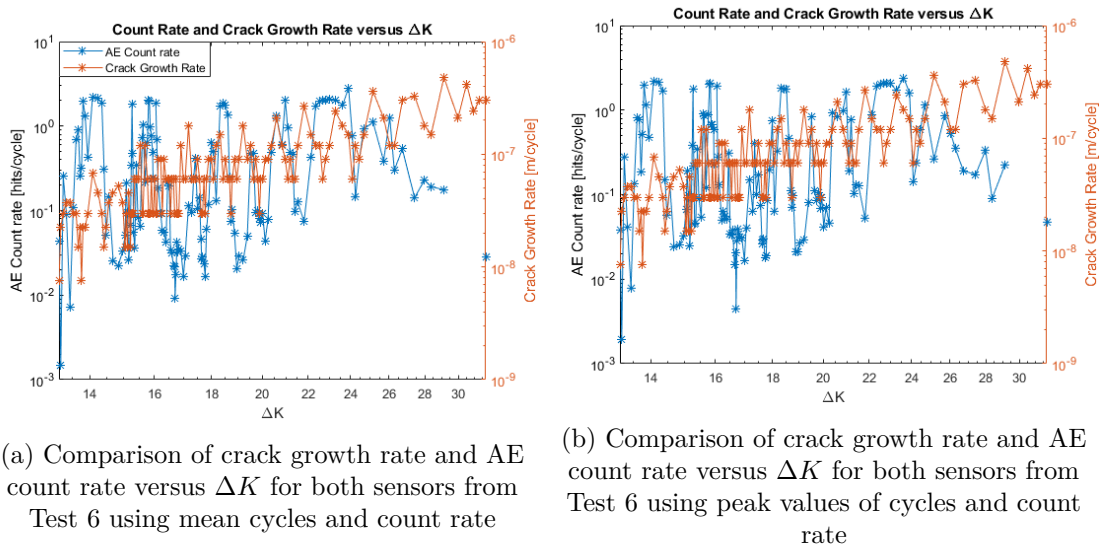


Figure 147: Crack growth rate and AE count rate versus ΔK from Test 6 using two different count rate procedures

Table 16 shows the count rate parameters obtained from the curves in figure 147. The very last point was ignored in the calculation, as this represented hits that certainly corresponded to stage III crack growth.

Test	Sensor	Method	$\log_{10}C_4$ (95% CBs)	n (95% CBs)	R^2
6	1,2	mean counts	-3.251 (-4.977, -1.526)	2.025 (0.6496, 3.400)	0.0439
	1,2	peak counts	-3.045 (-4.786, -1.304)	1.819 (0.431, 3.206)	0.0481

Table 16: Summary of AE count rate parameters and R^2 values, based on mean and peak count rate calculations of Test 6

4.4.2 Hit-Based parameters

Test 4

Figure 148 shows the first four moments of each hit waveform for Test 4.

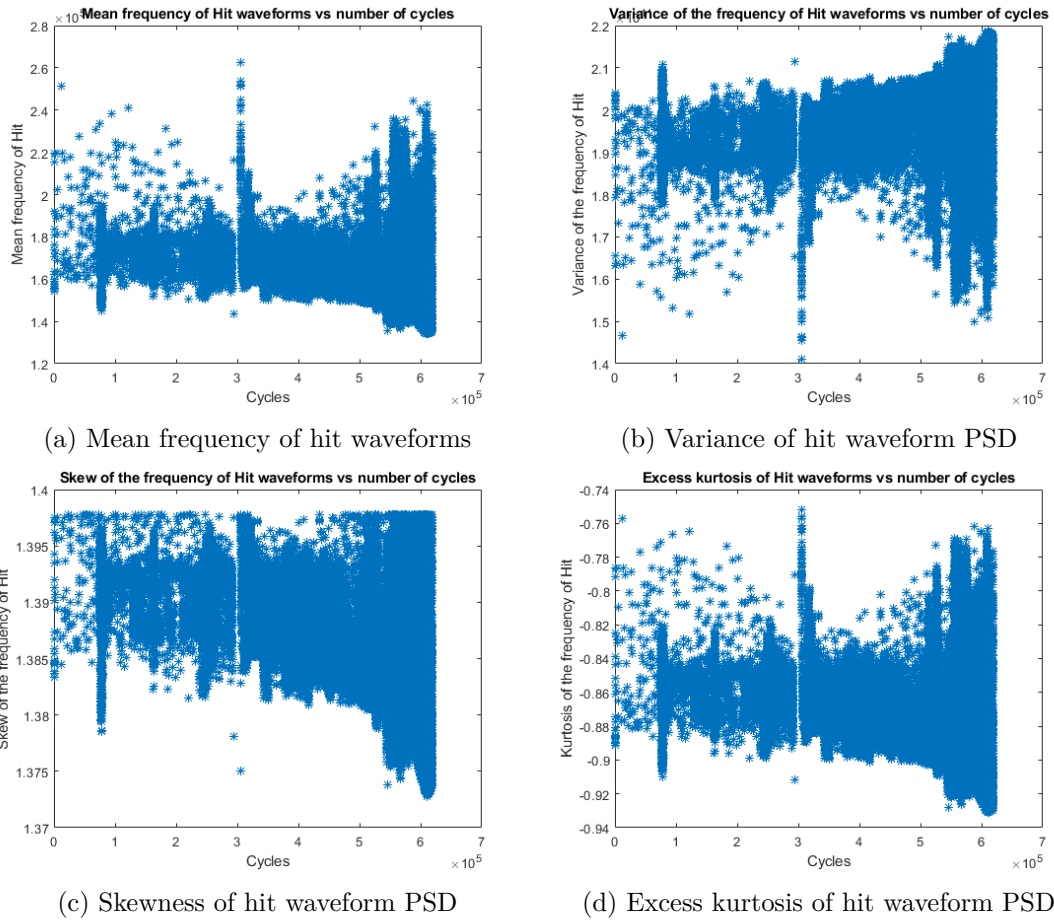
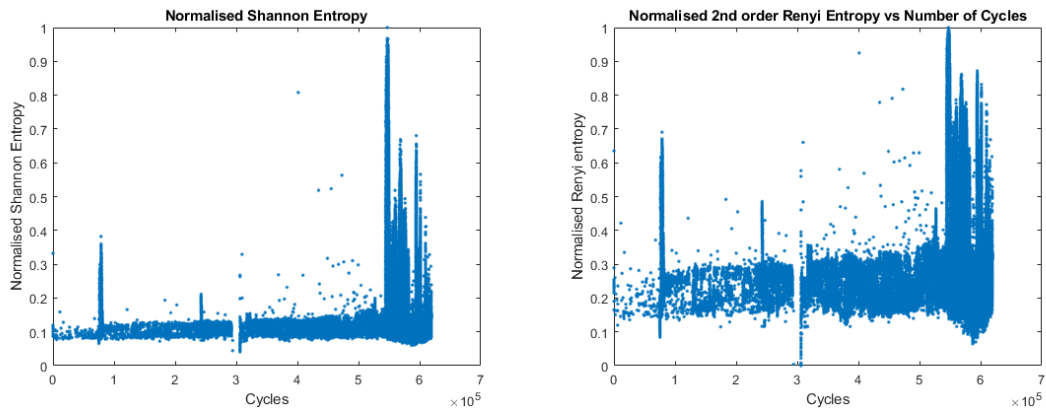


Figure 148: Statistical moments of hit waveform PSD from Test 4

Figure 149 shows Shannon's and 2nd order Renyi's entropy for each hit waveform from Test 4. Since the scale of the information entropy is meaningless except relative to other points in the same data set[102], the values were normalised.



(a) Shannon entropy production versus cycles from Test 4. (b) Renyi entropy production versus cycles from Test 4.

Figure 149: Information entropy production from Test 4

Test 5

Figure 150 shows the first four moments of each hit waveform for Test 5, based on data from either sensor, as well as for the combined data of both sensors.

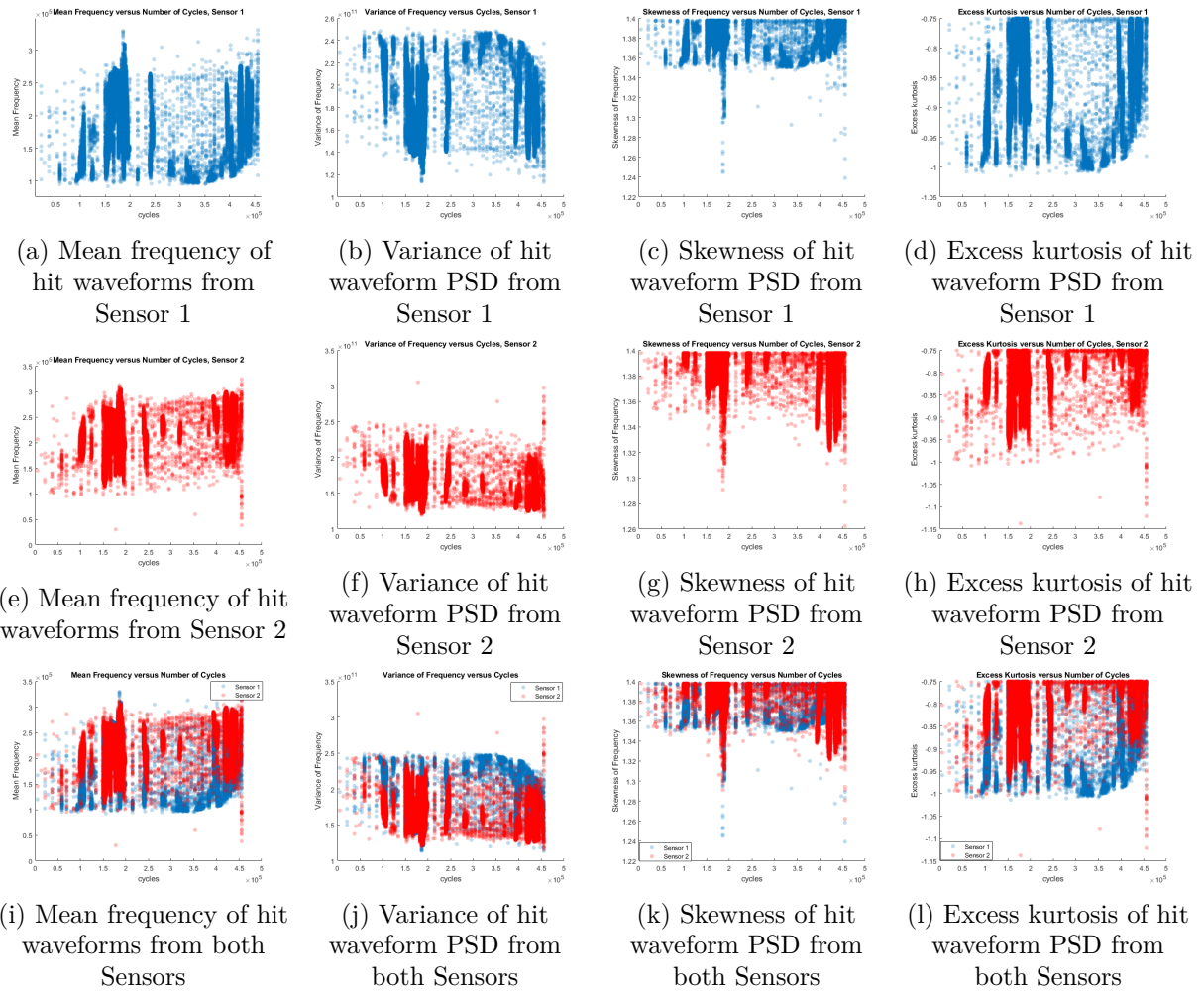
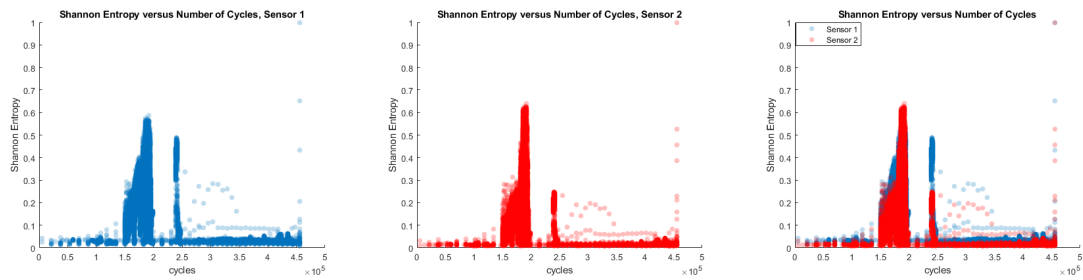


Figure 150: Statistical moments of hit waveforms PSD from Test 5

Figure 151 shows normalised Shannon entropy for the hit waveforms of Test 5 versus cycles. Figure 151a shows data from sensor 1, figure 151b for sensor 2, and figure 151c the total entropy from both sensors.



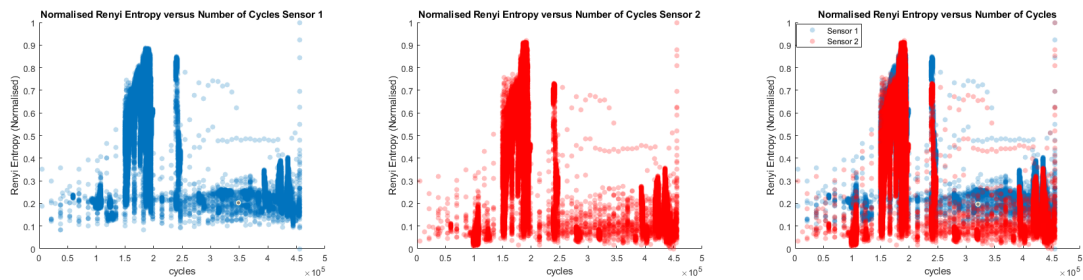
(a) Shannon entropy of hit waveforms versus cycles from Sensor 1 during Test 5

(b) Shannon entropy of hit waveforms versus cycles from Sensor 2 during Test 5

(c) Shannon entropy of hit waveforms versus cycles from both Sensors during Test 5

Figure 151: Comparison of normalised Shannon Entropy from Sensor 1 and Sensor 2 during Test 5

Normalised 2nd order Renyi entropy from Test 5 is shown in figure 152. 152a shows data from sensor 1, figure 152b data of sensor 2, and figure 152c the total entropy from both sensors.



(a) Renyi entropy of hit waveforms versus cycles from Sensor 1 during Test 5

(b) Renyi entropy of hit waveforms versus cycles from Sensor 2 during Test 5

(c) Renyi entropy of hit waveforms versus from both Sensors during Test 5

Figure 152: Comparison of normalised 2nd order Renyi Entropy from Sensor 1 and Sensor 2 during Test 5

Test 6

Figure 153 shows the first four moments of each hit waveform from Test 6. Data from both sensors were used. For better clarity, the data uses a logarithmic scale for the vertical axis.

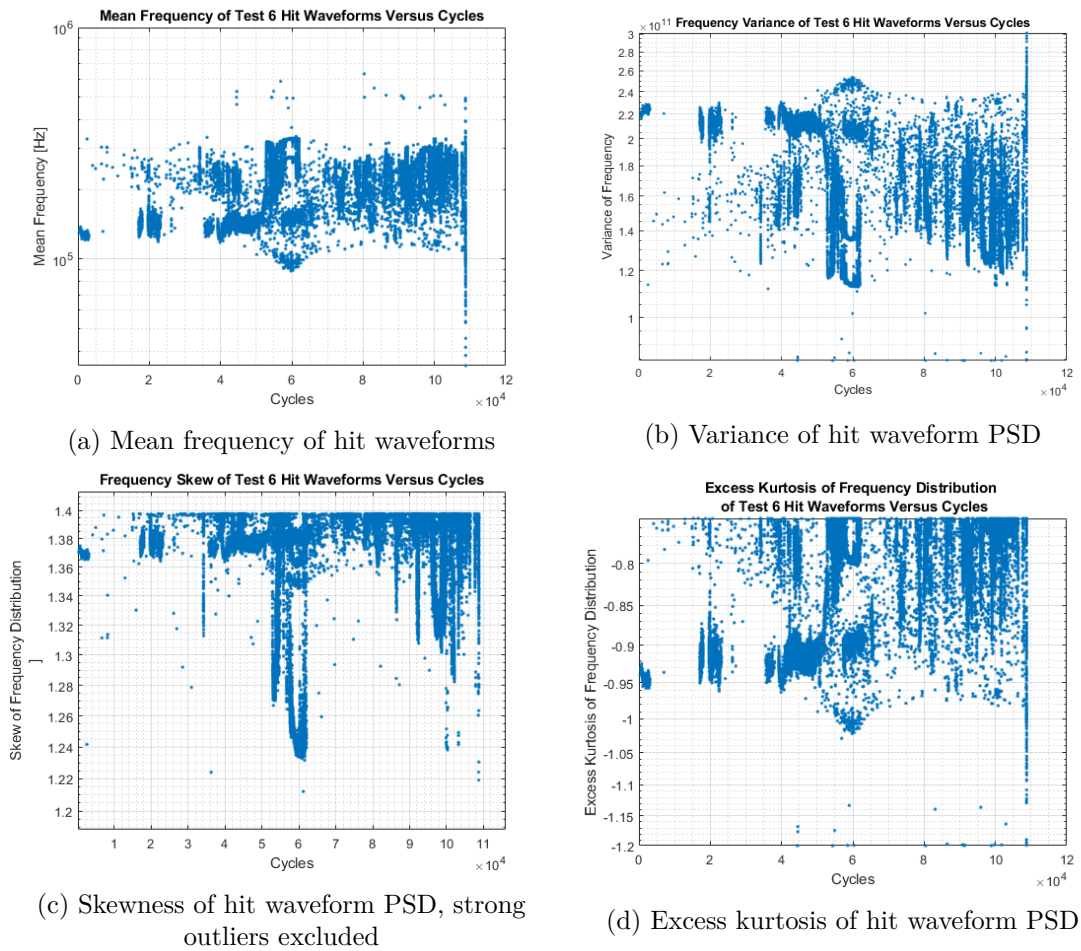
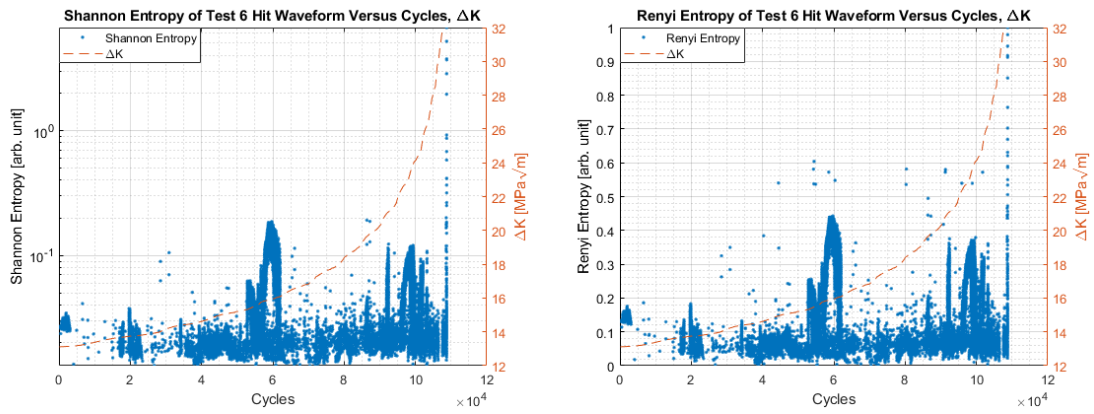


Figure 153: Statistical moments of hit waveform PSD from Test 6

Figure 154 shows Shannon's and 2nd order Renyi's entropy for each hit waveform from Test 6 based on data from both sensors. The Renyi entropy values were normalised, while the values of Shannon entropy were left as originally calculated.



(a) Shannon entropy production versus cycles from Test 6. (b) Renyi entropy production versus cycles from Test 6.

Figure 154: Information entropy production from Test 6

4.4.3 Signal Energy

Test 4

Figure 155 shows the RMS of the hit waveforms and streamed waveforms from Test 4 versus number of cycles.

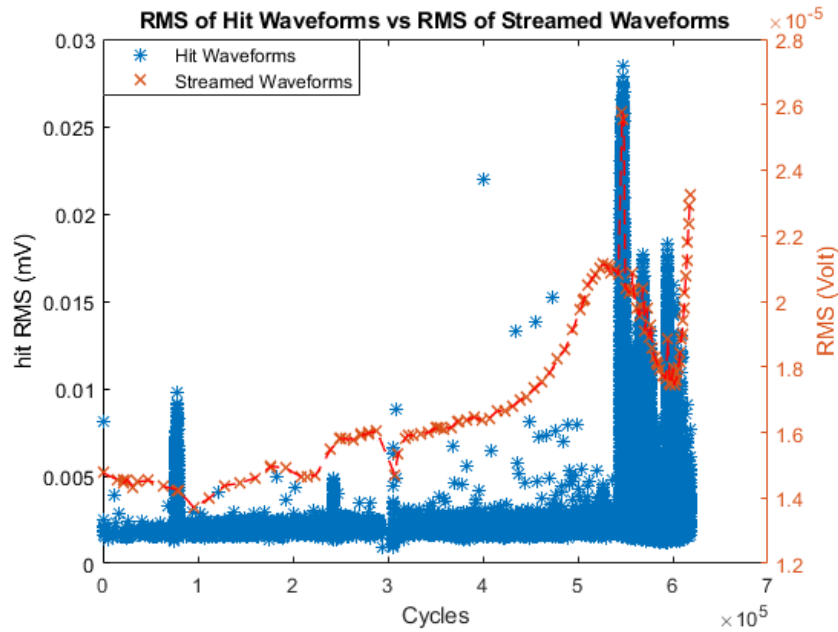
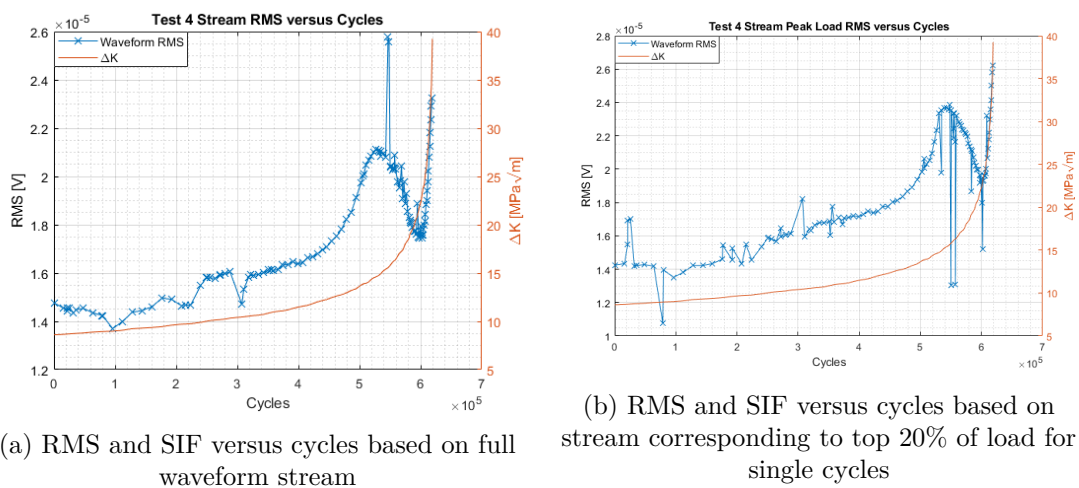


Figure 155: Comparison of RMS of streamed waveforms and hit waveforms from Test 4.

Based on the waveform stream, large spikes in the signal were sometimes observed at the mean and minimum loads. To get a better idea of how the signal energy evolved during the peak load, where AE is thought to occur, the waveform corresponding to loads above 80% of the maximum load was isolated for one cycle each stream. A comparison of the RMS of the full stream and the peak load signal of Test 4 is shown in figure 156.



(a) RMS and SIF versus cycles based on full waveform stream

(b) RMS and SIF versus cycles based on stream corresponding to top 20% of load for single cycles

Figure 156: RMS and SIF versus cycles from Test 6

Test 5

Test 5 was the first test which utilised two types of transducers, Micro-30 (sensor 1) and Nano-30 (sensor 2). Comparisons of these measurements were therefore of interest. Figure 157 shows the absolute signal energy of the hit waveforms from Test 5 based on the individual sensors and of both. The signal energy was used since it more clearly shows any differences between the sensors, due to squaring the signal.

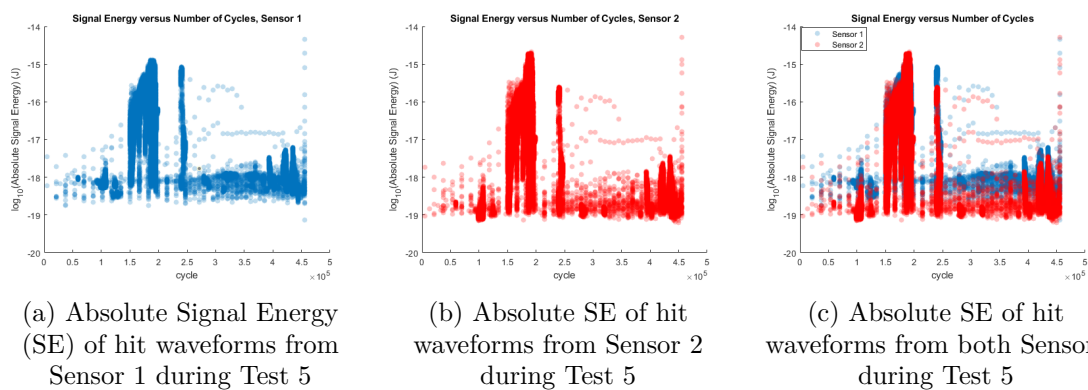


Figure 157: Comparison of absolute SE measurements from Sensor 1 and Sensor 2 during Test 5

A similar comparison based on the waveform stream is shown in figure 158, but using RMS instead of signal energy due to computational effort.

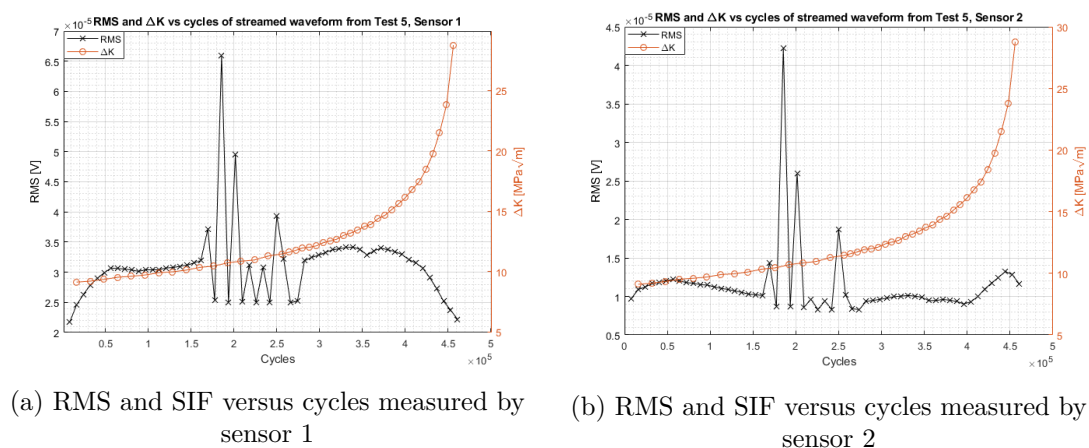
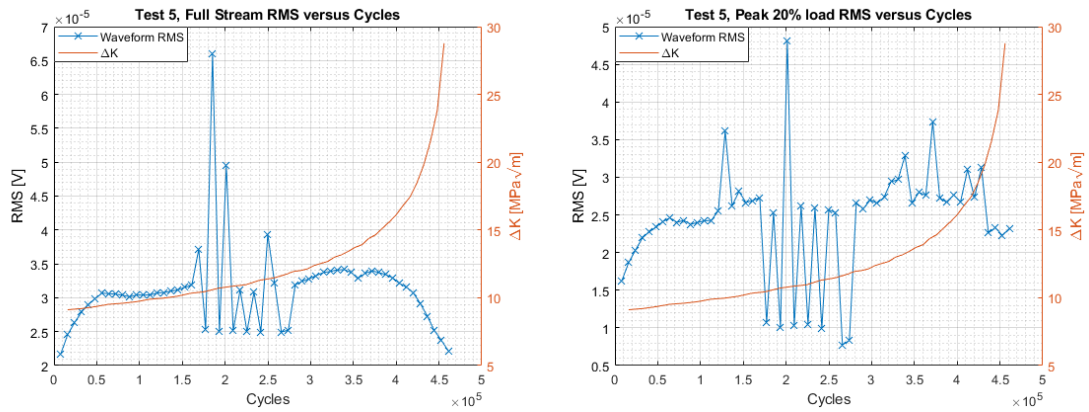


Figure 158: RMS and SIF versus cycles from Test 5

Just as for Test 4, signal peaks were observed at loads far below maximum. Figure 159 shows the voltage RMS of the streamed waveforms based on the full signal (fig. 159a) and the peak 20% load (fig. 159b). The data from sensor 1 was used for this purpose.



(a) RMS and SIF versus cycles based on full waveform stream

(b) RMS and SIF versus cycles based on stream corresponding to top 20% of load

Figure 159: RMS and SIF versus cycles from Test 5

Test 6

The RMS of hit waveforms versus cycles and ΔK is shown in figure 160, based on the data from sensor 1.

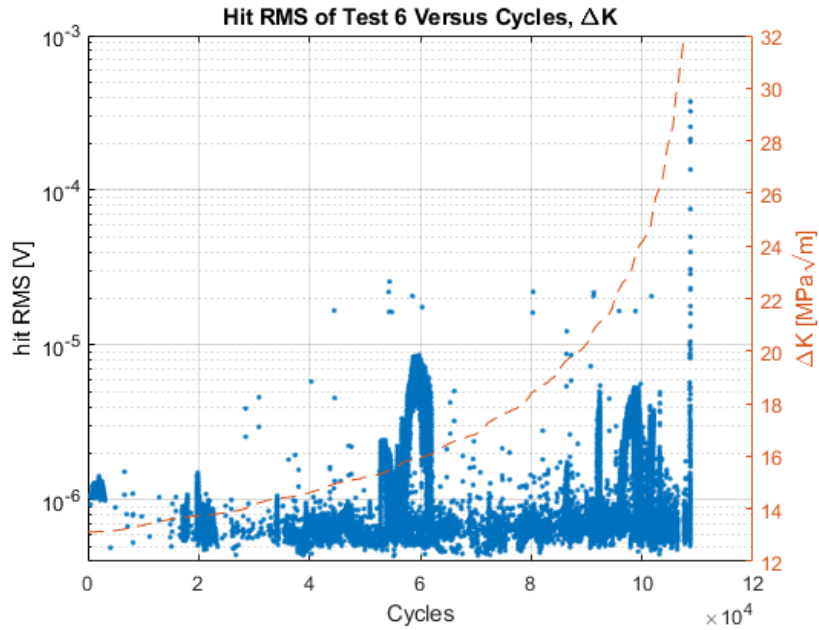
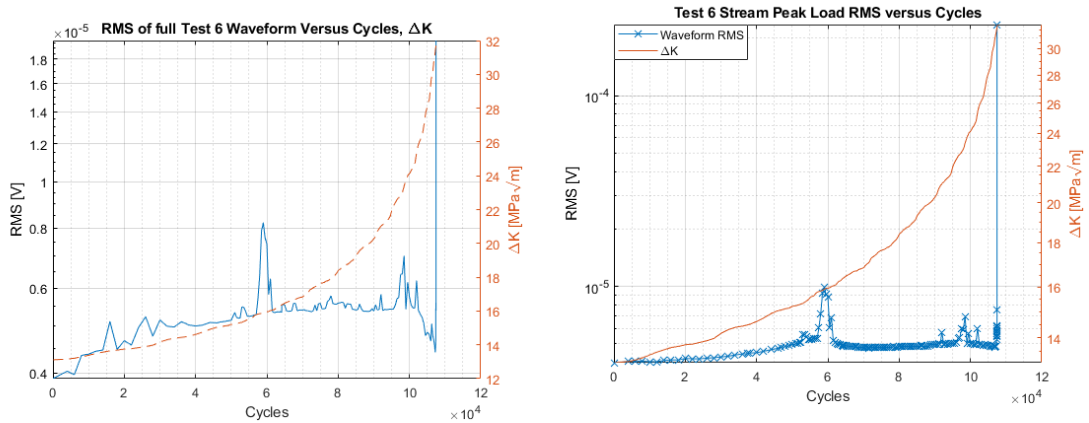


Figure 160: RMS of hit waveforms from sensor 1 in Test 6 plotted versus cycles, SIF range

RMS of streamed waveforms from sensor 1 is plotted against number of cycles and ΔK in figure 161. Figure 161a shows the results of using the data of the full stream, while figure 161b shows the results when the top 20% load was used, with data obtained from a single cycle.



(a) RMS and SIF versus cycles based on full waveform stream

(b) RMS and SIF versus cycles based on stream corresponding to top 20% of load. Note the logarithmic scale of the y-axis.

Figure 161: RMS and SIF versus cycles from Test 6

A closer look at the RMS of the streamed waveforms based on full cycles can be seen in figure 162

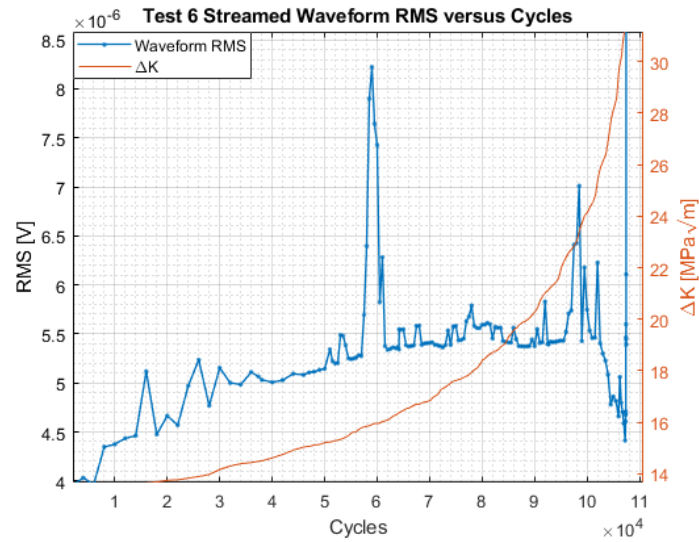


Figure 162: Close up of RMS and SIF versus cycles based on full waveform stream

4.4.4 Summary of Cumulative Hit Parameters

This section summarised the cumulative behaviour of some hit parameters from previous sections. Based on the plot from Test 4, showing large degree of similarity between different measurements of the same physical property (e.g. Shannon and Renyi entropy), only one measure of each property was included for Test 5 and Test 6.

Figure 163 shows the cumulative of hits, Shannon entropy, Renyi entropy, RMS and signal energy plotted against cycles and ΔK from Test 4 data.

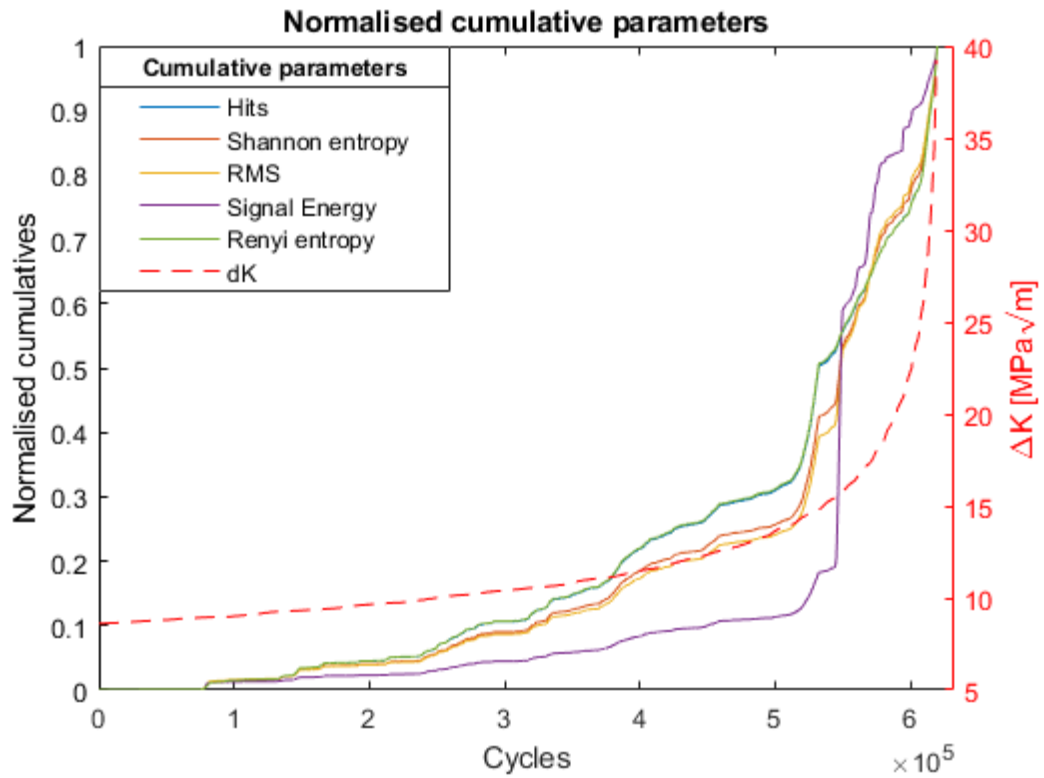


Figure 163: Normalised cumulative of Hits, Shannon Entropy, Renyi Entropy, RMS and Signal Energy versus number of cycles and ΔK from Test 4

Figure 163 shows the cumulative of hits, Shannon entropy, Renyi entropy, RMS and signal energy plotted against cycles and ΔK from Test 5 data.

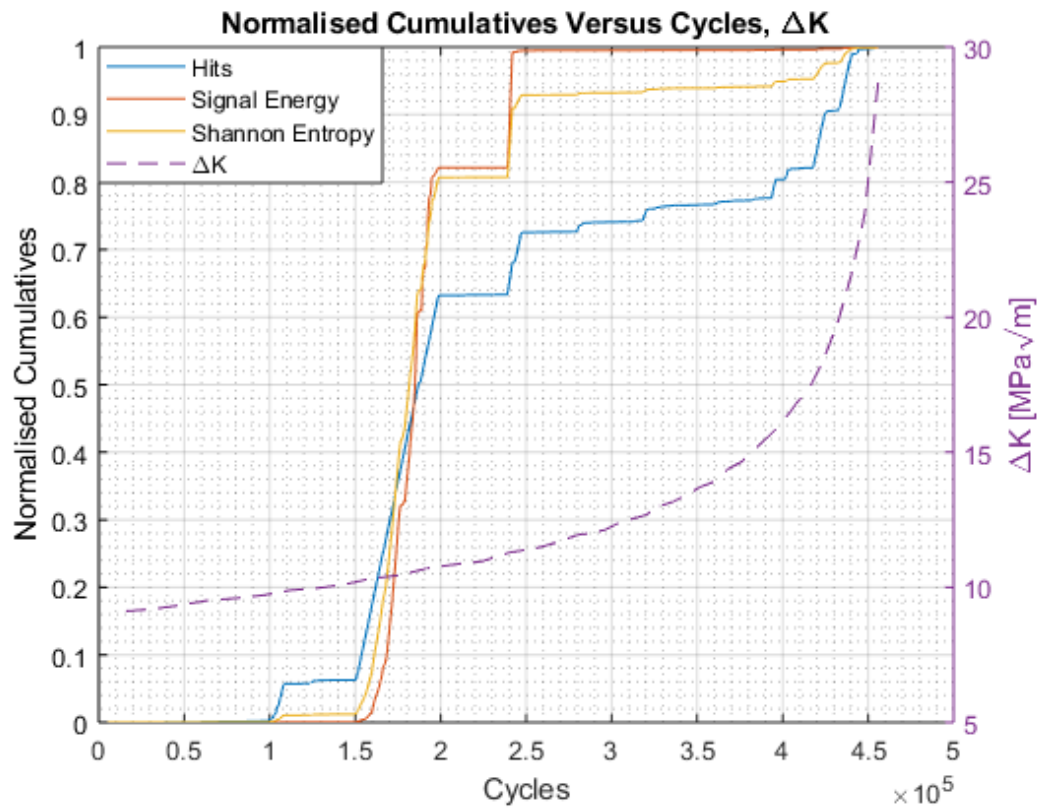


Figure 164: Normalised cumulative of Hits, Shannon Entropy, and Signal Energy versus number of cycles and ΔK from Test 5

Figure 163 shows the cumulative of hits, Shannon entropy, Renyi entropy, RMS and signal energy plotted against cycles and ΔK from Test 6 data.

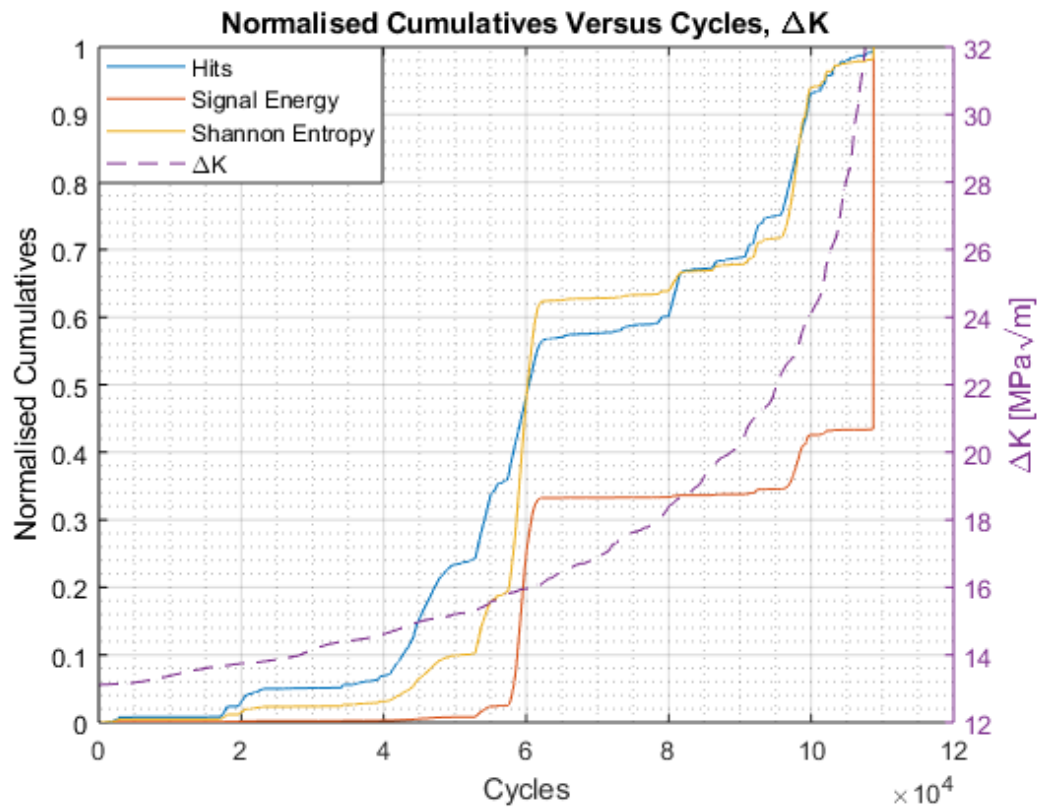


Figure 165: Normalised cumulative of Hits, Shannon Entropy, and Signal Energy versus number of cycles and ΔK from Test 6

4.4.5 Waveforms

In order to understand the cyclic behaviour of the AE signal, complete waveforms must be analysed. In this section, waveforms corresponding to an entire loading cycle are presented for selected streams of interest. The waveforms were extracted based on the load signals as determined either by an idealised sine with phase based on the trigger from section 3.3, or the recorded load signal from the Instron test machine. Some triggers were done manually for Test 4, and the AE signal was therefore not synchronised with the load. In the case that a trigger was manual, the waveform corresponding to a load was determined based on the shape of previous waveforms with known load case.

Test 4

The general evolution of the signal waveform and STFT of Test 4 is shown in figure 166, for one cycle of each given stream.

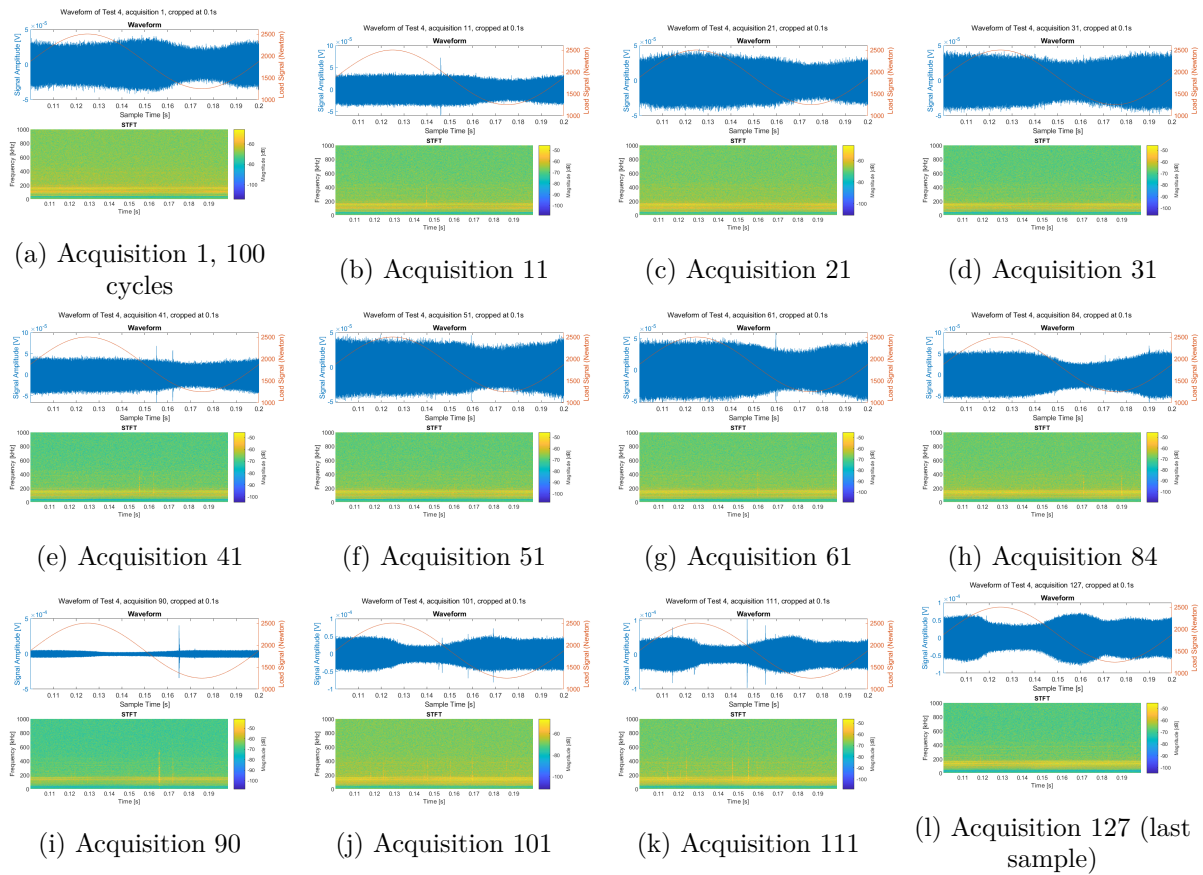
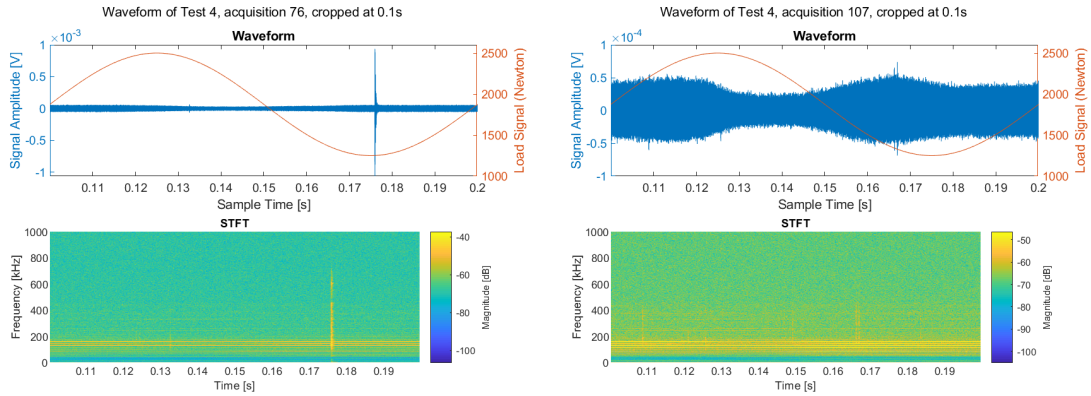


Figure 166: Waveform evolution during Test 4 from evenly distributed "true" acquisitions

Waveform and STFT for streams associated with points of interest in figure 156, which aren't shown in figure 166, are shown in figure 167, for one full cycle.



(a) Waveform of largest signal peak of figure 156a (b) Waveform of valley of figure 156a before Stage III

Figure 167: Waveforms of largest peak and lowest valley of RMS near the end of Test 4

Test 5

The general evolution of the signal waveform and STFT of Test 5 is shown in figure 168, for one cycle of each given stream.

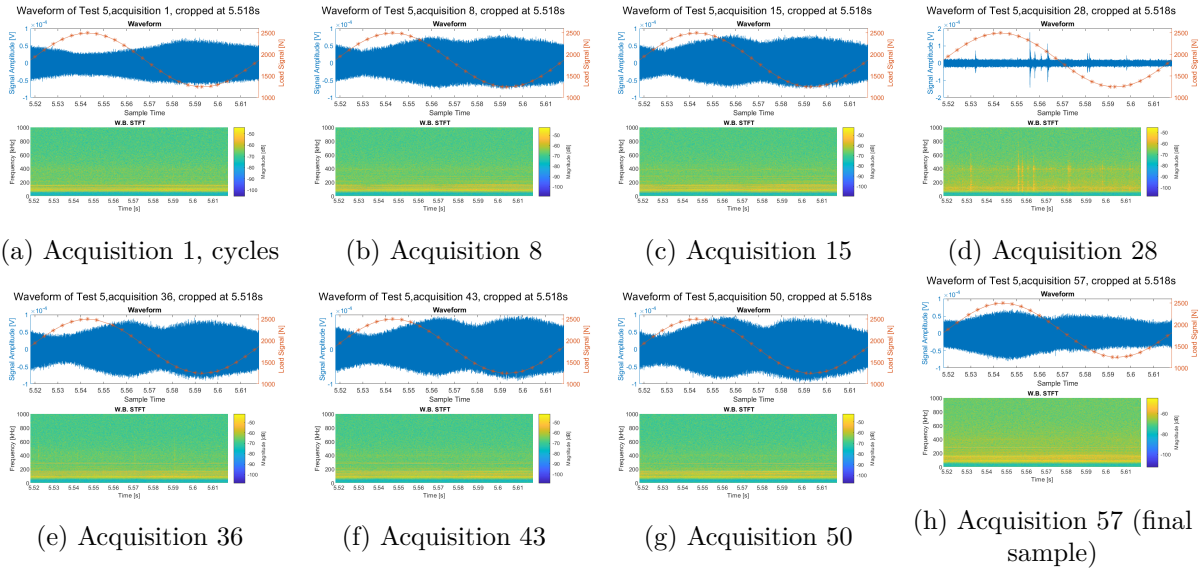
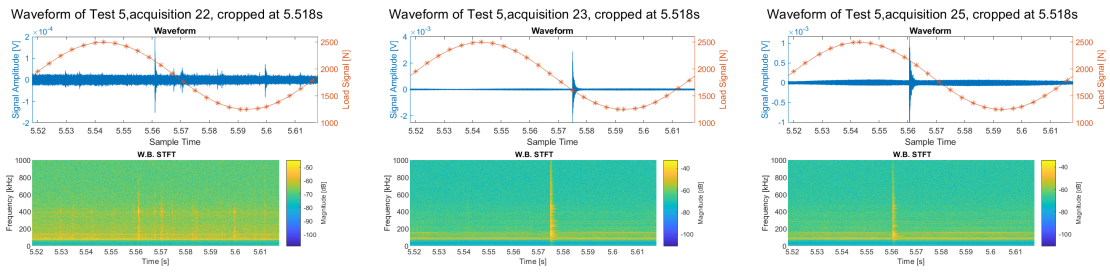


Figure 168: Waveform evolution during Test 5 from evenly distributed "true" acquisitions

Waveform and STFT for streams associated with points of interest in figure 159 are shown

in figure 169, again for a full cycle.



(a) Waveform of valley in figures 159a and 159b

(b) Waveform of peak in figure 159a, valley in figure 159b

(c) Waveform of peak in both figures 161a and 159b

Figure 169: Waveforms of selected peaks and valleys of RMS in figure 159 of Test 5

Test 6

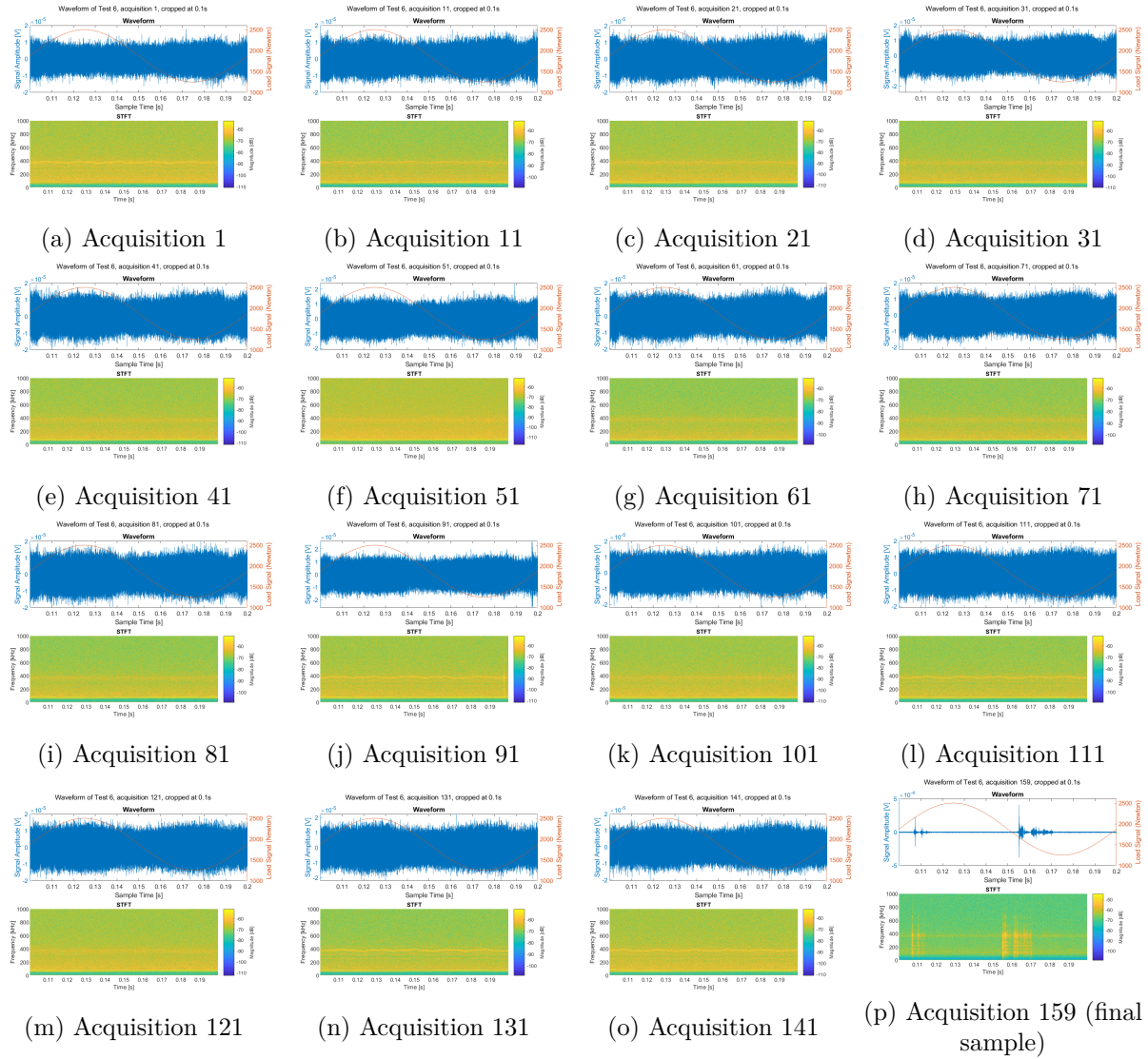
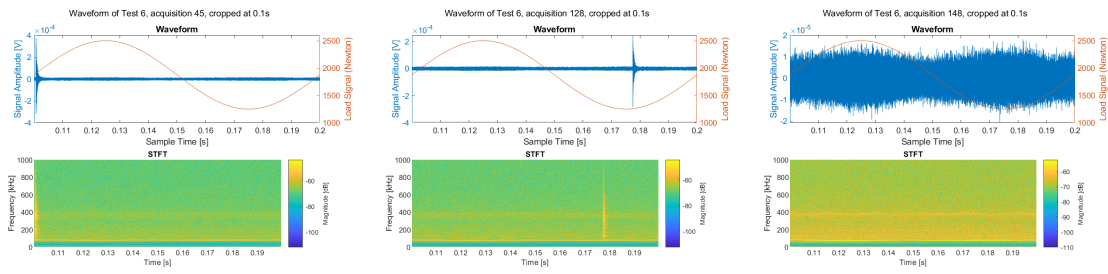


Figure 170: Waveform evolution during Test 6 from evenly distributed "true" acquisitions

Waveform and STFT for streams associated with points of interest in figure 161 are shown in figure 171, again for a full cycle.



(a) Waveform of RMS peak found in figure 161, 59000 cycles

(b) Waveform of RMS peak found in figure 161 at 98500 cycles

(c) Waveform of RMS valley found in figure 161 just before sharp spike, 107250 cycles

Figure 171: Waveforms of peaks and valleys from RMS of Test 6 in figure 161

4.4.6 Clustering

Clustering of the hit waveforms was attempted in order to identify different AE source mechanisms. Clusters were obtained using the methods described in section 3.6.1. The results of the best clustering, as determined either by visual inspection or the silhouette method, are shown.

Test 4

Due to the amount of hits registered during Test 4, quantitative assessment of the clustering was not possible as a result of unreasonably large computational time. Based on visual inspection of the temporal distribution of the clusters, PSD and STFT analysis of selected waveforms in each cluster, the best clustering was obtained using the PSD as the selection criterion for the case of 3 clusters.

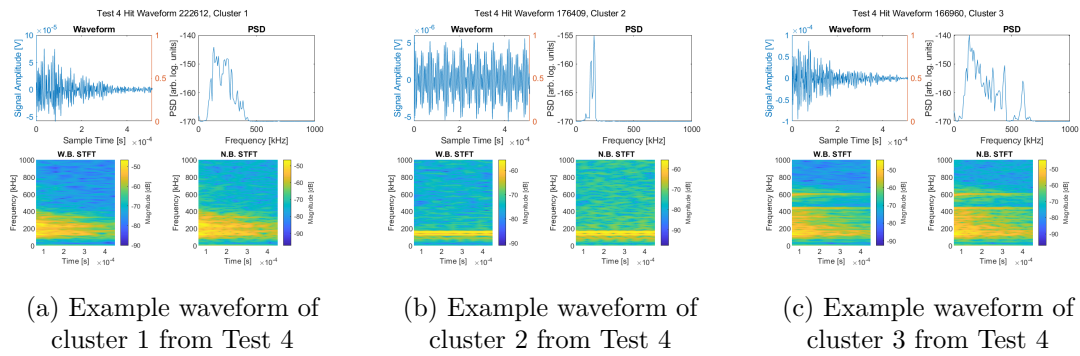


Figure 172: Example waveform of clusters from Test 4

The cumulative of each cluster is shown in figure 173 versus cycles along with ΔK . Due to the difference in total hits in each cluster, the values were normalised.

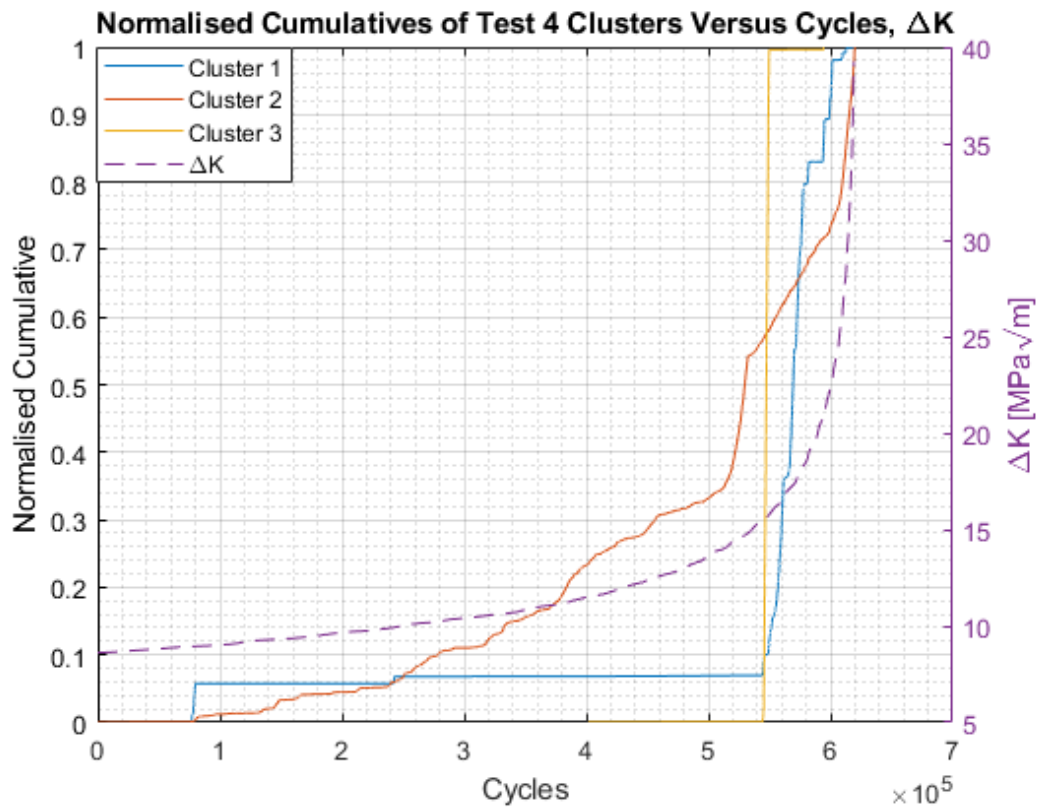


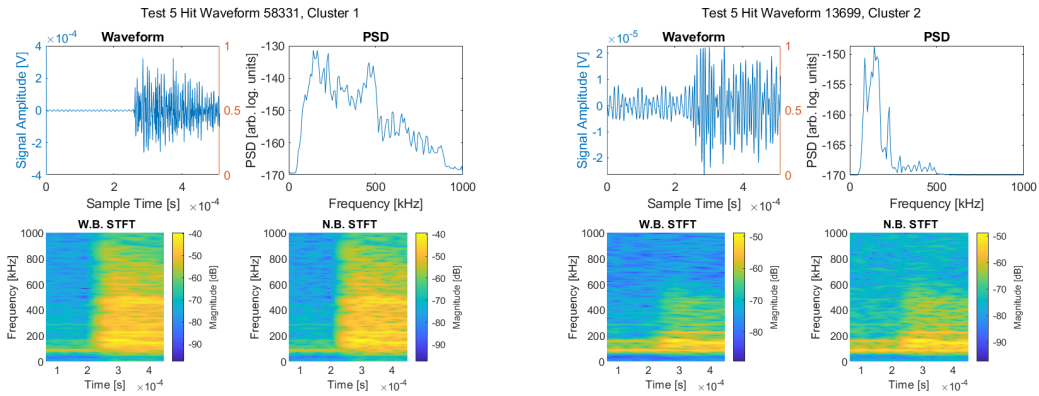
Figure 173: Normalised cumulative of clusters versus number of cycles and ΔK from Test 4

Test 5

Due to the amount of data from each sensor, and the different spectral characteristics of each sensor, clustering was only performed based on the hits from sensor 1 (Micro 30). The best number of clusters as determined by the silhouette criterion was 2, with a value of 0.832. For higher numbers of clusters, the silhouette value dropped significantly, as shown in table 17. Random samples were taken from each cluster, and the waveform, PSD, and STFT plotted, to evaluate the cluster qualities. It was confirmed by inspection of these samples that two clusters gave the best fit.

Number of Clusters	2	3	4	5	6
Silhouette value	0.832	0.733	0.671	0.671	0.662

Table 17: Cluster consistency determined by silhouette criterion of Test 5



(a) Example waveform of cluster 1 from Test 5 (b) Example waveform of cluster 2 from Test 5

Figure 174: Example waveform of clusters from Test 5

The cumulative of each cluster is shown in figure 175 versus cycles along with ΔK . Due to the difference in total hits in each cluster, the values were normalised.

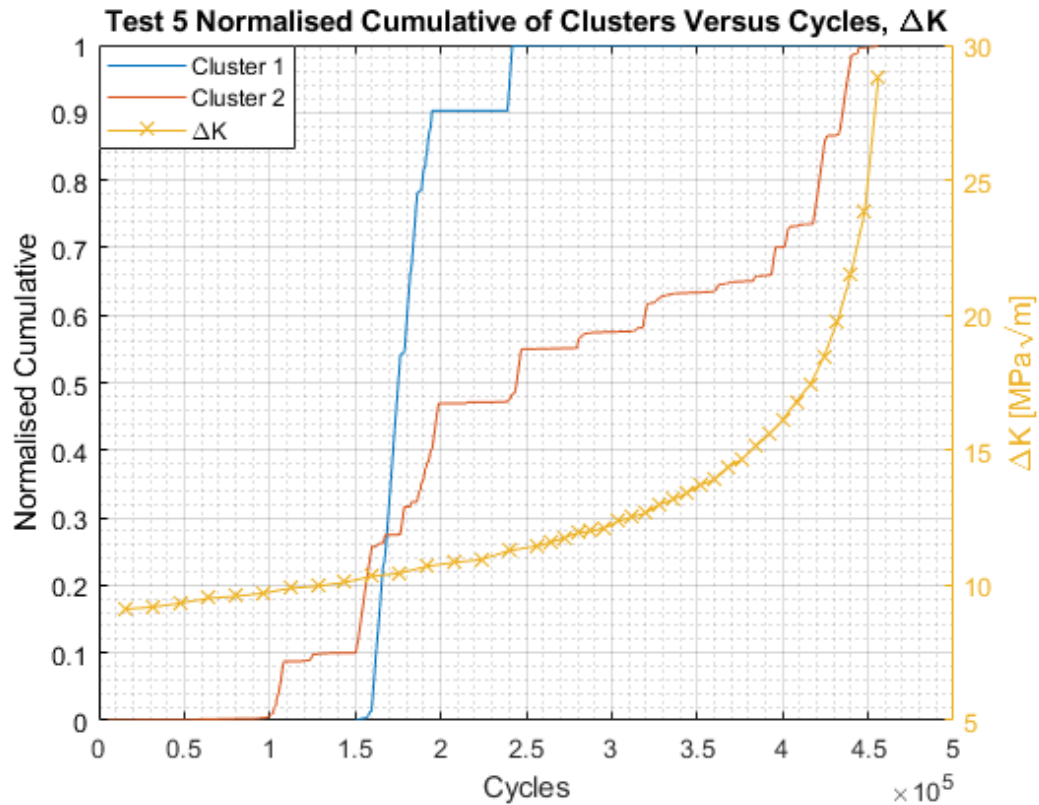


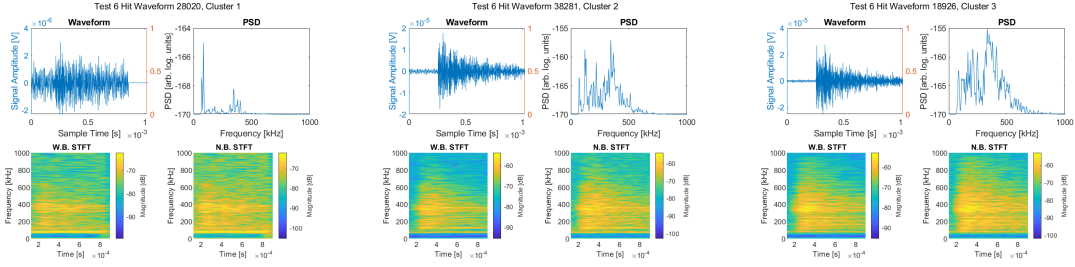
Figure 175: Normalised cumulative of clusters versus number of cycles and ΔK from Test 5

Test 6

Like for Test 5, clustering was based on the hit data from sensor 1 (Micro 30). Clustering was performed using the *kmeans* method with number of clusters ranging from 2 to 6, with PSD as the cluster data. From Test 6, the best number of clusters was found to be 3 by the silhouette criterion, with a value of 0.838. However, other cluster numbers obtained similar values, as shown in table 18. By further visual inspection of the waveform, PSD and STFT of random samples from each cluster, it was found that the best results were obtained using 4 clusters, where the 4th consisted of anomalies, as can be seen from figures 176 and 177.

Number of Clusters	2	3	4	5	6
Silhouette value	0.816	0.8379	0.7645	0.7939	0.7941

Table 18: Cluster consistency determined by silhouette criterion of Test 6

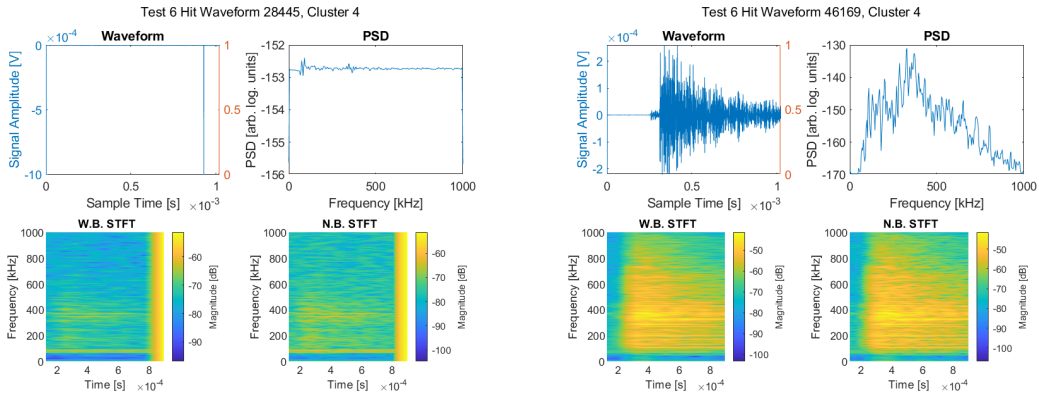


(a) Example waveform of cluster 1 from Test 6

(b) Example waveform of cluster 2 from Test 6

(c) Example waveform of cluster 3 from Test 6

Figure 176: Example waveform of clusters from Test 6



(a) Example waveform of anomalous cluster 4 from Test 6

(b) Example waveform of anomalous cluster 4 from Test 6

Figure 177: 2 of 5 waveforms from the anomalous cluster 4 from Test 6

The cumulative of each cluster is shown in figure 178 versus cycles along with ΔK . Due to the difference in total hits in each cluster, the values were normalised.

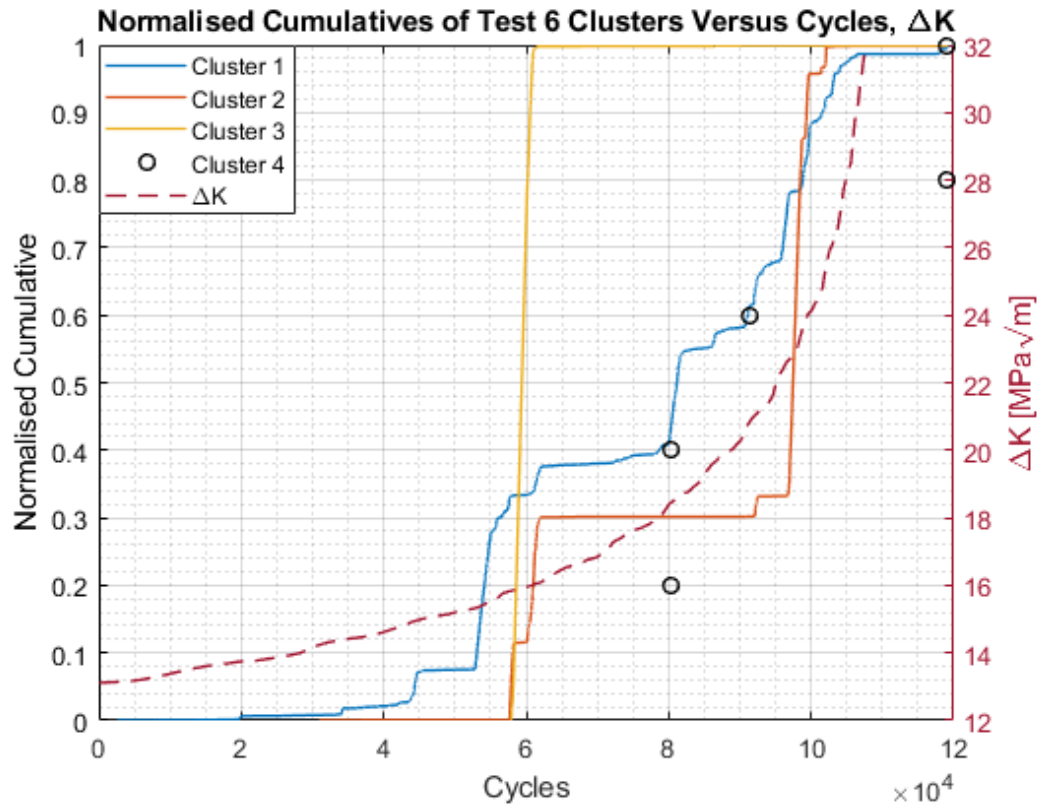


Figure 178: Normalised cumulative of clusters versus number of cycles and ΔK from Test 5

4.5 Comparison of results from different methods

4.5.1 DIC and IRT

Crack tip detection and the plastic zone size

The main focus in this section is on test 5, as it was the only test which allowed for good comparison of data due to the DIC analysis.

Figure 179 compares the crack length curves for both cameras. The initial crack length was longer on the DIC side of the sample. Figure 180 shows the beach-mark created when the test was started, which also shows that the initial crack length was larger in the DIC side.

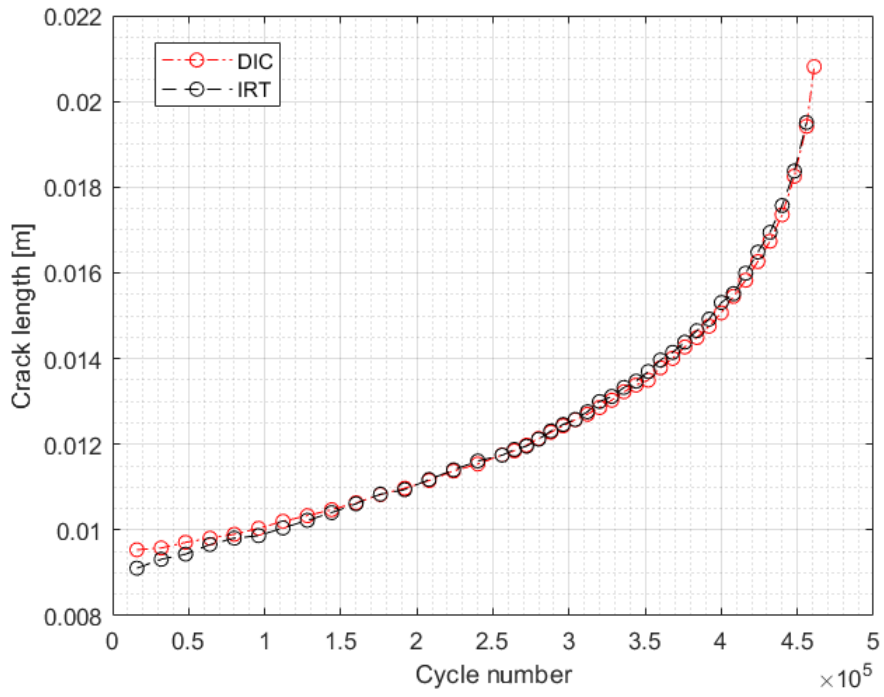


Figure 179: Crack length versus cycle count for test 5

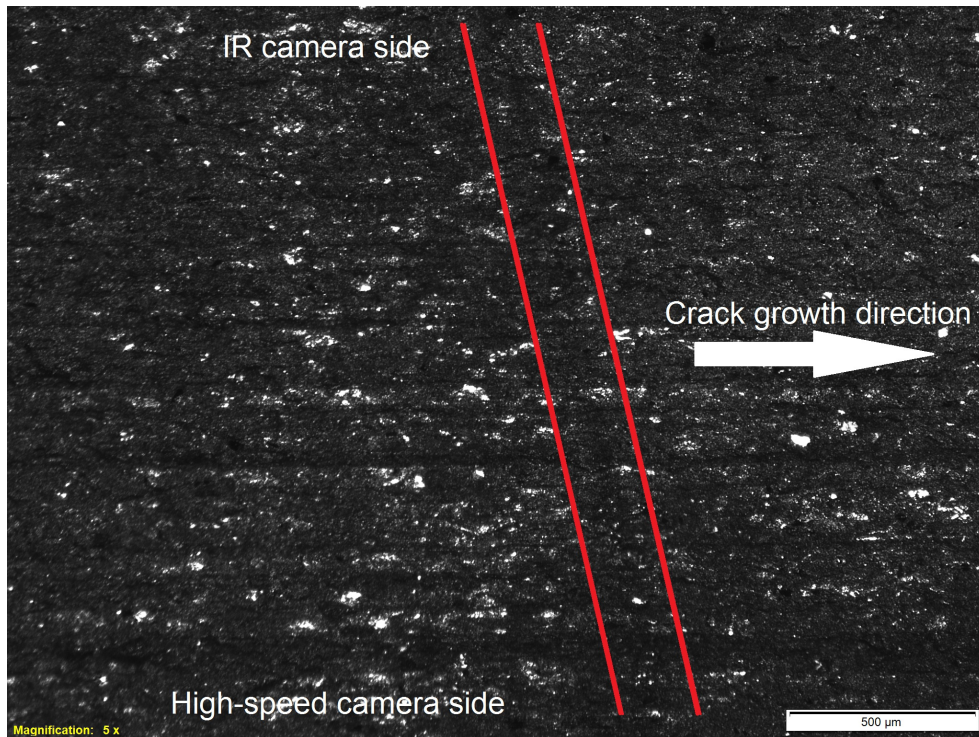


Figure 180: Fracture surface for test 5, benchmark separating the precracking from the actual test

Figure 181 plots the plastic zone size measured by the IRT and DIC, and compares it to the theoretical size predicted by LEFM in plane strain and plane stress conditions, and the Williams' stress field used in this project.

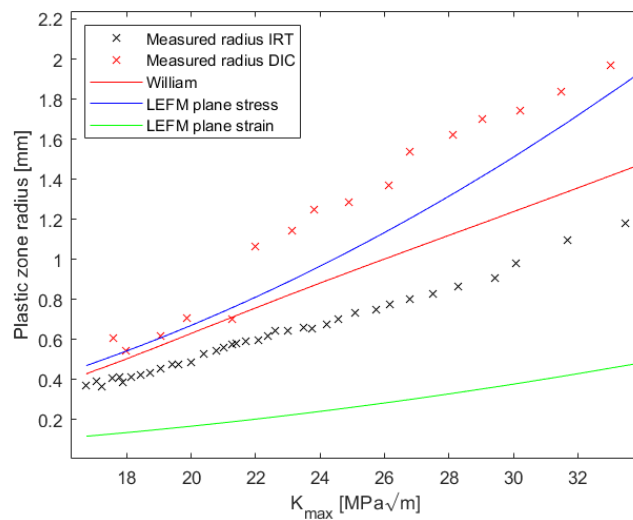


Figure 181: Plastic zone radius for test 5

Crack closure and stress intensity factor

The crack closure is shown in figure 182, and the effective stress intensity factor range in figure 183. The data seem in general to overlap each other.

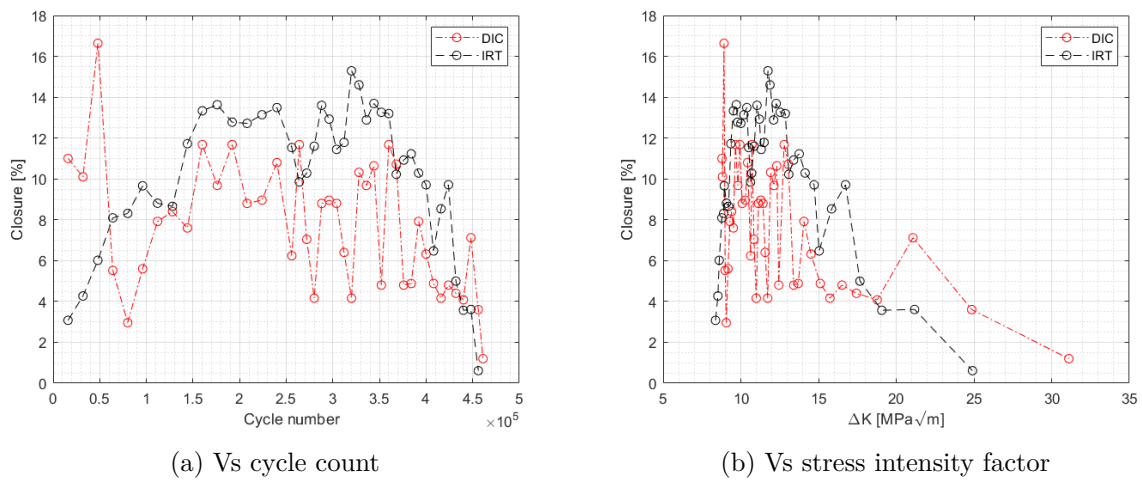


Figure 182: Crack closure for test 5

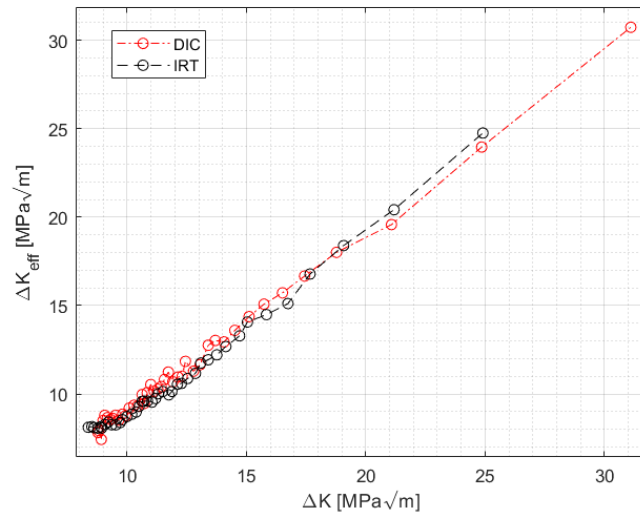


Figure 183: Effective stress intensity vs theoretical stress intensity for test 5

5 Discussion

5.1 Infrared Thermography

Every test had some interesting data, test 4 gave a good spread of sampling points, resulting in good crack growth curves and low spread in residuals after fit. The discrete Fourier analysis has also been performed on test 4. Test 5 was stopped right after every trigger, this allowed to measure the cooling rate of the region near crack tip when the waveform generator was stopped. Test 6 was mainly focused on stage III, and the last cycles of the test were a continuous recording. It was the only test where the stage III was properly captured, the filtering however did not work on this stage, and as it needs improvements, it remains as further work to get better data analysis out of stage III.

5.1.1 Thermoelastic constant

The thermoelastic parameter, has here been assumed to be constant. The theoretical value was lower, but assuming that $\frac{\partial E}{\partial T}$ is negative, equation 15 predicts an increase in the constant, so this is in agreement with the theory. The R used to find it was 0.1, but that is due to that initially, the tests were supposed to run at that ratio. The stress used to determine it, was set to 250MPa, as it was below the yield strength. The parameter seem to be adequate, as the results did look reasonable, especially for the monotonic plastic zone size, although it is an obvious improvement to not use a constant but rather a relation. If the parameter would have been inspected for different load cases, the error due to the parameter could be quantified, as at the moment it is unknown.

5.1.2 Data filtering

Section 4.2.2 shows some of the pictures acquired during the testing. The figures also show filtered pictures, rest pictures, and Laplacian of the filtered picture. From the rest

pictures in stage II, figures 57 and 58 it is clear that the filters work really well, even the crack details are removed and the fixed pattern noise due to paint is visible. The filtered picture represents the general temperature picture well. In stage III however, figures 60 and 61, when the process zone mentioned in section 4.2.9, the sharp edge in front of that zone, is removed during filtering. This implies that the filter removes too many details. This of course might be improved, as the detail coefficients in wavelet filtering might be chosen more carefully to keep more of the data. After initial filtering and crack tip determination, the region of interest might be selected, and more advanced algorithms for threshold selection might be used. This is of course time consuming, and as the last test, where these challenges were introduced happened relatively close to the deadline, there was a lack of time for filter improvements. In general, the figures in section 4.2.2 do also show that the crack tip detection works well.

5.1.3 Energy dissipation

All of the figures representing heat dissipation in section 4.2.3 show two curves, a red one showing the amplitude of a sine wave, and a black one, showing the mean value. The sine wave occurs due to the thermoelastic effect, and the mean value should represent the energy dissipated. The amplitude, or the red curves, are proportional to the stresses, which again are proportional to the stress intensity factor range, as shown in figures 80, 81, and 82, which is the reason for the relatively linear response in the plots versus stress intensity range.

The dissipated energy, mentioned above, is oscillating around zero, and the values calculated, are insignificant when compared to the confidence bands, also presented in the figures. There are likely several reasons for that, the method for the calculation was described in sections 2.3.2 and 3.4.6, and equation 17 is based on the Laplacian operator. It is very difficult to acquire a good picture of the Laplacian, both due to noise related to the measurement itself, as the temperature changes are very small, but also due to just physics.

Just as an example, the emissivity of the paint is around 95%, so the background is always reflected from the sample, and since the recording are taken under large magnification, and the camera is limited to the emission of electromagnetic radiation, the aperture size must be large, which causes a very shallow depth. This again results in that the camera is perpendicular to the sample, and even the reflection of the lens is visible in the pictures, even though covers are used to reduce this problem, the reflected background is not homogeneous. An other problem is that the magnification is large enough for the topography of the sample and the applied paint to cause reflections which vary across the sample.

The dissipated energy is not measurable compared to the noise mentioned above, especially in stage II. Much of the noise can be removed with filtering, but some of the noise has similar properties to the value of interest, and can not be filtered away easily. This problem is to an extent visible in figure 106, in the **Mean temp** column, as the dissipated energy should be visible as a region of increased temperature located at crack tip as that is where the stress amplitude is largest, which is somehow visible in the last rows of figure 107. This was however stage III, and the same phenomenon could not be observed in stage II, especially when compared to the noise seen around the crack tip in figure 106. An additional clue indicating the low energy dissipation are the temperature curves in figures 65, 69, and 75. The room temperature was not measured, but was around 20-21°C, the starting temperature of the samples differs due to the fact that test 4 was run with potential drop measurements, and tests 5 and 6 were not. The cooling properties of the specimen were not measured either, but the temperature increase was not large through most of the test, until very late in the test. Here it is important to note that test 5 did not capture stage III, nor the very last moments of stage II, so the increase in temperature is not as clear as in test 4 or 6. An source of error for these curves is that test 4 had current running through it due to potential drop measurements, which test 5 did not have. Test 6 on the other hand was paused somewhere in the transition from stage II to stage III, as illustrated in figure 75 with a blue line. The temperature overall did not increase by a significant amount overall, especially keeping in mind that the temperature of the surroundings was unknown. The

slopes are steep, however, after restarting the test. The further temperature development is seen in figure 113. The curves do suggest that the heat dissipation do increase significantly in the end of the test. The reason for which this is visible in the temperature curves and not the energy curves, is probably because of the region of calculation, which was a relatively small circle surrounding the crack tip, while the highest dissipation in stage III, as seen from the **Mean temp** column of figure 107 occurred behind, above, and underneath the crack tip, seen as a green cross in the figure. Most of stage III was also excluded from the energy plots as the data would not be representative due to poor filtering. The region of interest chosen for energy calculations, was where the largest temperature amplitudes occur, whereas the energy dissipated in stage III seem to occur in a different region.

It did look like the heat dissipation in stage III was captured, and it was all just a matter of good post processing to measure the value of it. These results did lead to a further inspection of stage II where the dissipation could not be captured. This was done on data from test 5, since the test was stopped just after every trigger, and the recording continued for an additional second. The cooling gradient would be related to energy dissipation when the test was running. This can be shown with the same equation, equation 17. This method should be more precise, as it is based on the change in the temperature, which is much easier to measure precisely, and is less affected by the noise described in this section. The cooling rate of a small region surrounding the crack tip was measured, the area was 11 times 11 pixels, and the analysis was done without any filtering or processing at all. The temperature response of the region of interest is shown in figure 70. The slope of the flat part of the curve was measured, by applying a linear fit, also seen in the figure, and the resulting slopes as well as the confidence intervals were plotted in figure 71. This figure does also not show any measurable or significant values, if energy would be dissipated as heat while the machine was running, this should cause a negative slope after the dissipation was stopped. All of the discussion above suggest that the heat dissipation with the current setup is not measurable in stage II.

The remaining noise in the pictures seem to be constant, and can likely be reduced by taking

a reference picture, and subtracting it from the results. This is a potential improvement, but would require a more precise control of cameras position, as the crack grows out of cameras FOV. However increasing the amount of dissipated heat would be the improvement with largest impact on the results, as it is simply easier to measure. This can be done by for example increasing the test frequency, which of course has some other drawbacks, as it affects the precision of measurements. For the moment it does however look like the next improvement, as it both increases the dissipated heat, but also makes the TSA more precise as the temperature change due to thermoelasticity is less affected by conduction, especially in a region of high stresses.

5.1.4 Stress intensity factor

The calculations of stress intensity factor range were presented in figures 76a, 77a, and 78a, and the percent crack closure in figures 76b, 77b, and 78b. The closure is based on the ratio between the measured stress intensity and the theoretical stress intensity calculated from equation 49. It is important to note that the measured stress intensity depends heavily on a theoretical stress field, here Williams' series was used with coefficients from equation 9. The stress field is an elastic stress field, it does not take into consideration the plastic zone, and the stresses occurring in it as well as behind the crack tip which might cause crack closure and such. Another factor influencing the measured value is the thermoelastic parameter, as it has been assumed to be constant. The value of this parameter, was measured at stress state significantly different from the stress level at which the stress intensity has been measured. More precise determination of the relation between stress state and the temperature response is a further improvement of the analysis.

Now that the sources of error are clarified, the values seem reasonable, especially when compared to DIC as described in section 5.4.1. There is a linear trend between the measured stress intensity and the peak stresses measured as seen in figures 80, 81, and 82. An important note here is that both of them are measured using the same thermoelastic

parameter, so one of the sources of error measured above is included into both of them. It is also not unreasonable to assume that some crack closure was present, which would imply that the measured stress intensity would be lower than the theoretical which did not account for closure. All of the curves in figures 76b, 77b, and 78b have some trends that also might look similar, as both start at a higher value and decrease a bit. The region of increased closure for high stress intensity in tests 4 and 6, does seem somehow unreasonable and should be compared with other techniques as DIC, but unfortunately this was not done in this work, as the DIC analysis was done on test 5 which did not reach this region. Assuming that the behaviour is an error, it might be caused by wrong value of the thermoelastic parameter as the stresses become larger, or due to the theoretical stressfield used to measure closure. This is clear in figures 76a and 78a as the slope between the theoretical stress intensity factor, and the measured stress intensity factor changes. It might also just be that the parameters or algorithms just might need some tuning, as they remained at their initial values without any bench-marking or adjustments. For low ΔK , the method do seem to give very good results, as discussed in section 5.4.1, and does look promising.

5.1.5 Stress fields

The stress fields in figure 79 do look representative, as they are comparable to those predicted by Williams' series, with the exception that they deviate in the region near the crack tip. The stress amplitude also seem to be a bit lower than the one predicted by theoretical model, this might be due to crack closure as well as other factors mentioned in section 5.1.4. The general shape, and size seem to be adequate.

The stress amplitude measured in the plastic zone, do also seem useful and reasonable compared to the true stresses in tensile tests. The peak von Mises stresses in the plastic zone, seen in figures 80, 81 and 82, start at a level of around 200MPa (300MPa for test 6 as it had a longer initial crack) which is close to the proportionality limit from figure 121.

Around the transition to stage III, the stresses in figures 80 and 82 seem to be roughly around 1000MPa which is around the stress level occurring in tensile tests at necking in figure 125. This together with the process zone established in stage III seen in section 4.2.9 might imply that the same instability causing necking, causes an acceleration in the crack growth occurring in stage III, as the stresses in that process zone change from being load controlled to displacement controlled. This is of course a bold statement and would require further inspection.

5.1.6 Plastic zone

Phase shift plastic zone

The phase shift plastic zone had one fundamental challenge, namely that the load signal was not logged, so the phase shift found was relative. For this reason, only the region which according to Díaz et al. [30] is the of reversed plasticity was used. This region has a higher peak and is easier to determine, whereas the region caused by monotonic plasticity is not as clear from the Fourier analysis. In general the Fourier analysis is very time consuming, and the camera had a large magnification, so only the region near the crack tip was analysed. An clear improvement is to log the load signal and the precise time when the logging was started, since each frame of the camera has the time, then the frame and load would be known, and precise shift could be calculated. An other solution to the problem is to decrease the resolution and instead analyse a larger region of interest, then the region of zero shift would be easier to identify, and could be used as the reference. Reducing the amount of cycles in each acquisition to not include the whole recording would also make the analysis more rapid to perform, and all of these points should be implemented in the future work.

The region of reversed plasticity is still a useful size, but the monotonic plasticity could be used for comparison with other methods based on stress analysis and theoretical models in section 4.2.7. It could also be used as the region of calculation for the energy dissipation

measurements.

Figure 95a shows what seem to be a linear increase in plastic zone size compared to stress intensity factor, but the trend seem to deviate from linearity in the end of the test. The noise in the figure is relatively large, and the trend is therefor very uncertain.

The shape of the zone seem to be "D" shaped for most of the test, with the flat part behind the crack, figure 97. This is not surprising, and the reason is clear in figure 106, where the *P1* column shows the phase-map which was used to determine the plastic zone. And the red region has a blue region behind it, probably caused by the crack faces, and the blue region makes the red region flat where they meet, this causes the D-shape. In the end of the test, likely in stage III, the shape changed. This is clear in figure 97, acquisition 101, and in the last rows of figure 107. The reason is the large amount of plasticity, which does also imply that the test reached stage III.

The whole Fourier analysis was not as useful as initially intended. It was performed on only one test, but the challenges and problems have been identified, and will be improved.

Laplacian plastic zone

The plastic zone based on Laplacian, was just an experiment, to see if it will give any valuable information. The general scatter seem to be smaller compared to phase shift, of course the large scatter in phase shift might be due to lack of a reference from load signal. The trend of this region seem also to be linear when compared to stress intensity factor although also here, it looks like there might be a deviation from linearity for test 4 for high stress intensity values, as seen on figure 95b, just as with phase shift analysis, but overall all of the tests give a linear trend. Figure 103 have a significant increase on the last measured point, which might be due to stage III, but might also be an outlier. This method also gives the smallest region defined as plastic zone.

An important note regarding the method is that the algorithm is based on second order derivatives, which are very sensitive to noise. The noise has to be removed by filtering,

here Gaussian filtering, which might influence the measurement, especially for small zones. An other note is that the method might be affected by conduction, figure 97 shows that for some of the measurements, the Laplacian region, was fully within the phase shift zone. The first problem with filtering would be most visible in figures 95b, 100, and 103 for low K values, but the curve does not seem to be flat in that region. The initial value of the size is also reasonable as it is almost the same as the size of the monotonic plastic zone, this can be seen in figure 96. It should be further inspected how this process zone changes in frequency, as maybe the adiabatic conditions are not met, and this might be a factor determining the size of this region. It would be also interesting to further compare the size of this plastic zone with respect to the crack growth rate.

Von Mises plastic zone

The monotonic plastic zone was found based on TSA combined with ratios between principals stresses from Williams' series to find von Mises stresses. The analysis assumed that the stress amplitude can be divided by $(1 - R)$ to find the maximum stresses occurring in the elastic region, as it is the stress amplitude that is measured. This is a fair assumption if crack closure is minimal. The plastic zone radius is shown in figures 98, 101 and 104, and some comparisons for the measured and theoretical plastic zone shapes is shown in figures 99, 102, and 105. These figures were limited to recordings where the whole plastic zone was within the FOV.

In general, the plastic zone based on LEFM, predicted a larger plastic zone (assuming plane stress conditions), and a parabolic curve when compared to stress intensity. The measured size had values lower than the plane stress LEFM model, and seem to exhibit a linear trend, not a parabolic one. The plastic zone size predicted by the implemented model of Williams' expansion do predict a linear trend, and seemed to correspond quite well with the measured values, especially when looking at the contour plots in figures 99, 102, and 105. The shapes of the measured plastic zone is very close to the shape predicted by Williams' series, even as the shape changes with increased stress intensity factor. The

shape has of course some noise, but the similarity is still very good.

The main problem in comparing theoretical, measured stress fields, is that the theoretical stress fields implemented, are elastic stress fields, and for this reason, they are expected to deviate from the plastic fields. The stresses in the plastic zone are significant, they are much larger than the yield stress, as figures 80, 81, and 82 suggest. The presented plastic zone is monotonic, and the actual monotonic stress state is difficult to extract from the IR data. The cyclic plastic zone would be much easier to compare, as the stress amplitude is directly related to the actual measured value. The cyclic plastic zone however would require knowledge about cyclic yield strength of the material which is unknown at this point.

5.1.7 Crack growth curves

Two methods of crack tip detection were implemented. First assumed that the largest temperature amplitude occurs at crack tip, whereas the second found the crack tip based on fitting the Williams' stress field to the measured data. The crack growth curves based on secant method are compared in figures 84, 88, and 92, and the crack tip calculated with Williams' stress field, seem to have less scatter, and so do the R^2 in tables 8 and 9 suggest. The polynomial filtering shown in figures 85, 89, and 93 however, do show better results and higher R^2 values for the crack tip based on TSA. This might be due to that the scatter for the TSA method is more random, or that it has less outliers.

The transition to stage III is more clear for the Williams method crack tip, due to less scatter. The coefficients seem to be in general in reasonable agreement, and the values seem reasonable as it is a ductile material. The plots of the crack growth versus the measured stress intensity are also plotted in figures 86, 90, and 94, and both the plots and coefficients look well, as the crack closure was minimal. A much more interesting comparison is to inspect how the R ratio affects the coefficients based on the measured stress intensity, but this remains as further work.

5.1.8 Stage III

Due to poor filtering and lack of time for improvements, only a qualitative analysis of stage III was done. The transition to stage III seem to occur when a process zone of high energy dissipation is established. The nucleation of this process zone is shown in figure 108, and an established process zone in figure 112. Most of this process zone, if not all of it, seem to have its origin behind the crack tip, and it looks that it is this region that is responsible for the increased crack opening displacement. Further, it seem like the process zone increases in size, and that the shape does change, mainly the angle at which it occurs with the crack plane, as this angle seem to decrease. Due to the process zone, the temperature in the sample starts increasing in stage III, and here the energy dissipation is much easier to capture. An other interesting phenomenon was observed in the last cycle before failure, figure 110, here the crack jumped 0.075mm, which released very large amounts of energy, the maximum temperature measured in the sample increased to approximately 46°C, as seen in figure 113. The energy release did not occur in the process zone described above, but rather in between the wings of the process zone. Maybe it applies in general that the heat dissipation due to crack propagation occurs in front of crack tip, and the process zone is just an additional phenomenon causing the acceleration in stage III.

It looks like the stresses do increase through stage II, but the material is capable of carrying the load although it is in the plastic region. The process zone that is created in stage III dissipates a lot of energy, which suggests that a lot of plastic work is done here. The reason might be that the material is not able to harden any more, and that the stresses in this region are not controlled by the loads, but rather by the displacements, and the displacements are again determined by the remaining material where the stresses are still load controlled. This principle of such a process zone might be compared to the necked region of a tensile test. In a tensile test, after the ultimate tensile strength is reached, the stresses are displacement controlled, as the initial cross section is not capable of carrying higher loads. The true stresses do still increase in the material, but the load capacity is

reduced.

The energy dissipation is also observed in the Fourier analysis. The second order term amplitude (**A2** in figure 107) becomes clear when compared to stage II (figure 106). This suggests that the energy dissipated due to cyclic deformation becomes visible in stage III, which agrees with the statements above.

5.2 High-speed imaging and DIC

5.2.1 Influence of vignetting on DIC analysis

When analysing the images using the DIC there was suspicion that the light spot fixed to the middle of FOV will introduce some error to the analysis of a moving object. The analysis presented in section 4.3.1 show that the vignetting influence is so small that it can be neglected when analysing the images. In other words, there is no need for additional filtering in order to reduce error in DIC analysis. The DIC algorithm finds a correlation between subsets independent of the light spot. The subset radius was set to 15 pixels, subset of this size is small compared to the width of a light spot which may span on 70% of image. Thus the supposed influence of vignetting should reduce to an increase in the average grayscale value in each subset, without affecting the high-frequency content. Here, the high-frequency content stands for the sudden, local changes in grayscale values arising from speckle pattern, which is further used to find the correlation in DIC software. These high-frequency values are not affected when applying the Gaussian low-pass filter.

A certain deviation in the displacement values was observed at measuring point number 3 as seen in figures 116 and 117. However, the scatter common for both filtered and unfiltered images, also a scatter resulting from image quality, spatial resolution and DIC parameters is significantly larger than the deviation resulting from filtering. In addition, the scale of this deviation is very small. As it follows from figure 116d, the largest difference in

displacements was 3×10^{-4} mm while the resolution of images used was around 1×10^{-2} mm/pixel.

5.2.2 The tensile tests

The overall goal with the tensile test in case of high-speed imaging and DIC was to extract the values of elastic modulus, proportionality limit, Poisson's ratio, true stress when ultimate tensile strength is reached, and in addition verify other material properties claimed by supplier. This test was also supposed to verify correctness of DIC analysis using *Ncorr* software.

The main point in section 4.3.2 was to compare strains obtained using DIC with those found using extensometer. Unfortunately the strains found using extensometer were unreasonably small, giving elastic modulus around 2.33 times higher than expected. After multiplication of extensometer strain with this factor, it can be seen that the overall shape of strain as function of time is quite similar for both methods as presented in figure 119b. Since calibration of the extensometer, and preparation of the testing machine to the tensile test was performed by the third part, there is a suspicion that the extensometer wasn't calibrated properly before starting the test. If the strains from extensometer were found using formula 57, it might be that the wrong value of original gauge length was used. Right before the test, a distance between the blades of extensometer was reduced from 22.5 mm to 12.5 mm. In addition, it follows from the images used for DIC that the final span of the extensometer blades was rather around 11 mm than 12.5 mm. It may in some extend explain the difference by factor of 2.33.

Rationality of the elastic modulus values presented in section 4.3.3 is to be discussed. Elastic modulus was found to be 193.0 GPa and 191.3 GPa for specimen 1 and 2 respectively. This is in agreement with material data available on different material suppliers web-pages [128–130] which all claim the elastic modulus of 316L to be 193 GPa. Elastic modulus for specimen 4 was found to be 203 GPa. This is higher than the other values found, but

in this case the amount of images used to find strain in elastic regime was a 1/3 of the amount used when analysing specimen 1 and 2.

From the stress-strain curves it follows that the material has no clear yield point, one can rather see smooth transition to the plastic regime where stress is not longer linearly proportional to the strain by Hookes' law. In such materials one use rather proportionality limit and offset yield strength ($\sigma_{0.2\%}$) as it's the case in this work.

The stress-strain curves showing the whole test until fracture are similar and mostly overlap until the ultimate tensile strength is reached, and the necking sets in. When the necking starts, the stress-strain relationship starts to deviate between specimens and ROI used. This behaviour is expected. In case of use of different ROIs, the strain close to final fracture should be larger for shorter ROI (12.5 mm) since ΔL is divided by smaller gauge length value L than for the case of longer ROI (19.5 mm). In case of strain deviation when using the same L , the difference can be caused by different location of area of necking on the specimen. The ROIs have been placed on the middle of the sample, while the area of necking occurred closer to the upper end in case of both specimens 1 and 2.

What can be seen from comparing strains around elastic regime from specimen 1, 2 and 4 (figures 121 and 120) is that the strain in elastic region from specimen 4 contain significantly less scatter compared to former two. The DIC analysis was performed several times, and the results as well as scatter were quite similar despite the different DIC parameters selected. This may have several explanations. The analysis of elastic region of specimen 4 included analysing of around 30 images, this is significantly less that 300 and 320 images used for specimen 1 and 2 respectively. This reduction could have a smoothing effect. Another reason is use of the different DIC pattern. Speckle pattern on specimen 4 was created by applying the black dots on a white background. Since the testing order was opposite to the numbering order of specimens, the issues with peeling off paint on specimens 3 and 4 were detected, and the last two specimens (1 and 2) were repainted before testing. After repainting they had white dots on black background since matte black paint didn't peeled off, even when the necking occurred. Another important reason was a size of the

FOV and the spatial resolution. The FOV when testing specimen 4 was set so the 1 pixel corresponded to 0.027 mm, while for specimens 1 and 2 the spatial resolution was about 0.052 mm per pixel. This difference was caused by the goal with the experiment. Test with extensometer (specimen 4) was interrupted at some point because of the limited travel length of the extensometer. For this reason, the specimen could cover a larger area of the cameras FOV. The last two tests were supposed to capture the whole test until final fracture, and thus the spatial resolution was lower. However, when creating whole stress-strain curves, the time intervals between images were large and the scatter was almost invisible as it can be seen on figures 123 and 124. Additionally, the tool for calculating the strains out of displacements was created by one of the authors of this work. This tool doesn't take account to any rotation of the specimen which could occur due to misalignment of a specimen inside the grips, or other effects which could occur during the tensile test. It only looks at vertical displacements following the Lagrangian description, also the description where the reference configuration is the configuration at $t = 0$. One example of mentioned misalignment in the grips can be seen in figure 47b, this particular figure shows analysis of specimen 2. The shape of displacement field at this figure explain why its important to take average value of all displacements in extreme, i.e. at upper and lower edge of displacement fields. Thus the possible sources of error are as follows:

- Sampling rate. Reduction in amount of images used in DIC analysis may have smoothing effect and decrease the scatter.
- Quality of the random pattern used for DIC analysis, and the paint for creating it have an significant influence on the results.
- The resolution in mm per pixel is another possible source of error.
- The strains were computed using the tool which doesn't take account for rotation of specimen which may occur during tensile testing.

5.2.3 COD, crack closure and the effective SIF analysis

Determination of image corresponding to maximum load

One of the major issues which could affect the results when analysing the crack opening displacement was a correct determination of image corresponding to the moment when the load was on its maximum. For all the tests with exception of test 5, the problem was solved by external triggering system which provided a triggering TTL signal at the mean load, further determination of image corresponding to maximum load was straight forward when having the information about the test frequency, and the frame rate. The problem become much more severe when the test 5 was running, and the majority of the results from DIC analysis presented in this work come from this test. In test 5, the triggering signal was send directly from the fatigue testing machine since the authors wanted a trigger signal both when the test was running, and after a short stop in order to take a reference image at zero load for plastic zone determination. Unfortunately, the time delay between sending the trigger signal, and reaching the max/min load was random, and additional actions had to be made in order to solve this issue. Problem was solved in to steps. First, the frame corresponding to the alleged largest crack opening was estimated by visual inspection by looking at the raw recordings from the camera. When it was done, a frame corresponding to minimum load was simply found knowing the test frequency and the frame rate used. Frame corresponding to minimum load was further used in step two, which was the initial DIC analysis. In such analysis, the largest difference in vertical displacements was tracked for two arbitrary points where each was placed on different side of the crack, and both had the same horizontal distance to the crack tip. The result of this action is seen at figure 184. The symmetry of the obtained curve was used to find the image corresponding to maximum COD, which was assumed to correspond to the maximum load.

Influence of the crack tip position

Correct determination of the crack tip position is crucial when analysing the crack closure level. It has been found that the opening load P_{op} strongly depends on the horizontal

distance to the crack tip. Figure 128 show that P_{op} is significantly higher for distances close to the crack tip, and the highest P_{op} which was typically found for a distances closest to the crack tip was used to determine the final P_{op} level for given acquisition. This shows that incorrect determination of a crack position may underestimate P_{op} introducing the error to the analysis. The difference of ± 2 pixels in horizontal direction is not that significant as it can be seen at figure 185, but the difference of 5 pixels and more may introduce significant error as seen at figure 128. The magnitude of opening is much more influenced by correct determination of crack tip position than P_{op} , but the COD magnitude was not used for any purpose in this work.

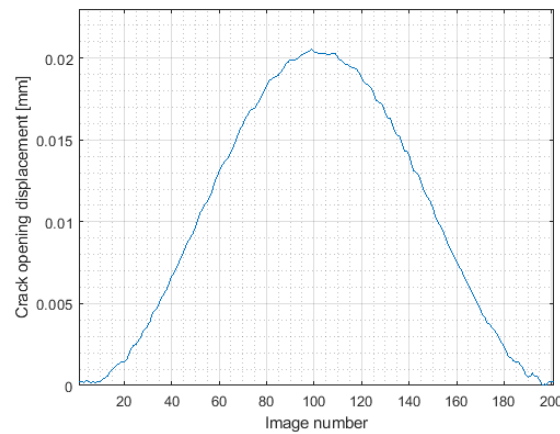


Figure 184: Determination of frame corresponding to the maximum load

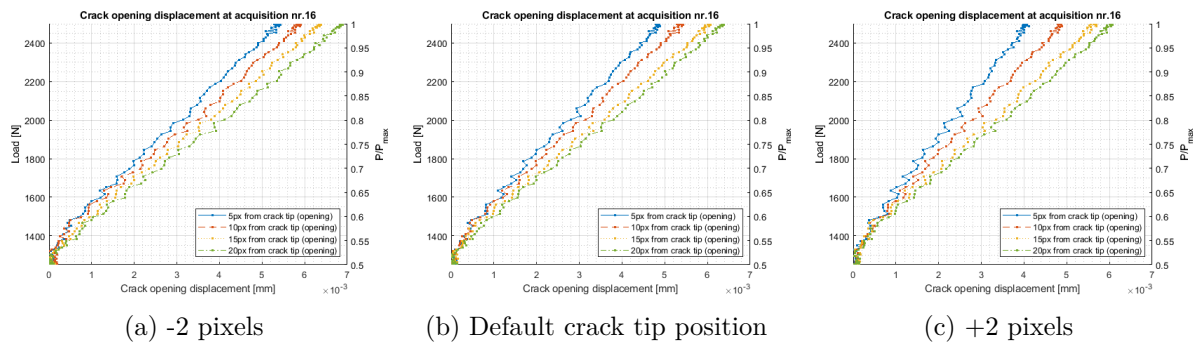


Figure 185: Plots of applied load versus COD showing the influence of assumed crack tip position

Other issues which could affect the results

To ensure the high quality of CODs data, the initial determination of alignment, and amount of measuring pair of points with determination of $L1$ and $L2$ was made according to literature [59]. More details and explanation of $L1$ and $L2$ are available in section 3.5.6. The trial and error showed that selecting $L2$ values which were too low result in quite noisy, and unrepresentative measurements. The appropriate $L2$ was found when the COD magnitude didn't increase significantly for increasing $L2$ when holding the $L1$ constant.

The tool for calculating the CODs was developed by one of the authors of this work, this tool does not take into account any rotation of the specimen. It only analyses the vertical displacement array by tracking the vertical displacement of measuring points. The initial plan in this work was to employ *Ncorr post* post-processing tool, but the authors of this work didn't manage to resolve errors arising from incompatibility of mentioned post-processing tool with currently used versions of *MATLAB*.

Another thing that is clearly visible when looking at figure 128 is that the noisiness of COD decrease with increasing ΔK . This is because the magnitude of COD increases, while the systematic error causing the scatter seem to be constant for increasing ΔK . The source of this scatter unknown, but it may come from the DIC analysis, the DIC parameter selection, or the lens distortion which was not corrected when analysing the CODs, and the crack closure level. González et al. [61] in their study of crack closure after the overload mention which DIC parameters were used. For the 2248×2048 pixel image resolution they used subset radius of 35 pixels, step size of 7 pixels and strain window size of 15. In this work, the COD analysis was performed with 1024×1024 pixel images, subset radius of 15 pixels, subset spacing of 1 pixel and strain radius of 15.

There was significant difference in scatter on applied load-COD-curves between test 4, and the test 5. Scatter observed on the latter one was significantly lower than in test 4, even though the determination of an image corresponding to the maximum load was much easier in test 4 than in test 5. There were two main differences between these two tests. The size of

the FOV in test 4 was approximately $9.8\text{mm} \times 9.8\text{mm}$, while it was about $4.2\text{mm} \times 4.2\text{mm}$ in the test 5. Another significant difference was the random pattern applied. In test 4, the surface was painted with black dots on white background, while the sample number 5 was heavily etched in order to create pattern of random imperfections on its surface. Since the results for both COD, and the stress analysis were unsatisfactory due to the scatter in test 4, the change in random pattern used for a size of FOV as in test 4 is necessary in order to increase quality of obtained data.

One of the possible error sources was a shape of the load function, test frequency and the way the images were captured. Different authors deal with this problem in different ways. Tong et al. [57] used load with trapezoidal waveform with 20 second loading/unloading, and the 4 second hold at maximum, and minimum load in order to capture 48 images for one load cycle. Vasco-Olmo [59] in their study used test frequency of 10 Hz. However they periodically paused the test in order to allow acquisition of an complete load and unload cycle at lower frequency with the CCD camera. González et al. [61] used strategy with reducing the loading velocity from 10 Hz to 0.05 kN/s when capturing the images. In this work, authors used capability of the high-speed camera to capture similar series of images but without interrupting the experiment. Compared to results obtained by other authors, the scatter was satisfactory low, especially for the test 5 and the high magnitude of COD typical for high values of ΔK .

One of the problems that has been discovered during the experiment was vibrating of the HSI system. This problem was discovered when running at 25 Hz, and resulted in images out of focus, or the FOV movement perpendicular to the crack growth direction. This introduced the error to the analysis. One possible reason was the eigenfrequency of the high-speed camera and lens system. The camera with a lens was a heavy ($> 10\text{kg}$) system that was attached to motorized translation stage further attached directly to the frame of the testing machine. The contact area of the camera with translation stage was small, and vibrations from testing machine could possibly hit the resonance frequency of the camera system when running the experiment. The problem was solved by connecting camera han-

dle with the end of the lens with rubber bands which were supposed to work as a damper, and reducing the test frequency to 10 Hz when running the actual experiment.

5.2.4 Strain fields, stress fields and plastic zone

Following discussion focuses mostly on the test 5 since it gave most useful data in DIC analysis even though it did not capture the stage 3.

Influence of lens distortion

When running the DIC analysis in order to estimate the size of the plastic zone it has been found that the strain fields are strongly affected by a kind of paraboloid surface incorporated to desirable strains. This effect, and its influence on the stress analysis is presented in figures 186, and 187, and is caused by systematic error in 2D DIC analysis due to the lens distortion. This problem has been widely described in paper of Pan et al. [131]. Authors mention possible reasons of the lens distortion effect as: quality of camera lens, the position-, and the motion of the considered point. They propose use of the lens distortion correction factor in order to get rid of this effect. The authors of *Ncorr* [118] mention that the process of determining the lens distortion correction factor requires DIC analysis to be run on images taken during rigid body translation tests, and then performing a least squares analysis to solve for the lens distortion parameter. In this work, the problem was recognised during the DIC analysis after capturing the data from test 5, so no actions were made in order to avoid this effect before the tests. However, the *Ncorr* software provides users a lens distortion correction option which follows from the equation number 6 in mentioned paper of Pan et al. [131]. In this work, the correction factor k_1 was found by trial and error to be -6×10^{-8} , and was introduced when formatting displacements to every set of images when performing the stress analysis. Strains and stresses after correction can be seen in figure 188.

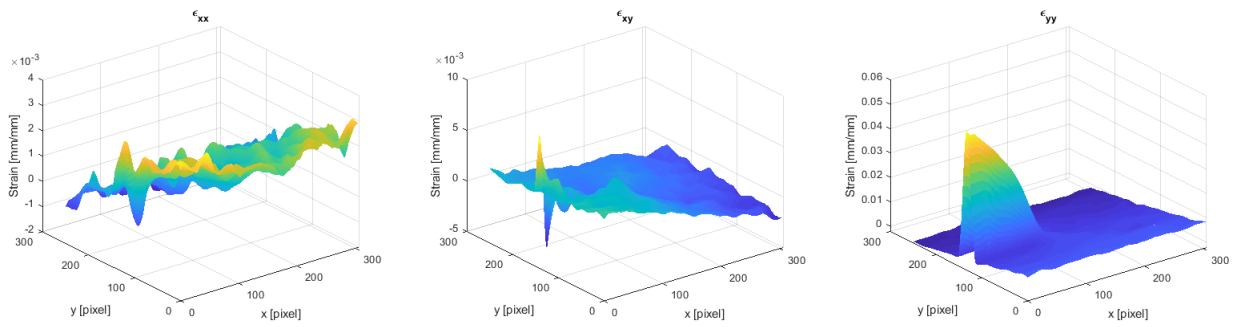
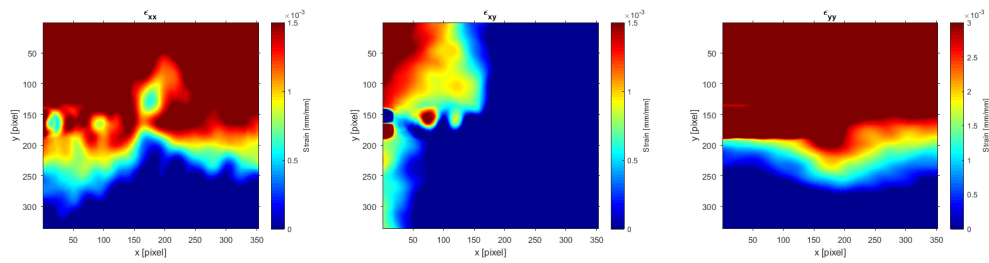
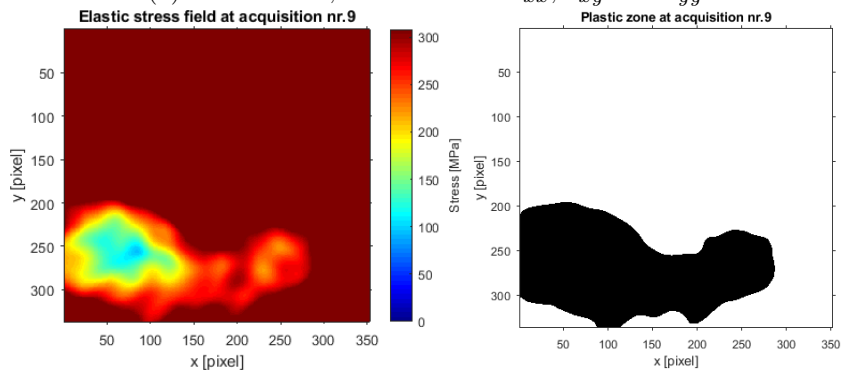


Figure 186: Strains affected by lens distortion, from the left: ϵ_{xx} , ϵ_{xy} and ϵ_{yy}



(a) Strain fields, from the left: ϵ_{xx} , ϵ_{xy} and ϵ_{yy}



(b) Stress field

(c) Plastic zone

Figure 187: Strain and stress fields affected by lens distortion

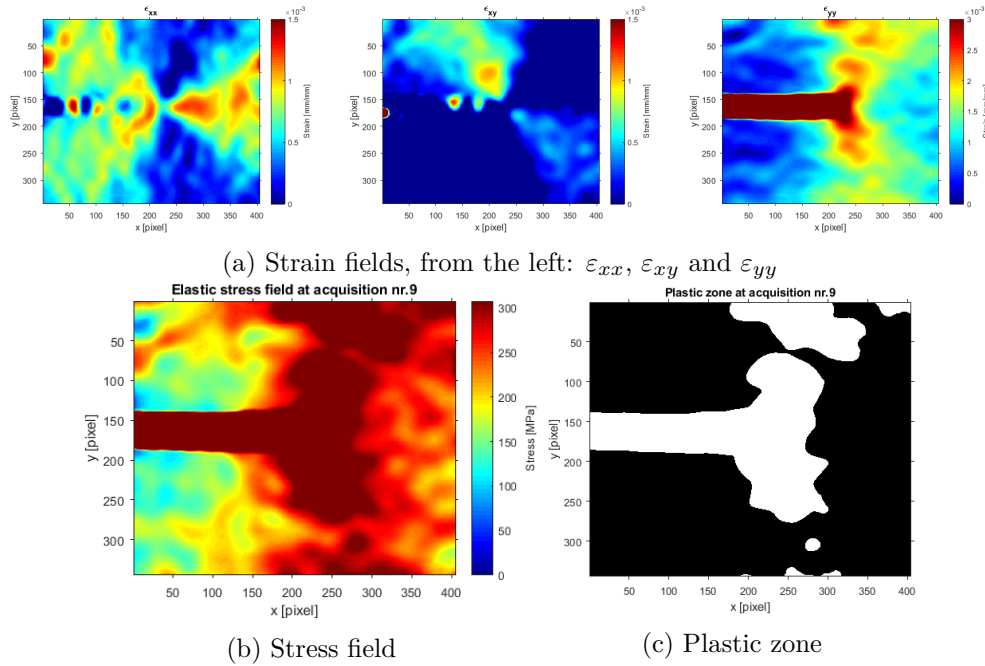


Figure 188: Strain and stress fields with lens distortion correction factor of -6×10^{-8}

Rationality of assumptions and error sources

In following, other aspects of the plastic zone determination and assumptions made are to be discussed. The plastic zone was estimated by finding the equivalent von Mises stress and considering the crack tip zone within which the equivalent stress exceeds the tensile flow stress, also the yield stress for ductile solids according to Suresh [6, p. 302]. Gao et al. [1] used only von Mises stresses in their work, while Vasco-Olmo [58] used both von Mises, and Tresca criteria for plastic zone estimation. In this work, only equivalent von Mises criterion was used. When it comes to calculating the stress fields out of strain fields, none of mentioned the authors describe how the stresses were calculated. In this work, the plane stress assumption was made when calculating σ_x , σ_y and τ . This assumption was made based on low thickness of the sample and the fact that the stresses are observed on the surface of the specimen. Chowdhury and Sehitoglu [132] lists a research where it has been found that when making the finite element models, and assuming the plane stress conditions, the material around the crack tip flows from the bulk perpendicular toward the

crack flanks resulting in the hourglass like deformation. This was observed during test 6, especially at the stage III. Plane strain assumption has not been tested in this work and should be considered in the future.

Another aspects that could influence the quality of the results is mentioned problem with determination of the maximum load. For the plastic zone determination, the image corresponding to the maximum load was the same as the image with maximum COD as described in previous section. Due to the scatter and problems with precise determination of frame corresponding to maximum load, it might be that the real load corresponding to image used was slightly below P_{max} .

As mentioned in section 3.2.2, the proper choice of DIC parameters has a huge influence on scatter and accuracy of the final results. In addition, the *MATLAB*-tool for calculating the stresses and the plastic zone was developed by one of the authors of this work. This tool simply perform the point-wise multiplication of the strain matrices with the stiffness matrix and finds the stresses in Cartesian coordinates. The latter ones are further used to calculate the equivalent von Mises stress, here the point-wise multiplication is also used. The strain matrices exported from *Ncorr* were not filtered during the analysis. The way the radius of the plastic zone was found may raise doubts since its shape was far from being a circle, and despite this fact the radius was found as $r = \sqrt{A/\pi}$, where A is the area of the plastic zone. The radius obtained this way is easier to compare to the size of the plastic zone obtained by IRT, and the theoretical models. The figure 132c show that use of the height for determining the size is also possible, however the scatter is much higher compared to the size obtained using plastic zone area. In addition to mentioned issues with estimating the size, the FOV used had size $4.2mm \times 4.2mm$ and the upper part of the plastic zone started to expand out of the FOV around acquisition number 23, and thus the size of the lower half of the plastic zone multiplied by 2 was used for remaining acquisitions. For stress-, and plastic zone analysis in this work, only results from test 5 were presented. The random pattern used in specimen 4 was too coarse, and the stress fields obtained analysing these data were quite noisy. As it follows from the figure 24, the random pattern used in test 4 was created with the paint. Even though the results were somehow

useful in determination of CODs, the determination of stress fields became a challenge. McCormick and Lord [52] mentioned that the natural surface of the component or structure may have sufficient image texture for DIC application. For test 5 a heavily etching of polished surface was used in order to create random pattern. Results of this action are quite satisfactory. The only problem with this method is danger of the etching influence on the material strength, which was not measured, or investigated. To prevent the alleged influence of etchant, the specimen was rinsed with the ethanol immediately after the etching, and washed in ultrasound bath for a few minutes afterwards. Summarising, the following were the possible sources of error when determining the stress fields and the plastic zone using DIC:

- Lens distortion.
- Choice of DIC parameters.
- Plane stress assumption and the method for calculating the stresses.
- Problems with determination of the image corresponding to P_{max} .
- Speckle pattern used.
- Method for calculating the radius of the plastic zone.

5.2.5 Fatigue crack growth curves and Paris' law parameters

Test 1

For HSI and test 1, two different FOVs were used to obtain the crack length data. The first one, with approximate size of $1.4\text{mm} \times 1.4\text{mm}$, and second one with size $12.9\text{mm} \times 12.9\text{mm}$. Since the test was load controlled, the mean load and load amplitude were kept constant. Thus an increase in ΔK was only caused by increase in a . This made it easy to distinguish between both of FOVs used for the HSI when looking at $da/dN - \Delta K$ curve at figure 134b. The points for ΔK above $8.65 \text{ MPa}\sqrt{\text{m}}$ correspond to larger FOV when the spatial resolution was reduced from $1.44\mu\text{m}/\text{pixel}$ to $12.5 \mu\text{m}/\text{pixel}$ making precise determination of crack tip much more difficult. For about 50 measurements, the difference in crack length was either 2 or 3 pixels which corresponded to $25 \mu\text{m}$ or $37.5 \mu\text{m}$ between measurements respectively. This effect vanishes for high ΔK values when crack increment was larger and has no strong influence on the reasonability of the FCG parameters obtained.

Test 4

The $da/dN - \Delta K$ -curves obtained during test 4 had a high scatter compared to results from test 5 as it follows from figure 135b. Totally 85 acquisitions were made during this test. There are two possible explanations of large scatter; the FOV used was large, and the sampling rate was high compared to test 5. The size of the FOV was approximately $9.8\text{mm} \times 9.8\text{mm}$, together with a coarse speckle pattern providing uncertainty in determination of correct crack length. The sampling rate was step-wise reduced during the test; at the beginning the acquisitions were taken every 16000 cycle, and further reduced to 8000, 4000, 2000 and finally 1000 cycles. This resulted in relatively small crack growth da between the acquisitions. Probably a smaller spread would be obtained by merging some of the measurements.

Test 5

In test 5, there were only 42 measurements of crack length. The sampling frequency was low, for the start of the test, one acquisition for a crack length estimation was made for each 16000 cycles. It was reduced to 1 sampling per 8000 cycles from acquisition number 16. The size of the FOV was $4.2\text{mm} \times 4.2\text{mm}$ during the whole test. The low size of the FOV together with low sampling frequency resulted in low spread and good fit of the data. The coefficient of determination R^2 was whole 0.938 and 0.996 for the secant and incremental polynomial method respectively for test 5. This fact is of special interest when determining C and m since the test 5 captured only stage II, where the Paris' law is valid.

5.2.6 Crack initiation, propagation and transition to stage III

Crack initiation

The whole precracking for specimen 3 was captured, results from observation are presented in section 4.3.8. The goal with such observation was to see how the crack is initiated and how it behaves as it grows, especially in the initial phase of precracking when the high P_{max} are used. In this work, the initial P_{max} was set to 3.5kN resulting in $\Delta K \approx 16.1\text{MPa}\sqrt{\text{m}}$ when the crack length $a = 6\text{mm}$ was used. When looking for the same ΔK value at FCG curves in section 4.3.7 it can be seen that it correspond to late stage II and stable crack growth. As mentioned in 4.3.8, the crack initiated at the grain boundary and was therefore difficult to detect. It continued until it met another grain boundary where it was arrested. It continued transgranular using other path and moving in zigzag manner. This zigzag behaviour was observed for the whole precracking process as seen in figure 137 and may suggest following the slip systems [6, p. 335]. The zigzag is clear, but the "teeth" are short. It may suggest that the crack followed slip plane for a short period of time and than chose a more favourable path (or a slip plane) closer to the middle of the sample resulting in crack growth perpendicular to the far field tensile axis. Etching used in preparing the sample 3 seemed to be too strong and made observation of crack propagation difficult. Thus, for the

test sample number 6 no etching was used at all.

Stable crack propagation

The picture from the first acquisition of test 6 is presented in figure 139a. What is interesting is the visible zone of plastic deformation left after the precracking, even though the last precracking load used was below the P_{min} used in the actual test. As mentioned in section 4.3.8, a discontinuity in the crack closure is observed. The opening load P_{op} is high in the portion of the crack between the crack tip, and the plastically deformed zone, while the crack portion between the mentioned zone and the machined notch seem to be always opened. This behaviour is similar to what tends to happen during overload [61]. Since no random pattern was applied to the sample, the level of closure was not quantified in test 6, all observations follow from the visual inspection.

During the test some branching of the crack was observed as it follows from figure 140. As it follows from literature [6, p. 335], the crack growth involves alternating, or simultaneous flow along two different slip systems. Thus, it might be that for a single grain where the crack was propagating, 2 of 12 slip systems were active simultaneously assuming 316L as metal having a FCC crystal structure. Since the crack tend to propagate in direction perpendicular to the far-field load axis in mode I [133], the crack finally followed slip plane more parallel to the crack direction.

During test 6, the development of plastic envelope was observed. By plastic envelope the authors mean the area of plastically deformed material left by "active" plastic zone ahead of the crack tip. As it follows from figures 141 and 142, this zone is characterised by uneven surface and the presence of slip bands on a single grains. This envelope is more, and more pronounced as the crack propagates. The slip bands are best visible in stage III as it follows from figure 142b. The slip bands seem to hide and appear during the load cycle, thus the majority of them is not persistent.

Transition to stage III

Finally, the remarks from the transition from stage II to stage III, and the stage III itself will be presented. The experiment was interrupted between stage II and stage III of the crack growth, because the cameras required the change of parameters for proper capturing of stage III and the final failure. In opposition to stage II where only one load cycle was recorded once for several thousands of cycles, the whole stage III was recorded as one 42 second long recording. From what can be seen using the high-speed camera, the start, or the end of the transition from stage II to the stage III of FCG is difficult to clearly determine. However, several phenomena suggesting the transition to stage III occurs and will be discussed in the following.

The crack growth rate becomes high, the FCG-curves suggests that at the very end of stage II, the da/dN is up to 5 $\mu\text{m}/\text{cycle}$. This increases significantly in the stage III, but the growth rate was not measured in stage III, the reasons will be mentioned later. The transition between the "active" plastic zone ahead of the crack tip, and the plastic envelope left by plastic zone becomes more and more pronounced. It can be seen that the area of the "active" plastic zone raised towards the lens, while the plastic envelope was almost on the same distance to the lens as the virgin, unaffected material. This rising was observed by the loss of the camera focus on the "active" plastic zone, and appearance of the shadow corresponding to the slope between the plastic zone and the plastic envelope. The possible explanation of this "high" difference is the material flow. As mentioned earlier, Chowdhury and Sehitoglu [132] lists a research where it has been shown that the material flows from the bulk perpendicular towards the crack flanks in the finite element analysis when assuming the plane stress conditions for a very thin plates. This kind of behaviour is possible to observe for C(T)-specimens used in this work.

As mentioned, the crack growth rate was not measured when analysing the data from HSI because the plastic zone raised towards the lens and the camera loss its focus. With other words, the depth of field was too short to capture all phenomena when filming stage III. In addition, the shadow caused by material flow made it impossible to precisely determine

the crack tip position. Finally, the crack left the upper edge of the FOV for a few cycles before the final failure. The literature [6, p. 358] suggest that at stage III there should occur static fracture modes as: cleavage, intergranular separation and the fibrous failure in addition to the striation formation. Unfortunately, due to the problems described, these were not captured. Proper capturing of the stage III with high-speed camera remains as a further work. Following actions should enable satisfactory results in future attempts:

- The FOV when capturing the stage III should be larger. Larger FOV will result in increase in depth of field and avoid the loss of focus.
- If one wish to use similar magnification, or even higher than one used in this work (smaller FOV), then the development, and use of automated focus adjustment should be considered. Reduction of the test frequency may have significant impact on the test results in such case.
- The specimen should not be removed from the testing machine between the precracking and the actual test which was a case in test 6 in this work. This resulted in the crack growth in certain angle to the axis of specimen, and as result, the height of the high-speed camera had to be adjusted several times during the test 6. This problem was easiest to observe at the end of the stage III, when the crack left the upper edge of the FOV for a few cycles before the final failure.

5.3 Acoustic Emission

5.3.1 Quality of Data

Acoustic emission is a very sensitive technique, with many possible sources of noise or disturbances to the data. Since the tests were performed using different equipment and data acquisition methods, both the susceptibility to noise, and the factors influencing the data were different for each test. This section highlights some issues that were encountered, both in general and specifically for each test.

Effect of Sensor

The specimen-to-sensor interface, and the sensor itself, are responsible for transferring the acoustic waves from the specimen, and convert it into a readable voltage signal. As a result, they have a large influence on the data obtained during the test. The sensors used in this work was PAC Nano-30 sensors and PAC Micro-F30 sensor. It was discovered that both sensors had strong resonance frequencies which dominated their power spectrum. The effect can be seen in figure 190, showing the signal when no crack growth is occurring for each sensor. Since these frequencies were limited to the lower end of the AE spectrum, it was thought that a high-pass filter could be used to negate the effect of these resonances. It was found however, that doing so removed too much information. Activating other modes required significantly more energy, and even if they could be activated, most of the energy was still expended by the lower frequency resonances in most cases. This can clearly be seen in figure 191, as well as in the STFT in figures 156,159 and 161. An attempt at filtering out the lower end frequencies in Test 4 is shown in figure 189. As can be seen, even after filtering, the signal grew to be dominated by the very same frequencies as the crack grew, and the signal became stronger.

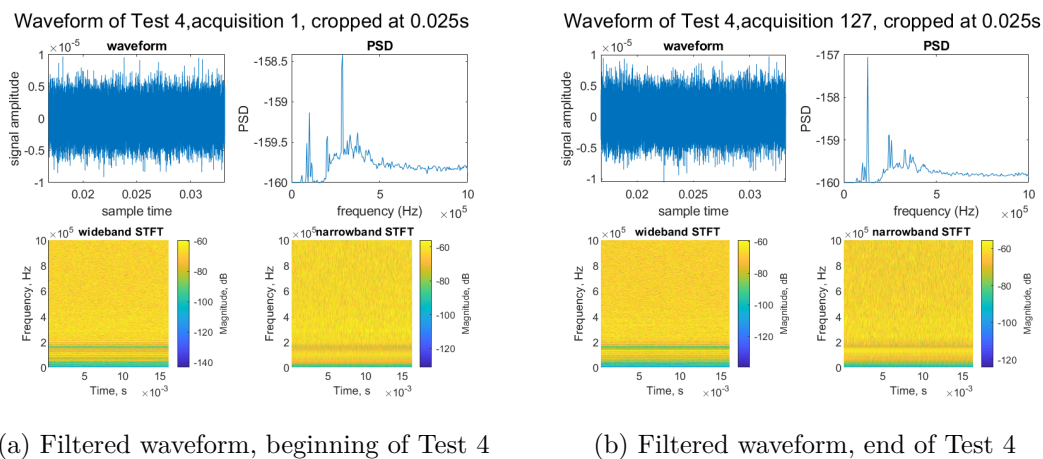
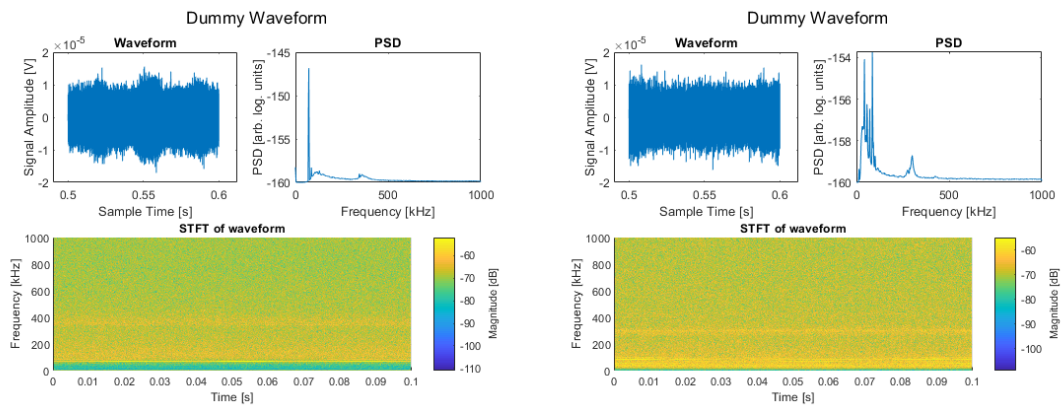


Figure 189: high-pass filtered waveform and frequency content of early and late stages of Test 4

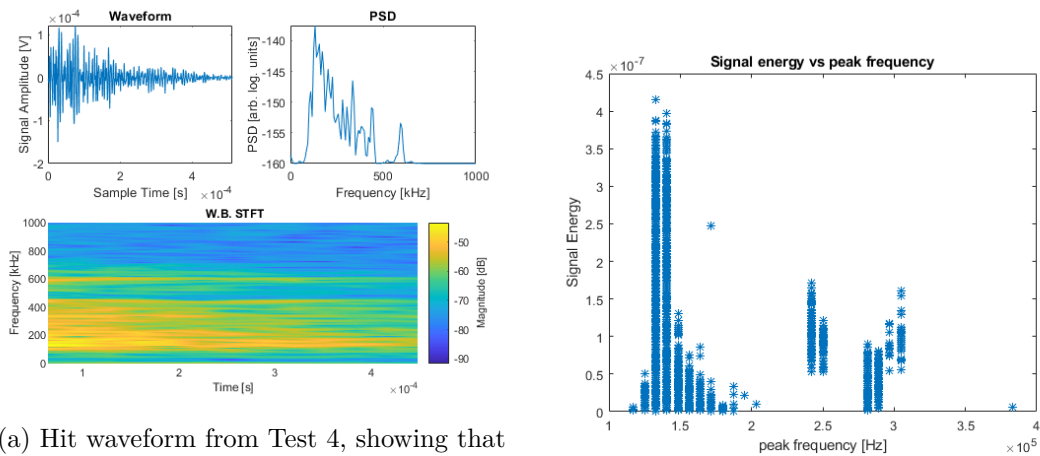
The presence of these resonances made analyses based on the spectral content of the signal

more difficult. Since most of the signal power was located in these resonance frequencies, several approaches were rendered less effective. As is evident from the figures in section 4.4.2, the statistical moments obtained from the PSD are by and large similar. Analysis based on these were therefore more difficult. The quality of the clustering was also affected. Since there were constant, large frequency spikes occurring in the same frequencies, with similar amplitudes, throughout the test, and for all waveforms, it was difficult to separate the waveforms into clusters due to the innate similarity between them. Likewise, this reduced the effectiveness of the decomposition method described in section 3.6.2.



(a) Sensor 1 response during dummy testing (b) Sensor 2 response during dummy testing

Figure 190: Frequency response of Micro-30F sensor (fig. 190a) and Nano-30 sensor (fig. 190b) during dummy testing performed before Test 6



(a) Hit waveform from Test 4, showing that most of the signal power is located in the resonant frequencies, even when the waveform has a wideband frequency content. It can also be seen that the waveform has been truncated, and misses the waveform initiation.

(b) Signal energy and corresponding frequency from Test 4, showing an alternative view of the resonance effect.

Figure 191: Figure showing difficulties of analysis of spectral data.

Test 4

Test 4 was the first test conducted utilising the Instron test machine, and as such, some problems were encountered in analysing the data. For one, it was found that the settings used in the hit waveform parameters were sub-optimal. Since no pre-trigger length was used, some waveforms were truncated, resulting in loss of information. An example of such a waveform can be seen in figure 191a. As a result, the base continuous signal from before the waveform could not be determined, and thus, certain typical hit parameters such as rise-time could not be calculated.

Unlike the succeeding tests, while two sensors were attached to the specimen, only one sensor (sensor 1, on top) was active for both hit detection, and waveform streaming. This was due to the *MATLAB* code used at that time being unable to separate data from multiple streaming channels from each other. Since only one channel was used for streaming data, so too was only one channel used for hit detection. As a result, methods such as source location could not be utilised.

Another potential problem in this test was the use of *Molykote BR2 Plus* as both the couplant and as a means of electrical insulation. As far as could be determined, there's no reason to doubt the quality of the resulting interface. However, as mentioned in section 3.2.3, EMI was a large source of noise during the experimental set-up. It was believed at the time of Test 4 that the ceramic interface together with the couplant was sufficient to isolate the sensor from the specimen and test machine. This might not have been the case, as the signal level observed both during dummy testing and Test 4 were multiple times higher than the ideal case for the PCI-2 of around a voltage of 6mV.

During this test, a significant number of hits were recorded which solely contained the resonant frequencies described previously. It is believed that these represented the continuous signal crossing the threshold value as a result of a threshold value set too close to the baseline signal. As the crack propagated and the continuous signal strength rose, the threshold was increased by 1decibel in an attempt to compensate. Despite this, the signals were still detected interspersed with ordinary AE signals with a distinguishable peak and decay. Since the threshold had already been increased it was not desirable to increase it further; increasing the threshold also removed lower amplitude examples of ordinary signals. As is discussed in later sections, the inclusion of these hits related to the continuous signal was not necessarily a problem.

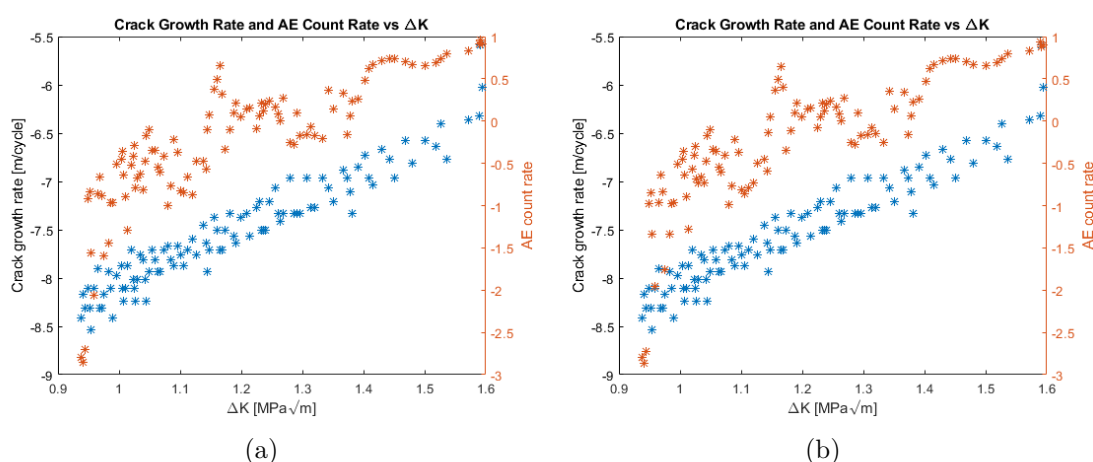


Figure 192: Count rate curves with 36dB threshold and 41decibel threshold shows no major differences

Test 5

In Test 5, the Micro-F30 sensor was introduced due to the resonance experienced when using the Nano-30 sensors in the previous test. The Micro-F30 sensor was used on top of the specimen (sensor 1), while one of the Nano-30 sensors was used on the bottom (sensor 2). As a result, several changes were introduced to the set-up which might have influenced the data from Test 5. For one, the couplant and electrical insulator was changed. Instead of *Molykote BR2 Plus*, thin paper wetted to saturation by hydraulic oil was used. This was believed to improve the electrical isolation, since the paper would prevent the insulation layer (i.e. oil) from being compromised from the compression when mounting the sensors. This was believed to possibly have occurred during Test 4. Since the oil was significantly less viscous than the grease, a concern was reduced transmission of shear waves, but extensive use of the wetted paper method by previous researchers allayed this. Based on the results obtained in Test 6, it is thought that the wetted paper was applied incorrectly in Test 5. During the set-up of Test 6, the signal was originally quite noisy, but after re-applying the paper and straightening it, the level was significantly reduced, even when the cyclic load was applied. It is possible that the paper was slightly rippled or crumpled after application in Test 5, and therefore either did not provide sufficient electrical isolation, or produced some kind of rubbing effect. Other changes were related to the settings in the *AEwin* software. Based on the truncated data of Test 4, a pre-trigger length of 256 was used. As a result, half the recorded hit waveform consisted of the base continuous signal, rather than the hit. Significant information stored in the hit waveform was therefore lost, and any energy parameter calculated from the hits would not be representative of the true signal. This was a result of misinterpretation of the units of the pre-trigger. Since the hit waveform length was given in number of sampling points, it was believed that the pre-trigger signal was so as well. Thus, using 256 as pre-trigger length should have resulted in a quarter of the signal being pre-trigger, since there was 1024 sampling points per hit waveform. Instead it seems likely that the pre-trigger was given in micro-seconds, as 1024 sampling points corresponds to 512 μ s length, and half

the waveform consisted of the pre-trigger signal. Another change in the software was the setting of the threshold value for the sensors. A value of 35dB was used in Test 4, and was raised to 36decibel during the test; this value was used from the start in Test 5 for sensor 2. For sensor 1, the threshold was originally 36dB, but was quickly raised in 1dB increments to 40dB during the first minutes of the test due to the continuous signal intermittently crossing the threshold. As a result of this, the hit data from Test 5 was not directly comparable to that of Test 4 for several reasons. The sensors used were partially different, the sensors that were the same were located differently on the specimen and in relation to the test machine, the threshold values were different and the amount of continuous signal permitted to be recorded therefore different.

A variable that potentially had an influence on the data was the loading and triggering scheme. Since the load was periodically reduced to zero in order to obtain reference images for DIC analysis, the ΔK value for the following cycle was equal to K_{max} . This was effectively a type of overload which are known to temporarily reduce AE, until the crack has surpassed the process zone affected by the overload[80]. Due to the triggering scheme used during the test, the overload was not captured by the AE recordings, as AE was triggered before the overload occurred. AE was in, other words, triggered as far away from the initiation of the overloads as possible, which might have reduced their effect on the streamed waveforms. By looking at the cumulatives of figure 175, it looks like rapid increases in the total hits can be seen to occur in bursts closely matching some points of crack length measurement by the IR camera, followed by periods of near stagnation. The camera was triggered close to the occurrence of the overloads. This might imply that the emissions were located temporally in the region preceding, or during the overload.

Test 6

In test 6, a lower static noise level was observed than in previous tests. It was not immediately obvious whether this was genuinely a lower level of noise, or if it was simply poorer

contact between the AE transducers and the specimen. Pencil-lead break tests had been performed for all specimens. However, due to the amplification of 60dB, the PCI-2 board was saturated during the peak emission of the pencil-lead break. Discerning a difference in the contact between the sensors was therefore difficult.

Based on the previous tests, the hit waveform parameters were modified. The length of each waveform was raised from 1024 sampling points to 2048 sampling points, in order to be certain to capture the entire waveform of the hit. Based on the experience of Test 5, the pre-trigger length was reduced to 128. The resulting waveform recordings were therefore of higher quality than for the previous tests. One drawback, however, was that due to the increased length, a larger part of the waveform consisted of the recorded continuous signal. Therefore, some parameters, such as RMS and the information entropies, were affected. The RMS of a waveform was obviously lower, since a larger percentage of the signal was the lower amplitude continuous signal. For the information entropies, the probability of achieving a higher voltage became lower, which should have resulted in higher entropy for these values. At the same time, there were more values, so the averaging effect would be higher.

A large source of potential issues for the hit-based approach was the threshold level used. Due to the significantly higher signal levels of the previous test, the initial threshold was set too high (36dB) for sensor 1. It was subsequently lowered in 1dB increments until a value of 29dB over the course of the first 200 seconds. It is likely that this level was also too high, since the continuous signal was only around half the amplitude of the threshold. But since the hit-production had started to ramp up at this point, lowering it further was thought to affect the results. Due to a higher signal level of the second sensor (Nano-30), the original threshold level of 36dB seemed alright, since the continuous signal was only slightly lower than this. Due to this erroneous threshold setting, a lot of low-amplitude AE was lost to the hit-based approach. Since it is assumed that the AE activity is related to the crack length or SIF, useful information is still obtained, since the amount of higher amplitude signals should scale over time, relative to the start. General trends in the data should

therefore still be visible. But the finer details related to the evolution of the continuous signal, such as dislocation movement in the plastic zone were most likely not visible in the hit-based approach. The relatively high threshold value might help explain some of the scatter seen during the Test for the count rates in section 5.3.2, since the less predictable strong burst signals account for a significant portion of the total hits. But at the same time, figure 192 shows that, at least for Test 4, raising the threshold from 36dB to 40dB in post-processing did not significantly alter the count rate curve. However, it is possible that this 4dB raise was not enough to significantly alter which mechanisms that could be detected.

A sign that could point towards a higher data quality of Test 6 compared to Test 4 and 5, is the presence of a nearly constantly present, yet oscillating frequency band around 400kHz in the streamed waveforms. The band is clearly visible in the acquisitions shown in figure 170. The presence of these oscillating bands is good, since it means that more than just the lower frequency resonances were activated. It seems reasonable that, while the continuous signal should have a similar frequency content, the exact frequencies that are present should not be constant, as the sources of the signal is an amalgam of signals (section 2.6.1).

5.3.2 Count rate versus FCG curves

This section discusses the AE count rate curves and parameters described in section 4.4.1.

From the figures in section 4.4.1 it is more or less clear that there is a linear relationship between the count rate and ΔK in the Paris regime. Unlike what is typically described in the literature[80; 99], the exponent n was found to be similar to the FCG exponent m . In Test 4, it was in fact exactly the same as found by IR measurements in section 4.2.6. This is in line with the claims of Bassim et al.; Roberts and Talebzadeh [134; 135] that for high R-ratios, the Paris exponent and count rate exponent should be close to equal. This

could be explained due to decreased closure effects for high R-ratios, which will reduce the amount of hits during the same amount of cycles, and thus reduce the count rate exponent, n . In Test 5, the value of the exponent was higher than for Test 4. Due to the scatter, there is great uncertainty in the true value, but one possible reason for the value obtained is the periodic introduction of zero load. Thus, the R-ratio was momentarily 0, which might have been enough to increase the effective count rate. In Test 6, the value of n was significantly lower than the previous tests. The cause of this is not entirely understood. It could in part be due to the large scatter in the data. By removing the last few points, as well as some of the largest count rate values obtained early in the test, it was possible to reach a value of $n = 3.305$. This shows that due to scatter, a few points can have a large influence.

As can be seen from figures 144, 146 and 147, there is significant scatter in the data, and which seems to increase in each test from Test 4 to Test 6. There are several possible causes of the effect. In part, this can be explained by the fact that the number of hits decreases for each test, from over 300 000 in Test 4, to around 80 000 per sensor in Test 5, and finally to 16 000 and 32 000 for sensor 1 and 2 in Test 6. Since there are fewer hits overall, anomalous hit production due to phenomena such as avalanche-like dislocation motion [63] will create large peaks and valleys in the hit production, seeing as there are fewer "steady" hits with which they would be averaged. This effect can clearly be seen from the curves of both Test 4 and Test 5. Comparing the count rate curve in figure 144, to the RMS versus cycles and ΔK in figure 156a, one can see a sudden increase in count rate right before ΔK reaches $15\text{MPa}\sqrt{\text{m}}$, which corresponds to the spike in RMS seen in figure 156a. Likewise, high count rates can be seen between $10\text{MPa}\sqrt{\text{m}}$ and $12\text{MPa}\sqrt{\text{m}}$, which corresponds to the spikes in RMS seen in the vicinity of 200 000 cycles in Test 5. Since the number of total hits in Test 4 was significantly greater than in Test 5, this could explain why, while the effect was visible in both count rate curves, the magnitude of the deviation was greater in Test 5. Another explanation related to the previous point, has to do with the time interval between each sample, and the intermittent nature of AE.

The count rate was calculated as the change in total hits divided by the change in cycle count between two crack length measurements (and therefore ΔK). Since AE can be produced in short, discrete bursts, this can lead to high count rates if the time between crack length measurements is short. Another cause seems to be related to the supposed emission source. In Test 4, the continuous signal began to cross the threshold value at a certain point, which cause the threshold to be increased. Even after compensating for this by removing hits with amplitudes corresponding to the previous threshold value, a lot of hits corresponded purely to the continuous signal, as exemplified in figure 193. Therefore, there was a steady source of hits proportional to the crack length, and possibly related to the SIF, were produced as seen in figure 194, which due to the averaging effect, reduced the scatter potentially created by sudden bursts of emissions.

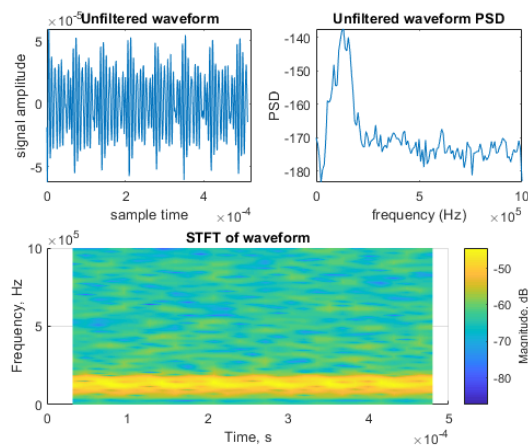


Figure 193: Noisy waveform with strong frequency peak

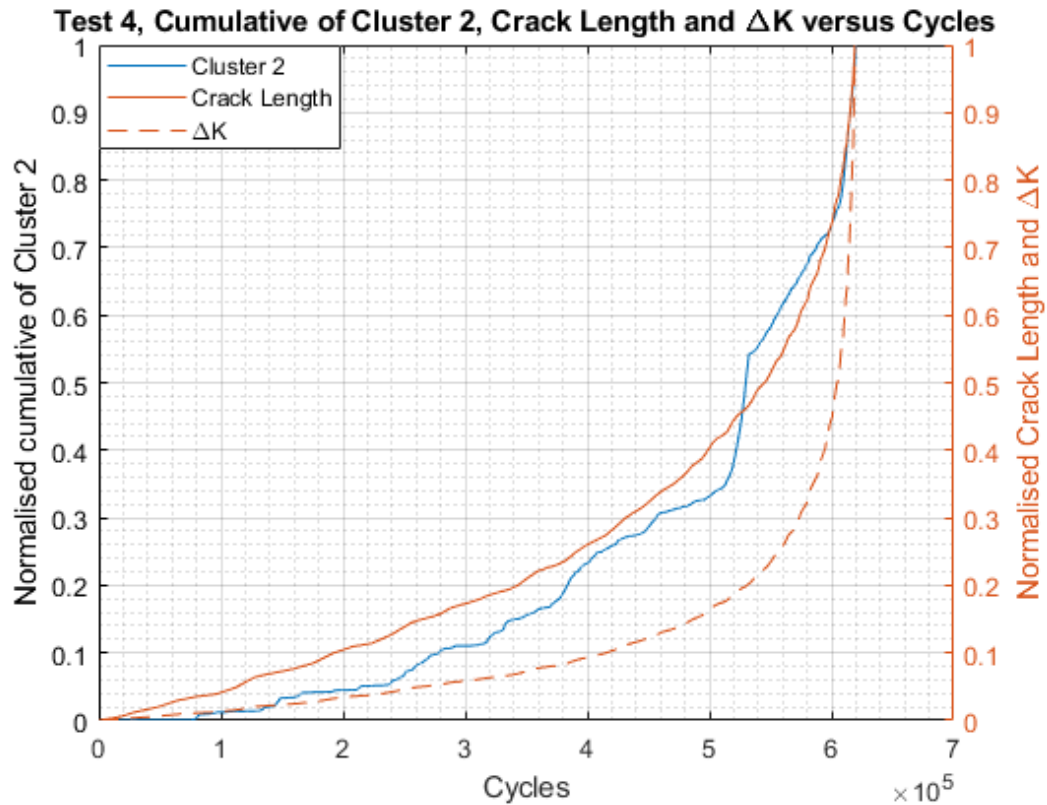


Figure 194: Close relationship between cluster 2 from Test 4 and crack length, ΔK

The fact that the hits were grouped together in groups corresponding to a crack length measurement is in itself a source of scatter, due to potential errors in the number of cycles corresponding to the hits and the crack length measurement, in addition to errors in the crack length measurement itself. The cycle count corresponding to a hit was calculated based on the timestamp in each hit filename; the time of each hit was compared to the time of the first hit. Since the tests were sometimes halted, this introduced errors which had to be manually corrected. This correction was not necessarily completely accurate. Since the hits were grouped together based on this cycle count compared to the cycle count of the crack length measurement, this might have caused erroneous grouping for some hits. Reducing this effect was part of the reason for using the mean counts as the primary method for calculating the count rate.

5.3.3 Signal Peaks in Stage II

Common to all tests was the presence of sudden spikes in signal strength occurring in regions expected to consist of steady crack growth, and for which none of the other methods showed any abnormalities. This region for Test 4 and Test 6 is highlighted in figure 195 for the case of hit waveform RMS, and is comparable to the rise in RMS seen in the streamed waveforms of figure 156a and 162.

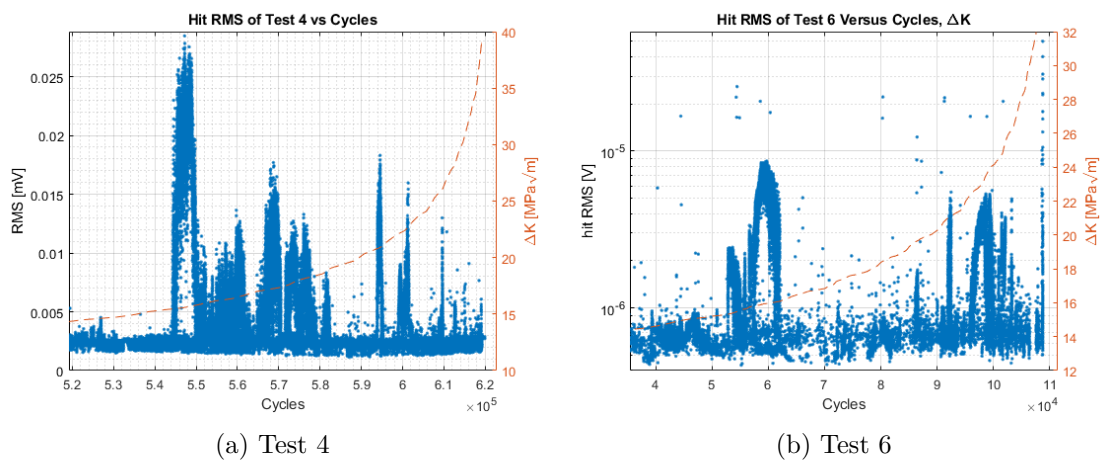


Figure 195: RMS of hit waveforms of Test 4 and Test 6 towards the end stages of each test

For both Test 4 and Test 6, the onset of this sharp increase in signal strength was at a ΔK of around $15\text{MPa}\sqrt{\text{m}}$, while for Test 5 it arose at a ΔK of about $10\text{MPa}\sqrt{\text{m}}$. A smaller scale rise in signal strength can be seen in the hit data from Test 4 at around $10\text{MPa}\sqrt{\text{m}}$ as well. This early peak was too brief to be captured by the waveform stream. Since Test 6 was pre-cracked until a large crack-length, any similar behaviour in the early Stage II cannot be determined for the test.

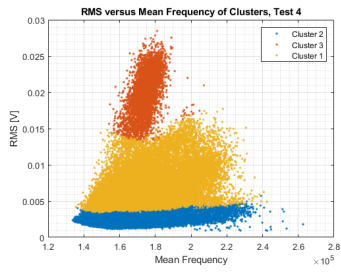
From the comparison between the RMS of the waveforms of full cycles versus the waveforms of only the top 20% load, it is clear that while the effect can be seen during the peak load, the majority of these peak signals occur during the lower loads. This is substantiated by the waveforms seen in figures 166,167,168,169,170 and 171. Large spikes in the voltage occurred most frequently during unloading, as can be seen in figure 166i, which corresponds

to the peak of figure 156a. It is therefore unlikely that most of these peaks correspond to AE generated due to crack propagation. Possible other sources of the signals must be considered, but the relatively short duration of the phenomenon makes it difficult to draw confident conclusions. The immediate assumption is that the signal is due to some closure effect. Based on the IRT and DIC results, this seems like it could explain the cyclic location of such signals as seen in figure 166i, 167a and 171b, which occurred at closure loads as determined by IRT and DIC. However, as can be seen, e.g. in figure 169b, many peaks occur around the mean load during the unloading stage. This is far above the closure loads as determined by IRT or DIC. There must therefore be another cause for these signals. It is possible that it was still related to crack closure, but due to friction between jagged crack surface edges contacting before large-scale closure occurred. Yet, this still does not explain why this behaviour was only present for limited times and roughly between a 50000 cycle interval. In this work, the fracture surfaces of the specimens were not analysed to any large degree. Without looking at the fracture surface it is difficult to support the jagged-edge hypothesis, as only the HSI image of the last test can view the crack edge. Another possibility is that the spikes are due to some resonance effect, but this would not account for why the occurrence was different in Test 5 compared to Test 4 and Test 6. At this moment there is not enough data to draw definite conclusions, and more work is therefore necessary. A clear next step is analysis of the fracture surfaces of each test, and compare them to the AE signals.

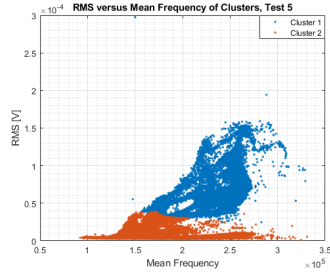
5.3.4 Clustering

The main purpose of performing clustering on the AE data, was to identify and categorise different signal sources, i.e. crack propagation mechanisms versus machine noise, and observe their development as the crack propagated. The clustering in this work was performed based on the k-means algorithm described in section 2.6.6. This choice was done based on its simplicity in terms of implementation, and its low processing time. This was necessary due to time constraints, but resulted in clusters which were less than ideal.

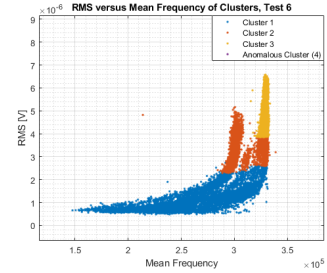
From a physical point of view, an immediate concern is the fact that each test had different number of clusters. Since each cluster was supposed to correspond to a unique source mechanism, this indicates a fault in the clustering. For example, Test 5 had only two clusters. If working perfectly, the continuous-like signals should then be separated from more burst-like signals, but separation of closure emissions from propagation emissions is not possible. Looking at the waveforms in figures 172, 174 and 176, together with the cumulatives in figures 173,175 and 178, some remarks can be made regarding the clusters. In Test 4, 3 clusters were identified. Cluster 2 seems to be consisting of continuous-like signals, almost solely consisting of a resonance frequency of the Nano-30 sensor. Clusters 1 and 3 are burst-type, and have similar time-stream representations, the only difference being the involvement of a higher frequency component in cluster 3. From the cumulative, it seems like Cluster 2 corresponds to the low-energy "base-line" signal. Cluster 3 consists purely of Stage II peaks identified near a SIF-range of $15\text{MPa}\sqrt{\text{m}}$. Cluster 1 consists of the early stage signal peak, and lower-amplitude peaks occurring in the Stage II peak region and into Stage III. However, looking at figure 197a or 198a it is obvious that there is a large degree of overlap between clusters, since the mean frequencies are wideband and as each cluster was plotted, it overlaid previous clusters. Another issue, then, is that the clusters are functionally just a rough separation based on energy content. The same behaviour can be seen for the other tests as well, meaning that it was not solely a problem due to using PSD as clustering criterion while using the resonant sensor, but due to the k-means method of clustering itself.



(a) RMS versus mean frequency of clusters in Test 4

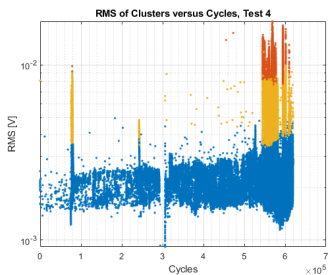


(b) RMS versus mean frequency of clusters in Test 5

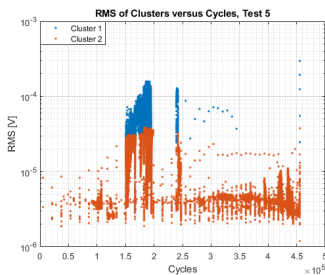


(c) RMS versus mean frequency of clusters in Test 6

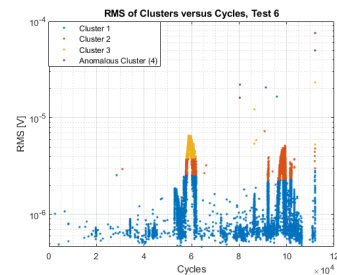
Figure 196: RMS versus mean frequency of the clusters from each test, showing that kmeans doesn't follow the evident contours



(a) RMS versus cycles of clusters in Test 4

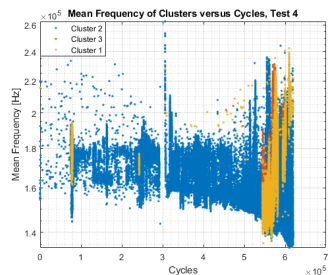


(b) RMS versus cycles of clusters in Test 5

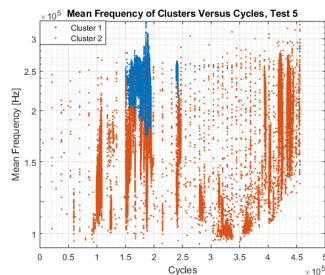


(c) RMS versus cycles of clusters in Test 6

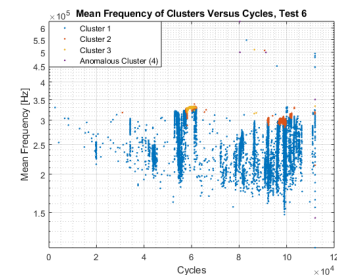
Figure 197: RMS versus cycles of the clusters from each test showing poor grouping



(a) Mean frequency versus cycles of clusters in Test 4



(b) Mean frequency versus cycles of clusters in Test 5



(c) Mean frequency versus cycles of clusters in Test 6

Figure 198: Mean frequency versus cycles of the clusters from each test

5.3.5 Transition From Stage II to Stage III

The primary interest for the project was to predict the transition from Stage II to Stage III of the FCG. Based on the parameters calculated from the hit-based waveforms and the analysis of the streamed waveforms, an attempt at establishing predictors of Stage III growth can be made. The clearest trend, and perhaps the most physically rooted one, is the change in waveform RMS as the crack is propagated. It can be seen for all tests that as Stage III approaches near the end of Stage II, the signal first rises and then falls. For Tests 4 and Test 6, where the waveform was streamed during Stage III, it can be seen that the signal rises very sharply upon reaching Stage III. Test 5, for which no streams were captured during Stage III experiences only the rise and fall of the signal RMS, seen in figures 159. However, looking at the signal energy from the hit waveforms in figure 157, one can observe the same behaviour in Test 5.

Due to the signal spikes discussed in section 5.3.3, it was of interest to see whether this rise-fall-rise behaviour was present only due to the effect of the closure emissions, or if it was a possibly crack growth related phenomenon. Figures 156b, 159b and 161b show that the same behaviour still occurred even when only the top 20% load is accounted for. Thus, it is likely also related to cyclic plasticity or crack propagation or both. The question is then what mechanisms are responsible for this behaviour.

As mentioned in section 2.5.2, the main sources of AE in ductile materials are related to dislocation-mediated plasticity, and it is therefore natural to approach the problem from the viewpoint of the cyclic plasticity. As the plastic zone is generated, AE is released due to mechanisms such as dislocation glide [65; 69]. Assume that the plastic zone has been already generated in the course of previous loading, and then the next cyclic load is applied. The established plastic zone has already been hardened, and dislocation movement inside the plastic zone is largely inhibited. As the crack is propagated slightly, the SIF increases slightly, and the crack front moves ahead. New unhardened material is thus exposed to plasticity, and dislocation motion occurs, resulting in new emissions. As the crack

propagates further and further, the area of the newly affected material should increase, resulting in, on average, increased dislocation motion and accordingly, the AE signal should be stronger. This could explain the slow rise in RMS as the crack propagates. From IRT and DIC analyses in previous sections, it is seen that the radius of the plastic zone appears to scale linearly with SIF. The change in the virgin plastic zone should then scale with the square of SIF, i.e. $4\Delta K^2$ for $R = 0.5$. Figure 199 shows that this simple assumption does not fully account for the the RMS peaking. This has multiple explanations. For one, using the RMS as a measure of the signal strength does not result in correct units. Additionally, the voltage is not necessarily directly proportional to the strength of the AE wave, and certainly not to the dislocations in motion. Leaving behind the quantitative considerations, and only considering an unknown, yet positive relation between the newly generated plastic zone and the RMS of the AE signal. As the crack advances, the region of plasticity expands. At some point when Stage III is approaching, the material might have experienced a sort of saturation of its capability for dislocation motion, reducing the signal strength. As the crack, and thus SIF-range, increased further, and the region of instability approached, the material lost its ability to contain the dislocations, suddenly releasing stronger AE signals. This is still highly speculative, and does not necessarily explain the behaviour seen by other parameters and the other methods.

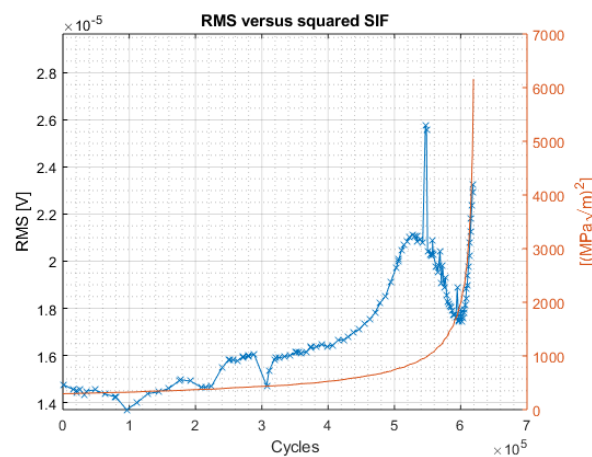


Figure 199: RMS and squared SIF versus cycles, Test 4

Expanding the analysis to include other parameters, more information might be obtained. Due to the stable signal composed of the lower-end resonance frequencies, the mean frequency of hits corresponding to these signals were expected to be distinguishable from those corresponding to wider-band signals, which were thought to be related to other mechanisms. From figure 196, 196 and 198, it is clear that the clusters are poor means of extending the analysis of the Stage II to Stage III transition, as they appear to be nearly purely a classification of energy. The spectral distribution, as characterised by their statistical moments, show no clear distinction between the clusters. Certain conclusions can still be drawn from comparisons of the data. There seems to be a general trend towards a wider distribution of the mean frequency as the crack grows, or as strong signals are generated. This indicates that there might be a difference in the mechanisms causing the AE. As discussed in section 5.3.4, the quality of the clusters was poor. This effect is therefore not captured very well by the clusters. However, there seems to be a certain correlation between signal strength and mean frequency, where the stronger signals tend to have a higher frequency content, especially for the Micro-F30 sensor. This indicates that the signals have significant activity in the higher frequency range, suggesting that the mechanisms causing the strongest signals are able to overcome an "activity valley", and thus are able to activate other frequencies than just the low-frequency resonances. However, this mean frequency behaviour is not consistent between the tests and sensors, and identifying the transition from stage II to stage III on this basis is difficult.

5.4 Comparison of the results

Following section discusses the agreement and reasons to eventual differences of the results obtained using different techniques.

5.4.1 DIC and IRT

Crack length measurements and crack growth curves

As figure 179 presents, there is close agreement between crack lengths measured using HSI and IRT camera. All the acquisitions were taken in the same moment with exception of the last point captured with the high-speed camera. The figure shows a deviation at the start of the test but it is due to the crack front not being perpendicular to the crack growth direction. As it can be seen in figure 180, there is a clear beachmark separating the precracking from the actual test. As the test went on, the crack front straightened up and deviation between the measurements reduced. The methods do in general agree well with each other.

The exponents m obtained from FCG curves are 3.377 (3.096, 3.659) for high-speed imaging and 2.909 (2.504, 3.315) for IR-camera for secant method used. For the incremental polynomial method the exponents were 3.530 (3.452, 3.607) for high-speed imaging and 3.079 (2.947, 3.221) for IR-camera. The difference in exponents and the fact that they are not in each others confidence bands may be also due to crack front angle. As the crack front occurs at an angle the methods will observe different crack lengths for the same growth rates. This is also visible in figure 179. In the calculations of ΔK , the different methods used their own data for crack growth calculations. If a common crack length would be used instead, the difference would have likely been reduced, but the change in crack front angle might still affect the results.

Plastic zone measurements

Figure 181 presents comparison of the theoretical plastic zone sizes with the values measured by both HSI and IRT camera. Westergaard solution (shown as the blue and green lines) show parabolic behaviour, this is due to equations 3 and 4, and the fact that $r_{pl} = \alpha(K_I/\sigma_{0.2\%})^2$, where α is numerical constant. The Williams' stress field shows a linear behaviour of the plastic zone size with respect to stress intensity factor, and so do

the measured values. For the precision of plastic zone measurements, DIC data seem to have noise affecting the shape of the contours, and therefore affecting the radius as discussed in section 5.2.4. IRT on the other hand does have less noisy data, but the method itself is based on some assumptions. The method calculates the stress amplitude, and divides it by $(1 - R)$ to find the maximum stresses. Crack closure will likely affect these results, but the measured closure was low, and was therefore assumed negligible. Corrections for closure might be however made, but the results seem reasonable, especially in figure 99, 102, and 105.

Effective SIF and crack closure

Figure 182 shows the measured crack closure. The data from DIC seem to have somehow more scatter than those measured by IRT, but the general agreement is very good. For tests 4 and 6 (figures 76b and 78b), where the closure was measured over a wider stress intensity range, the closure seemed to have increased again for larger stress intensity values which does not seem reasonable. A comparison with DIC should however be made before drawing any further conclusions, but the reason might be both due to the thermoelastic parameter, and the theoretical stress field used to calculate the value. This remains as further work. What is expected from literature [57] is that the P_{op} and thus crack closure level should decrease with increasing ΔK . However, the rate of crack closure decreasing is difficult to determine since the crack closure is a complex phenomenon as described in section 2.2.4. Even though the closure in tests 4 and 6 seem to increase in the end of the test, does not mean the calculation is wrong, as it does not measure the closure directly as DIC, but rather the effective stress intensity factor.

6 Conclusion and further work

6.1 Conclusion

The in-situ test setup designed within the project worked out well, even though it did require a lot of improvements in all experimental aspects in the beginning. The tuning done with the setup to make the test included: the common trigger system for the equipment, recognising the significance of insulating plastic bushings between the specimen and the grips, designing the AE sensor holders, galvanic insulation of the testing frame and the AE equipment by using the isolation auto-transformer, installing a motorised motion stage for the high speed camera, shielding from surroundings for the IR camera, optimising the speckle pattern on the specimen surface for the best DIC results. The experimental parameters including the test frequency, load ratio, and even the material selection, were made as a compromise to satisfy all of the sophisticated techniques used. It was possible to acquire data from all of the methods although the AE technique faced the most significant challenges caused, in general, by the choice of material - ductile hot rolled 316L steel generated the AE with the very low signal to noise ratio due to the ductile fracture mechanism.

IRT exhibited very promising results in many aspects related to the energetic approach to the crack growth. All of the acquired data were based on the same experimental setup. Every experiment consistently resulted in the reproducible fatigue crack growth curves, stress analysis of which lead to determination of both monotonic and cyclic plastic zone, stress analysis in the plastic zone, crack closure and effective stress intensity measurements, and energy dissipation. Additionally, the discrete Fourier analysis is also possible to perform on the same data. Most of these analysis did work really well, revealing the quantitative features of the fatigue crack growth curves, plastic zone size and stress distribution around the crack tip. Some other delicate issues such as crack closure require further investigation and validation, although the first results in this regard do look promising as well. Fur-

ther improvements are still awaiting in the discrete Fourier analysis and heat dissipation measurements.

RVI alone, or combined with the DIC showed promising results as well. The different results were obtained depending on the observation technique used. The images captured on the polished samples provided information about the crack growth rate, as well as the mechanism occurring during crack initiation, propagation, and final failure. The specimens prepared in order to be used in DIC analysis provided essential quantitative information about the strain, and stress fields, plastic zone, crack opening displacements, and thus crack closure, and enabled direct measuring of effective stress intensity factor. Although all the trials, and methods were successful with exception of capturing the final failure of the specimen, the quality of the obtained results is to be increased. The list of improvements is left as the further work.

AE obtained data from the hit-based method and waveform streaming. Some problems were encountered due to the resonant nature of the sensors' response, as well as other issues. AE count-rate curves were acquired for each test, in good agreement with previous researchers and crack growth curves from IRT and HSI/DIC data. Crack propagation mechanisms were attempted to be identified by using the k-means clustering procedure with a different level of success. The pronounced signal peaks were initiated between $10\text{MPa}\sqrt{\text{m}}$ and $15\text{MPa}\sqrt{\text{m}}$, which could possibly be an identifier of a transition between intermittent crack propagation and propagation for each loading cycle, but further study is necessary to confirm this. Waveforms and their PSD and STFT were calculated for both hits and streams, obtaining the time and frequency evolution of the signals. A promising, characteristic rise and fall in the signal energy has been identified as an indicator of the imminent stage III crack growth.

The test results obtained using IRT and HSI are quite comparable with regard to the crack growth rate, effective stress intensity factor, crack closure, and plastic zone size - the pivotal components in any LEFM analysis and fatigue design. The former three parameters showed excellent pairwise agreement, while for the plastic zone measurements, the general

trend agreed although the size of the plastic zone differed. This reflects the fact that the plastic zone is actually loosely defined in the LEFM, and, therefore, this poses new challenges to the LEFM foundations when those applied to structural materials.

6.2 Further work

Improvements for infrared thermography

The results from IRT were in general good, although some improvements still remain.

- Improvement of filtering and data analysis in stage III. This stage was captured, but at the moment, only qualitative analysis was done.
- Improve energy analysis. The main problem was that the dissipated heat, was too low in stage II. A higher frequency would likely increase the signal to noise ratio, but was not used due to the other techniques.
- Use a linear motion stage for the IR camera, just like that for the high speed camera. This will allow to make the adjustment of the camera automatic while testing. The data can potentially be analysed in real time while the camera's position is being software controlled. It would also allow to take precise reference pictures and improve the overall analysis.
- The Fourier analysis gave limited results due to lack of reference signal. Improving the trigger to also log the exact load signal at the same time the pictures are taken would improve the results. The analysis is very time consuming, and the region of interest is limited. Reducing the resolution, and the amount of cycles to analyse would likely increase the speed significantly.
- The crack closure measurements looked very good when compared to DIC, but in the region of the high stress intensity the closure increased again. This seem like a sort of error, but the DIC analysis did not capture it, so further inspection will be required to determine the reason causing it.

Improvements for the high speed camera

There are several improvements which remain as the further work.

- For the qualitative observation of stage III, there should be considered new experiments in order to capture the crack behaviour at the very last cycles before the fracture. Two different options are proposed: experiment with larger FOV which will avoid the loss of focus, or the experiment with equal, or smaller FOV that used in experiment. For reduced size of FOV, the automation of adjusting the focus should be considered.
- It has been found that the lens distortion is a severe issue strongly affecting the data when performing the DIC analysis. In future DIC attempts, this problem should be carefully examined.
- Calculation of the stress fields out of strain fields was carried out using plane-stress assumption, the trials using plane-strain conditions remain as further work. For a C(T) specimen with size as used in this work, a larger FOV for stress analysis with DIC should be considered as the plastic zone left the FOV in stage II during the test presented in this work.
- Correct determination of COD, and thus crack closure level is very sensitive to the assumed crack position, which was a challenge using DIC in this work. A new, or at least more efficient method for determination of a crack position should be considered in future attempts.
- The satisfactory speckle pattern used for DIC analysis was obtained using the etching. However, the influence of heavy etching on the sample was not investigated. In the future, this influence is to be investigated or a new way of creating the random pattern is to be proposed.
- A trials on calculating strain energy density using DIC should be performed.

Improvements for Acoustic Emission

While some useful data was obtained in this work, several improvements could be made in order to verify the existing results and refine some of the methods which were implemented.

- Fracture surfaces should be analysed using scanning electron microscope. This would allow for correlating AE signals to the features of the fracture surface, which could confirm hypotheses suggested in this work. It would also allow for more informed explanations of unexpected phenomena, such as the stage II signal spikes.
- More advanced clustering algorithms should be implemented. This will increase the quality of the clusters, and thus, the AE sources will be identified more clearly.
- More advanced time-frequency analysis should be performed. In this work, only STFT was used, which is inflexible due to the fixed time and frequency resolution. Using wavelets instead has the potential to reveal more information, and allow for more advanced analysis of the streamed data.
- Analysis based on decomposed streamed signals should be expanded. Decomposition is powerful for obtaining more quantitative data from the streams, and allows for comparison to, or replacing of traditional hit method.
- Tests with other loading and frequency parameters should be performed. A higher frequency will yield higher strain rates, and thus stronger AE. Testing other R-ratios would also be of interest, and would reveal the extent of closure effects on the signals.
- New tensile tests and FCG tests should be performed, with a focus on observing the necking and stage III. Comparison of the signal during necking and stage III could help determine the validity of the hypothesis proposed in section 5.1.8 regarding the parallel between necking instability and stage III instability.

General improvements

- Implement an option to trigger the equipment at given crack length intervals instead of cycle intervals.
- As mentioned, logging system for the load applied would in general give precise information about load for every method.
- When performing the tests in order to measure the crack closure, and the use of AE is not of interest, one could employ the clip-on gauge as additional method.

References

- [1] Hongli Gao, Zhaonian Zhang, Wei Jiang, Kaiyong Zhu, and Ao Gong. Deformation fields measurement of crack tip under high-frequency resonant loading using a novel hybrid image processing method. *Shock and Vibration*, 2018, 2018. ISSN 1070-9622. doi: 10.1155/2018/1928926. URL <https://www.hindawi.com/journals/sv/2018/1928926/>.
- [2] Marie Smith-Solbakken and Emil Aall Dahle. Alexander I. Kielland-ulykken – store norske leksikon, Jan 2019. URL https://snl.no/Alexander_I._Kielland-ulykken.
- [3] 1954 Great Britain. Court of Inquiry into the Accidents to Comet G-Alyp on 10th January, 1954 Comet G-Alyy on 8th April, Great Britain. Ministry of Transport, and Civil Aviation. *Civil aircraft accident : report of the court of inquiry into the accidents to comet G-ALYP on 10th January, 1954 and Comet G-ALYY on 8th April, 1954*. London : H.M.S.O, 1955. At head of title: Ministry of Transport and Civil Aviation.
- [4] R.C. Alderliesten and J.J. Homan. Fatigue and damage tolerance issues of glare in aircraft structures. *International Journal of Fatigue*, 28(10):1116 – 1123, 2006. ISSN 0142-1123. doi: <https://doi.org/10.1016/j.ijfatigue.2006.02.015>. URL <http://www.sciencedirect.com/science/article/pii/S0142112306000314>. The Third International Conference on Fatigue of Composites.
- [5] P Paris and F Erdogan. A critical analysis of crack propagation laws. *Journal of Basic Engineering*, 85:528–533, 1963. ISSN 0098-2202. doi: 10.1115/1.3656900. URL <http://dx.doi.org/10.1115/1.3656900>.
- [6] S. Suresh. *Fatigue of Materials*. Cambridge University Press, 2 edition, 1998. doi: 10.1017/CBO9780511806575.
- [7] M.L. Williams. On the stress distribution at the base of a stationary crack. *Journal of Applied Mechanics*, 24:109–114, 01 1957.
- [8] C.T. Sun and Z.-H. Jin. Chapter 3 - the elastic stress field around a crack tip. In C.T. Sun and Z.-H. Jin, editors, *Fracture Mechanics*, pages 25 – 75. Academic Press, Boston, 2012. ISBN 978-0-12-385001-0. doi: <https://doi.org/10.1016/B978-0-12-385001-0.00003-1>. URL <http://www.sciencedirect.com/science/article/pii/B9780123850010000031>.

- [9] Q Xiao and B.L. Karihaloo. Coefficients of the crack tip asymptotic field for a standard compact tension specimen. *International Journal of Fracture*, 118:1–15, 11 2002. doi: 10.1023/A:1022618930492.
- [10] P. Lukáš and L. Kunz †. Role of persistent slip bands in fatigue. *Philosophical Magazine*, 84(3-5): 317–330, 2004. doi: 10.1080/14786430310001610339. URL <https://doi.org/10.1080/14786430310001610339>.
- [11] Qingyuan Wang, Muhammad Kashif Khan, and Claude Bathias. Current understanding of ultra-high cycle fatigue. *Theoretical and Applied Mechanics Letters*, 2(3):031002, 2012. ISSN 2095-0349. doi: <https://doi.org/10.1063/2.1203102>. URL <http://www.sciencedirect.com/science/article/pii/S2095034915301434>.
- [12] G.E. Totten. Fatigue crack propagation. *Advanced Materials & Processes*, 166:39–41, 05 2008.
- [13] Wolf Elber. Fatigue crack closure under cyclic tension. *Engineering Fracture Mechanics*, 2(1):37–45, 1970. ISSN 0013-7944. doi: [https://doi.org/10.1016/0013-7944\(70\)90028-7](https://doi.org/10.1016/0013-7944(70)90028-7). URL <http://www.sciencedirect.com/science/article/pii/0013794470900287>.
- [14] W Elber. The significance of fatigue crack closure. *Damage Tolerance in Fatigue Aircraft Structures*, 486, 02 1971. doi: 10.1520/STP26680S.
- [15] Jim Lucas. What is infrared? *LiveScience*, 2015. URL <https://www.livescience.com/50260-infrared-radiation.html>.
- [16] Flir Systems. *The Ultimate Infrared Handbook for R&D Professionals*. Flir Systems, 2012. URL http://www.hoskin.ca/wp-content/uploads/2016/10/flir_thermal_camera_guide_for_research_professionals.pdf.
- [17] John D. Clayton. *Nonlinear Mechanics of Crystals*, chapter Thermoelasticity, pages 197–272. Springer Netherlands, Dordrecht, 2011. ISBN 978-94-007-0350-6. doi: 10.1007/978-94-007-0350-6_5. URL https://doi.org/10.1007/978-94-007-0350-6_5.
- [18] Minh Phong Luong. Fatigue limit evaluation of metals using an infrared thermographic technique. *Mechanics of Materials*, 28(1):155–163, 1998. ISSN 0167-6636. doi: [https://doi.org/10.1016/S0167-6636\(97\)00047-1](https://doi.org/10.1016/S0167-6636(97)00047-1). URL <http://www.sciencedirect.com/science/article/pii/S0167663697000471>.

- [19] Andrew L. Gyekenyesi and George Y. Baaklini. Thermoelastic stress analysis: The mean stress effect in metallic alloys. *The Journal of Strain Analysis for Engineering Design*, 33(2):93–104, 1998. doi: 10.1243/0309324981512841. URL <https://doi.org/10.1243/0309324981512841>.
- [20] A.K. Wong, R. Jones, and J.G. Sparrow. Thermoelastic constant or thermoelastic parameter? *Journal of Physics and Chemistry of Solids*, 48(8):749 – 753, 1987. ISSN 0022-3697. doi: [https://doi.org/10.1016/0022-3697\(87\)90071-0](https://doi.org/10.1016/0022-3697(87)90071-0). URL <http://www.sciencedirect.com/science/article/pii/0022369787900710>.
- [21] D.E. Oliver. Stress pattern analysis by thermal emission (spate). *Exper. Tech.; (United States)*, 12, 3 1988.
- [22] Behzad V. Farahani, Paulo J. Tavares, and P.M.G.P. Moreira. Sif determination with thermoelastic stress analysis. *Procedia Structural Integrity*, 2:2148 – 2155, 2016. ISSN 2452-3216. doi: <https://doi.org/10.1016/j.prostr.2016.06.269>. URL <http://www.sciencedirect.com/science/article/pii/S2452321616302803>. 21st European Conference on Fracture, ECF21, 20-24 June 2016, Catania, Italy.
- [23] Anastasia Iziumova, Alexei Vshivkov, Alexandr Prokhorov, Anastasia Kostina, and Oleg Plekhov. The study of energy balance in metals under deformation and failure process. *Quantitative InfraRed Thermography Journal*, 13(2):242–256, 2016. doi: 10 . 1080 / 17686733 . 2016 . 1212527. URL <https://doi.org/10.1080/17686733.2016.1212527>.
- [24] G. Meneghetti and M. Ricotta. Evaluating the heat energy dissipated in a small volume surrounding the tip of a fatigue crack. *International Journal of Fatigue*, 92:605 – 615, 2016. ISSN 0142-1123. doi: <https://doi.org/10.1016/j.ijfatigue.2016.04.001>. URL <http://www.sciencedirect.com/science/article/pii/S0142112316300494>. Fatigue crack paths 2015.
- [25] F. Ancona, R. De Finis, G.P. Demelio, U. Galietti, and D. Palumbo. Study of the plastic behavior around the crack tip by means of thermal methods. *Procedia Structural Integrity*, 2:2113 – 2122, 2016. ISSN 2452-3216. doi: <https://doi.org/10.1016/j.prostr.2016.06.265>. URL <http://www.sciencedirect.com/science/article/pii/S2452321616302761>. 21st European Conference on Fracture, ECF21, 20-24 June 2016, Catania, Italy.
- [26] G La Rosa and A Risitano. Thermographic methodology for rapid determination of the fatigue limit of materials and mechanical components. *International Journal of Fatigue*, 22(1):65 – 73, 2000. ISSN 0142-1123. doi: [https://doi.org/10.1016/S0142-1123\(99\)00088-2](https://doi.org/10.1016/S0142-1123(99)00088-2). URL <http://www.sciencedirect.com/science/article/pii/S0142112399000882>.

- [27] G. Meneghetti and M. Ricotta. The heat energy dissipated in a control volume to correlate the crack propagation rate in stainless steel specimens. *Frattura ed integrità strutturale*, 11(41), 2017. ISSN 1971-8993. doi: <https://doi.org/10.3221/IGF-ESIS.41.40>. URL <https://www.fracturae.com/index.php/fis/article/view/IGF-ESIS.41.40>.
- [28] Lovre Krstulović Opara. Application of thermography in analysis of fatigue strength of materials and structures. *HDKBR INFO Magazin*, 3(2):3–11, 2013. URL <https://hrcak.srce.hr/148795>.
- [29] A. Risitano and G. Risitano. Determining fatigue limits with thermal analysis of static traction tests. *Fatigue & Fracture of Engineering Materials & Structures*, 36(7):631–639, 2013. doi: 10.1111/ffe.12030. URL <https://onlinelibrary.wiley.com/doi/abs/10.1111/ffe.12030>.
- [30] F. A. Díaz, E. A. Patterson, R. A. Tomlinson, and J. R. Yates. Measuring stress intensity factors during fatigue crack growth using thermoelasticity. *Fatigue & Fracture of Engineering Materials & Structures*, 27(7):571–583, 2004. doi: 10.1111/j.1460-2695.2004.00782.x. URL <https://onlinelibrary.wiley.com/doi/abs/10.1111/j.1460-2695.2004.00782.x>.
- [31] F.A. Díaz, J.R. Yates, and E.A. Patterson. Some improvements in the analysis of fatigue cracks using thermoelasticity. *International Journal of Fatigue*, 26(4):365–376, 2004. ISSN 0142-1123. doi: <https://doi.org/10.1016/j.ijfatigue.2003.08.018>. URL <http://www.sciencedirect.com/science/article/pii/S0142112303002007>.
- [32] E. A. Schwarzkopf. Combining visual and numeric data to enhance understanding of fatigue and fracture properties and mechanisms. *Application of Automation Technology in Fatigue and Fracture Testing and Analysis*, pages 153–162, 2014. doi: 10.1520/STP157120130086. URL <https://doi.org/10.1520/STP157120130086>.
- [33] H. Z. Xing, Q. B. Zhang, C. H. Braithwaite, B. Pan, and J. Zhao. High-speed photography and digital optical measurement techniques for geomaterials: Fundamentals and applications. *Rock Mechanics and Rock Engineering*, 50(6):1611–1659, Jun 2017. ISSN 1434-453X. doi: 10.1007/s00603-016-1164-0. URL <https://doi.org/10.1007/s00603-016-1164-0>.
- [34] P W W Fuller. An introduction to high speed photography and photonics. *The Imaging Science Journal*, 57(6):293–302, 2009. ISSN 1368-2199.
- [35] Peter W.W. Fuller. High-speed cinematography. In Michael R. Peres, editor, *The Focal Encyclopedia of Photography (Fourth Edition)*, pages 539–543. Focal Press, Boston, fourth edition edition, 2007. ISBN 978-0-240-80740-9. doi: <https://doi.org/10.1016/B978-0-240-80740-9.50106-9>. URL <https://www.sciencedirect.com/science/article/pii/B9780240807409501069>.

- [36] Stanford Computer Optics. <https://stanfordcomputeroptics.com/products/iccd-framing-camera.html>, 2018.
- [37] P. L. Reu and T. J. Miller. The application of high-speed digital image correlation. *The Journal of Strain Analysis for Engineering Design*, 43(8):673–688, 2008. doi: 10.1243/03093247JSA414. URL <https://doi.org/10.1243/03093247JSA414>.
- [38] Bud R. and Warner D. *Instruments of Science: An Historical Encyclopedia*. Routledge, 1 edition, 1997. ISBN 9780815315612.
- [39] A E Huston. High-speed photography and photonic recording. *Journal of Physics E:Scientific Instruments*, 11(7):601–609, july 1978. doi: 10.1088/0022-3735/11/7/001.
- [40] Yang Ju, Heping Xie, Xi Zhao, Lingtao Mao, Zhangyu Ren, Jiangtao Zheng, Fu-Pen Chiang, Yongliang Wang, and Feng Gao. Visualization method for stress-field evolution during rapid crack propagation using 3d printing and photoelastic testing techniques. In *Scientific Reports*, 2018. doi: 10.1038/s41598-018-22773-0. URL <https://www.nature.com/articles/s41598-018-22773-0>.
- [41] F Yusof and P J Withers. Real-time acquisition of fatigue crack images for monitoring crack-tip stress intensity variations within fatigue cycles. *The Journal of Strain Analysis for Engineering Design*, 44(2):149–158, 2009. doi: 10.1243/03093247JSA440. URL <https://doi.org/10.1243/03093247JSA440>.
- [42] Wendelin J. Wright, Rachel R. Byer, and Xiaojun Gu. High-speed imaging of a bulk metallic glass during uniaxial compression. *Applied Physics Letters*, 102(24):241920, 2013. doi: 10.1063/1.4811744. URL <https://doi.org/10.1063/1.4811744>.
- [43] Shaofeng Sun, Xiying Chen, Nilesh Badwe, and Karl Sieradzki. Potential-dependent dynamic fracture of nanoporous gold. *Nature Materials*, 14(9):894–898, 09 2015. URL <https://search.proquest.com/docview/1767089379?accountid=12870>.
- [44] L.Y. Yang, Q. Sun, X.N. Zhao, and Y.B. Wang. Experimental study on wing crack behaviours in dynamic-static superimposed stress field using caustics and high-speed photography. *Journal of Engineering Science and Technology Review*, 7(3):17–23, 2014. ISSN 17919320.
- [45] Ralph Jacobson. *The manual of photography : photographic and digital imaging.*, 2000.
- [46] J. S. Courtney-Pratt. A review of the methods of high-speed photography. *Reports on Progress in Physics*, 20(1):379–432, 1957. ISSN 0034-4885.

- [47] Stellan Hertegård, Hans Larsson, and Thomas Wittenberg. High-speed imaging: applications and development. *Logopedics Phoniatrics Vocology*, 28(3):133–139, 2003. doi: 10.1080/14015430310015246. URL <https://doi.org/10.1080/14015430310015246>.
- [48] Madhu S. Kirugulige, Hareesh V. Tippur, and Thomas S. Denney. Measurement of transient deformations using digital image correlation method and high-speed photography: application to dynamic fracture. *Appl. Opt.*, 46(22):5083–5096, Aug 2007. doi: 10.1364/AO.46.005083. URL <http://ao.osa.org/abstract.cfm?URI=ao-46-22-5083>.
- [49] Sidney Ray. Chapter 6 - photographic and geometrical optics. In Elizabeth Allen and Sophie Triantaphillidou, editors, *The Manual of Photography (Tenth Edition)*, pages 103 – 117. Focal Press, Oxford, tenth edition edition, 2011. ISBN 978-0-240-52037-7. doi: <https://doi.org/10.1016/B978-0-240-52037-7.10006-7>. URL <http://www.sciencedirect.com/science/article/pii/B9780240520377100067>.
- [50] L. N. Y Wong and H. H Einstein. Using high speed video imaging in the study of cracking processes in rock. *Geotechnical Testing Journal*, 32(2):1–17, 2009. ISSN 0149-6115.
- [51] M. Seleznev and A. Vinogradov. Note: High-speed optical imaging powered by acoustic emission triggering. *Review of Scientific Instruments*, 85(7):076103, 2014. doi: 10.1063/1.4890436. URL <https://doi.org/10.1063/1.4890436>.
- [52] Nick McCormick and Jerry Lord. Digital image correlation. *Materials Today*, 13(12):52 – 54, 2010. ISSN 1369-7021. doi: [https://doi.org/10.1016/S1369-7021\(10\)70235-2](https://doi.org/10.1016/S1369-7021(10)70235-2). URL <http://www.sciencedirect.com/science/article/pii/S1369702110702352>.
- [53] J. Blaber, B. Adair, and A. Antoniou. Ncorr: Open-source 2d digital image correlation matlab software. *Experimental Mechanics*, 55(6):1105–1122, Jul 2015. ISSN 1741-2765. doi: 10.1007/s11340-015-0009-1. URL <https://doi.org/10.1007/s11340-015-0009-1>.
- [54] Bing Pan, Huimin Xie, and Zhaoyang Wang. Equivalence of digital image correlation criteria for pattern matching. *Appl. Opt.*, 49(28):5501–5509, Oct 2010. doi: 10.1364/AO.49.005501. URL <http://ao.osa.org/abstract.cfm?URI=ao-49-28-5501>.
- [55] H Lu and P D. Cary. Deformation measurements by digital image correlation: Implementation of a second-order displacement gradient. *Experimental Mechanics*, 40:393–400, 12 2000. doi: 10.1007/BF02326485.

- [56] D. A. Crump, J. M. Dulieu-Barton, and R. K. Fruehmann. Challenges in synchronising high speed full-field temperature and strain measurement. In *Thermomechanics and Infra-Red Imaging, Volume 7*, pages 1–7, New York, NY, 2011. Springer New York. ISBN 978-1-4614-0207-7.
- [57] J. Tong, S. Alshammrei, T. Wigger, C. Lupton, and J.R. Yates. Full-field characterization of a fatigue crack: Crack closure revisited. *Fatigue & Fracture of Engineering Materials & Structures*, 41(10):2130–2139, 2017. doi: 10.1111/ffe.12769. URL <https://onlinelibrary.wiley.com/doi/abs/10.1111/ffe.12769>.
- [58] James M. N. Christopher C. J. Patterson-E. A. Díaz F. A. Vasco-Olmo, J. M. Deformation fields measurement of crack tip under high-frequency resonant loading using a novel hybrid image processing method. *Fatigue and Fracture of Engineering Materials and Structures*, 39:969–981, 2016. ISSN 8756-758X. doi: doi:10.1111/ffe.12436. URL <https://doi.org/10.1111/ffe.12436>.
- [59] James M. N. Díaz F. A. Antunes-F.V. Vasco-Olmo, J. M. Experimental evaluation of ctod in constant amplitude fatigue crack growth from crack tip displacement fields. *Frattura ed Integrità Strutturale*, 11:157 – 165, 2017. doi: <http://dx.doi.org/10.3221/IGF-ESIS.41.22>. URL <http://hdl.handle.net/10026.1/10506>.
- [60] J. Hosdez, J-F. Witz, C. Martel, N. Limodin, D. Najjar, E. Charkaluk, P. Osmond, and F. Szmytka. Fatigue crack growth law identification by digital image correlation and electrical potential method for ductile cast iron. *Engineering Fracture Mechanics*, 182:577 – 594, 2017. ISSN 0013-7944. doi: <https://doi.org/10.1016/j.engfracmech.2017.05.037>. URL <https://www.sciencedirect.com/science/article/pii/S001379441630515X>.
- [61] G. L. G. Gonzáles, J. A. O. González, J. T. P. Castro, and J. L. F. Freire. Detecting fatigue crack closure and crack growth delays after an overload using dic measurements. In Jay Carroll, Shuman Xia, Alison M. Beese, Ryan B. Berke, and Garrett J Pataky, editors, *Fracture, Fatigue, Failure and Damage Evolution, Volume 7*, pages 57–65, Cham, 2018. Springer International Publishing. ISBN 978-3-319-62831-8.
- [62] Joel Leong, Michael Brady, and J O'D McGee. Correction of uneven illumination (vignetting) in digital microscopy images. *Journal of clinical pathology*, 56:619–21, 09 2003. doi: 10.1136/jcp.56.8.619.
- [63] Kristián Máthis and František Chmelík. Exploring plastic deformation of metallic materials by the acoustic emission technique. In Wojciech Sikorski, editor, *Acoustic Emission*, chapter 2. IntechOpen, Rijeka, 2012. doi: 10.5772/31660. URL <https://doi.org/10.5772/31660>.

- [64] B.A. Auld. *Acoustic fields and waves in solids*. A Wiley-Interscience publication. Wiley, 1973. ISBN 9785885013437. URL https://books.google.no/books?id=_2MWAwAAQBAJ.
- [65] C. R. Heiple and S. H. Carpenter. Acoustic emission produced by deformation of metals and alloys - a review. part 1. *Journal of Acoustic Emission*, 6:177–204, sep 1987. URL https://www.aewg.org/jae/JAE-Vol_06-1987.pdf.
- [66] Haiyan Li, Jianying Li, Xiaozhou Liu, and Alex Fok. Non-destructive examination of interfacial debonding in dental composite restorations using acoustic emission. In Ning Hu, editor, *Composites and Their Applications*, chapter 7. IntechOpen, Rijeka, 2012. doi: 10.5772/51369. URL <https://doi.org/10.5772/51369>.
- [67] Hajime Hatano. Quantitative measurements of acoustic emission related to its microscopic mechanisms. *The Journal of the Acoustical Society of America*, 57(3):639–645, 1975. doi: 10.1121/1.380480. URL <https://doi.org/10.1121/1.380480>.
- [68] K. Ono, H. Cho, and M. Takuma. The origin of continuous emissions. *Journal of Acoustic Emission*, 23:206–214, 2005. URL https://www.aewg.org/jae/JAE-Vol_23-2005.pdf.
- [69] C. R. Heiple and S. H. Carpenter. Acoustic emission produced by deformation of metals and alloys - a review. part 2. *Journal of Acoustic Emission*, 6:215–237, December 1987. URL https://www.aewg.org/jae/JAE-Vol_06-1987.pdf.
- [70] K. Ono. Current understanding of mechanisms of acoustic emission. *The Journal of Strain Analysis for Engineering Design*, 40(1):1–15, 2005. doi: 10.1243/030932405X7674. URL <https://doi.org/10.1243/030932405X7674>.
- [71] Physical Acoustics Corporation. *PCI-2 based AE system user's manual*. Physical Acoustics Corporation, 195 Clarksville Road, Princeton Jct., NJ 08550-5303, 2 edition, 10 2004.
- [72] Manindra R. Kaphle. *Analysis of acoustic emission data for accurate damage assessment for structural health monitoring applications*. PhD thesis, Queensland University of Technology, 2012. URL <https://eprints.qut.edu.au/53201/>.
- [73] A. Danyuk, I. Rastegaev, E. Pomponi, M. Linderov, D. Merson, and A. Vinogradov. Improving of acoustic emission signal detection for fatigue fracture monitoring. *Procedia Engineering*, 176:284 – 290, 2017. ISSN 1877-7058. doi: <https://doi.org/10.1016/j.proeng.2017.02.323>. URL <https://www.sciencedirect.com/science/article/pii/S1877705817308329>. Proceedings

of the 3rd International Conference on Dynamics and Vibroacoustics of Machines (DVM2016) June 29–July 01, 2016 Samara, Russia.

- [74] Physical Acoustics Corporation. Aewin, 2018.
- [75] Darrell R. James and Steve H. Carpenter. Relationship between acoustic emission and dislocation kinetics in crystalline solids. *Journal of Applied Physics*, 42(12):4685–4697, 1971. doi: 10.1063/1.1659840. URL <https://doi.org/10.1063/1.1659840>.
- [76] N. Kiewewetter and P. Schuller. The acoustic emission from moving dislocations in aluminium. *physica status solidi (a)*, 38(2):569–576, 1976. doi: 10.1002/pssa.2210380218. URL <https://onlinelibrary.wiley.com/doi/abs/10.1002/pssa.2210380218>.
- [77] John Douglas Eshelby. The interaction of kinks and elastic waves. *Proceedings of the Royal Society of London A: Mathematical, Physical and Engineering Sciences*, 266(1325):222–246, 1962. ISSN 0080-4630. doi: 10.1098/rspa.1962.0058. URL <http://rspa.royalsocietypublishing.org/content/266/1325/222>.
- [78] S. H. Carpenter and C. M. Chen. The acoustic emission generated during the plastic deformation of high purity zinc. *Journal of Acoustic Emission*, 7:161–166, oct 1988. URL https://www.aewg.org/jae/JAE-Vol_07-1988.pdf.
- [79] N. Thompson and D.J. Millard. Xxxviii. twin formation, in cadmium. *The London, Edinburgh, and Dublin Philosophical Magazine and Journal of Science*, 43(339):422–440, 1952. doi: 10.1080/14786440408520175. URL <https://doi.org/10.1080/14786440408520175>.
- [80] T.C. Lindley, I.G. Palmer, and C.E. Richards. Acoustic emission monitoring of fatigue crack growth. *Materials Science and Engineering*, 32(1):1 – 15, 1978. ISSN 0025-5416. doi: [https://doi.org/10.1016/0025-5416\(78\)90206-9](https://doi.org/10.1016/0025-5416(78)90206-9). URL <https://www.sciencedirect.com/science/article/pii/0025541678902069>.
- [81] Z.F Wang, J Li, W Ke, and Z Zhu. Characteristics of acoustic emission for a537 structural steel during fatigue crack propagation. *Scripta Metallurgica et Materialia*, 27(5):641 – 646, 1992. ISSN 0956-716X. doi: [https://doi.org/10.1016/0956-716X\(92\)90354-H](https://doi.org/10.1016/0956-716X(92)90354-H). URL <https://www.sciencedirect.com/science/article/pii/0956716X9290354H>.
- [82] Adrian A. Pollock. Material brittleness and the energetics of acoustic emission. In Tom Proulx, editor, *Experimental Mechanics on Emerging Energy Systems and Materials, Volume 5*, pages 73–79, New York, NY, 2011. Springer New York. ISBN 978-1-4419-9798-2.

- [83] T.M. Morton, R.M. Harrington, and J.G. Bjeletich. Acoustic emissions of fatigue crack growth. *Engineering Fracture Mechanics*, 5(3):691 – 697, 1973. ISSN 0013-7944. doi: [https://doi.org/10.1016/0013-7944\(73\)90047-7](https://doi.org/10.1016/0013-7944(73)90047-7). URL <https://www.sciencedirect.com/science/article/pii/0013794473900477>.
- [84] T. M. Morton, S. Smith, and R. M. Harrington. Effect of loading variables on the acoustic emissions of fatigue-crack growth. *Experimental Mechanics*, 14(5):208–213, May 1974. ISSN 1741-2765. doi: 10.1007/BF02323071. URL <https://doi.org/10.1007/BF02323071>.
- [85] Kanji Ono. Acoustic emission in materials research – a review. *Journal of acoustic emission*, 29, 01 2011.
- [86] V. Moorthy, T. Jayakumar, and Baldev Raj. Influence of micro structure on acoustic emission behavior during stage 2 fatigue crack growth in solution annealed, thermally aged and weld specimens of aisi type 316 stainless steel. *Materials Science and Engineering: A*, 212(2):273 – 280, 1996. ISSN 0921-5093. doi: [https://doi.org/10.1016/0921-5093\(96\)10206-9](https://doi.org/10.1016/0921-5093(96)10206-9). URL <http://www.sciencedirect.com/science/article/pii/0921509396102069>.
- [87] G. T. Hahn, R. G. Hoagland, and A. R. Rosenfield. Local yielding attending fatigue crack growth. *Metallurgical Transactions*, 3(5):1189–1202, May 1972. ISSN 1543-1916. doi: 10.1007/BF02642452. URL <https://doi.org/10.1007/BF02642452>.
- [88] Z.F. Wang, J. Li, W. Ke, Y.S. Zheng, Z. Zhu, and Z.G. Wang. Acoustic emission monitoring of fatigue crack closure. *Scripta Metallurgica et Materialia*, 27(5):1691 – 1694, 1992.
- [89] R.O. Ritchie. Mechanisms of fatigue-crack propagation in ductile and brittle solids. *International Journal of Fracture*, 100(1):55–83, Nov 1999. ISSN 1573-2673. doi: 10.1023/A:1018655917051. URL <https://doi.org/10.1023/A:1018655917051>.
- [90] Avraham Berkovits and Daining Fang. Study of fatigue crack characteristics by acoustic emission. *Engineering Fracture Mechanics*, 51(3):401 – 416, 1995. ISSN 0013-7944. doi: [https://doi.org/10.1016/0013-7944\(94\)00274-L](https://doi.org/10.1016/0013-7944(94)00274-L). URL <https://www.sciencedirect.com/science/article/pii/001379449400274L>.
- [91] H. Chang, E.H. Han, J.Q. Wang, and W. Ke. Acoustic emission study of fatigue crack closure of physical short and long cracks for aluminum alloy ly12cz. *International Journal of Fatigue*, 31(3): 403 – 407, 2009. ISSN 0142-1123. doi: <https://doi.org/10.1016/j.ijfatigue.2008.08.008>. URL <http://www.sciencedirect.com/science/article/pii/S0142112308002119>.

- [92] J.A. Pascoe, D.S. Zarouchas, R.C. Alderliesten, and R. Benedictus. Using acoustic emission to understand fatigue crack growth within a single load cycle. *Engineering Fracture Mechanics*, 194: 281 – 300, 2018. ISSN 0013-7944. doi: <https://doi.org/10.1016/j.engfracmech.2018.03.012>. URL <http://www.sciencedirect.com/science/article/pii/S0013794417306847>.
- [93] JA Simmons and HNB Wadley. Theory of acoustic emission from phase transformations. *JOURNAL OF RESEARCH of the National Bureau of Standards*, 89(1):55–64, 1984.
- [94] A Mateo, G Fargas, and A Zapata. Martensitic transformation during fatigue testing of an aisi 301ln stainless steel. In *IOP Conference Series: Materials Science and Engineering*, volume 31, page 012010. IOP Publishing, 2012.
- [95] Zhen-zhong Yu and Philip C. Clapp. Quantitative analysis of acoustic emission signals. *Journal of Applied Physics*, 62(6):2212–2220, 1987. doi: 10.1063/1.339525. URL <https://doi.org/10.1063/1.339525>.
- [96] Zi-long Zhou, Jing Zhou, Longjun Dong, Xin Cai, Yi-chao Rui, and Chang-tao Ke. Experimental study on the location of an acoustic emission source considering refraction in different media. *Scientific Reports*, 7, 2017. URL <https://doi.org/10.1038/s41598-017-07371-w>.
- [97] Ki-Bok Kim, Dong-Jin Yoon, Jung-Chae Jeong, and Seung-Seok Lee. Determining the stress intensity factor of a material with an artificial neural network from acoustic emission measurements. *NDT & E International*, 37:423–429, 09 2004.
- [98] Mengyu Chai, Jin Zhang, Zaoxiao Zhang, Quan Duan, and Guangxu Cheng. Acoustic emission studies for characterization of fatigue crack growth in 316ln stainless steel and welds. *Applied Acoustics*, 126:101 – 113, 2017. ISSN 0003-682X. doi: <https://doi.org/10.1016/j.apacoust.2017.05.014>. URL <http://www.sciencedirect.com/science/article/pii/S0003682X17304577>.
- [99] Mengyu Chai, Zaoxiao Zhang, Quan Duan, and Yan Song. Assessment of fatigue crack growth in 316ln stainless steel based on acoustic emission entropy. *International Journal of Fatigue*, 109:145 – 156, 2018. ISSN 0142-1123. doi: <https://doi.org/10.1016/j.ijfatigue.2017.12.017>. URL <http://www.sciencedirect.com/science/article/pii/S0142112317304644>.
- [100] Farhan Tanvir, Tariq Sattar, David Mba, Graham Edwards, Elvin Eren, and Yoann Lage. Identification of fatigue damage evolution in 316l stainless steel using acoustic emission and digital image correlation. *MATEC Web of Conferences*, 165:22007, 01 2018.

- [101] Dongxin Xu and Deniz Erdogmus. *Renyi's Entropy, Divergence and Their Nonparametric Estimators*, pages 47–102. Springer New York, New York, NY, 2010. ISBN 978-1-4419-1570-2. doi: 10.1007/978-1-4419-1570-2_2. URL https://doi.org/10.1007/978-1-4419-1570-2_2.
- [102] E. Beadle, J. Schroeder, B. Moran, and S. Suvorova. An overview of renyi entropy and some potential applications. In *2008 42nd Asilomar Conference on Signals, Systems and Computers*, pages 1698–1704, Oct 2008. doi: 10.1109/ACSSC.2008.5074715.
- [103] Md Yeasin Bhuiyan, Jingjing Bao, Banibrata Poddar, and Victor Giurgiutiu. Toward identifying crack-length-related resonances in acoustic emission waveforms for structural health monitoring applications. *Structural Health Monitoring*, 17(3):577–585, 2018. doi: 10.1177/1475921717707356. URL <https://doi.org/10.1177/1475921717707356>.
- [104] Y. Zhang, X. Huang, S. Li, and X. Liu. Spectral character analysis of sandstone under saturation condition in rupture procedure. *Yantu Lixue/Rock and Soil Mechanics*, 34(6):1574–1578, 2013.
- [105] P. Welch. The use of fast fourier transform for the estimation of power spectra: A method based on time averaging over short, modified periodograms. *IEEE Transactions on Audio and Electroacoustics*, 15(2):70–73, June 1967. ISSN 0018-9278. doi: 10.1109/TAU.1967.1161901.
- [106] T.F. Quatieri. *Discrete-time Speech Signal Processing: Principles and Practice*. Prentice-Hall signal processing series. Prentice Hall PTR, 2002. ISBN 9780132429429.
- [107] Wikimedia Commons. Stft windows, 2005. URL https://en.wikipedia.org/wiki/Short-time_Fourier_transform/media/File:STFT_-_windows.png.
- [108] Alexei Vinogradov, Dmitry Orlov, Alexei Danyuk, and Yuri Estrin. Effect of grain size on the mechanisms of plastic deformation in wrought mg–zn–zr alloy revealed by acoustic emission measurements. *Acta Materialia*, 61(6):2044 – 2056, 2013. ISSN 1359-6454. doi: <https://doi.org/10.1016/j.actamat.2012.12.024>. URL <http://www.sciencedirect.com/science/article/pii/S1359645412008828>.
- [109] D. Gagar, P. Foote, and P.E. Irving. Effects of loading and sample geometry on acoustic emission generation during fatigue crack growth: Implications for structural health monitoring. *International Journal of Fatigue*, 81:117 – 127, 2015. ISSN 0142-1123. doi: <https://doi.org/10.1016/j.ijfatigue.2015.07.024>. URL <http://www.sciencedirect.com/science/article/pii/S014211231500242X>.


- [110] B.S. Everitt, S. Landau, M. Leese, and D. Stahl. *Cluster Analysis*. Wiley Series in Probability and Statistics. Wiley, 2011. ISBN 9780470749913.
- [111] David Arthur and Sergei Vassilvitskii. K-means++: The advantages of careful seeding. In *Proceedings of the Eighteenth Annual ACM-SIAM Symposium on Discrete Algorithms*, SODA '07, pages 1027–1035, Philadelphia, PA, USA, 2007. Society for Industrial and Applied Mathematics. ISBN 978-0-898716-24-5. URL <http://dl.acm.org/citation.cfm?id=1283383.1283494>.
- [112] M. Kharrat, E. Ramasso, V. Placet, and M.L. Boubakar. A signal processing approach for enhanced acoustic emission data analysis in high activity systems: Application to organic matrix composites. *Mechanical Systems and Signal Processing*, 70-71:1038 – 1055, 2016. ISSN 0888-3270. doi: <https://doi.org/10.1016/j.ymssp.2015.08.028>. URL <http://www.sciencedirect.com/science/article/pii/S0888327015003908>.
- [113] E8/E8M-16a. Standard test methods for tension testing of metallic materials. Standard E8/E8M-16a, ASTM International, West Conshohocken, PA, 2016. URL https://doi.org/10.1520/E0008_E0008M-16A.
- [114] E647-15e1. Standard test method for measurement of fatigue crack growth rates. Standard E647-15e1, ASTM International, West Conshohocken, PA, 2015. URL <https://doi.org/10.1520/E0647-15E01>.
- [115] E407-07(2015)e1. Standard practice for microetching metals and alloys. Standard E407-07(2015)e1, ASTM International, West Conshohocken, PA, 2015. URL <https://doi.org/10.1520/E0407-07R15E01>.
- [116] Hisao Fukui, Jiro Hasegawa, Kuniji Ichida, and Teiichi Ohkouchi. Video tracking of a fatigue crack with a long distance microscope. *Japanese Journal of Applied Physics*, 30(4R):886, 1991. URL <https://stacks.iop.org/1347-4065/30/i=4R/a=886>.
- [117] R Harilal and M Ramji. Adaptation of open source 2d dic software ncorr for solid mechanics applications. *Conference: 9th International Symposium on Advanced Science and Technology in Experimental Mechanics, At New Delhi, India Cite this publication*, 11 2014. doi: 10.13140/2.1.4994.1442.
- [118] Ncorr Open source 2D digital image correlation MATLAB software. <http://www.ncorr.com/index.php>, 2019. Accessed: 2019-05-02.

- [119] V. Nežerka, J. Antoš, J. Litoš, P. Tesárek, and J. Zeman. An integrated experimental-numerical study of the performance of lime-based mortars in masonry piers under eccentric loading. *Construction and Building Materials*, 114:913 – 924, 2016. ISSN 0950-0618. doi: <https://doi.org/10.1016/j.conbuildmat.2016.04.013>. URL <http://www.sciencedirect.com/science/article/pii/S0950061816305517>.
- [120] The MathWorks. *MATLAB and Computer Vision System Toolbox Release 2018B*. The MathWorks, Inc., Natick, Massachusetts, United States., 2018.
- [121] Bell K. *Konstruksjonsmekanikk (Del II: fasthetslære)*. Fagbokforlaget, 1 edition, 2015. ISBN 9788245018486.
- [122] H.L. Dunegal. Modal analysis of acoustic emission signals. *DECI NEWSLETTERS AND REPORTS*, 1997. URL http://cdn.scoreltd.com/pdf/technical-reports/atlanta/modal_analysis_ae_signals.pdf.
- [123] Eraldo Pomponi and Alexei Vinogradov. A real-time approach to acoustic emission clustering. *Mechanical Systems and Signal Processing*, 40(2):791 – 804, 2013. ISSN 0888-3270. doi: <https://doi.org/10.1016/j.ymssp.2013.03.017>. URL <http://www.sciencedirect.com/science/article/pii/S0888327013001179>.
- [124] Sebastian Borucki, Jacek Luczak, and Dariusz Zmarzły. Using clustering methods for the identification of acoustic emission signals generated by the selected form of partial discharge in oil-paper insulation. *Archives of Acoustics*, 43(2), 2018.
- [125] Dezső László Beke, Lajos Daróczi, László Zoltán Tóth, Melinda Kalmárné Bolgár, Nora Mohareb Samy, and Anikó Hudák. Acoustic emissions during structural changes in shape memory alloys. *Metals*, 9(1), 2019. ISSN 2075-4701. doi: 10.3390/met9010058. URL <http://www.mdpi.com/2075-4701/9/1/58>.
- [126] Axel Röbel. Analysis/resynthesis with the short time fourier transform, 2006. URL http://recherche.ircam.fr/anasy/roebel/amt_audiosignale/VL2.pdf.
- [127] Lu Zhang, Didem Ozevin, David He, William Hardman, and Alan Timmons. A method to decompose the streamed acoustic emission signals for detecting embedded fatigue crack signals. *Applied Sciences*, 8(1), 2018. ISSN 2076-3417. doi: 10.3390/app8010007. URL <http://www.mdpi.com/2076-3417/8/1/7>.

- [128] ASM Aerospace Specification Metals. <http://asm.matweb.com/search/SpecificMaterial.asp?bassnum=MQ316Q>, 2019. Accessed: 2019-05-01.
- [129] Atlas Steels. http://www.atlassteels.com.au/documents/Atlas_Grade_datasheet_316_rev_Jan_2011.pdf, 2011. Accessed: 2019-05-01.
- [130] AZO Materials. <https://www.azom.com/article.aspx?ArticleID=2382>, 2004. Accessed: 2019-05-01.
- [131] Bing Pan, Liping Yu, Dafang Wu, and Liqun Tang. Systematic errors in two-dimensional digital image correlation due to lens distortion. *Optics and Lasers in Engineering*, 51(2):140 – 147, 2013. ISSN 0143-8166. doi: <https://doi.org/10.1016/j.optlaseng.2012.08.012>. URL <http://www.sciencedirect.com/science/article/pii/S014381661200259X>.
- [132] P. Chowdhury and H. Sehitoglu. Mechanisms of fatigue crack growth – a critical digest of theoretical developments. *Fatigue & Fracture of Engineering Materials & Structures*, 39(6):652–674, 2016. doi: 10.1111/ffe.12392. URL <https://onlinelibrary.wiley.com/doi/abs/10.1111/ffe.12392>.
- [133] C. S. Pande. *Fundamentals of Fatigue Crack Initiation and Propagation: Some Thoughts*. Springer International Publishing, Cham, 2016. ISBN 978-3-319-48105-0. doi: 10.1007/978-3-319-48105-0_1. URL https://doi.org/10.1007/978-3-319-48105-0_1.
- [134] M.N. Bassim, S.St. Lawrence, and C.D. Liu. Detection of the onset of fatigue crack growth in rail steels using acoustic emission. *Engineering Fracture Mechanics*, 47(2):207 – 214, 1994. ISSN 0013-7944. doi: [https://doi.org/10.1016/0013-7944\(94\)90221-6](https://doi.org/10.1016/0013-7944(94)90221-6). URL <http://www.sciencedirect.com/science/article/pii/0013794494902216>.
- [135] T.M. Roberts and M. Talebzadeh. Acoustic emission monitoring of fatigue crack propagation. *Journal of Constructional Steel Research*, 59(6):695 – 712, 2003. ISSN 0143-974X. doi: [https://doi.org/10.1016/S0143-974X\(02\)00064-0](https://doi.org/10.1016/S0143-974X(02)00064-0). URL <https://www.sciencedirect.com/science/article/pii/S0143974X02000640>.

Appendix A Miscellaneous

Figure 200 shows an excerpt from the material certificate of the material used for the test specimens. The chemical composition and some other properties are shown.



CHANDAN STEEL LIMITED
(GOVT. OF INDIA RECOGNISED EXPORT HOUSE)
ISO 9001 : 2008 CERTIFICATE No. 04 100 011022-53

ADM. OFFICE: 504, SUKHI SAGAR, N. S. PATKAR MARG, MUMBAI 400 007, INDIA
Tel.: 91-22- 66290600. Fax.: 91-22-66290633/34
Website : www.chandansteel.net
Email : cs1@chandansteel.net
I/c. No.:
I/c. Date:

WORKS: Plot No. 35, G. I. D. C., Umbergaon
Dist Valsad, Gujarat - 396 171.
Tel.: 91-260- 308 9999 Fax.: 91-260 308 9872
E-mail : exports@chandansteel.net

F824 QC 09 / 02 / 10.12.2012

INSPECTION CERTIFICATE 3.1
ACCORDING TO EN 10204 : 2005


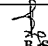
E.A. Smith A S, Avd. Smith Stal Vest Bergen Idrettsvegen 155, 5353 Straume NORWAY		 4027460	Test Certificate No. : EXP/00441 - 45/2013-2014 Date of Issue : 31.08.2013 P.O. No. : 32873 SC_No. & Date : 13-14/00226, Dt. 20.06.2013 Invoice No. & Date : EXP/00441/2013-14 Dtd.31.08.2013								
PRODUCT STAINLESS STEEL FLAT BARS [HRAP]		LENGTH		Net Wt.							
		Ordered	Actual	292 Kgs.							
		6 - 6.10 Mtrs.	6 - 6.10 Mtrs.								
Heat No.	Grade AISI/DIN	Size mm	Tolerance	Process Route							
13/938	316L/1.4404	50 x 10 mm	DIN 1017/EN 10058	Electric Melting, A.O.D. Refining, Continuous Casting							
CHEMICAL COMPOSITION (Weight %)											
	C	Si	Mn	P	S	Cr	Mo	Ni	Cu	Ti	N
Min.	-	-	-	-	-	16.50	2.00	10.00	-	-	-
Max.	0.030	1.00	2.00	0.045	0.030	18.50	2.50	13.00	-	-	0.1100
Results	0.024	0.50	1.75	0.035	0.017	16.89	2.02	10.02	-	-	0.0520
MECHANICAL PROPERTIES											
Specified Values	Test Method :- EN 10002-1					Hardness	Test Method :- BS EN 10045-1				
	Proof Strength		Tensile Strength	Elongation after	Reduction		Charpy (V) Impact Test (2mm) at				
	N/mm ² /MPa		N/mm ² /MPa	Fracture A	of Area		20 °C (Joules)				
	0.2%(Rp0.2)	1%(Rp1.0)	(Rm)	%	%	(BHN)	Sample Size - 10 x 7.5 x 55 mm				
	I	II	III					Avg.			
Results	308	356	612	53	65	174-177	138	145	160	147.67	
Remarks:											
1. Hot Rolled, Shot-Blasted and Pickled.						2. Solution annealed at 1050 °C.					
3. Cold Bend Test Satisfactory.						4. PMI test done 100% & found Satisfactory.					
5. Material is free from radio-active contamination.											
6. Intergranular Corrosion test carried out as per EN/ISO 3651-2-1998 (Test method A) found satisfactory.											
7. Micro structure reveals- equiaxed grains of Austenite & free from carbide Precipitation.											
8. The material conforms to EN - 10088 - 3-2005 & DIN 1017/EN 10058 Specification.											
9. Location of sample - off centre, Direction - Longitudinal, Test Temp - Room Temp., Shape of Test Piece - Flat.											
10. Marking details - Company Logo, Size, Grade & Heat No.											
BUNDLE NO.: 14						COLOUR : GREY					
It is hereby certified that the above results are true and correct in every details and are meeting the requirements of specification & purchase order.						 B.S. RAUTEA MANAGER - QUALITY ASSURANCE					

Figure 200: Chemical composition and properties of the material used for the test specimens

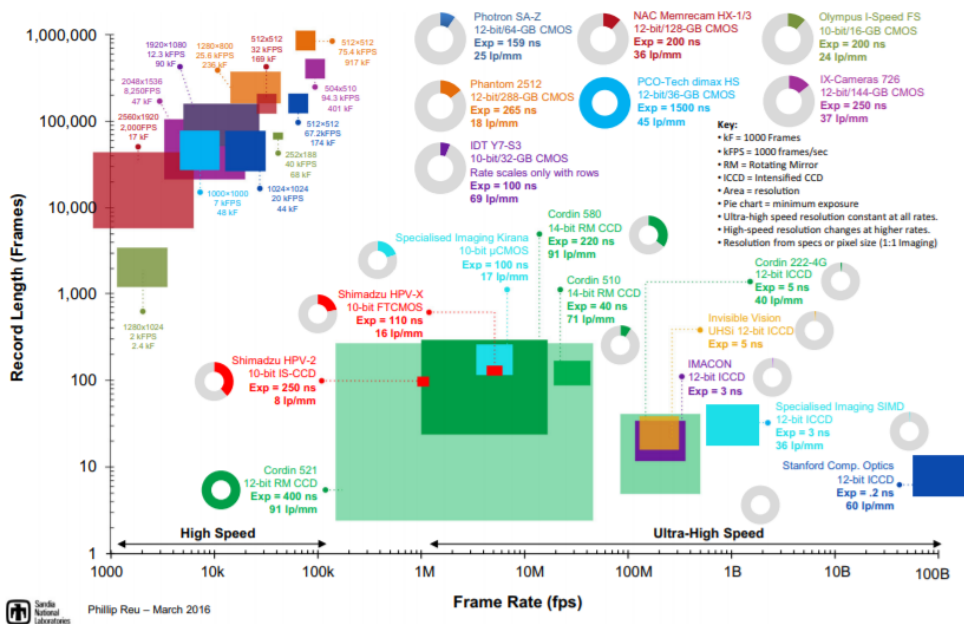


Figure 201: Survey of HS imaging technology. Figure includes Photron SA-Z used in this work. Adopted from: H. Z. Xing, Q. B. Zhang, C. H. Braithwaite, B. Pan, and J. Zhao. High-speed photography and digital optical measurement techniques for geomaterials: Fundamentals and applications. *Rock Mechanics and Rock Engineering*, 50(6):1611–1659, Jun 2017. ISSN 1434-453X. doi: 10.1007/s00603-016-1164-0. URL <https://doi.org/10.1007/s00603-016-1164-0>, courtesy of Dr. Reu [37]

Source	Typical duration (s)
Sunlight	Continuous
Tungsten filament lamps	Continuous
Continuous arc sources and gas discharge lamps	Continuous
Flash bulbs	$0.5 - 5 \times 10^{-3}$
Electronic flash	$10^{-3} - 10^{-6}$
Argon bomb	$10^{-6} - 10^{-7}$
Electrical spark	$10^{-6} - 10^{-9}$
X-ray flash	$10^{-7} - 10^{-9}$
Pulsed laser	$10^{-6} - 10^{-12}$
Super radiant light sources	10^{-9}
LED	Continuous or up to 5×10^{-7}

Table 19: Types of lightning used in high-speed photography (after P W W Fuller. An introduction to high speed photography and photonics. *The Imaging Science Journal*, 57(6):293–302, 2009. ISSN 1368-2199)

